

# **Microphotronics and Nanoislands Integrated Lab-on-Chips (LOCs) for the Detection of Growth Hormones in Milk**

JAYAN OZHİKANDATHIL

A Thesis

in

the Department

of

Mechanical and Industrial Engineering

Presented in partial fulfillment of the requirements for the  
Degree of Doctor of Philosophy (Mechanical Engineering) at

Concordia University

Montreal, Quebec, Canada

August 2012

© Jayan Ozhikandathil 2012

**CONCORDIA UNIVERSITY  
SCHOOL OF GRADUATE STUDIES**

This is to certify that the thesis prepared

By: **Jayan Ozhikandathil**

Entitled: **Microphotonics and Nanoislands Integrated Lab-on-Chips  
(LOCs) for the Detection of Growth Hormones in Milk**

and submitted in partial fulfillment of the requirements for the degree of  
DOCTOR OF PHILOSOPHY (Mechanical Engineering)

complies with the regulations of the University and meets the accepted  
standards with respect to originality and quality.

Signed by the final examining committee:

\_\_\_\_\_ Chair  
Dr. H. Akbari

\_\_\_\_\_ External Examiner  
Dr. K. Venkatakrishnan

\_\_\_\_\_ External to Program  
Dr. Z. Kabir

\_\_\_\_\_ Examiner  
Dr. R. Bhat

\_\_\_\_\_ Examiner  
Dr. R. Sedaghati

\_\_\_\_\_ Thesis Supervisor  
Dr. M. Packirisamy

Approved by \_\_\_\_\_  
Dr. A. Dolatabadi, Graduate Program Director

August 3, 2012

\_\_\_\_\_  
Dr. Robin A.L. Drew, Dean  
Faculty of Engineering and Computer Science

## ABSTRACT

### **Microphotronics and Nanoislands Integrated Lab-on-Chips (LOCs) for the Detection of Growth Hormones in Milk**

**Jayan Ozhikandathil, Ph.D.**  
**Concordia University, 2012**

Lab-on-a-chips (LOCs), alternatively called micro total analysis systems ( $\mu$ TAS) are miniaturized chemical or biological analytical devices that integrate one or several laboratory functions on a single chip. LOCs handle small amount of sample volume and enable the analysis and detection with enhanced performances in short time.

This thesis focuses on developing LOC platforms for the detection of growth hormones such as bovine somatotropin (bST) and recombinant bovine somatotropin (rbST) in milk. Bovine somatotropin is a polypeptide growth hormone naturally produced by the anterior pituitary gland in mammals, which has strong influences on the biological effects such as growth, developments and reproductive functions. The bST is useful to increase the milk and meat production. With the emergence of the recombinant DNA technology, large quantities of artificial hormones called recombinant bovine somatotropin (rbST) are produced and used for the production of milk and meat in dairy industry. Use of growth hormones for the production of milk and meat is still controversial due to its potential effects on animal and human health. Hence, there is a huge demand for highly sensitive, rapid and low cost devices for the detection of growth hormones. Currently, the growth hormones are detected by large equipment which needs large amounts of reagents and bio-liquids in addition to longer analysis time. In this context, there is a large demand for developing a miniaturized bio-analytical platform for the rapid and precise screening of

growth hormones in milk. In this thesis, development of LOC platforms for the labeled and label-free detection of growth hormone is attempted.

The labeled detection of the rbST was demonstrated in a low cost lab-on-a-chip platform fabricated by integrating an optical microfluidic system on silica-on-silicon (SOS) waveguide with a PDMS (polydimethylsiloxane) microfluidic chip. In order to achieve higher sensitivity and specificity, a novel cascaded waveguide coupler (CWC) system is designed and fabricated on the silica-on-silicon platform. A novel method of fabricating nano-island morphology is developed for the label-free detection of bovine growth hormone. Experimental and theoretical analysis of tuning the gold nano-island morphology is investigated and implemented for the label-free detection of growth hormone. Subsequently, the nano-island morphology is integrated into a PDMS microfluidic chip and a LOC is realized. A low cost, all polymer lab-on-a-chip is developed by integrating silver-PDMS nanocomposite by in-situ synthesis of nanocomposite inside the microfluidic chip and detection of growth hormone is also demonstrated. The nano-islands are integrated into silica-on-silicon waveguides for the development of a nano-enhanced evanescent wave sensor for the detection of rbST. Extraction of growth hormone from milk by solid phase extraction and its detection are also demonstrated. Finally, a monolithically integrated LOC on silica-on-silicon (SOS) comprising of microfluidics, optical waveguides and Echelle grating based spectrometer is realized. The simulation and integration process of a micro-spectrometer with the optical waveguide and microfluidic channel are also presented.

## ACKNOWLEDGEMENTS

I would like to express my profound thanks to Dr. Muthukumaran Packirisamy for being my thesis supervisor and giving me the opportunity to realize this work in Optical Bio-Microsystems laboratory MIE, Concordia University. I could not have finished this thesis without his guidance, constant encouragements and financial supports. I had a lot of very interesting and enlightening discussions with him throughout this work.

I would like to express my sincere thanks to Dr. Simona Badilescu for introducing me to the nano-biosensing experiments. I had a lot of very useful discussions with her on nano-biosensors.

I express my sincere thanks to Dr. Rolf Wuthrich for helping me with my device fabrication experiments in the early stages of this thesis work.

I would like to thank Dr. Pierre Pottier for the useful discussions on the FDTD modeling, and Mr. Dylan Lu for training me with the handling of microfabrication equipments in ConSiM clean room of Concordia University.

I am thankful to all my colleagues in the Optical Bio-Microsystems laboratory. Thanks to Dr. Arvind Chandrasekaran, Dr. Roozbeh Ahmadi, Dr. Mohammad Kamal, Stefan Stoenescu, Hamid SadAbadi, Amir Sanati, Mahmoud Ghanbari and Carlos Gustavo for all their help.

I would like to greatly acknowledge the financial supports for the project from the granting agencies: Ministère du Développement Économique, Innovation et Exportation (MDEIE) Québec, Canadian Institute for Photonics Innovations (CIPI) and Valeo

Gestion, Montreal Canada and the technical support of Enablence Inc, Ottawa, Canada and SciMed Technologies Alberta, Canada.

I would like to acknowledge the encouragements and support Dr. Anil Suresh Kumar, Dr. Ramakrishna Reddy Vakiti, Dr. Balasubramanian Esakki, Dr. Hari Babu Boppudi and all my friends in Montreal who have made my stay in Montreal very memorable.

I express my sincere gratitude and thanks to my parents K. Raghavan and Janaki, my sister Rajani, brother Renjith and brother-in-law Vijayan for their strong support and encouragements.

*This thesis is dedicated my parents...*

## TABLE OF CONTENTS

(i)	List of Figures	(xiii)
(ii)	Nomenclature	(xxii)
(iii)	List of symbols	(xxv)
(iv)	List of Tables	(xxviii)
<b>Chapter 1:</b>	<b>Introduction and literature review</b>	<b>1</b>
1.1	Introduction	1
1.2	Lab-on-a-chips (LOCs)	11
1.3	Thesis motivation	22
1.4	Objective and scope of the thesis	23
1.5	Organization of the thesis in a manuscript-based format	25
1.6	Major contributions of the thesis	34
1.7	List of papers Published/Accepted/Submitted/to be submitted	35
<b>Chapter 2:</b>	<b>Silica-on-silicon waveguide integrated polydimethylsiloxane (PDMS) lab-on-a-chip (LOC) for fluorescence bio-detection</b>	<b>38</b>
2.1	Introduction	38
2.2	SOS-PDMS Optical-Microfluidic system	43
2.3	Silica-on-silicon (SOS) waveguide	45
2.4	Device fabrication and Integration	47
2.4.1	<i>Fabrication of SOS chip with waveguide and microfluidics</i>	47
2.4.2	<i>Diamond micromachining of the microchannel</i>	49
2.4.3	<i>PDMS microfluidic platform</i>	50
2.4.4	<i>Integration of PDMS and SOS chip</i>	52
2.4.5	<i>Optical measurement setup</i>	56
2.5	Results and Discussion	57
2.6	Conclusions	60
<b>Chapter 3:</b>	<b>Detection of fluorophore-tagged Recombinant Bovine somatotropin (rbST) by using Silica-on-silicon (SOS)-PDMS Lab-on-a-chip</b>	<b>62</b>
3.1	Introduction	62
3.2	SOS-PDMS Lab-on-a-chip	66

3.3	Experimental details .....	70
3.3.1	<i>Materials and reagents</i> .....	70
3.3.2	<i>Tagging of rbST with FITC</i> .....	71
3.3.3	<i>Tagging of rbST with Alexa-647</i> .....	71
3.3.4	<i>Fabrication of SOS waveguide</i> .....	72
3.3.5	<i>PDMS microfluidic chip</i> .....	73
3.4	Results and discussion .....	76
3.5	Conclusions.....	83
<b>Chapter 4: Detection of recombinant growth hormone by evanescent cascaded waveguide coupler (CWC) on silica-on-silicon (SOS).</b> .....		<b>85</b>
4.1	Introduction.....	85
4.2	Evanescent wave fluorescence sensor .....	89
4.3	Estimation of fluorescence collection efficiency of straight and s-bend waveguides.....	91
4.3.1	<i>The fluorescence collection efficiency of straight waveguide</i> .....	92
4.3.2	<i>The fluorescence collection efficiency of s-bend</i> .....	95
4.4	Fabrication of sensor chip .....	97
4.5	Experimental setup.....	102
4.6	Biosensing experiments.....	106
4.6.1	<i>Materials</i> .....	106
4.6.2	<i>Tagging of rbST with Alexa-647</i> .....	107
4.6.3	<i>Immobilization of fluorescently tagged-rbST on the sensor chip</i> .....	107
4.7	Results and discussion .....	109
4.8	Conclusions.....	111
<b>Chapter 5: Finite-Difference Time-Domain Simulation and implementation of a morphologically-tuned gold-nano-islands integrated biosensor</b> .....		<b>112</b>
5.1	Introduction.....	112
5.2	Localized surface plasmon resonance .....	114
5.3	Manufacturing of nano-islands on a substrate.....	117
5.4	FDTD modeling .....	121

5.5	Dependence of the size of gold nano-hemisphere on the optical absorbance spectrum .....	124
5.6	Modeling of morphology transformation.....	125
5.7	Sensitivity of LSPR of the gold nano-hemisphere to adsorbing protein layer.....	129
5.8	Refractive index sensitivity of gold nano-hemisphere .....	133
5.9	Conclusions.....	136
<b>Chapter 6: Gold nano-island structures integrated in a lab-on-a-chip (LOC) for plasmonic detection of bovine growth hormone .....</b>		
<b>138</b>		
6.1	Introduction.....	138
6.2	Experimental.....	143
6.3	Assembly of the microfluidic platform .....	146
6.4	The experimental procedure for the bio-sensing.....	148
6.5.1	Results and Discussion.....	149
6.5.1	<i>Tuning the morphology of the 3D gold nanostructure from nanoaggregates to nano-islands.....</i>	149
6.6	Sensing experiments: study of the reproducibility and sensitivity of nano-island sensors.....	154
6.7	Sensing experiments in a microfluidic device.....	160
6.8	Conclusions.....	163
<b>Chapter 7: Silver-polydimethylsiloxane nanocomposite integrated lab-on-a-chip for plasmonic detection of bovine growth hormone ....</b>		
<b>165</b>		
7.1	Introduction.....	165
7.2	Method.....	169
7.3	Experimental method and results .....	171
7.3.1	<i>Materials .....</i>	171
7.3.2	<i>Preparation of silver-PDMS nanocomposite substrate .....</i>	172
7.3.3	<i>Tuning of morphology and optical property of the silver-PDMS nanocomposite .....</i>	173
7.4	Procedure for the biosensing on silver-PDMS substrate .....	179
7.5	Fabrication of Lab-on-a-chip.....	183
7.6	Integration of silver-PDMS nanocomposite into a LOC environment .....	187

7.7	Biosensing in the Lab-on-a-chip .....	190
7.8	Conclusions.....	192
<b>Chapter 8: Nano-islands integrated evanescence-based lab-on-a-chip on silica-on-silicon and PDMS hybrid platform for the detection of recombinant growth hormone.....193</b>		
8.1	Introduction.....	193
8.2	Materials and method .....	198
8.2.1	<i>Materials</i> .....	198
8.2.2	<i>Gold nano-islands integrated LOC</i> .....	198
8.3	Fabrication of silica-on-silicon optical chip .....	201
8.4	Integration of nano-islands on the silica-on-silicon waveguide.....	203
8.5	Fabrication of the gold nano-island integrated LOC.....	206
8.6	FDTD simulation of the device.....	208
8.7	Experimental setup for nano-islands integrated LOC .....	212
8.8	Biosensing.....	215
8.8	Results and discussion.....	217
8.9	Conclusions.....	220
<b>Chapter 9: Detection of recombinant bovine growth hormone (rbST) in milk using gold nano-islands biosensor ..... 221</b>		
9.1	Introduction.....	221
9.3	Materials.....	223
9.3	Solid phase extraction (SPE) .....	224
9.4	Results and discussion.....	225
9.5	Conclusions.....	228
<b>Chapter 10: Monolithically integrated lab-on-a-chip on silica-on-silicon platform.....229</b>		
10.1	Introduction.....	229
10.2	Monolithically integrated lab-on-a-chip .....	230
10.3	Basics of diffraction grating .....	231
10.4	Modeling of concave grating based micro-spectrometer by FDTD.....	233
10.5	Fabrication of monolithically integrated lab-on-a-chip .....	236
10.6	Conclusions.....	238

<b>Chapter 11: Conclusions and future scope of the works .....</b>	<b>239</b>
11.1 Conclusions.....	239
11.2 Future works .....	245
References .....	246
<b>Appendix A: Low resistive silicon substrate as an etch-stop layer for drilling thick SiO<sub>2</sub> by Spark Assisted Chemical Engraving.....</b>	<b>264</b>
A1. Introduction.....	265
A2. Experimental details .....	267
A3. Results and discussion.....	269
<i>A3.1 Machining on (100) Silicon substrate.....</i>	<i>269</i>
<i>A3.2 DC micromachining of thick SiO<sub>2</sub> layer on low resistivity silicon ....</i>	<i>270</i>
<i>A3.3 Drilling using pulsed DC voltage .....</i>	<i>275</i>
A4. Conclusions.....	277

## List of Figures

- Figure 1.1** (a) Structure of amino acids and (b) formation of peptide.
- Figure 1.2** Evolution of the analytical methods for the detection of proteins (hormones, etc.) in various environments (food, soil, etc.)
- Figure 1.3** Reaction of FITC-Peptide conjugation.
- Figure 1.4** Classification of LOC based on the integration process, sensing and fluidic actuation schemes.
- Figure 1.5** A generalized block diagram representing various processes involved in the LOC (Figure adopted from Book: BioMEMS Science and engineering perspectives, S. Badilescu and M.Packirisamy 2011)
- Figure 1.6** Fluorescence detection systems on silica-on-silicon waveguide (Figure adopted from Ruano et al.2003).
- Figure 1.7** Fully integrated  $\mu$ TAS (Adapted from Balslev et al.)
- Figure 1.8** Optical waveguide and fluidic trench monolithically integrated on PDMS (Figure adopted from David A. Chang-Yen et al.).
- Figure 1.9** Hybrid integrated optical microfluidic system for the fluoresce detection (Adopted from Chandrasekaran et al.)
- Figure 1.10** Gold nanoparticle integrated microfluidic device for the label-free detection (Figure adopted from Yi Zhang et al.)
- Figure 2.1** (a) Schematic illustration of silica-on-silicon-PDMS Optical-Microfluidic system (b) SOS waveguide with a straight microchannel.
- Figure 2.2** Illustration of Silica-on-silicon waveguide.
- Figure 2.3** Silica-on-silicon (SOS) waveguides used for the fabrication of SOS-PDMS Lab-on-a-chip, (a) waveguide diced into 4.5X6.5mm sample, SEM image of SOS waveguide before (b) and after (c) polishing using diamond lapping film.
- Figure 2.4** (a) Top view showing the width and (b) Cross sectional view showing the depth of the microchannel fabricated by diamond micromachining method.

- Figure 2.5** Brass mold and PDMS chip
- Figure 2.6** (a) SOS-PDMS Lab-on-chip (b) Close up of the flow in transition microfluidic zone between SOS and PDMS chip.
- Figure 2.7** Opto-mechanical setup with SOS-PDMS Lab-on-a-chip.
- Figure 2.8** Fluorescence emission measured from QD 655 for different concentrations
- Figure 2.9** Variation of fluorescence intensity against the concentration of quantum dot.
- Figure 3.1** Schematic illustration of SOS-PDMS Lab-on-chip.
- Figure 3.2** Illustration of integration of SOS-PDMS Lab-on-a-chip, (a) 3D view of the microfluidic chip on PDMS and SOS chip and (b) sectional view showing the microfluidic path and SOS chip.
- Figure 3.3** (a) SEM of waveguide facet (b) PDMS microfluidic chip.
- Figure 3.4** (a) Microscope image of SOS waveguide with microchannel (b) SOS-PDMS Lab-on-a-chip.
- Figure 3.5** Experimental setup with SOS-PDMS Lab-on-a-chip.
- Figure 3.6** UV-Visible absorbance spectrum of (a) FITC conjugated rbST, (b) Alexa-647 conjugated rbST.
- Figure 3.7** Fluorescence detection of (a) FITC conjugated rbST and (b) Alexa-647 conjugate rbST.
- Figure 3.8** Fluorescence intensity measured in the LOC for the tagged and unbound fluorophores against the concentration,  $C_f$ .
- Figure 4.1** (a) Evanescent wave sensor, (b) Sketch of the SOS waveguide with antibody and tagged-antigen immobilized on core.
- Figure 4.2** (a) The FDTD model of waveguide with a point source (b) refractive index distribution of the model.
- Figure 4.3** (a) FDTD Simulation, (b) fluorescence collection efficiency against the distance  $d$  of the source from the waveguide for different waveguide widths.

- Figure 4.4** (a) FDTD simulation of fluorescence coupling of light by s-bend and (b) The estimated fluorescence collection efficiency against the radius (R) of the S-bend.
- Figure 4.5** Schematic of evanescent wave sensor using cascaded waveguide coupler in comparison with a straight waveguide.
- Figure 4.6** Fabrication process steps of SOS waveguide.
- Figure 4.7** Refractive index of the core and cladding layer against the wavelength.
- Figure 4.8** SEM micrograph of SOS waveguide, (a) s-bend coupler of the multiple waveguide system stage S1 (b) multiple waveguides in the stage 3 (S3) of cascaded waveguide coupler (c) etch profile of the waveguide (d) dimensions of the core of the waveguide.
- Figure 4.9** Experimental setup for the cascaded waveguide coupler sensor, (a) schematic of the experimental setup, and (b) photograph of the experimental setup.
- Figure 4.10** Experimental setup for imaging the end facet of waveguide, (a) schematic diagram of the setup, (b) photograph of the experimental setup and (c) microscope image showing the coupling of light to the waveguide taken from the top of the waveguide.
- Figure 4.11** (a) Microscope image showing the waveguide with light coupled (a) multiple waveguide (b) single waveguide.
- Figure 4.12** Image of the waveguide facet (a) Single waveguide (b) Multiple waveguide.
- Figure 4.13** Steps involved in the functionalization of waveguide chip, (a) modify the waveguide surface with APTES silane to absorb the anti-rbST (b) absorb anti-rbST and (c) block non-specific sites and (d) absorb the tagged rbST.
- Figure 4.14** Fluorescence signal recorded in the sensor chip after antigen-antibody binding for various concentrations of tagged-rbST, for (a) single waveguide (b) cascaded waveguide coupler.
- Figure 4.15** Variation of fluorescence signal against the concentration of tagged-rbST.
- Figure 5.1** Fabrication strategy of the gold nano-island structure on a substrate. (a) angled convective assembly (b) schematic of gold aggregates and (c) schematic of gold nano-islands structure.

- Figure 5.2** SEM micrographs of (a) Nano-cluster obtained after deposition (b) annealed at 400-450<sup>0</sup>C (c) annealed at 550-600<sup>0</sup>C.
- Figure 5.3** UV-Visible absorbance spectrum of (a) non-annealed sample, (b) samples annealed at 400-450<sup>0</sup>C, and (c) samples annealed at 550-600<sup>0</sup>C.
- Figure 5.4** (a) Schematic of the model (b) 3D-FDTD model of the gold hemisphere FDTD Simulation (c) Electric field distribution estimated by FDTD in the gold nano-hemisphere.
- Figure 5.5** (a) Measured LSPR spectrum (b) Simulated LSPR spectrum of the gold nano-hemisphere.
- Figure 5.6** (a) Optical absorbance spectrum of gold nano-hemisphere, (b) A red-shift of peak wavelength against the size of the gold nano-hemisphere.
- Figure 5.7** (a) FDTD Model of four hemispheres morphology (b) Refractive index distribution of the FDTD Model from the top of the model.
- Figure 5.8** (a) LSPR spectrum of the gold nano-hemisphere against the particle separation distance, *d*,
- Figure 5.9** The influence of spacing on near field coupling strength between four gold nano-hemispheres.
- Figure 5.10** Schematic of biosensor with gold hemispheres and a protein layer.
- Figure 5.11** Change of LSPR spectrum against the thickness of the protein layer with a refractive index of (a) 1.5 and (b) 1.4.
- Figure 5.12** Variation of LSPR peak against the thickness of the protein.
- Figure 5.13** Measured shift of LSPR band in various solvents
- Figure 5.14** Simulated LSPR spectrum of gold nano-hemisphere with protein layer having the refractive index of solvents.
- Figure 5.15** Measured and simulated variation of LSPR shift against change in refractive index.
- Figure 6.1** Schematic sketch of the convective assembly process of gold nanoparticles.
- Figure 6.2** Schematic sketch of the deposition of gold nanostructure on glass.
- Figure 6.3** Assembly process of the microfluidic device.

- Figure 6.4** Photograph of the nano-islands integrated microfluidic bio-sensor.
- Figure 6.5** Images of the non-annealed sample (a), sample annealed at 550<sup>0</sup>C for 1 hour (b) and enlarged images of the samples showing the stripping behavior (c).
- Figure 6.6** SEM images of 3D gold nanostructures, as deposited (a) and after annealing at 550<sup>0</sup>C for 1 hour (b) (the magnification is X100000 in both images and X200000 in inset).
- Figure 6.7** UV-Visible spectra of gold nanostructures deposited on glass, (a) before annealing and (b) after annealing at 550<sup>0</sup>C for 1 hour.
- Figure 6.8** UV-Vis spectra of gold multilayers non-annealed (a) and annealed at 500<sup>0</sup>C for 1h (b) (multilayers deposited from a colloidal solution with a lower concentration of Au, 25  $\mu$ g/mL).
- Figure 6.9** Sensitivity of the platforms to the change in the refractive index of the environment for the annealed and for the non-annealed sample (The error bar represents the standard deviation of 10 measurements).
- Figure 6.10** The shift of LSPR band over the binding time of the antibody (100 ng/ml) and antigen (40 ng/ml). (Error bar represents the standard deviation of 4 measurements).
- Figure 6.11** Spectra corresponding to a concentration of 40 ng/mL bST (antigen). Annealed gold nanostructure (550<sup>0</sup>C) (a), antibody was adsorbed on the sample (b) and the antigen was adsorbed on the gold holding the antibody. The shift due to antibody-antigen interaction is 10 nm. For clarity, the spectra corresponding to different intermediate states (functionalized gold nanoparticles, activated carboxyl group, etc.) are omitted.
- Figure 6.12** Sensing curve: Shift in the wavelength ( $\Delta\lambda$ ) versus antigen concentration (Inset: the sensitivity for low concentration of polypeptides (between 1 and 100 ng/ml.)) (Error bars represent the standard deviation of 10 measurements).
- Figure 6.13** Experimental setup of PDMS/ glass nano- integrated micro bio-sensor.
- Figure 6.14** Sensing results in the device.
- Figure 6.15** Sensing result in the microfluidic device.

- Figure 7.1** Schematic of the proposed Lab-on-a-chip.
- Figure 7.2** Images of the Ag-PDMS samples (a) non-annealed (b) annealed at 340<sup>0</sup>C (c) annealed at 370<sup>0</sup>C.
- Figure 7.3** SEM image of (a) non-annealed sample, (b) annealed at 340<sup>0</sup>C, (c) annealed at 370<sup>0</sup>C and (d) enlarged image (X75000)of sample annealed at 370<sup>0</sup>C.
- Figure 7.4** AFM characterization of silver-PDMS nanocomposite (a) non-annealed (b) annealed at 340<sup>0</sup>C, (c) annealed at 370<sup>0</sup>C and (d) line profile showing the height of the nanoparticle in composite.
- Figure 7.5** Absorbance spectrum of the silver-PDMS nanocomposite of (a) non-annealed, (b) annealed at 340<sup>0</sup>C (c) annealed at 370<sup>0</sup>C.
- Figure 7.6** Various steps in the biosensing.
- Figure 7.7** Shift of LSPR spectra of silver-PDMS upon antigen-antibody interaction, (a) LSPR spectrum of the silver-PDMS nanocomposite functionalized with antibody (100 ng/ml) and (b) LSPR spectrum of the composite after adding antigen (150 ng/ml).
- Figure 7.8** Effect of annealing temperature and concentration of bST on biosensing with Ag-PDMS substrate.
- Figure 7.9** Fabrication process steps of the lab-on-a-chip.
- Figure 7.10** Mold for the microfluidic device.
- Figure 7.11** Silver-PDMS nanocomposite integrated Lab-on-a-chip.
- Figure 7.12** Schematic top view of the test arrangement with UV-visible source and spectrometer.
- Figure 7.13** (a) Device under test (b) closer view of the test section of the device through microscope (c) Experimental setup for the Lab-on-a-chip.
- Figure 7.14** UV-Visible spectra recorded using the lab-on-a-chip, (a) Spectrum recorded before annealing the device and (b) Spectrum recorded after annealing the device.
- Figure 7.15** The sensing results conducted in the lab-on-a-chip, (a) spectrum recorded after adding the antibody (100ng/ml) and (b) spectrum after adding the antigen (100ng/ml).

- Figure 8.1** Schematic diagram of integration process of the LOC, (a) PDMS microfluidic chip (a) SOS optical chip integrated with gold nano-islands and (c) sectional view of the LOC.
- Figure 8.2** Fabrication process steps of gold nano-islands integrated LOC.
- Figure 8.3** SEM image of the SOS waveguide showing the sectional view of waveguide with the core and cladding dimensions.
- Figure 8.4** Illustration of the method of integration of gold nano-islands on the silica-on-silicon optical chip. (a) SOS waveguide in gold colloidal solution, (b) gold nano-structure on the waveguide and (c) Gold nano-islands on silica-on-silicon optical chip.
- Figure 8.5** SEM micrograph of gold nano-islands integrated silica-on-silicon waveguide (a) waveguide with gold nano-cluster (b) closer view of the nano clusters, (c) the waveguide after annealing and (d) closer view of waveguide after annealing.
- Figure 8.6** Schematic of the microfluidic chip.
- Figure 8.7** Gold nano-islands integrated LOC.
- Figure 8.8** FDTD model of the device.
- Figure 8.9** (a) Refractive index of the model (b) Electric field distribution in the model.
- Figure 8.10** (a) LSPR spectrum of the gold nano-islands integrated on the core of the SOS waveguide and (b) LSPR peak wavelength against the refractive index of the cladding of the SOS waveguide.
- Figure 8.11** Testing setup for nano-enhanced evanescence measurement (a) Schematic of the experimental setup (b) Photograph of the experimental setup.
- Figure 8.12** Transmittance spectrum recorded in the nano-island integrated LOC.
- Figure 8.13** Steps used in the detection of rbST in the nano-islands integrated LOC.
- Figure 8.14** Change of transmittance spectrum against the antibody-antigen interaction of rbST (a) Spectrum with gold nano-islands on the waveguide (b) spectrum after antibody (anti-rbST: 100 ng/ml) is adsorbed to the gold nano-islands and (c) spectrum after antigen (rbST: 800 ng/ml) is adsorbed to gold nano-islands.

- Figure 8.15** Effect of concentration of rbST on the shift of minimum transmittance due to antibody-antigen interaction of rbST.
- Figure 9.1** SPE C4 column setup.
- Figure 9.2** Absorbance spectrum of the protein mixture separated from milk.
- Figure 9.3** (a) Change of LSPR property of the gold nano-island structure in the variation stages of the immunoassay((1) before the starting the immunoassay, (2) after anti-rbST was adsorbed to the gold and (3) after rbST was adsorbed to the gold). (b) The sensing experiments carried out on various concentration of the rbST; shift of LSPR as a function of concentration of rbST (ng/ml).
- Figure 10.1** Schematic of monolithically integrated lab-on-a-chip.
- Figure 10.2** Diffraction on grating surface, showing the relation between the rays diffracted from the adjacent grooves.
- Figure 10.3** Rowland spectrograph configurations.
- Figure 10.4** FDTD model of the concave spectrometer.
- Figure 10.5** Efficiency calculated for the configuration shown in Figure 10.4, Aluminum coated grating facet is shown to be enhancing the efficiency.
- Figure10.6** (a) Photograph of the lab-on-a-chip (b) SEM images taken at different regions of Lab-on-a-chip: (A) At waveguide microfluidic intersection, (B) 8 Y Couplers (C) final Y coupler, (D) Photograph of the grating.
- Figure A1** (a) SEM micrograph illustrating the SiO<sub>2</sub> layer on silicon substrate (b) An illustration of the microholes on different places of SiO<sub>2</sub> Layer, (c) Tool electrode used for the SACE micromachining.
- Figure A2.** Relative movement of tool  $Z(t)$  and current signal in SACE machining of Silicon.
- Figure A3** (a) Progress of drilling depth  $Z(t)$  (Mean over 7 drillings) for different voltages (b) Maximum drilling depth  $Z_{max}$  after 7 seconds for various voltages.
- Figure A4** (a) SEM micrograph of drilled holes under different DC voltage, (b) Profile of etched holes under different DC voltages.
- Figure A5** Illustration of verticality of the hole as a function of voltage.
- Figure A6** Schematic of SACE drilling of SiO<sub>2</sub> deposited on Si by gravity-feed.

**Figure A7** (a) Pulse voltage used for SACE machining, (b) Progress of etching for pulses with various OFF time and constant ON time of 2 ms at 28V.

**Figure A8** (a) SEM micrographs of drilled hole with different pulse OFF time, and constant ON time. (b) Etch profile of hole with different pulse OFF time and constant ON time.

**Figure A9** Variation of verticality of the hole against of pulse OFF time.

## **Nomenclature**

$\mu$ CP	Microfluidic assisted Chemical Polishing
$\mu$ TAS	Micro Total Analysis System
AF647	Alexa Fluor 647
AFM	Atomic Force Microscope
APTES	Aminopropyltriethoxysilane
ATP	Adenosine Triphosphate
BioMEMS	Bio-Micro-Electro-Mechanical Systems
bGH	Bovine Growth Hormone
bST	Bovine Somatotropin
BSA	Bovine Serum Albumin
CCD	Charge-Coupled Device
CMOS	Complementary Metal Oxide Semiconductor
CMP	Chemical Mechanical Planarization
CNC	Computer Numerical Control
COC	Cyclic Olefin Copolymer
CWC	Cascaded Waveguide Coupler
DI	Deionized
DNA	Deoxyribo Nucleic Acid
DRIE	Deep Reactive Ion Etching
DWL	Direct Write Lithography
EDC	Ethyl-3-(3-dimethylaminopropyl) carbodiimide

ELISA	Enzyme-Linked Immunosorbent Assay
FDTD	Finite Difference Time Domain
MOSFET	Metal Oxide Semiconductor Field Effect Transistor
FEG-SEM	Field Emission Gun Scanning Electron Microscope
FFT	Fast Fourier Transform
FHD	Flame Hydrolysis Deposition
FITC	Fluorescein isothiocyanate
ISFET	Ion Sensitive Field-Effect Transistor
IPA	Isopropyl Alcohol
LbL	Layer-by-layer
LC-MS	Liquid Chromatography-Mass Spectrometry
LIF	Laser Induced Fluorescence
LOC	Lab-on-a-Chip
LSPR	Localized surface Plasmon Resonance
MEMS	Micro-Electro-Mechanical Systems
MW	Molecular Weight
NEET	Nano-Enhanced Evanesence detection Technique
NHS	N-hydroxysuccinimide
NP	Nanoparticle
NSL	Nano-Sphere Lithography
PBS	Phosphate Buffer Saline
PDMS	Polydimethylsiloxane
PECVD	Plasma Enhanced Chemical Vapor Deposition

PMMA	Poly Methyl Methacrylate
PML	Perfectly Matched Layer
POCT	Point-of-Care Testing
PON	Point-of-Need
rbST	Recombinant Bovine Somatotropin
RP-HPLC	Reverse Phase High-Performance Liquid Chromatography
RI	Refractive Index
RIA	Radioimmunoassay
RIE	Reactive Ion Etching
RIU	Refractive Index Unit
SACE	Spark Assisted Chemical Engraving
SEM	Scanning Electron Microscopy
SERS	Surface Enhanced Raman Scattering
SOC	Spectrometer-on-Chip
SOS	Silica-on-Silicon
SPE	Solid Phase Extraction
SPR	Surface Plasmon Resonance
TE	Transverse Electric
TFA	Trifluoroacetic acid
TLC	Thin Layer Chromatography
UV	Ultra Violet Light
UPLC	Ultra Performance Liquid Chromatography
QD	Quantum dot

## List of symbol

A	Absorbance
Ar	Area
$C_f$	Concentration of fluorophore
c	Velocity of light
cm	Centimeter
d	Distance
dp	Evanescent penetration depth
ds	Grove spacing
D	Diameter of nano-islands
Da	Dalton, $1 \text{ Da} = 1.660540 \times 10^{-24} \text{ kg}$
dB	Decibels
E	Electric field
I	Intensity of light
h	Hour
kDa	kilo Dalton
MHz	Mega Hertz
M	Molar
m	Order of diffraction
mW	milliwatt
mm	millimeters
mT	milli Torr

$n_c$	refractive index of cladding
$P_i$	Power of excitation
ng	nanogram
nm	nanometer
$\mu\text{g}$	microgram
$\mu\text{l}$	microliters
$\mu\text{m}$	micrometers, microns
$\mu_m$	Permeability
$\lambda$	Wavelength of light
$\lambda_m$	Absorbance peak wavelength corresponding to the medium.
$\lambda_w$	Absorbance peak wavelength corresponding to de-ionized water
$\Delta\lambda$	Plasmon shift
$\Delta n$	Index difference
$\varepsilon$	Extinction coefficient
$\theta$	Angle
$\theta_d$	Diffraction angle
$\theta_i$	Incident angle
$\theta_c$	Critical angle
$s$	Geometry factor of nanoparticles
wt	Weight
sccm	Cubic centimeters per minute
$^{\circ}\text{C}$	Degree Celsius
$Q_y$	Quantum yield

$W$	Watts
$\omega_p$	Plasma frequency of the free electrons
$\omega$	Angular frequency of the light
$\gamma$	Collision frequency of the electrons present in the bulk materials
$\alpha$	Polarizability
$\epsilon_m$	Dielectric constant of medium

## List of Tables

- Table 3.1** Optical properties of the fluorophores.
- Table 6.1** Solvents used for measuring the refractive index sensitivity of annealed and non-annealed sensing platforms.
- Table 10.1** Parameters used for the simulations.
- Table 11.1** Comparison of Lab-on-a-chips developed in this thesis.

# **Chapter 1: Introduction and literature review**

## **1.1 Introduction**

Bovine growth hormone (bGH), also known as bovine somatotropin (bST) is a protein molecule having a polypeptide chain of 191 amino acids [1]. The bST is produced naturally by the anterior pituitary glands of mammals and it has several complex biological functions such as growth, development and reproduction. The role of bST in lactation in mammals was identified in 1937[2]. The bST increases the tissue metabolism and the uptakes of nutrients leading to an enhanced synthesis of milk. Therefore, the bST has been employed in dairy industry as a growth promoter for enhancing the production of milk and meat. The level of bST in blood can be increased by injecting it in cattle and hence the milk yield is increased. The bST has also been used for the treatment of growth disorder such as dwarfism [3]. As the growth hormone increases the tissue metabolism, it has been reported to be misused in sports for increasing the muscle mass in humans and horses.

Polypeptides are made up of amino acids and they are the building blocks of proteins[4]. Figure 1.1 illustrates the formation of peptide chain from two amino acids molecules. The structure of amino acid is shown in Figure 1.1 (a).

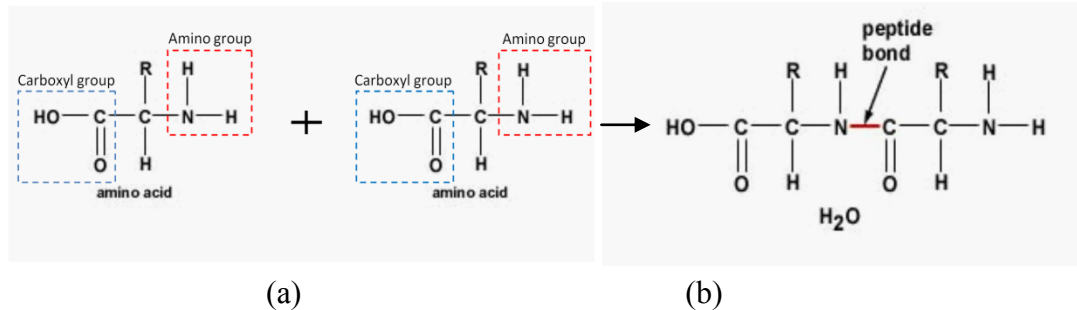


**Figure 1.1** (a) Structure of amino acids and (b) Formation of peptide[4].

The carboxyl (COOH) and amino (NH<sub>2</sub>) groups of two amino acid reacts and form the peptide bonds of polypeptides as shown in Figure 1.1(b). Research on polypeptides is significantly important because they are widely used as drugs in therapeutic treatment [5-7], disease markers [8, 9], antimicrobial animal feed additives and analytes for protein identification in proteome research [10].

The development of genetic engineering has made possible the cloning of polypeptides using recombinant DNA technology [11, 12]. The recombinant DNA technology could produce a large amount of artificial hormone for various applications. The artificial hormone is commonly referred to as recombinant bovine growth hormone (rBST) or recombinant bovine somatotropin (rbST). The chemical structure of rbST can be slightly different from the bST, because the manufacturing process of rbST may add a few extra amino acids at the end of bST molecules. The number of extra amino acids in the rbST may vary between 1 to 10 and it has been reported that these extra amines do not alter the biological activity [13]. As the recombinant DNA is a low cost technology, the production of large quantities of rbST can lead to misuse. Use of rbST is controversial [14-16], because it could be potentially harmful to the health of human and animal. The use rbST is legal in dairy

farming in some Asian countries, Mexico and USA. However, it is banned in Canada and European Union. Hence, there is a huge demand for a rapid and precise screening method for the growth hormone in dairy industry. The methods of detection of bovine growth hormone reported in literature are based on the protein detection methods by using macroscopic instruments which require long time, large amounts of biomaterial and reagents. This thesis aims at developing miniaturized sensor platforms so that the detection and analysis of bovine growth hormone can be carried out faster by using small amounts of biomaterials for the point of need (PON) applications.

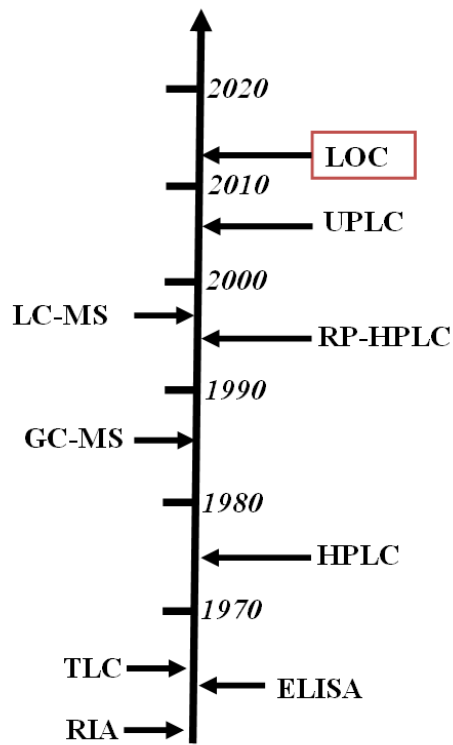


Figure 1.2 Evolution of the analytical methods for the detection of proteins (hormones, etc.) in various environments (food, soil, etc.)

An evolution chart of analytical methods reported in literature for the detection of traces of protein is given in Figure 1.2. The earliest methods of detection of protein are thin layer chromatography (TLC) [17], enzyme-linked immunosorbent assay (ELISA) and radioimmunoassay (RIA). High-performance liquid chromatography (HPLC) is a most widely used chromatography method for the past thirty years for the separation of proteins from a complex mixture, in which discrete volumes of sample are passed through column at various velocities. The nature of analytes is analyzed based on the time taken for the elution of sample through the column. Though the concept of gas chromatography-mass (GC-MS) spectrometry was introduced in the early 1960s [18], the successful demonstration of GC-MS for the drug detection, environmental analysis is carried out by the 90's[19]. The disadvantage of the GC-MS is that the analytes should be thermally stable under GC conditions [20]. The resolving power of the HPLC is greatly enhanced in ultra performance liquid chromatography (UPLC) [21] by reducing the size of the silica particle used on the separation column. The analytical method explained so far are based on large macroscopic instruments, hence the miniaturized analytical systems or lab-on-a-chip (LOC) is essential for the rapid and point-of-need (PON) applications. Several protein detection methods such as enzyme-linked immunosorbent assay (ELISA) [22, 23], radioimmunoassay (RIA) [24] or bioassay methods [25] and Surface Plasmon Resonance (SPR) [26] are demonstrated for the detection of growth hormone. ELISA is a widely used protein detection method, which works based on the immunoassay. In immunoassay, the concentration of protein is measured by a specific antigen (protein)-antibody interaction. For ELISA, a known amount of

antibody is introduced to the substrate functionalized with the unknown amount of protein to be detected. The reaction of antigen and antibody is detected by introducing an enzyme and the detection is carried out by observing the color change occurring on the substrate using a colorimetric method. The disadvantage of ELISA is that it predicts the concentration of bST in a relative term based on the affinity and concentration of antibody. RIA is a labeled detection approach, in which the antigen is tagged with a radioactive substance and hence the antigen-antibody interaction is detected by measuring the gamma rays by using a gamma counter. The radioimmunoassay requires special apparatus, license to use it and radiation safety precautions. Liquid Chromatography Mass Spectroscopy (LC-MS) is a powerful bioassay method widely reported for the screening of polypeptides, which has high sensitivity and specificity to the molecules of interest. Liquid chromatography is used to separate the protein of interest from a complex mixture of protein and detect by using mass spectroscopy. In mass spectroscopy, the proteins are ionized using gas phase, electron spray or chemical ionization method and proteins are separated based on mass-to-charge ratio and analyzed by electromagnetic fields. The LC-MS is a complex process and it requires expensive instruments. In surface plasmon resonance (SPR) sensors, a thin layer of noble metals such as gold or silver is coated on the sensing substrate. The surface plasmon waves are excited by coupling the light to a thin metal layer by a prism and the protein adsorbed on the metal layer changes the plasmonic property.

The proteins having aromatic amino acids exhibit intrinsic fluorescence properties, therefore, they can be detected and quantified through their emission properties [27].

Mary K Lawless et al. [28] reported the application of reverse phase high-performance liquid chromatography (RP-HPLC) for the separation and quantification of 36 amino acid peptides. This peptide has intrinsic fluorescence properties, therefore the detection was achieved by the excitation light of 280 nm and the emission recorded at 350 nm. The peptides having no fluorescent properties need to be tagged with the fluorescent material for the detection. In 1970, T.E.W Feltkemp et al. [29] published a work on tagging of Immunoglobulin G (IgG) with Fluorescein Isothiocyanate (FITC) and the use of column chromatography for the separation of labeled molecules. FITC has the absorption and emission peak at 495 nm and 525 nm respectively. The reaction leading to the formation of FITC conjugated polypeptides is illustrated in Figure 1.3, herein, the free amino group of peptides forms a stable thiourea bond with the FITC molecules.

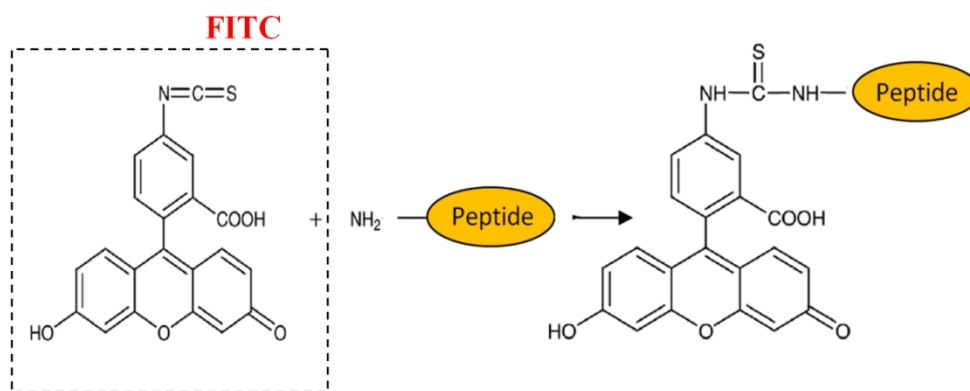


**Figure 1.3** Reaction of FITC-Peptide conjugation[30].

In this thesis, miniaturized analytical systems are developed for the detection of bST and rbST. Miniaturized analytical devices commonly referred to as micro total analysis systems ( $\mu$ TAS) or Lab-on-a-chips (LOCs) are fabricated by integrating one or multiple biochemical analytical process modules in a single chip [31]. One of the main process modules in the lab-on-a-chip is microfluidic circuits, which transport and handle small amount of bio-liquids and reagents for the detection and analysis. A detailed classification map of the lab-on-a-chips based on the integration process, sensing method and actuation schemes is illustrated in Figure 1.4 [32]. Two approaches of integration processes are commonly used for the lab-on-a-chip, namely, hybrid and monolithic integration.

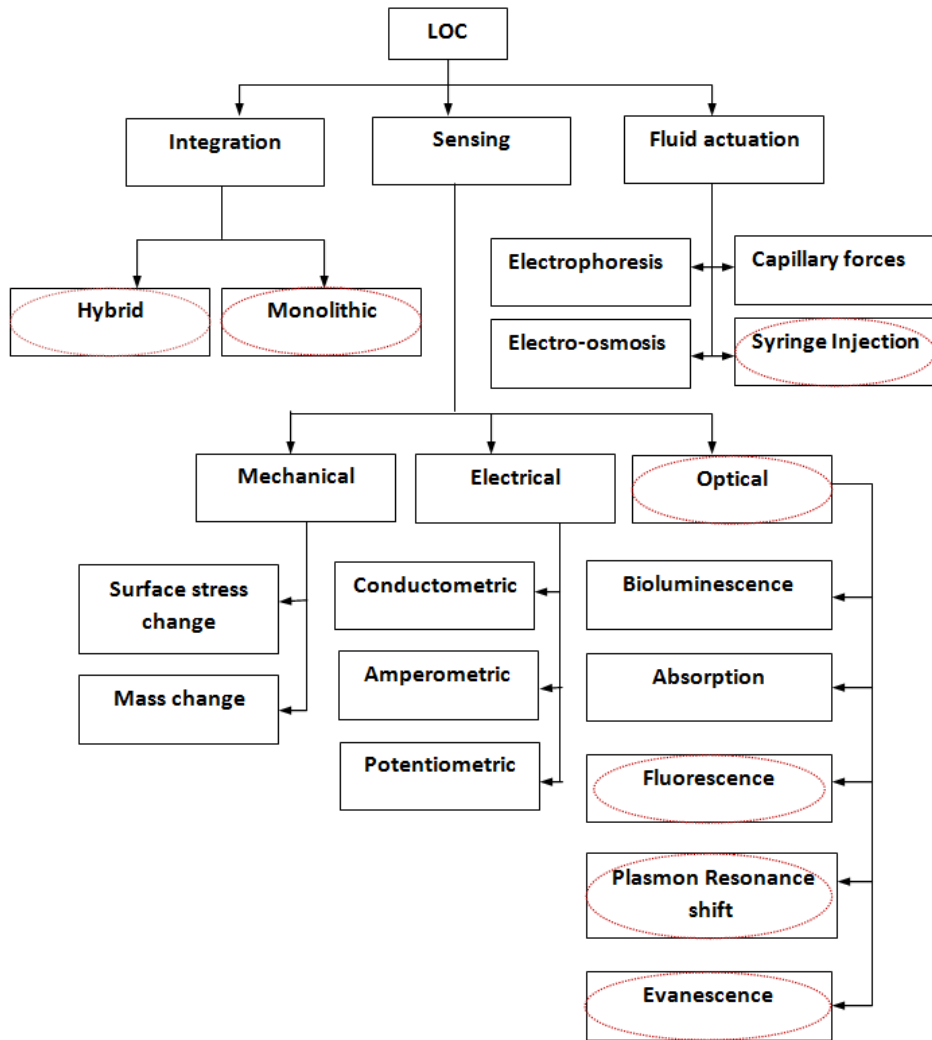


Figure 1.4 Classification of LOC based on the integration process, sensing and fluidic actuation schemes.

In monolithic integration, all the process modules are integrated in a single material platform, which is useful for the fabrication of a compact and portable device. However, often times, it is required to use different materials for various requirements of micro total analysis systems. Hence a hybrid integration approach will be suitable in this scenario. In this thesis both the hybrid and monolithic integration approaches

are investigated. The fluid actuation schemes used in the micro total analysis systems are electrophoresis, capillary forces, electro-osmosis and syringe injection. As the syringe injection is the simplest method, it is used in this work.

The sensing techniques used in the  $\mu$ TAS are mechanical, optical and electrical as illustrated in Figure 1.4. Mechanical detection of biochemical reactions are demonstrated with micro or nano-scale cantilever sensor chips [33]. The biochemical reaction performed on the cantilever introduces a change in surface stress or mass, which could be measured from the deflection or natural frequency of the cantilever. Optical based detection is the most generally used method because of their widespread use in biology and life science. A wide variety of detection methods are reported based on the change of property of light due to the biochemical reaction [32, 34]. Optical detection can be based on chemiluminescence [35], absorption, fluorescence, plasmon resonance shift or evanescence [36]. Absorption is an earliest optical detection method, which depends on the chromophores present in the biospecies that are responsible for the absorption of light. The biochemical reactions which release light are termed as chemiluminescent. Therefore the biodetection is possible through the chemiluminescent by detecting the light. Fluorescence detection is based on the fluorescent labels, which are tagged with biospecies, hence the monitoring of the biochemical reaction is possible by detecting the light emission from the fluorescent labels. Optical detections based on resonance shift are label free detection which can be implemented in either Surface Plasmon Resonance (SPR) or Localized Surface Plasmon Resonance (LSPR) [37]. This approach has been proven to have great potential as they are sensitive to the biochemical reaction occurring on a

sensing surface. Hence the plasmon resonance shift based detection is greatly employed for the affinity biosensors. In SPR sensors, a thin metallic layer is used to generate surface plasmon waves and the biochemical reaction happening on the metal layer modifies the plasmonic property. SPR sensors are already available commercially. Surface plasmon resonance produced in the nanoparticles is known as localized surface plasmon resonance (LSPR). The localized surface property of metallic nanoparticle and the shift of LSPR band can be used to monitor the biochemical reaction. At present, LSPR based sensors are gaining more attention due to simplicity in the optical setup and higher sensitivity. Evanescent wave, the exponentially decaying tail of the propagating wave is useful for the biodetection [38]. Evanescent wave sensors can be deployed in both fluorescence and absorption based detection.

In this thesis, optical method is used as the optical detection has higher sensitivity, good stability and good spatial resolution. A novel optical LOC developed by using silica-on-silicon waveguide and PDMS microfluidic chip is demonstrated for the detection of fluorescently tagged recombinant bovine growth hormone. Evanescence based sensor chip is developed by using a novel cascade waveguide coupler (CWC) with higher sensitivity and specificity. To adopt the LSPR based method in LOC, novel method of integration of nanoparticles in microdevices is required, and hence the micro-nano integration has been an interesting topic in micro total analysis systems research at present. A LSPR sensor is developed for the label-free detection of bovine growth hormone, in which a novel method of manufacturing gold nano-island is developed. This method is simple, low cost and compatible to integrate in

microfluidic chips. LSPR property of silver-PDMS nanocomposite is investigated for the label-free detection of bovine growth hormone. Subsequently, by synthesizing the silver-PDMS nanocomposite directly in the PDMS microfluidic device, a novel all PDMS lab-on-a-chip is developed. Finally, the evanesence and LSPR detection method are combined and a nano-enhanced evanesence sensor is developed by integrating gold nano-islands in silica-on-silicon optical chip and PDMS microfluidic chip.

## 1.2 Lab-on-a-chips (LOCs)

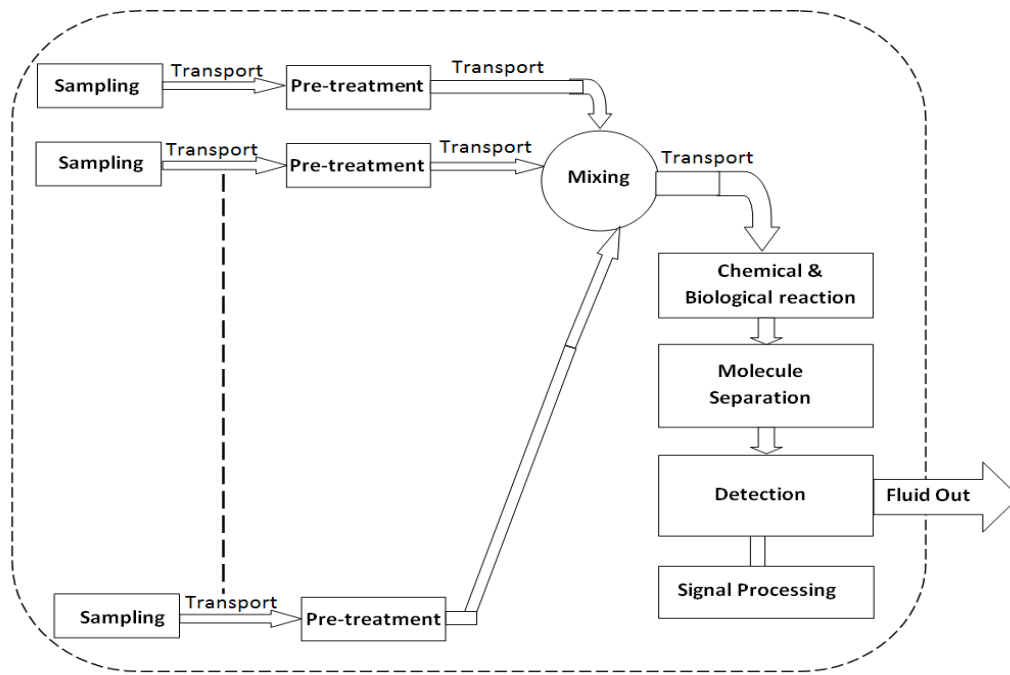


**Figure 1.5** A generalized block diagram representing various processes involved in the LOC (Figure adopted from Book: BioMEMS Science and engineering perspectives, S. Badilescu and M.Packirisamy 2011 [32] ).

Lab-on-a-chips (LOCs), also called micro total analysis systems ( $\mu$ TAS) are miniaturized analytical devices, which are fabricated by integrating one or multiple laboratory functions in a single chip. The size of the LOCs can be of the order of few millimeters to centimeters, therefore, they can be packaged and integrated with electronics for the realization of portable devices. Microfluidics is the integral component of LOCs, which enable the transportation and analysis of the biomolecules in micron scale and hence the samples and reagents required for the bio-analysis and detection can be of the order few nanoliters to microliters. As the detection and analysis is carried out by using small amounts of samples, the performance and throughput are very high and analysis time is much shorter. Figure 1.5 shows a generalized block diagram representation of  $\mu$ TAS [32]. A fully integrated  $\mu$ TAS is capable of transporting the samples and reagents through pre-treatments and mixing modules by using microfluidic circuits. Subsequently, the samples were transported to a biochemical reaction unit to undergo molecules separation and detection. By integrating the microfluidic and detection modules, many of the processes required for the bio-analysis and detection can be attained.

The concept of miniaturization of laboratory functions and its benefits are demonstrated for the first time by Manz et al. in the year 1990 [39], in which, theoretical performance of the miniaturized version of flow injections systems, chromatography and electrophoresis are compared with the existing macroscopic systems and found that the performances of the miniaturized devices have been greatly enhanced. In 1991, Manz and Verpoorte [40] fabricated a cell detection system by integrating a molecule separation unit based on [40] liquid chromatography

in a microfluidic channel. This system was fabricated by using anisotropic etching and bonding of silicon wafer. Electrochemical detection was used in the first fully synthesized  $\mu$ TAS developed by Verpoorte et al. in 1994 [41]. This system had two silicon micropumps connected with the Ion Sensitive Field-Effect Transistor (ISFET) using silicon rubber and demonstrated to be useful for the detection of pH and phosphate. In the early stages of  $\mu$ TAS, electrical detection was widely used in microdevices due to the easiness of miniaturization. However, the optical detection method is the most widely used approach in life science due to several advantages including higher sensitivity, better spatial resolution, higher discrimination ability and good stability [42]. Optical detection in microfluidic devices can be achieved either by directly coupling the light to the microfluidic channel or by the interacting the evanescent wave with biospecies [43, 44]. In the later, the microfluidic channel is placed near to the core of the waveguide so that the evanescent wave can interact with the biomolecuels [45].

In 1996, Ramsey and Jacobson [46] reported DNA fragment analysis carried out in an integrated micro device. Samples of DNA and enzymes were injected into the micro reaction chamber by electrophoresis, and a CCD camera was equipped with the experimental setup in order to imaging the particles by using laser induced florescence (LIF). The fluorescence measurements were carried out using the photomultiplier tube. This device was a microfluidic chip with optical detection and flow visualization tools were integrated externally.

In 1998, Burns et al.[47] fabricated a  $\mu$ TAS by integrating multiple components such as nanoliter liquid injector, sample mixer and positioning system, temperature

controlled reaction chamber, an electrophoretic particle separation system and a fluorescence detection system on silicon wafer. This device was fabricated by monolithic integration of multiple modules and photodetector onto a silicon platform and demonstrated to be useful for the analysis of DNA at nanoliter volumes.

In the early stages of LOCs, silicon micro fabrication technology was adopted for the fabrication of LOCs due to the availability of well-established integrated circuit fabrication process. However, in order to meet a large variety of requirements, other material platforms and novel fabrication methods are being investigated at present. Some of the polymeric materials such as polydimethylsiloxane (PDMS), Poly (methyl methacrylate) (PMMA) were found to be excellent for the fabrication of  $\mu$ TAS because of the cost-effective fabrication methodologies and excellent material properties supporting  $\mu$ TAS functionalities. PDMS has several advantages: it is biocompatible, optically transparent and easily moldable to any complex 3D structures by soft lithography, therefore, it has been widely used for the fabrication of  $\mu$ TAS. In the year 2000, Bartholomeuze et al. [11] reported a bioluminescence method using PDMS microfluidic device, in which, a PDMS microfluidic channel was fabricated by using SU8 mold and sealed with glass lid. The chip was demonstrated to be able to monitor the change of concentration of intracellular Adenosine Triphosphate (ATP) during the reaction with the luciferase in correlation with the change in light intensity.

Fabrication of  $\mu$ TAS on integrated optical platform has several advantages, as semiconductor fabrication technologies can be used for the fabrication of microphotonics and microfluidic parts. In 2001, Friis et al. [48] fabricated a

microfluidic channel on silica-on-silicon waveguide and sealed the channel with polysilicon by anodic bonding, and it was used for flow cytometry. Absorption and fluorescence detection were carried out by pumping 100 $\mu$ M fluorescein to the microchannel and exciting with a laser of 488nm coupled to the waveguide. The attenuation of the silica-on-silicon (SOS) waveguide is very low in the order of 0.01dB/cm [49] and hence the SOS is attractive for the integration of micro-optical components.

In 2003, Ruano et al. [50] published a work on a fluorescence based biodetection system, in which they fabricated several microphotonic components such as waveguides, beam splitter, S-bend and Y-branch on silica-on-silicon platform using flame hydrolysis deposition (FHD), photolithography and silica micromachining. The microfluidic channel and reservoir were micromachined on the silica-on-silicon waveguide and by using two thick PDMS layers, the microfluidic channel was sealed. The fluorescence detection ability of the device was demonstrated with Cy 5 dye. Figure 1.6 shows the schematic of the integration of the device proposed by Ruano et al. [50].

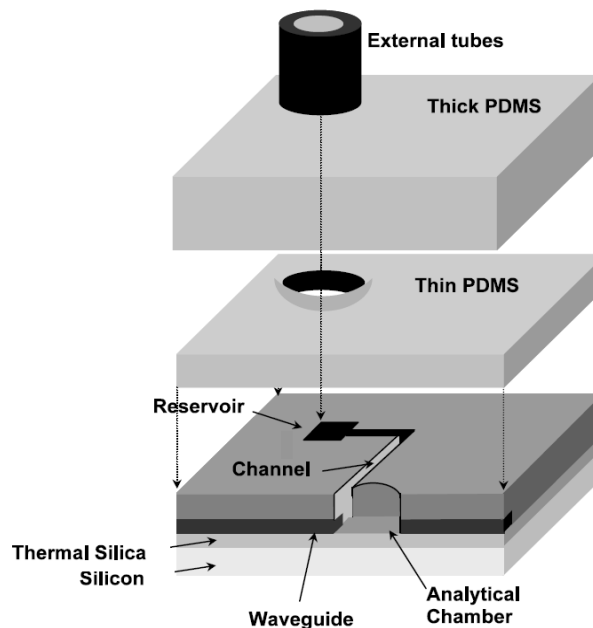


**Figure 1.6** Fluorescence detection system on silica-on-s-silicon waveguide (Figure adopted from Ruano et al. [50]).

The use of multiple material platforms for the integration of  $\mu$ TAS got significant attentions because the properties of different materials can be exploited for various applications. Optical properties and photo patterning qualities of SU8 paved the way to build  $\mu$ TAS by integrating optical waveguide and microfluidics. In 2003, Mogensen et al. [51] integrated a SU8 waveguide with a microfluidic channel for the detection of bromothymol cells through absorption measurements. This work was focused on the characterization of photonics aspects of the device. SU8 is used as the core of the waveguide and oxidized silicon wafer or Borofloat glass as top and bottom cladding for the vertical confinement of light in the waveguide. Air is used as the lateral cladding medium for simplifying the fabrication process. With SU8 negative photo resist and PDMS, a hybrid integrated LOC was fabricated by Leeds et al. [52]

in 2004. In their work, the qualities of SU8 and PDMS are used for the integration of an optical waveguide with microfluidic channel. Since the refractive index of SU8 is 1.6, SU8 was used as the core of the waveguide and PDMS with refractive index of 1.43 was used for the cladding and microfluidic chip was fabricated on PDMS.

Monolithic integration of dye laser, waveguides, microfluidic channel, diffusion mixer and photo detectors is demonstrated for the  $\mu$ TAS by Balslev et al. [53] in 2004 and the device is shown in Figure 1.7. In this device, waveguide and microfluidics are fabricated out of SU8 on silicon platform. Fluorescence detection was achieved by the inbuilt photo detector and dye laser.

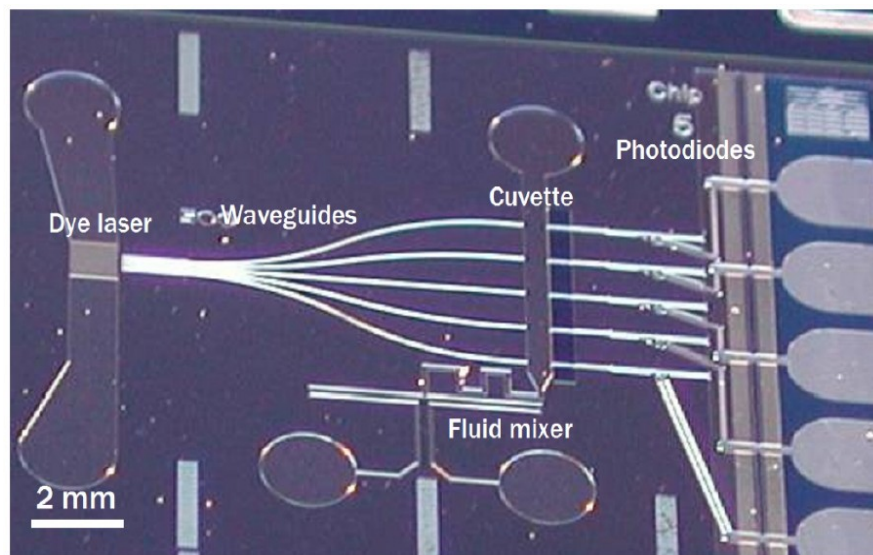


**Figure 1.7** Fully integrated  $\mu$ TAS (Adopted from Balslev et al. [53])

In 2005, David A. Chang-Yen et al. [54] published a work on monolithic integration of optical waveguide and microfluidics on PDMS as illustrated in Figure 1.8. Curing

temperature of PDMS is varied to achieve different refractive indices for the core and cladding of the waveguide. They demonstrated a good confinement of light and an attenuation of PDMS waveguide was 0.3dB/cm. However, this device was not demonstrated for any bio applications. The attenuation of PDMS waveguide was several orders higher compared to the silica-on-silicon waveguide.

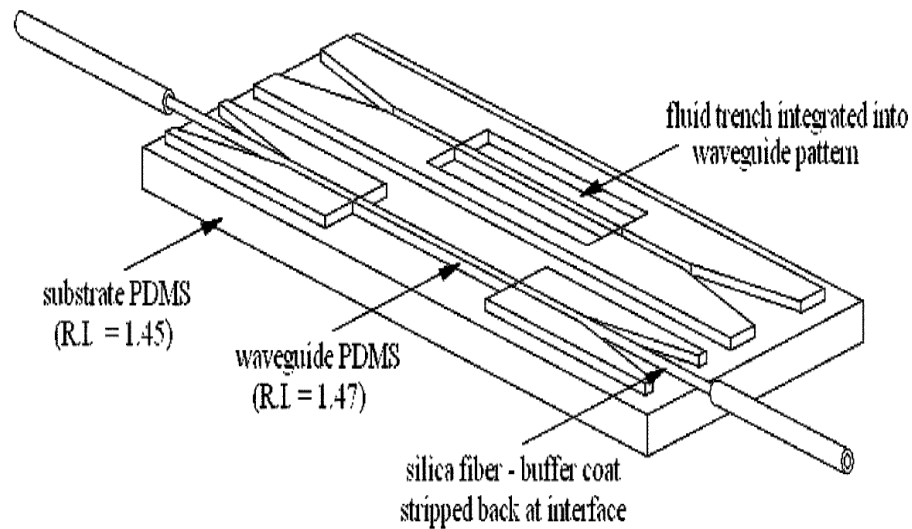


**Figure 1.8** Optical waveguide and fluidic trench monolithically integrated on PDMS (Figure adopted from David A. Chang-Yen et al. [54]).

Detection of multiple analytes is possible through the fluorescent labeling of multiple biomolecules with different types of fluorophores having different excitation and emission characteristics. In order to separate the emission spectra and excitation signals for each labeled analytes, a spectrometer has to be integrated with the chip. Chandrasekaran et al.[55] reported an optical microfluidic system of hybrid integrated excitation laser and spectrometer-on-chip (SOC) [56] for the fluorescence based bio-

detection. The schematics of this device is shown in Figure 1.9, In this study, microfluidic chip is fabricated on silicon and excitation light from a fiber laser is focused to the detection zone in a free space optical arrangement, An Echelle grating based spectrometer is arranged in the system to collect the fluorescence. This hybrid integrated system cannot be made portable for the point of care detection as the collection and excitation fibers need to be equipped with micromanipulators. Moreover, alignment of fibers with microfluidics is critical in this setup.

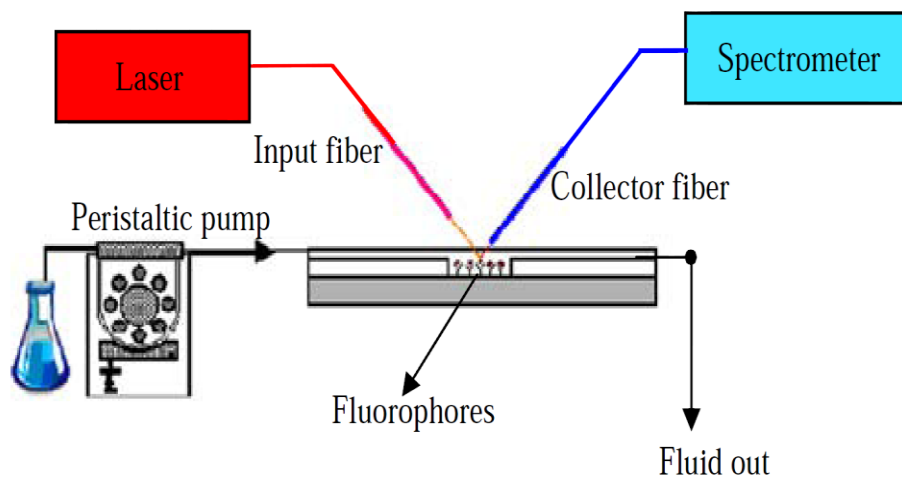


**Figure 1.9** Hybrid integrated optical microfluidic system for the fluorescence detection (adopted from Chandrasekaran et al. [55])

The main disadvantage of the labeled detection is the cost and time required for optimizing the labeling conditions. The label free detection depends on the inherent property of the biomolecules of interest. The detection by simply measuring the absorption of light by biomolecules is one of the earlier approaches, which are based on the absorption of light by the chromophores in the biospecies. The sensitivity and

reliability of the simple absorption based approach is limited and hence the other techniques by using Surface Plasmon Resonance (SPR), carbon nanotubes, nanowires and nanoholes are also reported for the label free detection [34]. In SPR sensor, a thin metal layer is deposited on a substrate and the propagating Plasmon waves are produced by coupling the light to the metal layer. The property of the plasmon wave changes when the biospecies are adsorbed on to the metal layer. Noble metal nanoparticles such as gold and silver have huge application potentials in the biosensing and hence they have been already demonstrated for many biosensing applications due to their plasmonic properties.

In recent years, the use of nanotechnology in the miniaturized biosystems has been greatly addressed in literature [57]. Integration of nanomaterials in microfluidics channel facilities the application of unique properties of nanoparticles for the biosensing with the handling of small amounts of bioliquids. Integration of SPR sensor in microfluidic device has been already implemented and a commercial device called Biacore 3000 is already available. However, the light coupling optics in SPR system is complex and hence Biacore 3000 systems still requires large apparatus.

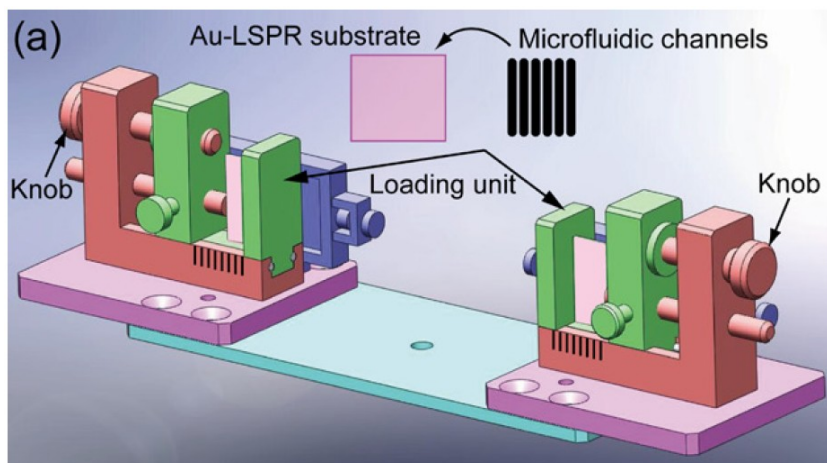


**Figure 1.10** Gold nanoparticle integrated microfluidic device for the label-free detection (Figure adopted from Yi Zhang et al. *Lab- on a chip* [58])

Integration of gold nanoparticle in a microfluidics device is reported for the biodetection [58], herein the gold monolayer was deposited on quartz substrates by silane layer and subsequently integrated with a microfluidic device fabricated on cyclic olefin copolymer (COC). In a recent work, a multiplexed label free detection of protein is demonstrated with the integration of nanoparticles in a microfluidic environment [58]. The schematic representation of the device is shown in Figure 1.10. An optical bench holding the light source and spectrometer are designed and implemented with the microfluidic chip having multiple parallel channels to carry out a multiplexed protein assay.

The nanofabrication methods must have certain qualities in order to adapt them for the integration of nano-structures in microfluidics. The adhesion of nanostructure with microfluidic device, the feasibility to deposit nanostructures with various size and shape and the easiness of implementation of illumination and optical

measurements setup are essential qualities required for the integration of nanomaterials in microfluidics devices.

### **1.3 Thesis motivation**

As outlined in the literatures, large quantities of artificial hormones are synthesized and misused in sports and dairy industry due to the advancement of recombinant DNA technology. The use of artificial hormone is controversial because of its potential side effects on the health of human and animal. Hence there is a large demand for a rapid and precise detection device. Traditionally, the detection and estimation of concentration of growth hormone in milk is carried out by macroscopic instruments. A miniaturized sensing device that is easy to use at the point-of-need (PON) would be required for an effective controlled use of growth hormone.

From the literatures on lab-on-a-chip, it is evident that various methods of improving fluorescence detection sensitivity in lab-on-a-chip device are still required. In addition, the integration of nano-structures in microfluidic devices can also produce LOCs with enhanced performances. Most importantly, a cost effective fabrication methods for making LOCs with enhanced performances has always a great demand.

In this thesis, optical detection method is adopted for the development of lab-on-a-chip because of the higher sensitivity and stability. The labeled and label-free detections have their own merits and demerits, hence, both of the approaches are used for the detection of growth hormone. There are challenges to be addressed in the integration process of microfluidic and optical components for the realization of lab-on-a-chip devices with higher sensitivity.

It is indeed necessary to develop novel nanofabrication technologies for the development of nano-integrated microfluidic devices. The unique SPR optical property of nanostructure is useful for the biosensing with higher sensitivity. The fabrication method of nanostructure should also be compatible with the fabrication process of microfluidic devices.

Developments of LOCs on the polymer could significantly reduce the cost of fabrication and material, so that a low cost device can be developed. Hence a low cost method of integration of nanostructures with the polymer LOC platform for optical detection needs be developed.

#### **1.4 Objective and scope of the thesis**

The main objective of the thesis is to develop optical lab-on-a-chip device for the detection of growth hormone in milk.

The main objective of the thesis is achieved through following sub-objectives:

1. Develop a low cost optical microfluidic system for the realization of a lab-on-a-chip.
  - a. A hybrid integrated lab-on-a-chip on silica-on-silicon and PDMS.
  - b. Test the fluorescence detection ability and sensitivity.
2. Optimize the labeling condition of growth hormone and detect in the lab-on-a-chip and analyze the detection limit and sensitivity.
  - a. Optimize the labeling condition with different types of fluorophores with growth hormone and test the sensitivity in the lab-on-a-chip.

3. Increase the sensitivity and specificity of the detection by developing a novel evanescent wave based fluorescence sensor and analyze the detection limit and performance.
  - a. Simulation and analysis of evanescent coupling efficiency and testing the performance of the device with fluorophore tagged growth hormone.
4. Develop a label-free based sensor using gold nano-island and integrate into a microfluidic device.
  - a. Simulation and development of novel nanofabrication method for the deposition of nano-islands and test the refractive index sensitivity of the sensor platform.
  - b. Test the label-free sensing ability of the nano-islands on the glass substrate and subsequently develop a method to integrate them in a microfluidic chip for the realization of lab-on-a-chip.
5. Develop a low cost LOC by using silver-PDMS nano-composite for label free detection of growth hormone.
6. Integrate the nano-island on a silica-on-a-silicon waveguide for the nano-enhanced evanescent lab-on-a-chip and test label free detection sensitivity of the device.
7. Separation of growth hormone from milk and detection.
8. Develop a monolithically integrated lab-on-a-chip by integrating microfluidic channel, optical waveguide and spectrometer on chip.

## 1.5 Organization of the thesis in a manuscript-based format

This thesis is written in manuscript-based format with 11 Chapters. In the present Chapter, main objective and sub-objectives are explained. A brief introduction of the existing methods of detection of growth hormone and various significant methods reported for the developments of lab-on-a-chip devices are reviewed. The application potentials of nanomaterials for the biosensing and the importance of integrating them in LOC device are examined. The thesis chapters are arranged to address the objective of the thesis explained in Section 1.4 and the thesis is formatted according to the “Thesis Preparation and Thesis Examination Regulations (version-2011)” of the School of Graduate Studies at Concordia University. The Chapters 2-8 are duplicated from one published journal article, three journal papers accepted for publication, and four submitted or to be submitted journal articles. The Sections, Figures and the Equations in the duplicated articles are numbered as per the thesis regulation. A single reference list is presented in Reference section. Conclusion and the future recommendations are explained in the chapter 11.

### **Chapter 2 is duplicated from the article published in Journal of Biomedical**

**Optics:** This chapter covers the Objective 1(a) and 1(b) of the “objective and scope” of the thesis explained in Section 1.4

Ref [59]: *Jayan Ozhikandathil and Muthukumarn Packirisamy “Silica-on-silicon (SOS) Waveguide Integrated PDMS Lab-on-a-chip for Quantum dot Fluorescence Bio-detection” J. Biomed. Opt. 17, 017006 (2012). (Impact Factor: 3.188)*

Integration of microfluidics and optical components is an essential requirement for the realization of optical detection in lab-on-a-chip (LOC). In this work, a novel hybrid integration of silica-on-silicon (SOS) waveguide and polydimethylsiloxane (PDMS) microfluidics for realizing optical detection based biochip is demonstrated. SOS is a commonly used platform for integrated photonic circuits due to its lower absorption coefficient of silica and the availability of advanced microfabrication technologies for fabricating complicated optical components. However, the fabrication of complex microfluidics circuits on SOS is an expensive process. On the other hand, any complex 3D and high-aspect-ratio microstructures for the microfluidic applications can be easily patterned on PDMS using soft lithography. By exploring the advantages of these two materials, the proposed hybrid integration method greatly simplifies the fabrication of optical LOC. Two simple technologies—namely, diamond machining and soft lithography—were employed for the integration of an optical microfluidic system. Use of PDMS for the fabrication of any complex 3D microfluidics structures, together with the integration of low loss silica-on-silicon photonic waveguides with a straight microfluidic channel, opens up new possibilities to produce low-cost biochips. The performance of SOS-PDMS-integrated hybrid biochip is demonstrated with the detection of laser induced fluorescence of quantum dots. As quantum dots have immense application potential for biodetection, they are used for the demonstration of biodetection.

**Chapter 3 is duplicated from the article accepted for publication in IEEE Sensor**

**Journal:** This chapter covers the Objective 2 of the “objective and scope” of the thesis explained in Section 1.4

Ref[60]: *Jayan Ozhikandathil, Simona Badilescu and Muthukumaran Packirisamy “Detection of Fluorophore-Tagged Recombinant Bovine Somatotropin (rbST) by using Silica-on-silicon (SOS)-PDMS Lab-on-a-chip” Accepted for publication in IEEE Sensor Journal, 2012.(Impact Factor: 1.5)*

The presence of potentially harmful substances in milk is a concern for consumers. The discovery of the recombinant DNA technology allowed the production of large quantities of recombinant bovine somatotropin (rbST), which is allowed to be used to increase the milk and meat production in many countries. The use of recombinant bST (rbST) is controversial because of its potential effects on animal and human health. Use of the existing large instruments for the detection of rbST suffers from disadvantages such as the need of large quantities of reagents, increased time of assays and most importantly, the high-cost of equipments. In this work, a novel optical lab-on-a-chip (LOC) is proposed for the detection of a fluorophore-tagged rbST. The advantages of silica-on-silicon (SOS) platform for the optical waveguide and polydimethylsiloxane (PDMS) for microfluidics are exploited for the fabrication of a low cost lab-on-a-chip. The tagging of rbST with two different types of fluorophores such as FITC and Alexa Fluor (AF)-647 is carried out and used for the detection in the proposed lab-on-a-chip.

**Chapter 4 is duplicated from the article accepted with minor modifications by the Journal of Biophotonics:** This chapter covers the Objective 3 of the “objective and scope” of the thesis explained in Section 1.4

Ref: *Jayan Ozhikandathil and Muthukumarn Packirisamy “Detection of recombinant growth hormone by evanescent cascaded waveguide coupler on silica-on-silicon” accepted to Journal of BIOPHOTONICS 2012. (Impact Factor: 4.343)*

An evanescent wave based biosensor is developed on the silica-on-silicon (SOS) with a cascaded waveguide coupler (CWC) for the detection of recombinant growth hormone. SOS is an attractive platform for binding the antigen and antibodies with fluorescent complexes within the evanescent wave penetration depth in order to perform the fluoroimmunoassay. So far, U-bends and tapered waveguides are demonstrated for increasing the penetration depth and enhancing the sensitivity of the evanescent wave sensor. In this work, a monolithically integrated sensor platform containing a cascaded waveguide coupler with optical power splitters and combiners designed with S-bends and taper waveguides is demonstrated for an enhanced detection of recombinant growth hormone. In the cascaded waveguide coupler, a large surface area to bind the antibody with increased penetration depth of evanescent wave to excite the tagged-rbST is obtained by splitting the waveguide into multiple paths using Y splitters designed with s-bends and subsequently combining them back to a single waveguide through tapered waveguide and combiners. Hence a highly sensitive fluoroimmunoassay sensor is realized. Using the 2D FDTD (Finite-difference time-domain method) simulation of waveguide with a point source in Rsoft FullWAVE, the fluorescence coupling efficiency of straight and bend section of

waveguide is analyzed. The sensor is demonstrated for the detection of fluorescently-tagged recombinant growth hormone with the detection limit as low as 25 ng/ml.

**Chapter 5 is duplicated from the article prepared to submit to the IEEE Journal of Photonics:** This chapter covers the Objective 4(a) of the “objective and scope of the thesis” explained in Section 1.4

Ref: *Jayan Ozhikandathil and Muthukumaran Packirisamy “Finite-difference time-domain simulation and implementation of a morphologically-tuned gold nano-islands integrated biosensor”*, Prepared to submit to the IEEE Journal of Photonics (Impact Factor: 2.344)

This chapter presents simulation analysis and implementation of morphology tuning of gold nano-islands structure deposited by a novel convective assembly technique. The gold nano-islands were simulated using 3D Finite-Difference Time-Domain (FDTD) techniques to investigate the effect of morphological changes and adsorption of protein layer on the localized surface plasmon resonance (LSPR) properties. Gold nano-islands structures were deposited on glass substrate by a novel and low-cost convective assembly process. The structure formed by an uncontrolled deposition method resulted in a nano-cluster morphology, which was annealed at various temperatures to tune the optical absorbance property by transforming the nano-cluster to nano-island morphology by modifying the structural shape and interparticle separation distances. The dependence of the size and the interparticle separation distance of the nano-islands on the LSPR properties were analyzed in the simulation. The effect of adsorption of protein layer on the nano-islands structure was simulated and a relation between the thickness and the refractive index of the protein layer on

the LSPR peak was presented. Further, the sensitivity of the gold nano-island integrated sensor against refractive index was computed and compared with the experimental results.

**Chapter 6 is duplicated from the article accepted for publication in Journal of**

**Biomedical Optics**: This chapter covers the Objective 4(b) of the “objective and scope” of the thesis explained in Section 1.4

Ref [61]: *Jayan Ozhikandathil, Simona Badilescu and Muthukumaran Packirisamy “Gold Nano-island Structures Integrated in a Lab-on-a-Chip for Plasmonic Detection of Bovine Growth Hormone” Accepted for publication in Journal of Biomedical Optics July issue 2012. (Impact Factor: 3.188)*

Three dimensional gold nanostructures fabricated through a novel convective assembly method are treated thermally to obtain a nano-island morphology. The new structure is proved to be adequate for the detection of bovine growth hormone, by using an immunoassay method based on the Localized Surface Plasmon Resonance (LSPR) band of gold. The nano-island structures are integrated into a microfluidic device and the spectral measurements are done by introducing the device directly in the light beam of a UV-Visible spectrophotometer. The principal motivation of this work is the need for a simple and rapid method of detection of the hormone in milk and milk products.

**Chapter 7 is duplicated from the article submitted to Journal of Biomedical**

**Optics**: This chapter covers the Objective 5 of the “objective and scope” of the thesis explained in Section 1.4

*Ref: Jayan Ozhikandathil and Muthukumaran Packirisamy “Silver-Polydimethylsiloxane Nanocomposite integrated lab-on-a-chip for Plasmonic Detection of Bovine Growth Hormone” submitted to Journal of biomedical optics 2012. (Impact Factor 3.188)*

A novel method of integration of a silver-polydimethylsiloxane (PDMS) nanocomposite in a microfluidic channel for the realization of a lab-on-a-chip is reported in this chapter. The device is demonstrated for the plasmonic detection of bovine growth hormone. The feasibility of the application of plasmonic property of silver-PDMS nanocomposite substrate for the detection of antigen-antibody interaction is investigated. Subsequently, the nanocomposite was integrated into a microfluidic channel and the detection experiments were carried out in microfluidics environment as well. The experiments confirmed that the nanocomposite can be integrated into the microfluidic device without reducing the sensitivity achieved on the silver-PDMS substrates [62].

**Chapter 8 is duplicated from the article submitted to Biomicrofluidics Journal:**

This chapter covers the Objective 6 of the “objective and scope” of the thesis explained in Section 1.4

*Ref: Jayan Ozhikandathil and Muthukumaran Packirisamy “Nano-islands integrated evanescence-based lab-on-a-chip on silica-on-silicon and PDMS hybrid platform for the detection of recombinant growth hormone” submitted to Journal of Biomicrofluidics (Impact Factor: 3.896) article submitted to Biomicrofluidics AIP Journal.*

Integration of nano-materials in optical microfluidic devices facilitates the realization of miniaturized analytical systems with enhanced sensing abilities for biological and chemical substances. In this work, a novel method of integration of gold nano-islands in a silica-on-silicon-polydimethylsiloxane microfluidic device is reported. The device works based on the nano-enhanced evanescence technique achieved by interacting the evanescent tail of propagating wave with the gold nano-islands integrated on the core of the waveguide resulting in the modification of the propagating UV-visible spectrum. The biosensing ability of the device is investigated by FDTD simulation with a simplified model of the device. The performance of the proposed device is demonstrated for the detection of recombinant growth hormone based on antibody-antigen interaction.

**Chapter 9 explains the process of extraction of rbST from milk by using solid phase extraction technique and detection by using gold nano-islands:** This chapter covers the Objective 7 of the “objective and scope” of the thesis explained in Section 1.4

A label-free method is used for the detection recombinant bovine somatotropin in milk. The milk sample spiked with the rbST was separated by solid phase extraction technique. The detection of the rbST separated from milk is carried out by the plasmonic property of the gold nano-islands formed on a glass substrate through antibody-antigen interaction. The formation of nano-islands is by a simple, low cost and uncontrolled convective assembly process. The uncontrolled convective assembly technique resulted in a nano-cluster morphology which was not suitable for the

biosensing, hence the nano-cluster morphology was transformed to nano-island morphology by post-deposition heat treatment. The detection limit of rbST by using the nano-islands formed on glass substrate is as low as 5 ng /ml.

**Chapter 10 explains the FDTD simulation of spectrometer-on-chip and monolithic integration process of spectrometer-on-chip, microfluidic channel and optical waveguide on silica-on-silicon platform:** This chapter covers the

Objective 8 of the “objective and scope” of the thesis explained in Section 1.4

In this chapter, a multiple waveguide system, microfluidic channel and a micro-spectrometer are monolithically integrated on silica-on-silicon platform by using single step lithography and etching. A concave grating spectrometer is designed by 2D FDTD simulation and integrated with the microfluidics and waveguide for the realization of a miniaturized monolithically integrated optical LOC. The spectrometer is designed for the simultaneous detection multiple analytes labeled with various fluorophores. The fuorophores used for the detection of rbST are FITC and Alexa 647 with emission wavelength at 521 nm and 665 nm, respectively. Therefore the micro-spectrometer was designed to cover in the range of 500 to 700nm. Since the smallest feature size of the grating of the micro-spectrometer is 500 nm, the grating could not be fabricated with good precision. The fabrication of grating will be possible by using high-resolution lithography such as e-beam lithography.

## 1.6 Major contributions of the thesis

In this thesis, detection of bovine growth hormone in milk by using lab-on-a-chip platforms is achieved. Following are contribution in the field of the lab-on-chip achieved in this thesis.

1. A novel hybrid integration method for the realization an optical lab-on-a-chip is developed. Advantages of PDMS for the fabrication of microfluidic chip and the advantages of the silica-on-silicon waveguide for the optical chip and the proposed integration method greatly simplify the fabrication of low cost LOCs.
2. Optimization of labeling conditions of bovine growth hormone with two types of fluorophores such as Alexa-647 and FITC is achieved.
3. A novel cascaded waveguide coupler (CWC) system is proposed and implemented on silica-on-silicon waveguide for the evanescence based fluorescence detection with enhanced sensitivity. The fluorescent tagged bovine growth hormone is detected using the CWC systems.
4. Simulation and implementation of a novel method of formation of nano-islands for the label free detection of bovine growth hormone is carried out.
5. A novel method of formation of nano-island morphology on the glass substrate is achieved. This is a simple and low cost approach.
6. The nano-islands are integrated into a microfluidic environment and a low cost lab-on-a-chip is fabricated.
7. A novel method of integration of silver nanoparticles in PDMS microfluidic chip is developed and a low cost all polymer lab-on-a-chip is realized.

8. Method of manufacturing the nano-islands on the glass was successfully implemented for the formation of nano-island on the silica-on-silicon waveguide and a nano-enhanced evanescent wave lab-on-a-chip is developed.
9. Method of integration of a fully integrated lab-on-a-chip by integrating microfluidic, optical waveguide and spectrometer-on-chip.

## **1.7 List of papers Published/Accepted/Submitted/to be submitted**

### **Published/Accepted Journal articles:**

1. **Jayan Ozhikandathil** and Muthukumaran Packirisamy “Detection of recombinant growth hormone by evanescent cascaded waveguide coupler on silica-on-silicon” Accepted to Journal of Biophotonics 2012.(Impact Factor:4.24)
2. **Jayan Ozhikandathil**, Simona Badilescu and Muthukumaran Packirisamy “Detection of Fluorophore Tagged Recombinant Bovine Somatotropin (rbST) by Using a Silica-on-Silicon (SOS)-PDMS Lab-on-a-Chip” Accepted to IEEE Sensor Journal 2012. (Impact Factor: 1.437)
3. **Jayan Ozhikandathil**, Simona Badilescu and Muthukumaran Packirisamy “Gold Nanoisland Structures Integrated in a Lab-on-a-Chip for Plasmonic Detection of Bovine Growth Hormone” *Accepted to Journal of Biomedical Optics*. (2012).( Impact Factor: 3.188)
4. **Jayan Ozhikandathil** and Muthukumarn Packirisamy “Silica-on-silicon (SOS) Waveguide Integrated PDMS Lab-on-a-chip for Quantum dot Fluorescence Bio-detection” *Journal of Biomedical Optics* **17**, 017006 (2012). (Impact Factor: 3.188)
5. **Jayan Ozhikandathil**, Andrew Morison, Muthukumarn Packirisamy and Rolf Wuthrich “Low resistive silicon substrate as an etch-stop layer for drilling thick SiO<sub>2</sub> by spark assisted chemical engraving (SACE)” *Journal of*

*Microsystems technologies*, Vol 17, No: 3 pp 373-380 (2011). (Impact Factor: 1.071)

**Submitted Journal articles:**

6. **Jayan Ozhikandathil** and Muthukumaran Packirisamy “Nano-islands integrated evanescence-based lab-on-a-chip on silica-on-silicon and PDMS hybrid platform for the detection of recombinant growth hormone” *Submitted to AIP Biomicrofluidics* (Impact factor:3.896)
7. **Jayan Ozhikandathil** and Muthukumaran Packirisamy “Silver-Polydimethylsiloxane Nanocomposite integrated lab-on-a-chip for Plasmonic Detection of Bovine Growth Hormone” *Submitted to Journal of biomedical optics* 2012. (Impact Factor 3.188)

**To be submitted Journal articles:**

8. **Jayan Ozhikandathil** and Muthukumaran Packirisamy “Finite-difference time-domain simulation and implementation of a morphologically-tuned gold nano-islands integrated biosensor” *Prepared to submit to the IEEE Journal of Photonics* (Impact Factor: 2.344)
9. **Jayan Ozhikandathil** and Muthukumaran Packirisamy “Monolithically integrated lab-on-a-chip on silica-on-silicon” *To be submitted to ASME journal of micro-nano manufacturing.*
10. **Jayan Ozhikandathil**, Simona Badilescu and Muthukumaran Packirisamy “Detection of recombinant bovine growth hormone (rbST) in milk using gold nano-islands biosensor” *To be submitted to ASME Journal of nanotechnology in engineering and medicine.*

**Conference Proceedings articles:**

11. **Jayan Ozhikandathil**, Simona Badilescu and Muthukumaran “Gold nanostructure-integrated silica-on-silicon waveguide for the detection of antibiotics in milk and milk Products” *Paper presented in Photonics north conf. Montreal* June 2012.
12. **Jayan Ozhikandathil**, Simona Badilescu and Muthukumaran “Gold Nanoparticle Integrated PDMS Microfluidic Platform for Bio-Detection” *Proceedings of ICBME 2011* Manipal, India pp 327-330 (2011).

13. **Jayan Ozhikandathil**, Simona Badilescu and Muthukumaran Packirisamy “Synthesis and characterization of silver-PDMS nanocomposite for the biosensing applications” *Proc. SPIE* 8007, 800707 (2011).
14. **Jayan Ozhikandathil** and Muthukumaran Packirisamy, "PDMS waveguide integrated microfluidic chip for the detection of fluorophore tagged polypeptides," *Fibre and Optical Passive Components (WFOPC)*, 2011 7th Workshop on, 1-4, IEEE (2011).
15. **Jayan Ozhikandathil**, Muthukumaran Packirisamy “Silica-on-silicon (SOS)-PDMS platform integrated Lab-on-a-chip (LOC) for Quantum Dot applications” *Proc. SPIE*, Vol. 7750, 775004, (2010).
16. **Jayan Ozhikandathil**, Muthukumaran Packirisamy, Ion Stiharu, “Modeling and Analysis of Low Voltage Electro-Osmotic Micropump” *ASME Conf. Proc.* 2010, 323 (DOI: 10.1115/FEDSM-ICNMM2010-31213), (2010).
17. **Jayan Ozhikandathil**, Simona Badilescu and Muthukumaran Packirisamy “Synthesis and Optical Properties of Immobilized spherical and Non-spherical Gold Nanoparticles for Detection of Polypeptides and Microfluidics Applications” *Proc. of the International Conference on Nanotechnology: Fundamentals and Applications* Ottawa, Canada, (2010).

**Poster presentations:**

18. **Jayan Ozhikandathil**, Muthukumaran Packirisamy “Enhanced hybrid integration of photonics and microfluidics for bio-detection” *Poster presented at AGM of Canadian institute for photonics Innovations* June 2010, Niagara Falls, Canada.
19. **Jayan Ozhikandathil**, Muthukumaran Packirisamy “Silica-on-silicon Waveguide Integrated PDMS Lab-on-a-chip for Enhanced Detection of Fluorophore-Tagged Polypeptides” *Poster presented at AGM of Canadian institute for photonics Innovations* May 2011, Ottawa, Canada.
20. **Jayan Ozhikandathil**, Simona Badilescu and Muthukumaran “Modeling, fabrication and testing of a nanoislands integrated biosensor for the plasmonic detection of bovine somatotropin” *Nanoquebec Conference*, Montreal 2012.

## **Chapter 2: Silica-on-silicon waveguide integrated polydimethylsiloxane (PDMS) lab-on-a-chip (LOC) for fluorescence bio-detection**

### **2.1 Introduction**

The field of Micro Total Analysis Systems ( $\mu$ TAS) or Lab-on-a-chips (LOCs) has gained increased attention since its introduction by Manz *et al.* in 1990[39]. This is because of several advantages:  $\mu$ TAS perform bioanalysis and detection with higher sensitivity by using small amount of reagent volumes in short time. Typically, a bioanalytical process includes sampling, filtration, dilution, chemical reaction, separation, detection and quantification of molecules of interest. In order to perform all of these processes at micron scale, different process modules need to be miniaturized and integrated in a single chip. Adaptation of conventional micro fabrication technologies for the integration of  $\mu$ TAS is complicated and crucial. Several innovative approaches have been reported for the integration of micro total analysis systems [43, 44, 63]. Hybrid integration of  $\mu$ TAS by using different material platforms such as silicon, glass and polymeric materials such as polydimethylsiloxane (PDMS), Poly (methyl methacrylate) (PMMA) and SU-8 [51, 64-66] has also been reported. The main benefit of hybrid integration of  $\mu$ TAS is that the properties of different materials can be exploited for supporting different functionalities of  $\mu$ TAS. However, the fabrication process can be expensive and complex.

Even though there are many detection techniques reported for the bioanalytical process, fluorescent detection is still a widely used approach [42] as this method has many advantages including higher sensitivity, better stability, better spatial resolution

and high discrimination capability. Conventionally, fluorescent dyes or fluorescent proteins are used as diagnostic tool in immunoassays [67]. Fluorescent dyes are compatible for tagging with the biomolecules and detecting via photoluminescence properties. Emergence of quantum dots (QDs) replaces conventional dyes in immunoassays due to the enhanced fluorescence, narrow emission and wide absorption spectral width, greater stability against the photo bleaching, water solubility and biocompatibility. A review article by Hedi Mattoussi et al. [68] has furnished a detailed table of advantages of QDs over the fluorescent dye molecules for the biodetection. Miniaturized opto-fluidics biochips together with highly efficient fluorescent probes can facilitate bedside testing in hospital with small amounts of sample volume and enhanced sensitivity. However, a major drawback of the optical detection is the complexities involved in building an optical setup with a microfluidic channel. In this context, there is an increasing demand for the simpler, accurate and inexpensive methods of integration of optical microfluidic systems. A simpler approach of fabricating the optical detection module in  $\mu$ TAS is by integrating optical fibers directly into microfluidic channels [69]. Such systems are not compatible for integrating more optical components and fabricating portable devices. Moreover, they suffer a serious problem of misalignment of fibers with the microchannel. Fabrication of microfluidics and optical components using single material platform is a highly useful approach for the realization of portable and robust  $\mu$ TAS. For such a monolithic integration of optical waveguides, the materials having the better transparency to the wavelength of operation and feasibility of modifying the optical properties such as refractive index are essential. For a waveguide, light is confined

and propagated through a medium called core which is buried inside a cladding medium. The refractive index of the core must be slightly greater than the cladding in order to satisfy the condition of total internal reflection at the core-cladding interface and hence the light is guided through the core. The fabrication of microfluidic components requires the patterning of material into complex 3D high-aspect ratio structures and also they must be sealable with a strong leak-proof bonding. Therefore, the materials possessing all of the above stated properties are required for the monolithic integration of optical microfluidic systems.

PDMS has been identified as a suitable material for fabricating  $\mu$ TAS because of several advantages; it is bio-compatible, optically transparent down to the UV range making it attractive to fabricate optical components, easily moldable to any complex 3D microstructures by soft lithography which is a low cost fabrication process. D. A. Chang-Yen et al. [54] reported an attempt of developing waveguides and microfluidics monolithically on PDMS. The refractive-index requirements of core and cladding of waveguide is achieved by modifying the curing temperature of the PDMS. The complexity in the proposed process is that the curing of core and cladding must be done separately as the refractive index of PDMS is dependent on the curing temperature. The attenuation of the PDMS waveguide was 0.4dB/cm which is of several orders high as that of a SOS waveguide. The loss of the SOS waveguide is reported as low as 0.01dB/cm [49].

The silica-on-silicon (SOS) platform has been proven to be suitable for the miniaturization of monolithic-analytical systems [48, 70]. In SOS platform, silicon dioxide layers are deposited and micro machined on silicon substrate for realizing the

photonic components. The refractive index of the silica layers can be easily modified by varying the process parameters, therefore, the micro-optical components such as waveguide, couplers, grating based spectrometers[56] etc. can be fabricated. SOS is an interesting technology in the optical point of view as the existing, well-characterized semiconductor processing technologies can be readily adopted for the deposition of high quality oxide films. Since the optical absorption is very low for the silicon dioxide for the entire UV through near infrared regions, low loss optical components can be fabricated on it. The microfluidic components such as microchannels, reaction chambers and optical components can be monolithically integrated on SOS platform without any miss alignment issues. However, the fabrication issues reported in the literatures are deep micromachining of the silicon dioxide and hermetic sealing of the microfluidics circuits due to the non-planar topology of the waveguide.

As mentioned, the fabrication of optical components on SOS platform requires deposition, photo-patterning and anisotropic etching of silicon dioxide layers. In order to minimize the optical loss, the roughness of the etched-surface and verticality of the structures are to be given more attention. In addition, the core layer needs to be deeply buried, typically 15-20 $\mu\text{m}$  deep inside the cladding layers. Therefore, the silica layer has to be deeply etched (more than 20 $\mu\text{m}$ ) to bring the microfluidics to the optical path. Technologies such as Deep Reactive Ion Etching (DRIE) [71, 72]and Laser machining [73]are reported for the high-aspect ratio micromachining of silica layer, but they are expensive, complex and time consuming. Recently, a low-cost, nontraditional micromachining technology called SACE (Spark Assisted Chemical

Engraving) [74] has been employed for the machining of silica layer deposited on silicon substrate. Development of microfluidic channel and optical waveguide on SOS by using SACE is still underway due to high roughness surface associated with the SACE. Laszle *et al.*[75] have reported a method of making microchannel on glass by diamond sawing which is simple and can be carried out in a general laboratory environment. Even though this technique is suitable for fabricating straight microchannels, the machined-surface can be very rough.

In this work, a novel optical microfluidic system is developed by integrating silicon-on-silicon (SOS) waveguide on PDMS. Advantages of PDMS for the microfluidics circuits and SOS for the optical waveguide are exploited in this work. Due to the fabrication complexities and the higher attenuation of PDMS waveguide, SOS waveguide is used in this work. In the proposed integration method, by using two simple technologies, an optical microfluidic system is implemented using SOS waveguides and PDMS microfluidic chips. The diamond micromachining method is used for the fabrication of a straight microfluidic channel in SOS waveguide, which is simple and a cost-effective method. However, in order to have a fluidic system, the SOS chip is further integrated on a PDMS platform containing more microfluidics components. The microfluidic structures requiring high aspect-ratio were easily fabricated on PDMS by soft lithography which can be carried out in a general laboratory environment. The easily sealable nature of PDMS with PDMS or glass is exploited for the sealing of device using oxygen plasma treatment. The use of thin PDMS layer for the sealing of device could solve fabrications issues due non-planar topology of the waveguide.

The use of diamond machining together with the integration on PDMS made the fabrication of optical  $\mu$ TAS an easy and cost effective process. Diamond machining always results in a surface with high roughness which will reduce the optical coupling efficiency between the waveguide and microfluidics. Hence, a new chemical polishing facility called  $\mu$ CP (microfluidics assisted chemical polishing) was developed to improve the surface roughness. The proposed integration method opens up the feasibilities of fabricating optical  $\mu$ TAS comprised of any complex microfluidic systems such as separation systems, micromixers, micropumps etc. on PDMS followed by integrating SOS waveguide with a straight microchannel for the optical detection requirements. The roughness of the channel wall introduced from the diamond machining is smoothed by  $\mu$ CP.

## **2.2 SOS-PDMS Optical-Microfluidic system**

Figure 2.1(a) shows the schematic illustration of the SOS-PDMS integration process. This process is designed to implement an optical microfluidic system by using simple, easy and low-cost fabrication processes. Also, the process of integration of SOS and PDMS is designed to carry out in a general laboratory environment. As the optical property of the waveguide is very sensitive to the fabrication process and the quality of micromachining such as surface roughness and verticality of the structures, the fabrication of waveguide was carried out in a standard microfabrication facility. The microfluidic circuits on SOS platforms demands deep machining of silicon dioxide which is an expensive and tedious task in a standard semiconductor fabrication facility. Therefore the integration of microfluidics on SOS waveguide was

achieved by using the advantages of SOS and PDMS platforms as demonstrated in Figure 2.1(a). The assembly consists of two chips, one is the microfluidics chip on PDMS and the second chip is the microfluidics channel integrated optical waveguide on SOS platform. The PDMS platform is patterned by the soft lithography. This microfluidic platform contains a slot for fixing the SOS chip, liquid reservoirs, microchannel and a region where fluid is injected into the microfluidic channel on the SOS chip (fluidic injection zone). The SOS chip with a straight microchannel (Figure 2.1(b)) must be properly aligned with the microchannel in PDMS while bonding.

Two fabrication issues are considered while designing this integration process: sealing of the SOS waveguide with non-planar topology of waveguide and the alignment of microchannel in the waveguide and the PDMS platform. In this process, the bonding of the device was done by using oxygen plasma treatment. One of the main issues with the oxygen plasma bonding is that plasma-treated substrates must be immediately bonded without contaminating them. At the same time, the microchannels in the SOS chip and the PDMS platform must be carefully aligned. To solve this issue, the fluid injection zone is designed by chamfering the microchannel ends as shown in Figure 2.1(a). After bonding the SOS chip in the slot of PDMS, a thin layer of PDMS is used to seal the device. This thin PDMS layer is sufficiently flexible to fill all the non-planar regions of the waveguide and produce a leak proof hermetical sealing.

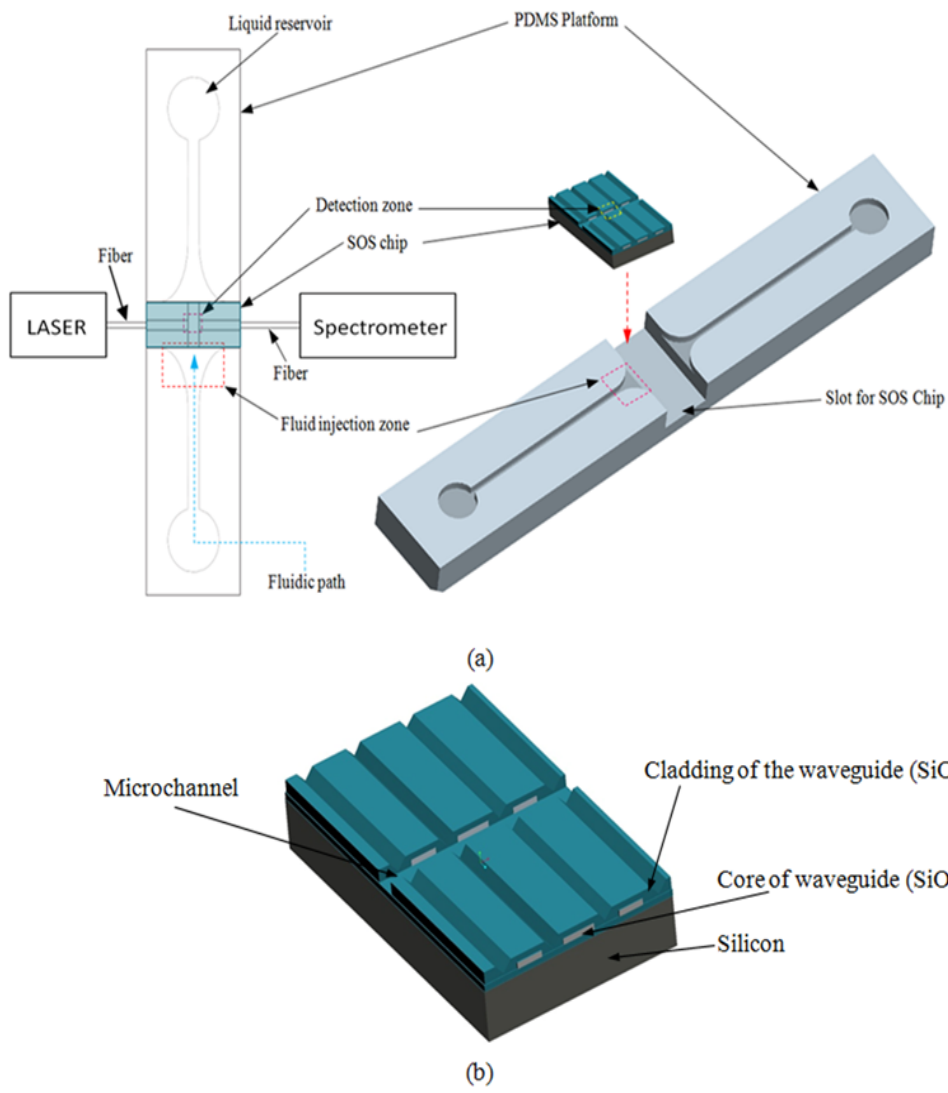


**Figure 2.1** (a) Schematic illustration of Silica-on-silicon-PDMS Optical-Microfluidic system (b) SOS waveguide with a straight microchannel.

### 2.3 Silica-on-silicon (SOS) waveguide

In silica-on-silicon technology, wave guiding is achieved by three layers of silicon dioxide, namely, bottom cladding, core and top cladding layers deposited on the silicon substrate. By choosing a slightly higher refractive index for the core than the cladding layer, the light can be vertically confined in the core. For the lateral

confinement, the core layer has to be structured to the desired width. After structuring the core layer, top cladding layer of silicon dioxide will be deposited. Such a buried core waveguide structure is used in this work. An illustration of crosssectional view of SOS waveguide is shown in Figure 2.2.

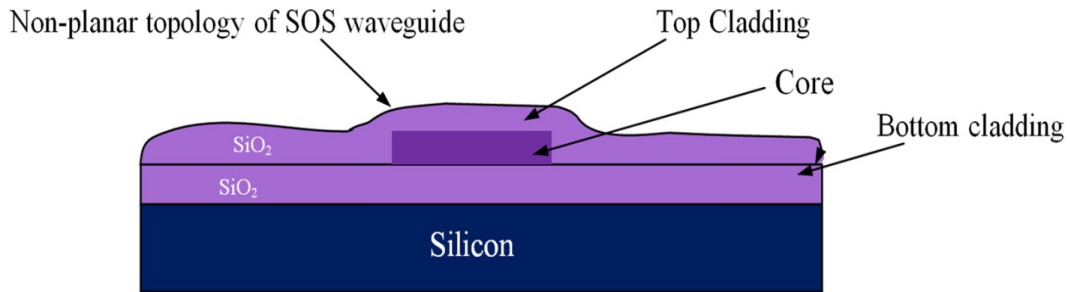


**Figure 2.2** Illustration of Silica-on-silicon waveguide.

Since the topology of the waveguide is non-planar, sealing of the microfluidic channels integrated on the SOS waveguide is a challenging task. Among the few techniques reported for the planarization of the waveguide topology, Chemical Mechanical Planarization (CMP) and etch back method are usually employed for the hermetic sealing of the microfluidic components machined on the SOS waveguide. In CMP, many parameters must be carefully controlled to obtain a reproducible outcome as the CMP is a combination of mechanical abrasion and chemical reaction [76]. Even though there are many commercial tools available for the CMP to precisely control the process parameters, they still suffer from issues such as feature-size-dependent polishing, hollow formation in wide features, and residual contamination. Etch back method is a technique used in microelectronics fabrication

process for the planarization of small unevenness ( $< 1\mu\text{m}$ ), which is not suitable for the present configuration. In order to adopt this technique for the waveguides having the unevenness of  $\sim 5\mu\text{m}$ , etching with two sacrificial layers is also reported [77].

Ruano et al. [50] reported monolithic integration of waveguide and microfluidic system including microchannel and liquid reservoirs by depositing glass by Flame Hydrolysis Deposition (FHD) and etching by deep reactive ion etching (DRIE) followed by sealing the device with the help of two PDMS layers. Herein, to get a hermetic sealing, a thin flexible PDMS layer is bonded between the non-planar waveguide and a thick PDMS layer containing the fluidic ports. This kind of double layer sealing is required since all the fluidic parts including the liquid reservoirs and microchannels were monolithically integrated on the waveguide, therefore the sealing layer should be sufficiently thicker and less flexible to fix the fluidic ports. In our work, the proposed SOS-PDMS integration greatly simplifies the issues with the sealing of the microfluidic channel. The main advantage of our method is that any complex 3D microfluidic components required for separation, mixing, and micropumping can be patterned on PDMS by soft lithography and integrated with SOS chip with a straight microfluidic channel to facilitate the realization of complex optical-LOCs through an easy and inexpensive process.

## **2.4 Device fabrication and Integration**

### ***2.4.1 Fabrication of SOS chip with waveguide and microfluidics***

The fabrication of SOS waveguide is carried out in a standard clean room facility (Enablance Ottawa, Canada). The waveguide fabrication starts with the deposition of

silicon dioxide layer on the silicon wafer ((100) orientation) by Plasma Enhanced Chemical Vapor Deposition (PECVD). The thickness of the bottom cladding layer was  $13\mu\text{m}$ . The refractive index of the bottom cladding layer was  $\sim 1.445$ . The refractive index of the core layer was measured as 1.457. For structuring the core layer ( $10\mu\text{m}$  width) of the waveguide, photoresist masking layer was patterned by using UV photolithography. The core layer was micromachined by Reactive Ion Etching (RIE). Finally, the top cladding layer was deposited with the process as that of the parameters of the bottom cladding layer for 5 hours. Due to the conformal deposition of top cladding layer on the patterned core layer, a thickness unevenness of around  $5\mu\text{m}$  was observed on the waveguide. Finally, the waveguide was diced into  $4.5\times 6.5\text{mm}$  samples as shown in Figure 2.3(a). Each  $4.5\times 6.5\text{mm}$  chip has six waveguides of  $\sim 10\times 5\mu\text{m}$  core cross sections separated by  $500\mu\text{m}$ . The waveguide facets were polished by using diamond lapping film of  $0.1\mu\text{m}$  particle sizes (Allied High tech) to enhance the coupling of light to the waveguide. In order to assess the quality of the waveguide facet, the facets were imaged by FEG-SEM. Figure. 2.3(b) and (c) show the SEM image of waveguide before and after polishing, respectively. The dimensions of the core and cladding are clearly visible in the SEM photo.

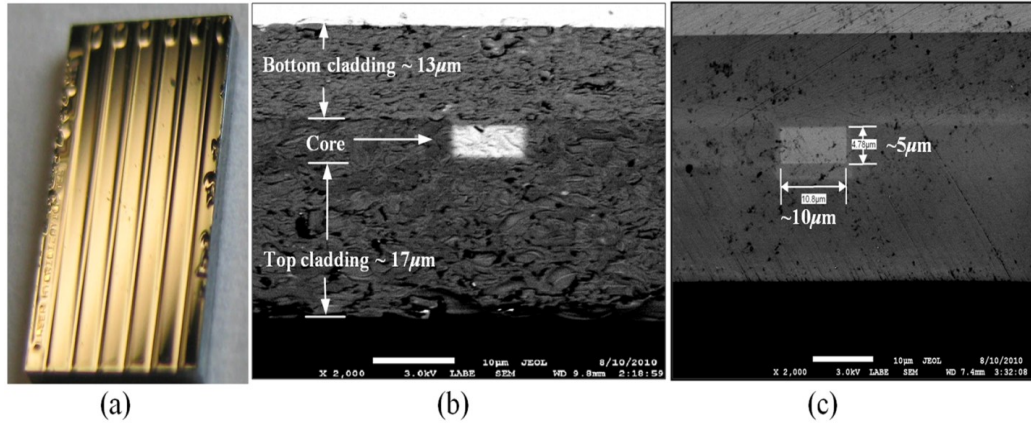


**Figure 2.3** Silica-on-silicon (SOS) waveguides used for the fabrication of SOS-PDMS Lab-on-a-chip, (a) waveguide diced into 4.5X6.5mm sample, SEM image of SOS waveguide before (b) and after (c) polishing using diamond lapping film.

#### **2.4.2 Diamond micromachining of the microchannel**

Esec 8003 dicing saw was used for the fabrication of microchannel on SOS waveguide. This machine was designed to cut semiconductor wafers into chips. The blade used in the setup is a steel ring with diamond particles having the size of 5 μm coated on it. The thickness of the blade was 100 μm. The blade was mounted on a high frequency air bearing spindle. The rotation speed of the wheel was set at 18000 rpm. Sample was fixed to the vacuum chuck by using an UV curable tape having the thickness of 80 μm. A height sensor is used in the setup to measure the height of the diamond saw from the chuck. The height of the blade was set to 540 μm in order to have a channel depth of ~100 μm (+/-10 μm). The machining speed was set to 1 mm/sec. Figure 2.4 shows the microscope image of the microfluidic channel fabricated on the SOS chip. The width and depth of the channel was measured by using an optical microscope, and they were ~110 μm as shown in Figure 2.4.

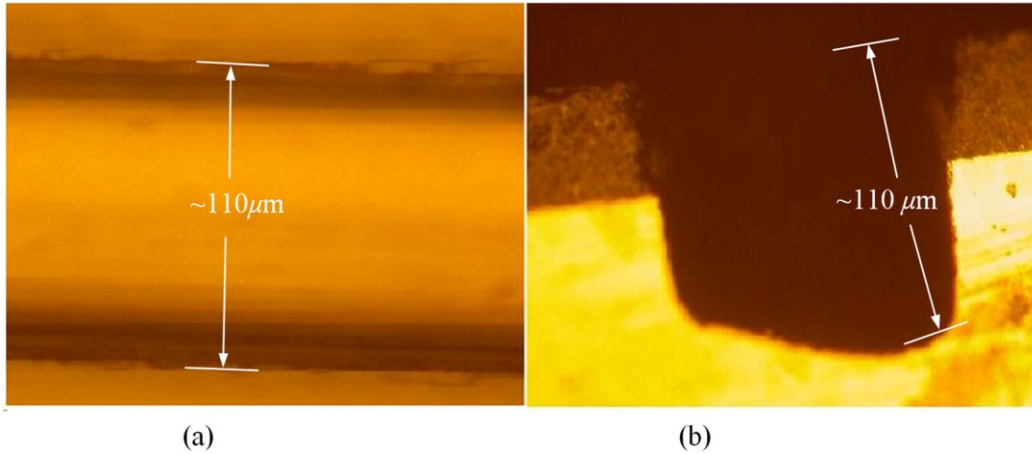


**Figure 2.4** (a) Top view showing the width and (b) Cross sectional view showing the depth of the microchannel fabricated by diamond micromachining method.

### **2.4.3 PDMS microfluidic platform**

The PDMS platform contains a slot for fixing the SOS chip, microfluidic channel and liquid reservoirs. The depth of the slot for fixing the SOS chip was  $560 \mu\text{m}$ . The depth of the microfluidic channel in the PDMS was  $80 \mu\text{m}$ . The mold for the PDMS platform was designed in commercial software called ProEngineer and fabricated on brass by CNC machining. A thin layer of gold was electroplated on the brass mold for the easy removal of PDMS, otherwise it was difficult. Soft lithography for the fabrication of PDMS platform is carried out in a general laboratory environment. PDMS platform is fabricated by a two-component silicone elastomer kit which is SYLGARD 184 obtained from the Dow Corning. The silicon base and curing agent (cross linker) are mixed in 10:1 (wt %) ratio. This mixture contains air bubbles generated from the mixing; hence the mixture was placed in a vacuum desiccator and degassed until all the gas bubbles were removed. Further, PDMS was casted on the brass mold and baked at  $80^{\circ}\text{C}$  for 5 hours. The baking temperature or time is not

critical as the optical property of the PDMS such as the refractive index is not a concern in the present work. The cross-linking time can be decreased by increasing the curing temperature. Figure 2.5 shows the brass mold and the PDMS platform fabricated by soft lithography.

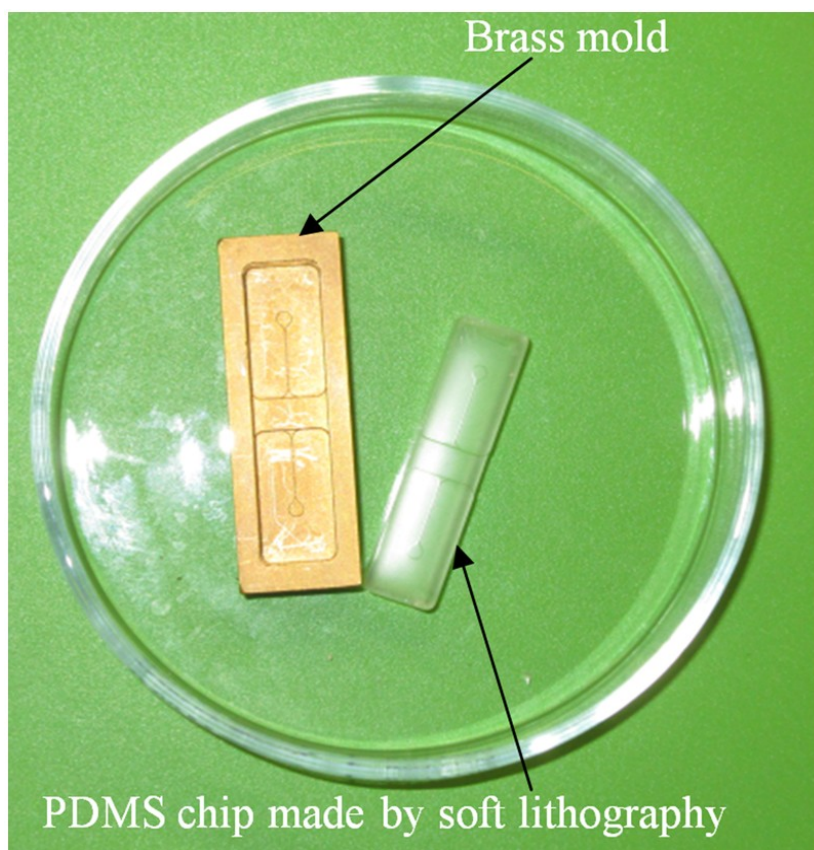


**Figure 2.5** Brass mold and PDMS chip.

#### ***2.4.4 Integration of PDMS and SOS chip***

Once the PDMS platform is fabricated, next step is the integration of SOS chip on it. The device fabrication involves two bonding process; first, the bonding of SOS chip on the slot of the PDMS platform, second is the sealing of the microfluidics channel by a thin layer of PDMS. Finally the fluid inlet and outlet tubes must be interconnected on top of the liquid reservoirs.

Oxygen plasma treatment was used for the bonding of the device. The exposure of oxygen plasma on the PDMS surface helps to clean the surface, together with the modification of hydrophobic nature of PDMS to the hydrophilic by converting the -O-Si(CH<sub>3</sub>)<sub>2</sub>- unit in PDMS to silanol group (Si-OH). The quality of the bond is determined by the exposure time and how quickly the samples are kept in contact after the exposure and before contaminating and losing the surface property. If there is any aligning task involved in the bonding, the bonding process requires extensive care and expertise. The plasma exposure is carried out in the instrument obtained from Harrick plasma. For the first bonding process of device fabrication, the back side of SOS chip (that is the silicon surface) and PDMS platform are washed in deionized (DI) water and dried with an air gun and loaded to the plasma instrument. The plasma chamber pressure was pumped down to 70mTorr and the oxygen was introduced at 10 sccm into the chamber. The plasma was created by RF power. The samples were exposed to the oxygen plasma for 35 seconds. Then the SOS chip was placed in the slot on PDMS and pressed. The region of transition of channel in PDMS to SOS chip is designed by chamfering the channel ends in order to eliminate the misalignment problem between the microfluidic channel in PDMS and the SOS chip,

resulting in no alignment issue due to the present bonding process. This bonding process forms a strong leak proof bond of chip on PDMS immediately. The next step of device fabrication is the sealing of the device. A thin flat layer of PDMS with the thickness of 2mm is used for sealing the device. The same process of preparation of PDMS explained before is used for the thin PDMS layer also, herein the PDMS was casted on a silicon wafer to obtain a flat layer. Before casting the PDMS, the silicon wafer was silanized with the vapor of trichlorosilane in a covered Petri dish on a hot plate at 55<sup>0</sup>C for 5 hours for promoting the easy removal of the PDMS. Then the wafer was placed in a Petri dish and poured the PDMS and baked at 80<sup>0</sup>C for 3 hours. Then the PDMS layer was peeled off from the wafer and cut into 1×4 cm samples. Two holes of 2 mm diameter were punched to insert the fluidic tubes. The position of the holes on the PDMS layer is on the position of liquid reservoirs in the PDMS platform. The PDMS platform with the SOS chip and the thin flat layer were cleaned in DI water and exposed to the oxygen plasmas as explained before. Then the samples were pressed with the elapse of no time. This process yields a hermetic and irreversible sealing of microfluidic channels. Then the fluidic tube (obtained from Gilson Mandel) having the inner diameter of 250 μm and the outer diameter of 2 mm was inserted into the hole punched on the PDMS layer and glued with a one-component silicon RTV adhesive obtained from the Dow Corning. This adhesive was selected to be highly viscous so that, before the completion of heating and curing, it does not reach the liquid reservoirs and blocks the microfluidic channel. Then sample was cured in the oven at 100<sup>0</sup>C for one hour. Figure 2.6(a) shows the photograph of the fully integrated SOS-PDMS lab-on-a-chip.

Steps	Process	Fabrication method
1	Integration of microfluidic channel on SOS waveguide	Diamond dicing
2	Fabrication of PDMS platform for the microfluidics chips	PDMS Soft lithography
3	Bonding of SOS chip with PDMS chip	Oxygen plasma treatment
4	Sealing of the channel	Oxygen plasma treatment

**Table 1.** Process steps involved in the fabrication of SOS-PDMS lab-on-a-chip.

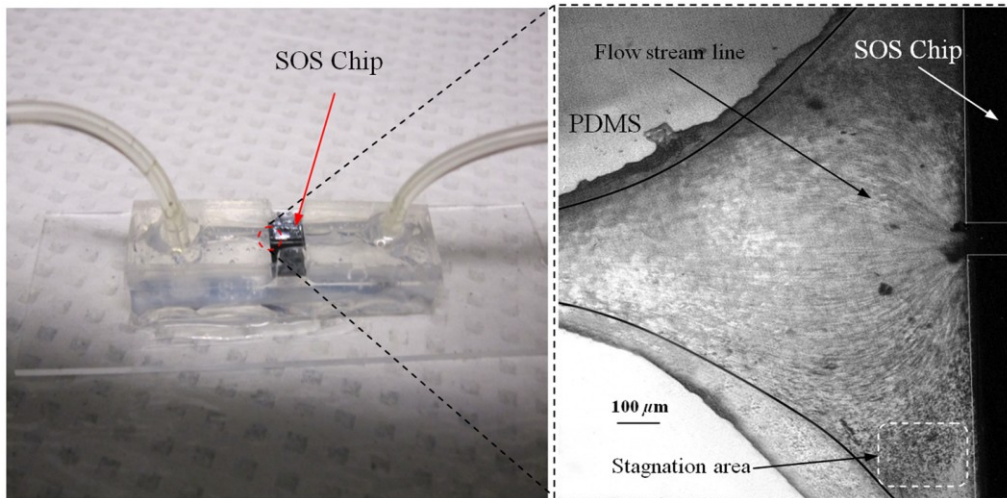


**Figure 2.6** (a) SOS-PDMS Lab-on-chip (b) Close up of the flow in transition microfluidic zone between SOS and PDMS chip.

The device was tested with micro flows in order to test for the flow behavior and the possible leakages. Initially, DI water was pumped by Minipuls™ 3 peristaltic pump.

The inlet velocity was varied slowly from 0.05m/s to 0.3m/s and no leakage was noticed. To test the flow behavior through the device, DI water containing the polystyrene spheres of  $5\mu\text{m}$  size, purchased from the Duke Scientific, (catalog number G0500) was used. The polystyrene spheres were dispersed in DI water at a volume fraction of  $10^{-6}$  and pumped through the device. The pumping was done under a microscope (Nikon ECLIPSE 80i) to image flow pattern. Figure 2.6(b) shows the flow through the fluidic injection zone imaged under the microscope, herein the inlet velocity was set at 0.1m/s. The flow stream line imaged with the help of polystyrene spheres showed that when the inlet velocity was increased to 0.2m/s, two fluidic stagnation areas were observed in the two corners of the fluid injection zone. When the fluidic was pumped below the 0.1 m/s, the stagnation area was reduced to the extreme corners of the fluidic injection zone as shown in the Figure 2.6(b). The liquid stagnation in the fluidic path is not favorable during the rinsing of the channel as it can accumulate the chemical wastes in the chip and would result in errors in the measurements. Therefore, the cleaning of the channel after each measurement was done at lower velocity.

Since the integration of the microchannel in SOS waveguide was done by diamond machining, the surface quality of the channel wall was needed further surface finishing so that the light coupling between the waveguide and the microfluidic channel was not affected. The quality of coupling of the excitation light to the microfluidic channel and the collection of the fluorescent light from the channel can be reduced significantly by the roughness of the channel wall. The channel wall surfaces were polished by microfluidic assisted chemical polishing ( $\mu\text{CP}$ ). A

commonly used silicon dioxide etchant which is Buffered hydrofluoric acid (BHF) was pumped through the channel for polishing the channel wall. Buffered hydrofluoric acid (BHF) was prepared from HF and ammonium fluoride in 1:6 ratios. The stability of PDMS in BHF was tested before pumping the BHF to the device. Several PDMS samples with microstructures were soaked in the BHF for different times and found that the microstructures were slightly deformed after about 15 minutes of soaking. Hence, in the case of  $\mu$ CP, BHF was pumped through the microchannel fabricated in SOS chip for 10 minutes at 0.2 m/s velocity in order to reduce the surface roughness of the microchannel wall fabricated by diamond machining.

#### ***2.4.5 Optical measurement setup***

A fiber-to-waveguide aligner setup was built for the fluorescence detection. Figure 2.7 shows the setup used for the fluorescence detection experiments. This setup includes two high precision micropositioners, fiber chucks and fiber holders obtained from the Newport. Micropositioners are five-axis controllable. Light from a fiber laser (OZ Optics, 635 nm, 1 m W) was directly coupled to the waveguide with the help of opto-mechanical setup. A multimode fiber is aligned with the waveguide for collecting the fluorescence signal and coupling to the spectrometer. A commercially available spectrometer (Ocean Optics USB 4000) was used for the fluorescence measurements.

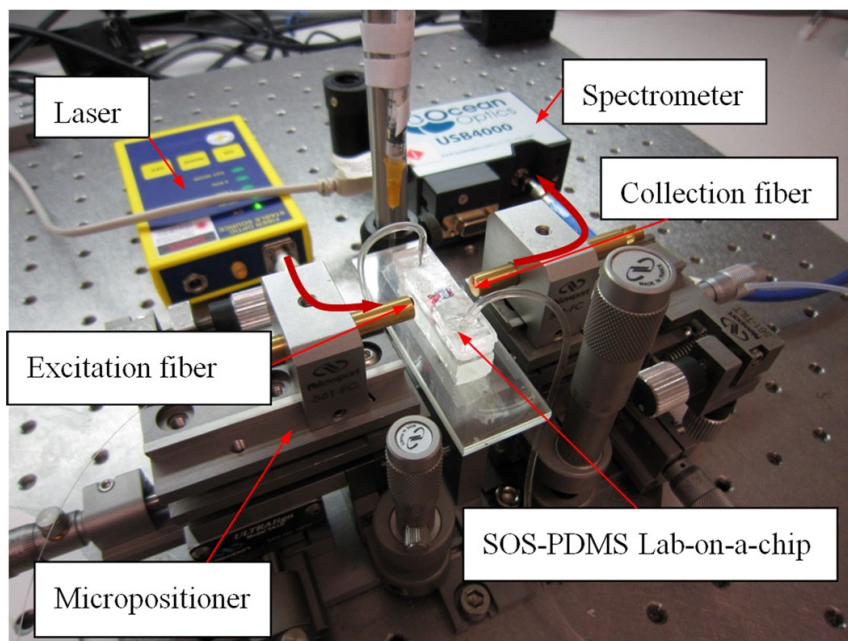


**Figure 2.7** Opto-mechanical setup with SOS-PDMS Lab-on-a-chip.

## 2.5 Results and Discussion

Fluorescence is one of the preferred ways of biodetection in many bioassays and other LOCs. Quantum dots (QDs) have many advantages over fluorophores such as narrow absorption peak, wide absorption band and good stability. As the QDs are used in many biodetection applications such as the detection of protein toxins (staphylococcal enterotoxin B, cholera toxin)[78], ricin, shiga-like toxin 1 (SLT), staphylococcal enterotoxin B (SEB)[79], *Escherichia coli* O157:H7 and *Salmonella typhimurium* [80] and the detection of single-nucleotide polymorphism in human oncogene p53 and for the multiallele detection of the hepatitis B and the hepatitis C virus [81]etc., the proposed LOC is demonstrated for the detection of fluorescence from QD in order to show the possibility for many bio-applications.

For the investigation of fluorescence detection capability of the SOS-PDMS LOC, the quantum dots (QD655) was used. QD 655 can be excited with any wavelengths below 650 nm and they produce a narrow emission peak at 655 nm. QD 655 was obtained from Invitrogen Company, and they are used as received. QD 655 was suspended in 50 mM borate buffer. QD655 was further diluted to different concentrations in DI water for investigating the detection limit of the device. Figure 2.8 shows the spectra of the fluorescence emission from the quantum dot (QD 655) recorded from the device. The quantum dot solution was pumped to the microchannel of the device and excited by laser light of 635 nm coupled to the microchannel through the fiber and SOS waveguide. A collection fiber was aligned at the other end of the SOS waveguide to couple the fluorescence light to the spectrometer. Since there is no filter used for removing the excitation signal, two peaks are visible in the Figure 2.8, one at 635 nm that corresponds to the excitation light and second one at 655 nm that corresponds to the emission from quantum dots. The three spectra in Figure 2.8 correspond to emissions from three different concentrations of the quantum dot. After taking the measurements for each concentration, the device was cleaned by pumping DI water for 3 minutes.

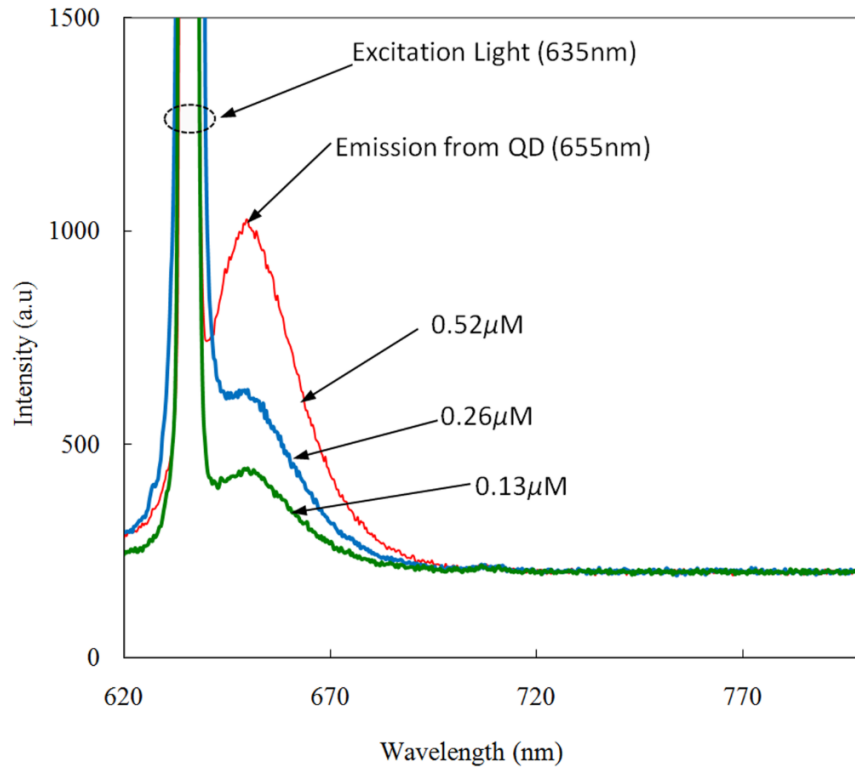


**Figure 2.8** Fluorescence emission measured from QD 655 for different concentrations.

From the Figure 2.3(b) and Figure 2.4(b), we know that the core of the waveguide is located  $\sim 15\mu\text{m}$  above the silicon surface and the depth of the microchannel is  $\sim 110\mu\text{m}$  respectively, that means the waveguide is located at  $1/3$  of the microchannel and only a portion of the sample flowing through the microchannel is detected. Hence, if there is any air bubble which tends to stay on top portion of the channel, the device cannot detect the signal correctly. In order to confirm there is no trapping of air bubbles, each measurement is repeated several times by pumping the solution through the microchannel and recording the measurements. The detection limit of the device is found to be as low as  $0.13 \mu\text{M}$ . A graph plotted between the fluorescence intensity

recorded in the spectrometer for each concentration of quantum dot is shown in Figure 2.9. As can be seen in the Figure 2.9, one can observe a linear variation between the fluorescence and concentration of quantum dots. This experiment demonstrates that the proposed LOC can be used for many bio-applications based on QD fluorescence detection.

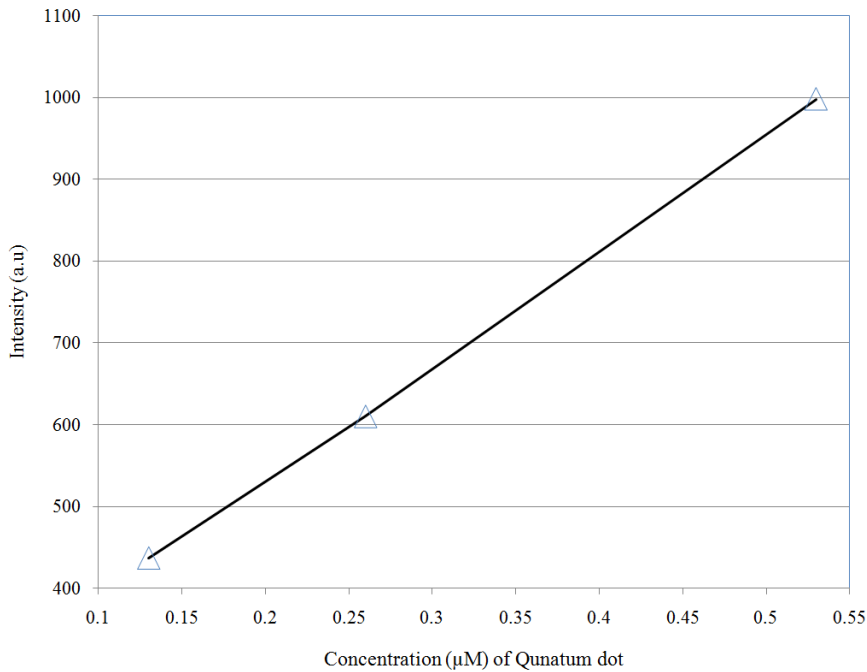


**Figure 2.9** Variation of fluorescence intensity against the concentration of quantum dot.

## 2.6 Conclusions

A new method of integrating an optical microfluidic system by using silica-on-silicon based microphotonics chip and PDMS based microfluidic chip was proposed. Two simple and low cost technologies, namely diamond micromachining and soft lithography were used for the fabrication of device. By exploiting the benefits of

PDMS for fabricating high-aspect ratio microfluidics structures together with the integration of low loss SOS photonics waveguides greatly simplifies the fabrication of optical micro total analysis systems. Furthermore, the optical loss from the roughness of channel wall introduced by the diamond machining was minimized by the microfluidic assisted chemical polishing of the channel wall in order to obtain the optical coupling between waveguide and microfluidic channel. The performance of the device was tested by detecting the laser induced fluorescence from quantum dots of different concentrations. The detection limit of the present device was found as low as  $0.13\mu\text{M}$  for the quantum dots 655. Thus the proposed SOS-PDMS integration demonstrates the possibility of realizing simple and less-expensive LOCs for bio-detection based on quantum dot fluorescence.

## **Chapter 3: Detection of fluorophore-tagged Recombinant Bovine somatotropin (rbST) by using Silica-on-silicon (SOS)-PDMS Lab-on-a-chip**

### **3.1 Introduction**

Bovine somatotropin (bST) is a polypeptide growth hormone naturally produced by the anterior pituitary gland of cows. The primary protein in the pituitary extract, which is responsible for the increase of milk production, is bST. The effect of bST on milk production was discovered in 1937[2]. Since the 80s, by using the recombinant DNA technologies [12], large quantities of hormones were produced and used to increase the milk production. The use of recombinant bST (rbST) is controversial [14, 82, 83] because of its potential effects on animal and human health, hence, it is forbidden in many countries. To provide meaningful information to consumers and to identify the rbST-treated animals, highly sensitive analytical methods are required.

The concentration of bST was traditionally estimated using, either an enzyme-linked immunosorbent assay (ELISA) [22, 23], a radioimmunoassay (RIA) [84] or bioassay methods [25]. ELISA assays have a limitation that is the concentration of antibody can only be reported in relative terms such as “titer”, that is, a combination of affinity and concentration. More recently, a sensitive method based on liquid chromatography-mass spectrometry (LC-MS), combined with electrospray ionization [13, 26, 85, 86] has been developed for the discrimination between the recombinant and the endogenous forms of somatotropin. The principal drawback of this approach is the complexity of the methodology, together with very expensive and large

instrumentation, which makes this method difficult to implement for the rapid detection of bST and rbST in milk. Surface Plasmon Resonance (SPR) biosensing method has also been suggested [26] for the detection of rbST, however, the measurements are carried out in an expensive plasmonic instrument such as Biacore 3000. In this context, developing a miniaturized analytical device that allows a rapid and precise detection of growth hormones becomes extremely important. The detection of rbST in milk is very important and still a challenging task, hence, this work proposes an optical lab-on-a-chip platform for the detection of fluorophore-tagged rbST. The advantages of the lab-on-a-chip are principally, a low consumption of reagents, portability, suitability for the Point of Need (PON) application, and low cost, compared to other existing methods.

Since 90s, miniaturized total analysis systems ( $\mu$ TAS), alternatively called Lab-on-a-chips (LOCs) have gained increased attentions as a major breakthrough in analytical chemistry. Though the concept of miniaturization of analytical systems was initially proposed [39] to enhance the analytical performances, later on, many other benefits such as low consumption of carriers, reagents and mobile phase have also been recognized [43, 63]. Moreover, the integration of multiple components in a single chip is also possible, by using the existing and new microfabrication technologies. Well-developed silicon microfabrication technologies were originally adopted for the fabrication of micro total analysis systems, however, for a wide range of applications, new materials and fabrication processes were also reported in literature [44, 70]. Silicon, glass and polymeric materials such as polydimethylsiloxane (PDMS) [54] poly (methyl methacrylate) (PMMA) [87] and SU-8 [64] are widely used material for

the fabrication of miniaturized total analysis systems.

Even though there are many techniques reported for the bio-detection, fluorescent detection is still a widely used approach [42] as it has many advantages including high sensitivity, stability, good spatial resolution as well as high discrimination capability. In order to implement an optical Lab-on-a-chip, an optical setup consisting of a light source coupled to the waveguide through a microfluidic channel, spectrometer and detectors have to be integrated. A traditional approach of setting up a free space beam across fluidic channel suffers disadvantages such as misalignment issues and hence an integrated optics platform has been proven [48, 50] suitable for the miniaturization of analytical systems.

Labeled and label-free are the two widely used methods of optical-based detection of biomolecules. Fluorescence detection is a widely used method of quantitative detection of biomolecules. Highly stable fluorescent probe are already demonstrated for the detection of DNA [88] and proteins [89]. Also, the labeled detection permits simultaneous detection of multiple targets by using multiple fluorescent probes having different emission properties. The main disadvantage of the labeled detection is the process involved in optimizing the labeling conditions of the fluorescent probe with biomolecules, however, a large variety of biologically important molecules are commercially available in fluorescent-labeled forms. On the other hand, main benefit of label-free detection method is the absence of labeling process and low cost.

In the case of the label-free methods, the optical resonance properties of metallic nanoparticles are extensively used for analytical purposes [41, 90, 91]. Fluorescent dyes [67] or quantum dots [68] are proven to be useful for labeling and detection of

various biomolecules. Fluorescein derivatives are used for a wide range of applications such as fluorescence microscopy, flow cytometry [92] and immunofluorescence-based assays [93]. FITC received the most attention for conjugation with proteins as it reacts with amino groups in peptides and forms stable thiourea bonds [94].

In this chapter, the detection of fluorophore-tagged rbST is demonstrated by using a low cost optical lab-on-a-chip. The advantage of PDMS for the fabrication of high-aspect-ratio microfluidics components and Silica-on-silicon (SOS) for the fabrication of optical waveguide is exploited for the fabrication of a lab-on-a-chip. By using soft lithography, any high-aspect-ratio 3D-microfluidics components, required for the lab-on-a-chip can be fabricated in a general laboratory environment without the need of any special expertise. The SOS waveguide is fabricated in a standard clean room and a straight microchannel is fabricated on SOS by using the diamond sawing technique. Finally, the SOS chip was integrated on the PDMS platform for the realization of a low cost optical lab-on-a-chip. In our previous work [59], the proposed lab-on-a-chip was demonstrated for the fluorescence detection of quantum dots. In the corresponding device, the excitation light was coupled to the microchannel through a waveguide and the fluorescence emission was collected through another waveguide, coupled to the spectrometer. Such an in-line excitation and collection of emission was possible due to the narrow emission spectrum of the quantum dots. In the present study, two types of dyes, FITC and Alexa-647 are used for the tagging and the detection of the rbST. Since the emission spectra of the dyes are wide, the in-line excitation resulted in the overlapping of the excitation and emission spectra in the

spectrometer, and hence a new testing scheme is used as illustrated in the Figure 3.1 in order to excite the species from the top of the microchannel. The tagging procedure for the rbST with two types of fluorophores such as FITC and Alexa-647 was optimized for maximizing the fluorophore-polypeptide ratio. The purpose of the present work is the optimization of the labeling process and the study of the proposed LOC platform, in view of further refinement of the method of detecting rbST. The aim of the paper is to study the fluorescence behavior of rbST-fluorophore conjugates and demonstrate the capability of the proposed LOC for reliable quantitative fluorescence detection and measurements. The present work demonstrates the possibility that the proposed LOC can be developed further for the detection of rbST in milk.

### **3.2 SOS-PDMS Lab-on-a-chip**

An optical microfluidic system is fabricated by a novel hybrid integration method. The use of PDMS for the fabrication of high aspect-ratio microfluidics circuits and silica-on-silicon planar waveguide technology for the fabrication of low loss optical waveguide are exploited in the hybrid integration process. By using soft lithography, a PDMS platform composed of a microfluidic channel and liquid reservoirs are fabricated in a general laboratory environment.

In SOS waveguide, wave guiding is achieved by three layers of silicon dioxide deposited on the silicon wafer. In order to achieve the vertical confinement of light, the refractive index of the second layer called core of the waveguide, must be higher than that of the first and second layers called cladding of the waveguide. For the

lateral guiding of light, the core layer has to be structured to the desired width by using micromachining techniques. Since the loss of the SOS waveguide depends on the fabrication process, the micromachining processes must be done with extreme care, therefore the fabrication of waveguide is carried out in a clean room in such a way that the loss is minimized. However, the micromachining of high-aspect-ratio microfluidics components on SOS platform is expensive and a challenging process. Hence a low cost fabrication method is proposed for the fabrication of an optical lab-on-a-chip.

A schematic sketch of the device proposed for the detection of fluorophore-tagged recombinant bovine somatotropin is shown in Figure 3.1. An SOS waveguide with a straight microfluidic channel is integrated on a PDMS platform containing the microfluidic components. The device is sealed with a thin PDMS slab. The fluorophore-tagged biomolecules that are to be tested will be pumped through the fluidic path as illustrated in Figure 3.1. The light from the laser for the excitation of tagged biomolecules is coupled to the microchannel from the top through the PDMS layer. The coupling of light from the top is useful to avoid the coupling of intense excitation light to the spectrometer. The emitted fluorescence light is collected through the waveguide and coupled to the spectrometer.

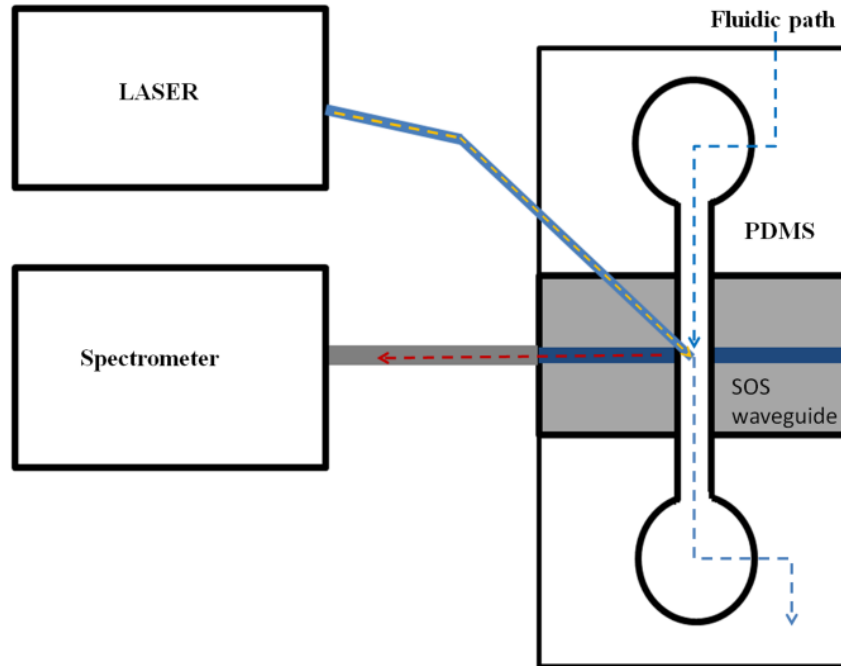


**Figure 3.1** Schematic illustration of SOS-PDMS Lab-on-chip.

The process of integration of SOS-PDMS lab-on-a-chip is illustrated in Figure 3.2(a). Two simple and low cost fabrication processes are used for the realization of an optical micro fluidic system. A detailed fabrication process of the device and the testing of micro flow behavior through the device are discussed in ref. [95]. A PDMS platform containing two liquid reservoirs, a microchannel and a slot for fixing the SOS waveguide is fabricated by soft lithography. Using a simple diamond sawing method, a microchannel is fabricated on the SOS waveguide. In the integration process, the SOS chip with a straight micro channel is bonded to the PDMS platform by using oxygen plasma treatment. During this process, after the exposure to plasma of PDMS and SOS chip, the samples must be kept in contact without any delay, and also the channel in the SOS must be properly aligned with the channel of PDMS. In

order to simplify the alignment task, the fluid transition region (where the fluidic is injected from the PDMS to SOS) between the SOS and PDMS is designed by chambering the channel in the PDMS as shown in Figure 3.2(a). The device is sealed by using a thin PDMS layer and the fluidic tubes are connected to the liquid reservoirs.

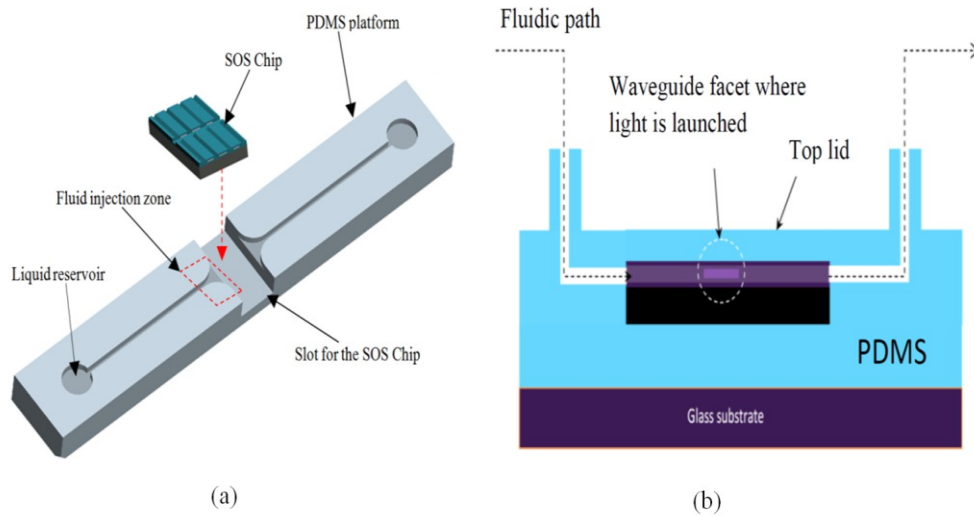


**Figure 3.2** Illustration of integration of SOS-PDMS Lab-on-a-chip, (a) 3D view of the microfluidic chip on PDMS and SOS chip and (b) sectional view showing the microfluidic path and SOS chip.

LOC detection can be considered as a competing technology only in terms of cost and simplicity even though the quality and the amount of information provided by a LOC are not comparable with mass spectroscopy. However, small and portable instruments have to be used for rapid field analysis and the proposed device represents a first step in this direction. After further refinement of the analytical process, a selective

detection of rbST will be possible.

In order to use the proposed method for the detection of rbST in milk, the milk containing the rbST must undergo a separation process such as solid phase extraction (SPE) to separate the rbST, which is not attempted in the present work. After the separation is carried out, the LOC and experimental techniques presented in this work can be used for the tagging of extracted milk containing rbST with the FITC or Alexa-647 for detecting rbST in milk. The accuracy of LOC detection will depend on purification and separation of rbST from milk. In this case of detecting rbST, the corresponding anti-rbST has to be absorbed on the functionalized microchannel wall, and only the tagged rbST will bind on the device for highly specific detection.

### **3.3 Experimental details**

#### ***3.3.1 Materials and reagents***

Recombinant bovine somatotropin (rbST, Molecular Weight- 22 kDa) was obtained from Cedarlane, ON, Canada. FITC, Alexa-647, Phosphate Buffered Saline (PBS) and sodium carbonate-bicarbonate were obtained from Sigma-Aldrich, Canada. The PBS tablet was dissolved in deionized (DI) water at 0.1M concentration and 7.2 pH. Sodium carbonate-bicarbonate was dissolved in DI water for the preparation of the buffer solution of concentration 0.1M and pH of 9.0. The rbST in the powder form was dissolved in sodium carbonate-bicarbonate buffer at a concentration of 1 mg/ml. A gel filtration column filled with Sephadex G-25 beads was used to separate the unreacted FITC. The use of Sephadex beads formed by cross linking dextran with epichlorohydrin was widely reported for the separation of biomolecules. The bed

volume and the bed height of the column were 3.5 ml and 2.6 cm respectively. The PDMS base and curing agent (SYLGARD 184 Kit) were obtained from Dow Corning.

### ***3.3.2 Tagging of rbST with FITC***

The procedure reported [29] for tagging Immunoglobulin G (IgG) with FITC was modified as explained below. 2 mg of FITC was dissolved in 2 mL of 0.1 M sodium carbonate-bicarbonate buffer solution. 1 ml of rbST was mixed with 200  $\mu$ l of FITC solution and the reaction was carried out for several hours and at different temperatures. The reaction mixture was stirred by using magnetic bars. The separation of labeled rbST was carried out by using column chromatography. The Sephadex G25M column was used for column chromatography. The column was stabilized by eluting with a PBS solution for one hour, prior to the separation process. Then the reaction mixture was added to the column and, the separation was carried out by collecting 10 fractions. To each fraction, 0.25 ml of PBS was added to the column and the presence of labeled peptides was assessed by measuring the UV-Visible spectrum.

### ***3.3.3 Tagging of rbST with Alexa-647***

The rbST solution was prepared in 0.1M sodium bicarbonate buffer at a concentration of 1mg/ml. Then, 1 ml of the rbST solution was mixed with 50 $\mu$ l of Alexa-647 solution of 5 mg/ml concentration in a small reaction vial. The reaction was carried out at different temperatures and times to find the best labeling condition. The

separation of the labeled rbST was carried out by using Sephadex G25M column. The column was stabilized by eluting with PBS for one hour prior to the separation process. The elution of column for the separation of labeled protein was carried out by adding 10 fractions of 2 ml PBS. Each fraction, (0.2 ml of PBS), was added to the column and the fractions were collected. The presence of the conjugate is assessed by measuring the absorbance spectrum in the UV-visible range. The fractions containing the conjugates are pooled together and stored in a solution of 2mM sodium at 5<sup>0</sup>C.

#### ***3.3.4 Fabrication of SOS waveguide***

The fabrication of waveguide starts with the deposition of silica layers on a silicon wafer of (100) orientation. Plasma Enhanced Chemical Vapor Deposition (PECVD) was used for the deposition of high quality films of silicon dioxide. The waveguide is composed of three layers of oxide having different refractive indices. The first and third layers of oxide called the cladding of the waveguide were deposited by tuning the process parameters to achieve the refractive index of 1.445. The thickness of the bottom cladding layer was 13 $\mu$ m as shown in Figure 3.3. The second oxide layer, called the core of the waveguide required higher refractive index than the cladding that is 1.457. Hence the light is propagated through the core by total internal reflection. Thickness of the core layer was 5 $\mu$ m as shown in Figure 3.3(a).

The core layer was machined to the desired width prior to the deposition of third oxide layer. The core layer was structured to 10 $\mu$ m by using UV photolithography and reactive ion etching (RIE). Finally the top cladding was deposited on the patterned core layer. A thickness unevenness of  $\sim$ 5 $\mu$ m was measured on the topology

of the waveguide. Finally the waveguide was diced into 4.5×6.5mm samples. The waveguide facets were polished by using a diamond lapping film of 0.1 $\mu$ m particle sizes (Allied Hightech). Figure 3.3(a) shows the SEM micrograph of the SOS waveguide facet and the dimensions of the core and cladding.

### **3.3.5 PDMS microfluidic chip**

The PDMS microfluidic chip was fabricated by soft lithography. The mold for the soft lithography was designed by the commercial software ProEngineer and fabricated on brass by CNC machining. For the soft lithography, the PDMS base and curing agent are mixed in 10:1 (wt ratio) followed by degassing the mixture in a vacuum desiccator to remove the gas bubbles. Then PDMS was poured into the brass mold and baked at 80<sup>0</sup>C for 5 hours. Figure 3.3 (b) shows the PDMS microfluidic chip fabricated by soft lithography.

As mentioned above, a straight microchannel was fabricated on the SOS waveguide by diamond micromachining. Esec 8003 dicing saw was used for the diamond micromachining. The height of the blade was set to 540  $\mu$ m in order to have a channel depth of ~100  $\mu$ m (+/-10  $\mu$ m). Figure 3.4 (a) shows the microscope image of the microfluidic channel fabricated on the SOS chip. Both the width and depth of the channel was measured by using an optical microscope, and they were ~110 $\mu$ m.

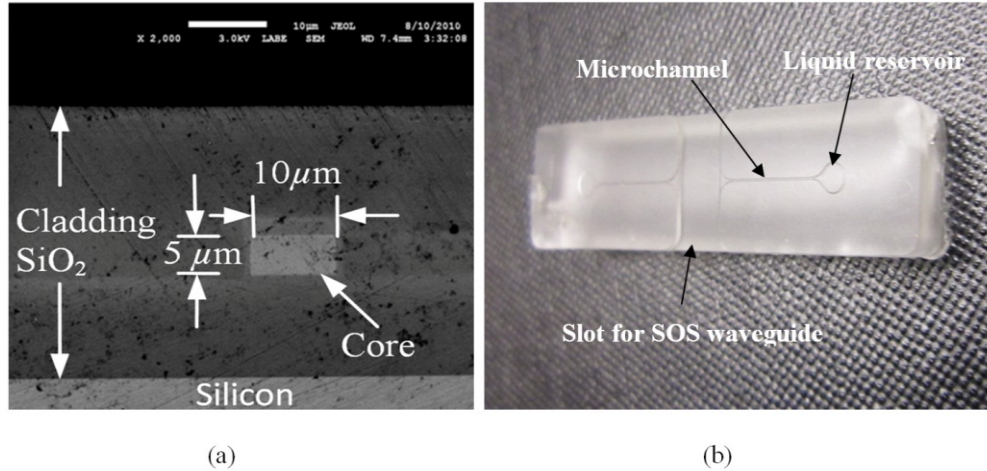


**Figure 3.3** (a) SEM of waveguide facet (b) PDMS microfluidic chip

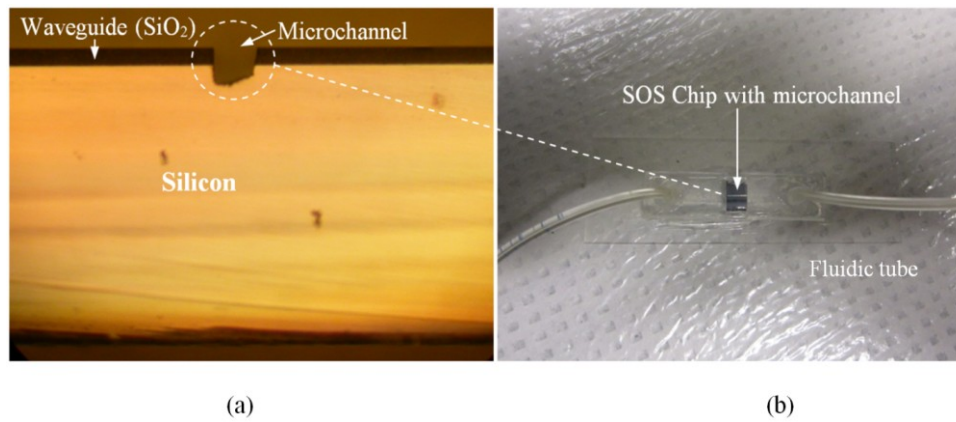


**Figure 3.4** (a) Microscope image of SOS waveguide with microchannel (b) SOS-PDMS Lab-on-a-chip

The SOS chip with microchannel was bonded to the PDMS platform by using oxygen plasma treatment. The PDMS and SOS chips were exposed to oxygen plasma for 30 seconds in a plasma cleaner obtained from Harrick plasma. Then the SOS chip was placed in the slot for the SOS chip and bonded immediately. A thin PDMS layer of 2 mm thick was used as the top lid of the device for sealing the micro channel. Two fluidic tubes are connected to the device to pump the sample to the device. Figure

3.4(b) shows the SOS-PDMS Lab-on-a-chip used for the detection of fluorescent-tagged rbST.

Since the diamond sawing was used for the fabrication of the microchannel, the coupling of the light from the microchannel to the waveguide would be adversely affected by to the roughness of the waveguide facet. Hence a novel approach of polishing the microchannel called microfluidic assisted chemical polishing ( $\mu$ CP) was used for polishing the wall of the microchannel. Buffered hydrofluoric acid (BHF) was pumped through the channel for polishing the channel wall. Buffered hydrofluoric acid (BHF) was prepared from HF and ammonium fluoride in 1:6 ratio. BHF was pumped through experimental set-up for the detection of fluorescence of rbST the microchannel fabricated in SOS chip for 10 minutes at 0.2 m/s velocity, which found to be enhancing the fluorescence collection from device.

Figure 3.5 shows the opto-mechanical setup used for the detection of fluorophore-tagged rbST. This setup consists of two micropositioners, optical fibres, light source and a spectrometer. The LOC was fixed on a 3-axis controllable micropositioner, and a 5-axis controllable micropositioner is used to align the fluorescence collection fiber with waveguide. The fluorescence collection fiber was coupled to the spectrometer. The excitation fiber was arranged in the top of the device as shown in Figure 3.5. A LED source (LS-450, 60 $\mu$ W Ocean optics) of 470 nm wavelength was used for the excitation of FITC tagged rbST and a fiber laser (OZ optics 1mW) of 635 nm wavelength was used for the excitation of Alexa-647 tagged rbST. A commercially available spectrometer (USB 2000) obtained from Ocean optics was used for the measurement of fluorescence spectrum.

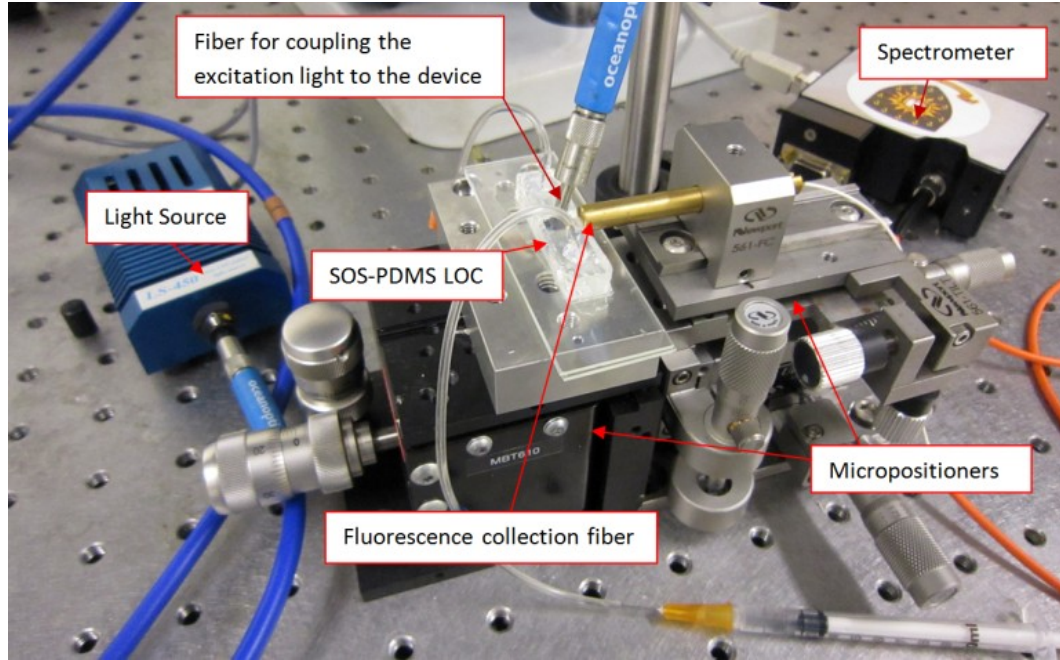


**Figure 3.5** Experimental setup with SOS-PDMS Lab-on-a-chip

### 3.4 Results and discussion

The absorbance spectrum of the conjugates showed two peaks, the one at 280 nm corresponds the absorption of rbST and the second one at 495 nm or 650 nm corresponds the absorption of FITC or Alexa-647, respectively. The concentration of fluorophore in the conjugates was estimated from the extinction coefficient which is measured from the absorbance at 495 nm or 650 nm in the absorbance spectrum of FITC or Alexa-647 conjugates, respectively. Though the extinction coefficient of the bound dye is reported [34] as slightly different from the unbound dye, for the calculation of the concentration of the bound dye, the extinction coefficient of

unbound dye was used. The molar concentration of bound dye in the conjugates was calculated using the formula [94]:

$$\text{Concentration of dye, } C_f = \frac{A_{dye}}{\epsilon_{dye}} \quad (3.1)$$

Where  $A_{dye}$  is the absorbance of conjugate due to the fluorophores and the  $\epsilon_{dye}$  is the extinction coefficient of unbound dye, which is expressed as the optical density of 0.1% dye solution measured in a 1 cm cell.

The concentration of rbST in the conjugate is estimated by using the formula [96]:

$$C(M) = \frac{A_{280} - (CF \times A_{dye})}{\epsilon_p} \quad (3.2)$$

Where CF is a correction factor as the dye also contribute a small absorbance at the 280 nm. This value was obtained from the manufacturer's data sheet of fluorophores.  $\epsilon_p$  is the molar extinction coefficient of rbST.

<b>Properties</b>	<b>FITC</b>	<b>Alexa-647</b>
Excitation wavelength	495nm	650nm
Emission wavelength	520nm	665nm
Extinction coefficient	70000M <sup>-1</sup> CM <sup>-1</sup>	239000M <sup>-1</sup> CM <sup>-1</sup>
Quantum yield	0.92	0.33

**Table 3.1.** Optical properties of the fluorophores

The degree of labeling of the conjugates is assessed based on the molar fluorophores-peptide ratio, which is given by [96]:

$$F/P = \frac{\text{Molar concentraion of dye}}{\text{Molar concentration of rbST}} \quad (3.3)$$

After the elution of the reaction mixture through the column by using PBS, the fractions 3 to 8 were found to be having conjugates from the UV-Visible absorbance spectra, therefore the fractions 3 to 8 were pooled together. Figure 3.6 shows the absorbance spectrum of conjugates separated by column chromatography after the reaction of rbST and FITC for 5 hours and at 5<sup>0</sup>C. The concentration of FITC, rbST and the degree of labeling (also called fluorophores /peptide ratio) of the conjugate were estimated from the absorbance spectrum of the conjugates. Table 3.1 gives the optical properties of the two conjugates used for the calculation.

The concentration of FITC in the conjugate was found as 14 $\mu$ M by using the Equation 3.1, herein the  $\epsilon_{dye}$  of FITC was 70000M<sup>-1</sup>CM<sup>-1</sup>[97] and the  $A_{dye}$  ( $A_{495}$ ) was 1, which was measured from the Figure 3.6(a). The concentration of rbST in the conjugate was estimated by using the Equation 3.2 as 1.33 $\mu$ M (or 30 $\mu$ g/ml), herein the  $A_{280}$  was measured from the Figure 3.6 (a) as 0.37. The extinction coefficient of the rbST,  $\epsilon_p$  was 14,960 M<sup>-1</sup>CM<sup>-1</sup> and the correction factor CF was 0.35. The molar fluorophores-peptide ratio of the FITC tagged rbST was calculated by Equation 3.3 as approximately 10.

Figure 3.6 (b) shows the absorbance spectrum of the Alexa-647 conjugates synthesized through the reaction of Alexa-647 with rbST for 3 hours at room temperature. The reaction mixture was stirred continuously throughout the reaction. This reaction time and temperature were found to be yielding the best F/P ratio.

Alexa-647 has the absorbance maximum at 650 nm. The concentration of Alexa-647 in the conjugates was calculated as 5.4  $\mu\text{M}$ , herein the  $\epsilon_{\text{dye}}$  of Alexa-647 is  $239000\text{M}^{-1}\text{CM}^{-1}$  [98] and the  $A_{\text{dye}}$  ( $A_{650}$ ) was measured from the Figure 3.6 (b) as 1.3. The concentration of the rbST in the conjugate was estimated by Equation 3.2 as  $8.75\mu\text{M}$  (or 19  $\mu\text{g/ml}$ ). The molar F/P ratio of the Alexa-647 conjugate was approximately 1.

To find the detection limit of the proposed Lab-on-a-chip, the conjugates were diluted to different concentrations in PBS and pumped to the device by using a syringe pump. After each measurement, the device was cleaned by pumping the DI water through the device for  $\sim 5$  minutes by a peristaltic pump.

Figure 3.7(a) shows the fluorescence detection from the FITC conjugates. Though the absorbance maximum of the FITC is at 495 nm, the FITC conjugate was excited by the LED source of 470 nm. The fluorescence emission recorded for the lower concentration of conjugates is given in the Figure 3.7(a). When the concentration of conjugates was reduced below the 312 ng/ml, no signal was obtained. Hence the detection limit of the device for the FITC tagged rbST was 312 ng/ml.

The fluorescence signal detected from Alexa-647 tagged rbST is shown in Figure 3.7(b). The Alex-647 emits light at 665 nm upon the excitation. The absorbance maximum of the Alexa-647 dye is 650 as shown in the Figure 3.6(b), however, for the excitation of Alexa-647 conjugates, a fiber laser of 635 nm was used. The Alexa-647 conjugate was diluted to lower concentrations to investigate the detection limit of device for the detection of Alexa-647 conjugates. The conjugate was injected to the device and excited through the PDMS top lid of the device by the fiber laser. The

fluorescence spectra recorded for 4 different low concentrations of conjugates is shown in the Figure 3.7(b). When the concentration of the conjugate was reduced to less than the 240 ng/ml, there was no signal recorded. The detection limit of the LOC for the Alex-647 conjugate is found to be lower than the FITC conjugate.

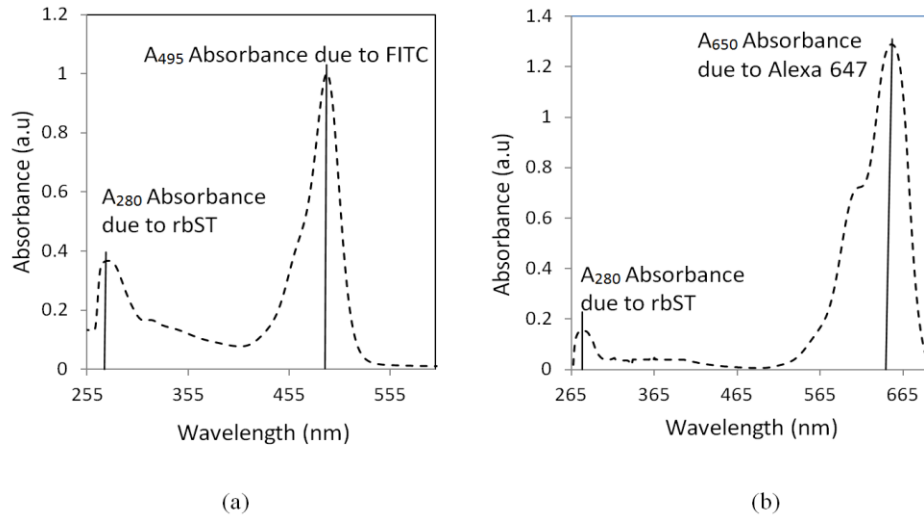


**Figure 3.6** UV-Visible absorbance spectrum of (a) FITC conjugated rbST, (b) Alexa-647 conjugated rbST.

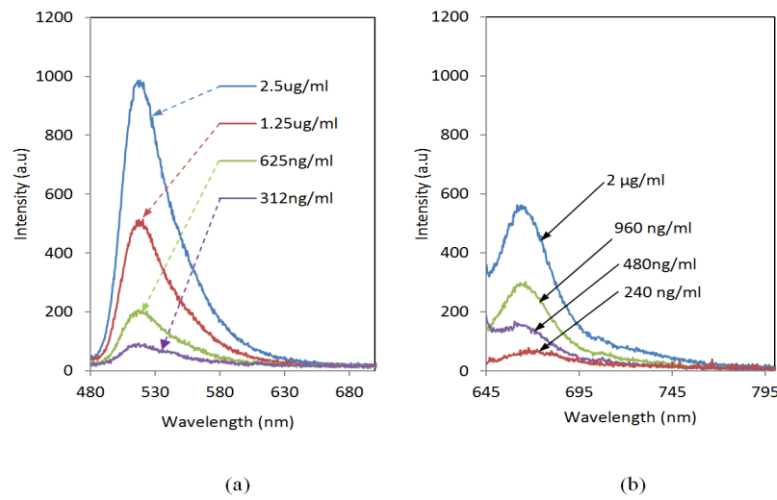


**Figure 3.7** Fluorescence detection of (a) FITC conjugated rbST and (b) Alexa-647 conjugate rbST.

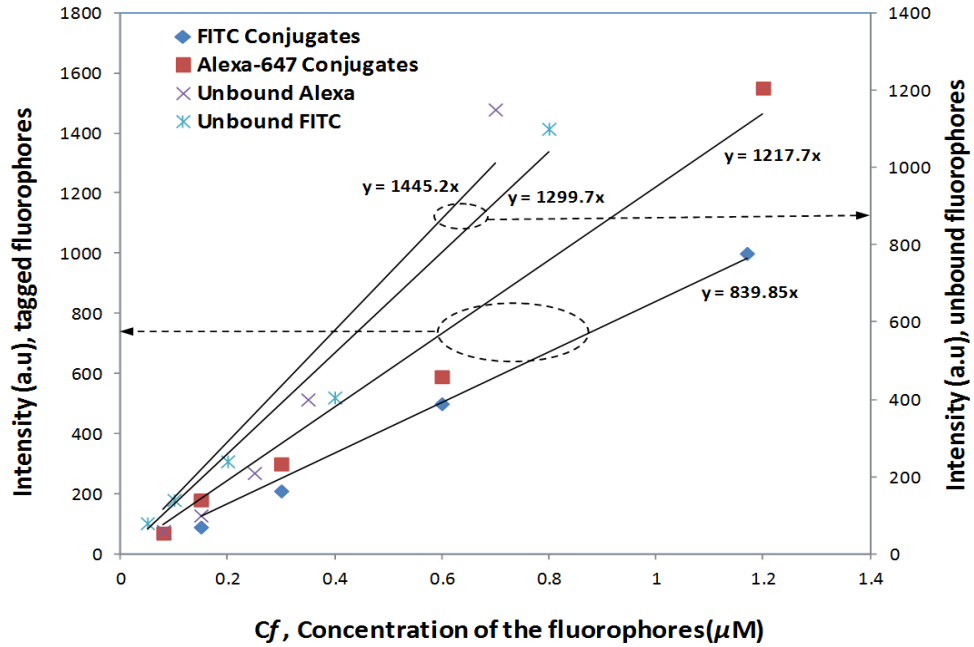


**Figure 3.8** Fluorescence intensity measured in the LOC for the tagged and unbound fluorophores against the concentration,  $C_f$ .

In order to compare the sensitivity of the Lab-on-a-chip for two conjugates, the concentration of fluorophores of the two conjugates,  $C_f$  given by Equation 3.1 is presented against the fluorescence intensity in Figure 3.8. The fluorescence intensity of the unbound fluorophores is also included in Figure 3.8 for comparison. The fluorescence intensity is proportional to the power of excitation, quantum yield and the extinction coefficient of the fluorophores. Since the quantum yield depends upon the degree of labelling [99], a precise estimation of sensitivity of the fluorescence detection becomes a complex problem.

The total power of excitation on the microchannel of width of  $110\mu\text{m}$ , was approximately  $37\mu\text{W}$  for FITC and  $29\mu\text{W}$  for Alexa-647. The intensity of the

fluorescence signal emitted by the fluorophores may be estimated by:

$$I_f = \frac{P_i}{A_r} \times Q_y \times \varepsilon \times C_f \times L \quad (3.4)$$

Where  $I_f$  is the fluorescence signal emitted by the fluorophores,  $P_i$  is the total power of excitation on the microchannel of area  $A_r$ ,  $\varepsilon$  is the extinction coefficient,  $C_f$  is the concentration of the fluorophores and  $L$  is a constant of the LOC which is proportional to the length of the light path from the excitation surface to the collection waveguide.

The Equation 3.4 can be written by replacing  $L/A_r$  with a constant  $K$ :

$$I_f = P_i \times Q_y \times \varepsilon \times C_f \times K \quad (3.5)$$

Hence, the ratio of intensity of FITC conjugates to that of Alexa-647 conjugates can be written as:

$$\frac{I_{FITC}}{I_{Alexa}} = \frac{P_{i,FITC} \times Q_{Y,FITC} \times \varepsilon_{FITC} \times C_{FITC} \times K}{P_{i,Alexa} \times Q_{Y,Alexa} \times \varepsilon_{Alexa} \times C_{Alexa} \times K} \quad (3.6)$$

Where  $P_{i,FITC}$  is  $37\mu W$ ,  $Q_{Y,FITC}$  is 0.92,  $\varepsilon_{FITC}$  is  $70000 M^{-1}cm^{-1}$ ,  $P_{i,Alexa}$  is  $29\mu W$  and  $Q_{Y,Alexa}$  is 0.33,  $\varepsilon_{Alexa}$  is  $239000 M^{-1}cm^{-1}$ . Therefore the Equation 3.6 is written as:

$$\frac{I_{FITC}}{I_{Alexa}} = 1.042 \times \frac{C_{FITC}}{C_{Alexa}} \quad (3.7)$$

For a given concentration of the fluorophores, that is for  $C_{FITC} = C_{Alexa}$  the ratio given by the Equation 3.7 is 1.042. From the Figure 3.8, the ratio of  $I_{FITC}$  to  $I_{Alexa}$  for the tagged fluorophores for a given concentration of fluorophores is 0.68, which is found

less than the estimated value of 1.042. The reason for this difference may be due to the decrease in the quantum yield of FITC due to higher degree of labelling. The similar analysis for the unbound fluorophores yielded a ratio of 0.89, which is close to the estimated value.

### **3.5 Conclusions**

The detection of tagged rbST was demonstrated by using a low cost lab-on-a-chip. The proposed device was fabricated by integrating silica-on-silicon waveguide with a straight microfluidic channel on a PDMS platform containing the microfluidic components. The rbST was tagged with two different types of fluorophores such as FITC and Alex 647. The experimental conditions of reaction of rbST with fluorophores are optimized for the highest F/P ratio. The fluorophore-tagged rbST was diluted to different concentrations and detected in the LOC. The detection limit of the device for both the conjugates was investigated. Though the F/P ratio of the Alexa-647 conjugates was less than the FITC conjugate, the Alexa-647 conjugate was detected at a concentration as low as 240 ng/ml. The detection limit of the FITC conjugate was found to be 312 ng/ml. The fluorescence detection sensitivity for the tagged and unbound fluorophores were estimated and found that the sensitivity of the tagged FITC is decreased from the unbound FITC, which may be due to the decrease in the quantum yield due to higher degree of labeling.

The detection limit of the present device is high, compared to the residual bST present in the milk, reported to be 1-10 ng/ml [100]. The rbST may be found in milk of the rbST treated animals and the amount of rbST can be of the order of hundreds of

ng/ml [101], depending on the extent of use of rbST in animals for increasing the milk and meat production. As the device is developed on the silica-on-silicon platform, it is possible to enhance the sensitivity of the device by many folds by using the SOS platform with monolithic integration of multiple waveguides and couplers with microfluidic circuits. In the future work, we focus on the increasing of the sensitivity by using a multiple waveguide system.

## **Chapter 4: Detection of recombinant growth hormone by evanescent cascaded waveguide coupler (CWC) on silica-on-silicon (SOS).**

### **4.1 Introduction**

The bovine growth hormone, also called bovine somatotropin (bST) is a naturally produced peptide hormone in cow, which has strong influences on the biological effects such as growth, developments and reproductive functions. The effect of bST on the production of milk was identified in 1937[2]. Since then, bST has been used for increasing the production of milk and meat. Since 80's, with the emergence of the recombinant DNA technology, large quantities of artificial hormones called recombinant bovine growth hormone also known as recombinant bovine somatotropin (rbST), are produced and extensively used for the production of milk and meat. Use of growth hormones for the production of milk and meat is still controversial [14, 16, 82] due to its potential effects on animal and human health. Hence, there is a huge demand for a highly sensitive, rapid and a low cost method for the detection of growth hormones in dairy industries.

The existing methods of detecting peptides include the enzyme-linked immunosorbent assay (ELISA) [22, 23], radioimmunoassay (RIA) [24, 84], bioassay methods [25], etc. Although the ELISA is a widely used method of detection of protein due to simplicity and low cost, it is a time consuming process, and it detects the antibody in a relative term such as "titer" that is a combination of affinity and concentration. Recently, the liquid chromatography-mass spectrometry (LC-MS) combined with electrospray ionization [13, 85, 86] has been demonstrated as a

powerful techniques for the detection of rbST, which could discriminate the recombinant and endogenous forms of the somatotropin. However, the LC-MS is a complex technique and requires expensive instrumentations. A surface plasmon based biosensor [26] is reported for the injection preparations by using the expensive instrumentation. In this work, a novel evanescent wave sensor, fabricated on the silica-on-silicon waveguide is proposed for the detection of fluorophore tagged recombinant bovine growth hormone.

Among the various methods of bio-detection, optical-methods by using fluorescence[69], surface plasmon resonance (SPR)[102] and evanescent wave-based methods[38, 103] are attractive approaches due to their higher sensitivity, better stability, better spatial resolution and high discrimination capability. Evanescent wave sensing methods have been widely reported for chemical and biological detection [104, 105]. The evanescent wave is the exponentially decaying tail of the guided mode in an optical waveguide, which is highly suitable for the transduction of surface-assisted phenomena that occur in the close proximity of the surface of the core of the waveguide. Evanescent wave based detection can be employed in both absorption and fluorescence modes. For the evanescent absorption sensors, the biomolecules are immobilized on the core of the waveguide, hence, the loss of the propagating waves due to the absorption of evanescent wave is used as the sensing mechanism. The absorption based detection is one of the earliest bio-detection methods, which is limited to the biomolecules having the chromophores which are responsible for the absorption of light. In the fluorescence sensor, the biomolecules are conjugated with certain fluorescent dyes and detected by exciting the conjugates

and measuring the fluorescence emission. The conjugates can be selectively adsorbed onto the waveguide surfaces having the immobilized antibody, thereby exciting the conjugates which are closely bound to the core of the waveguide by the evanescent wave. The fluorescence signal emitted by the conjugates is coupled back to the waveguide and analyzed by spectroscopy.

Evanescent wave sensors are implemented by using optical fibers [106] or planar waveguides [107]. In optical fiber-based evanescent wave sensor, the thickness of the cladding is reduced or removed so that the evanescent wave can interact with the species immobilized on the fiber. When the cladding is completely removed, the uncladded section of the fiber can be dipped directly in the aqueous buffer solution containing species for the sensing experiments. However, the mismatch in the V-number between the uncladded and cladded section of the fiber reduces the fluorescence collection efficiency for the fluorescence based evanescent sensors. V-number is an approximate number of propagating modes in the waveguides. The sensitivity of the evanescent wave sensors implemented by a straight waveguide with uniform diameter is less as the depth of penetration of evanescent wave is limited for such a configuration. Hence the length of the species evanescent-wave interaction length needs to be increased to achieve higher sensitivity. The evanescent penetration depth in a waveguide is given by:

$$d_p = \frac{\lambda}{2 \times \pi \times n_c (\sin^2 \theta - \sin^2 \theta_c)} \quad (4.1)$$

Where  $\lambda$  is the free space wavelength of the light propagating through the waveguide,  $n_c$  is the refractive index of core,  $\theta$  is the angle of ray at the core-cladding interface with respect to the normal and  $\theta_c$  is the critical angle. It can be seen from Equation

4.1 that the  $d_p$  is maximum when  $\theta$  approaches the critical angle. Therefore, alternative methods reported to increase the evanescent wave penetration depth are selective ray launching [108], use of fiber probes with tapered geometry [109] and use of bends [110] in waveguides. The tapering of the fiber probe could increase the evanescent wave penetration depth and also reduces the mismatch in V-numbers. The bending of the fiber could bring the angle  $\theta$  close to the critical angle, which transfers power from the guided modes to the leaky modes and hence more light is available to excite the tagged-species. The unclad fiber probes with U-bend is reported [110, 111] for enhancing the detection of bio-species. The U-bend could extend the evanescent wave deeper into the surrounding medium and hence the sensitivity has been increased.

Although the optical fibers are more versatile and easily available, planar waveguide sensors have several advantages. The mechanical robustness, feasibility of integration of multiple optical and microfluidics components for the realization of lab-on-a-chips, and the easiness of immobilizing biospecies for the specific detection are the major advantages of the planar waveguides over optical fiber based sensors. In this work, silica-on-silicon (SOS) waveguide is used for the realization of an evanescent wave sensor. SOS has been proven to be a low-cost and good platform for the integrated optical circuits as the existing well-characterized semiconductor processing techniques can be readily adopted for the fabrication of high quality oxide films necessary for the fabrication of low loss optical waveguides. SOS is also suitable for the integration of microfluidic components [95], hence the realization of miniaturized analytical systems is possible. In this work, a cascaded waveguide coupler system,

monolithically integrated on SOS platform was used for the detection of the recombinant bovine growth hormone. The waveguide pattern composed of a single waveguide split into multiple paths using s-bend couplers and subsequently combined to single waveguide was monolithically integrated on the SOS platform. The fluorescently tagged-rbST molecules are immobilized on the surface of the waveguide. By splitting of the waveguide into multiple paths, more area is available to immobilize the tagged-rbST. In addition, the penetration depth of the evanescent wave can be increased with the use of the s-bend and taper. In this paper, an evanescent wave sensor with enhanced sensitivity is realized by using cascaded coupler integrated with s-bends, tapers and splitters.

## **4.2 Evanescent wave fluorescence sensor**

A schematic illustration of the evanescent wave fluorescence sensor is shown in Figure 4.1. An s-bend section with fluorescently tagged bio-species placed around the core of the waveguide is shown in Figure 4.1(a). As the light propagate through the waveguide, the evanescent tail of the propagating wave can excite the tagged bio-species and the emitted fluorescence signals are coupled back to waveguide and analyzed.

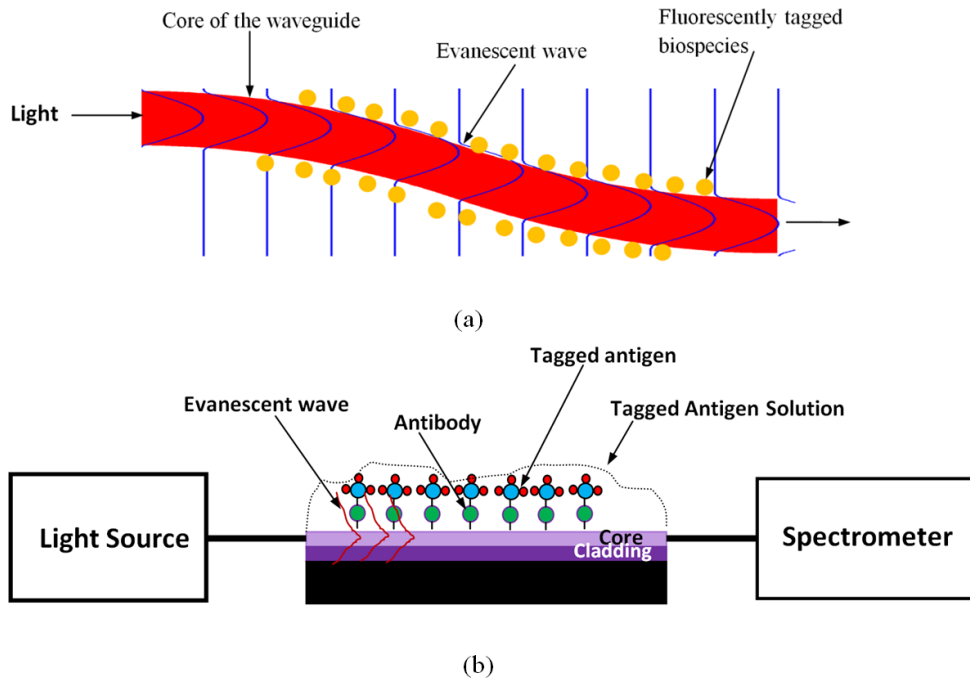


**Figure 4.1** (a) Evanescent wave sensor, (b) Sketch of the SOS waveguide with antibody and tagged-antigen immobilized on core.

In the SOS waveguide, two silicon dioxide layers of different refractive indices (RI) are deposited on the silicon wafer. The first layer with lower refractive index acts as a bottom cladding layer and the second layer with higher refractive index acts as a core of the waveguide. The antibody corresponding to the rbST is adsorbed on the core for the selective binding of the fluorescently tagged-rbST. The buffer solution containing the tagged-rbST is placed on the core, hence the solution containing bio-species acts as a top cladding layer of the waveguide. The antibody immobilized on the core interacts and binds with tagged-rbST on evanescent field of the core. Therefore, the tagged-rbST available within the vicinity of evanescent field is excited. The fluorescence signal emitted by the tagged-rbST is coupled back to the core through

multiple waveguides of the coupler and propagated through the waveguide and coupled to the spectrometer. The mechanism of the back-coupling of the fluorescence is explained in ref [112]. The back-coupled fluorescence occurs when the oscillations of the excited dipoles of the fluorophores which are closely bound to the core produce the electromagnetic near field and overlap with the evanescent tail of the guided modes and meet the conditions for the propagation of light in the waveguide. The theoretical and experimental investigation reported on the fluorescence collection efficiency of the fiber [113] and planar waveguide [107] structures demonstrate that the fluorescence collection efficiency increases with the V-number of the waveguide. In this work, the fluorescence collection efficiency of the straight and s-bend are simulated by FDTD techniques. The s-bend is chosen as it can be a basic element of the proposed cascaded waveguide coupler for enhancing the detection efficiency.

### **4.3 Estimation of fluorescence collection efficiency of straight and s-bend waveguides**

As explained before, in the evanescent-wave fluorescence sensors, the fluorophore-tagged biomolecules are selectively adsorbed to the core by the functionalized antibody molecules. The fluorescently-tagged molecules are excited by the evanescent tail of the propagating wave and the fluorescence signals emitted by the fluorophores are collected back to the core.

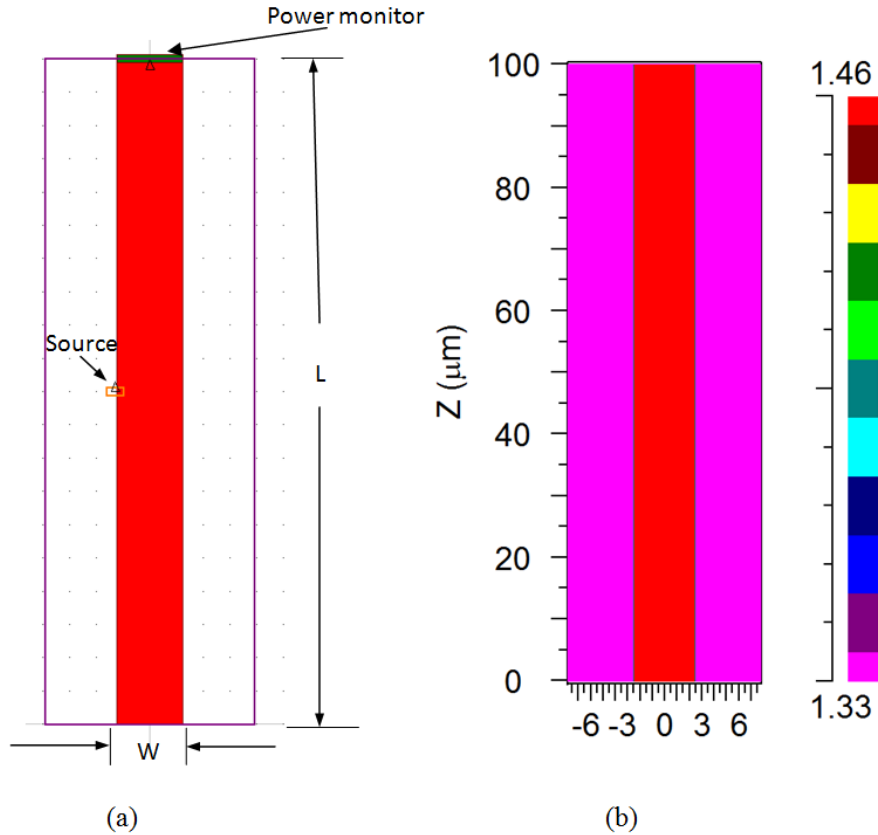
Ray optics is insufficient to explain the coupling of light from a light source located at the cladding of the waveguide. Using the Snell's law, it can be seen that any light beam that can penetrate into the core from the cladding cannot satisfy the condition

for total internal reflection, hence the rays that are refracted into the core leak out rapidly after few reflections at the core-cladding interface. However, by using the wave optics, we can see that the light sources located near the core-cladding interface can interact with evanescent tail of the guided modes by transferring some of the power from the light source to the guided mode by the evanescent wave coupling.

In order to estimate fluorescence collection efficiency of the straight and bend waveguides, FDTD simulation by using RSoft FullWAVE was carried out. A 2D model of waveguide with a point source of wavelength of 650 nm placed in the cladding near to the core was used for the FDTD simulation. A power monitor was placed at the end of the waveguide. The “fluorescence collection efficiency” is defined as the ratio of total power received in a power monitor to the total power radiated by the point source. The total power emitted by the point source is set to unity.

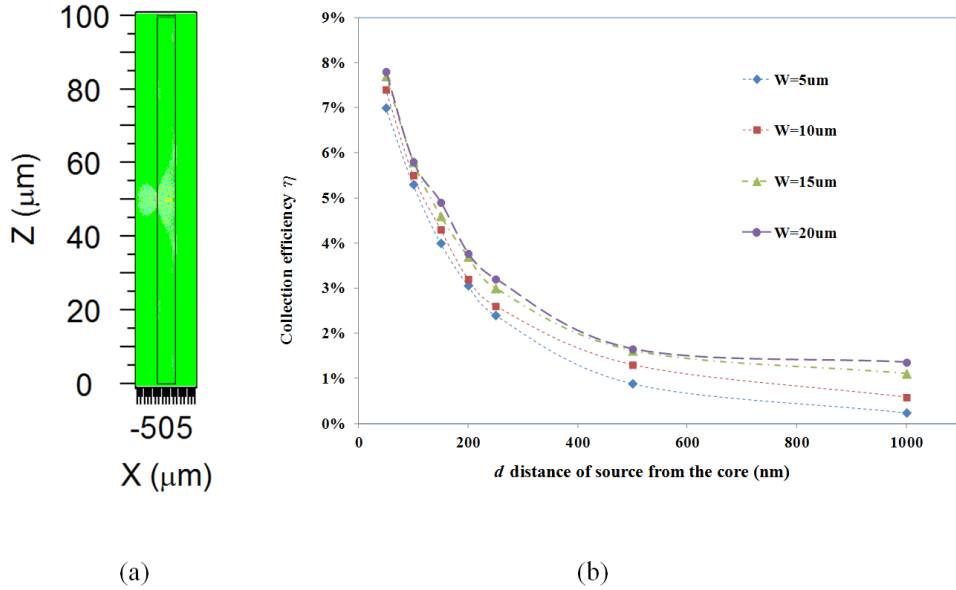
#### ***4.3.1 The fluorescence collection efficiency of straight waveguide***

Figure 4.2 (a) and (b) show the waveguide with a point source modeled in the FDTD and the refractive index distribution of the model, respectively. The refractive indices of the core and cladding are set to 1.46 and 1.33 respectively for silica and biological solution. The length,  $L$  of waveguide is kept at  $100\ \mu\text{m}$  and the width,  $W$  was varied from the  $5\ \mu\text{m}$  to  $20\ \mu\text{m}$ . The dependence of the location of light source on the collection efficiency was investigated first, and then the simulation was carried out by changing the width of the waveguide  $W$ . The distance  $d$  of the light source from the core was varied from 50 nm to 1000 nm.



**Figure 4.2** (a) The FDTD model of waveguide with a point source (b) refractive index distribution of the model.

Figure 4.3(a) shows the FDTD simulation showing the coupling of light from a point source kept at the cladding to the propagation mode. When the distance  $d$  of the source from the core was more than 500 nm, the collection efficiency was found negligible. An exponential relation between the  $d$  and collection efficiency can be observed in the Figure 4.3(b). When the  $d$  is decreased below the 200 nm, the coupling efficiency is increased rapidly. The dependence of the coupling efficiency on the width of the waveguide was also investigated.



**Figure 4.3** (a) FDTD Simulation, (b) fluorescence collection efficiency against the distance  $d$  of the source from the waveguide for different waveguide widths.

The fluorescence collection efficiency of the straight waveguide estimated for different widths ( $W$ ) of the waveguide shows that the increment of  $W$  slightly increases the efficiency. Similar effect was already observed in the fiber in the ref [113], and they have reported that the collection efficiency of the fiber is increasing with the  $V$ -number of the waveguide. In the present simulation, the refractive indices of the core and cladding are kept constant and the width  $W$  of waveguide is increased. Since the  $V$ -number is proportional to the width of the core and the number of guided modes supported by the waveguide, the field at the core-cladding interface is stronger and the collection efficiency increases with the  $V$ -number.

### 4.3.2 The fluorescence collection efficiency of s-bend

The suitability of the s-bend for the realization of the cascaded waveguide coupler is tested by estimating its fluorescence collection efficiency. Herein, the effect of radius of the s-bend is investigated on the fluorescence collection efficiency. The width and length of the s-bend were kept at  $20\mu\text{m}$  and  $100\mu\text{m}$  respectively in the FDTD simulation.

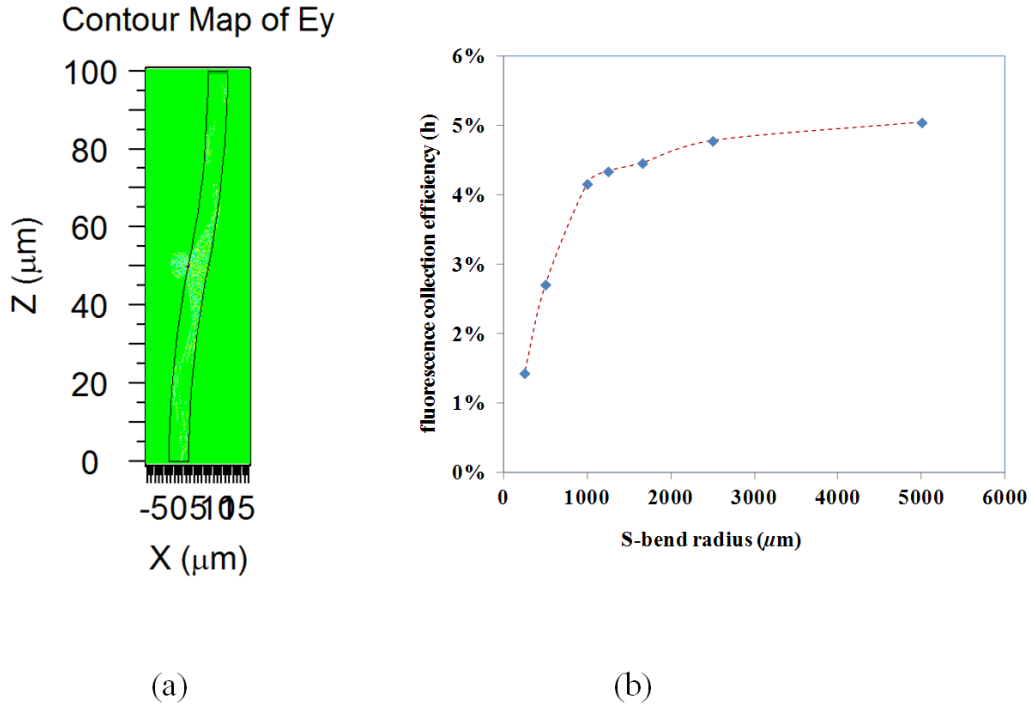


**Figure 4.4** (a) FDTD simulation of fluorescence coupling of light by s-bend and (b) The estimated fluorescence collection efficiency against the radius (R) of the S-bend.

For the estimation of the fluorescence collection efficiency of the s-bend, a point source was placed at  $100\text{ nm}$  away from the s-bends and a power monitor was placed at the end of the s-bend. The FDTD simulation showing the coupling of light from the

point source located in the cladding of s-bend is shown in Figure 4.4(a). Figure 4.4(b) shows the variation of the fluorescence collection efficiency against the radius of the s-bend. The efficiency dropped considerably when the bend radius was reduced below 1000 nm.

The simulation of straight and s-bend confirmed that when the radius of the s-bend is greater than 4 to 5 mm, the fluorescence collection efficiency was not significantly reduced from that of a straight waveguide. The reason for the reduction in efficiency is the bend loss. For the smaller bend radius, the collection efficiency is reduced significantly due to the due to the higher bend loss.

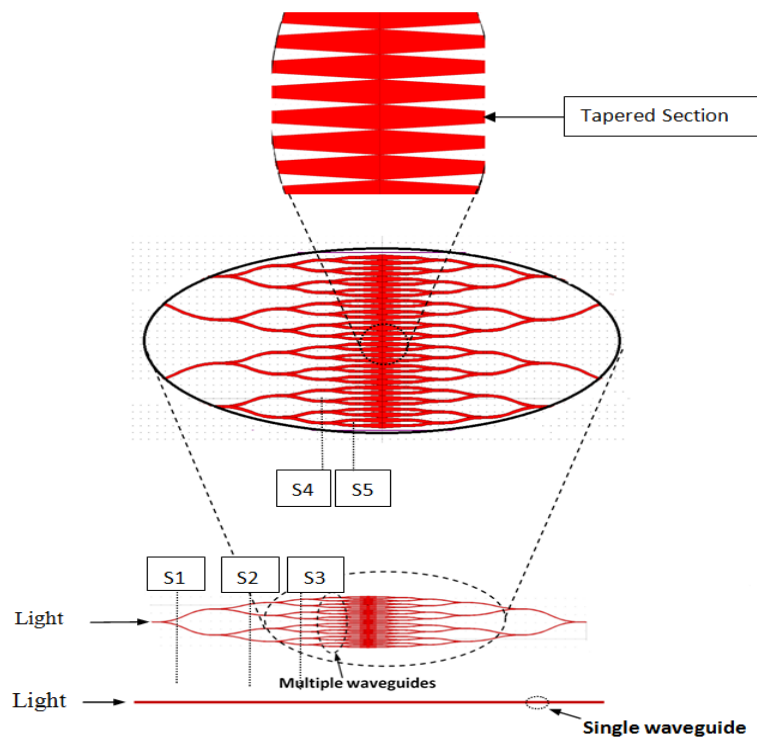


**Figure 4.5** Schematic of evanescent wave sensor using cascaded waveguide coupler in comparison with a straight waveguide.

The advantage of the s-bend for the evanescent wave sensor is that a multiple waveguide system can be realized by cascading Y-couplers made up of s-bends.

The sensor with multiple waveguides of 5 stages, namely S1, S2, S3, S4 and S5 as shown in Figure 4.5 is designed for evanescence coupling based sensing. The  $1 \times 2$  Y splitters were designed with s-bends. As shown in Figure 4.5, the light is coupled to a single waveguide which is split into multiple paths by  $1 \times 2$  Y splitters and after five stages of splitting, the waveguides are combined by  $2 \times 1$  power combiners. A taper section of the waveguide is placed between the splitters and combiners as shown in Figure 4.5 in order to enhance the evanescence coupling. The Y splitter was simulated by RSoft BeamPro<sup>TM</sup> and the bend radius was chosen to keep the bend losses at minimum. The bend radius of first stage, where a single waveguide is split into two branches, was 23 mm. The bend radii of successive stages are 35 mm, 40 mm, 45 mm and 50 mm. The width of waveguide is  $20 \mu\text{m}$  for cascaded waveguide coupler. In the tapered section, the width is increased to  $40 \mu\text{m}$  at the taper-end where a splitter and a combiner connect. An enlarged view showing the cascaded waveguide and tapers are also illustrated in Figure 4.5 for clearly showing the design. In the sensor chip, a single waveguide is also included as a reference to compare the sensitivity enhancement due to the cascaded waveguide coupler.

#### **4.4 Fabrication of sensor chip**

The SOS-waveguide chip is microfabricated in a clean room. The process steps involved in the fabrication of SOS-waveguide is illustrated in the Figure 4.6. The

fabrication process starts with deposition of silicon dioxide on a silicon wafer of 4 inch diameter and (100) orientation, by plasma-enhanced chemical vapor deposition (PECVD). PlasmaLab 80 Plus of Oxford instruments is used for the PECVD of silicon dioxide. For the deposition of cladding layer, the deposition chamber was pumped down to 1000 mT and temperature of substrate was raised to 300<sup>0</sup>C. The deposition gas mixture of silane and nitrogen (5 percent SiH<sub>4</sub>, 95 percent N<sub>2</sub>) at a flow rate of 170 sccm and nitrous oxide (N<sub>2</sub>O) at the flow rate of 710 sccm were introduced to the PECVD chamber. Subsequently, the plasma was created by RF power of 20W at 13.56 MHz. The rate of deposition was 50 nm/minute. The deposition was carried out for 4 hours and 30 minutes to yield an oxide layer of thickness of ~14 $\mu$ m for the bottom cladding of the waveguide. The process parameter is changed to achieve higher refractive index for the core layer. The flow rate of the mixture of silane and nitrogen (5 percent SiH<sub>4</sub>, 95 percent N<sub>2</sub>) is increased to 500 sccm and flow rate of N<sub>2</sub>O was increased to 500 sccm, and the RF power is increased to 200W at 13.56 MHz. The deposition is carried out for 45 minutes in order to get a thickness of 6  $\mu$ m for the core layer. The refractive index characterization of silicon dioxide was carried out by ellipsometry (Spectroscopic ellipsometer, Model: VASE, Sopra). The refractive index measured for the core and cladding layer at different wavelengths is presented in the Figure 4.7. The refractive indices were 1.445 and 1.457 for the cladding and the core respectively at a wavelength of 635 nm.

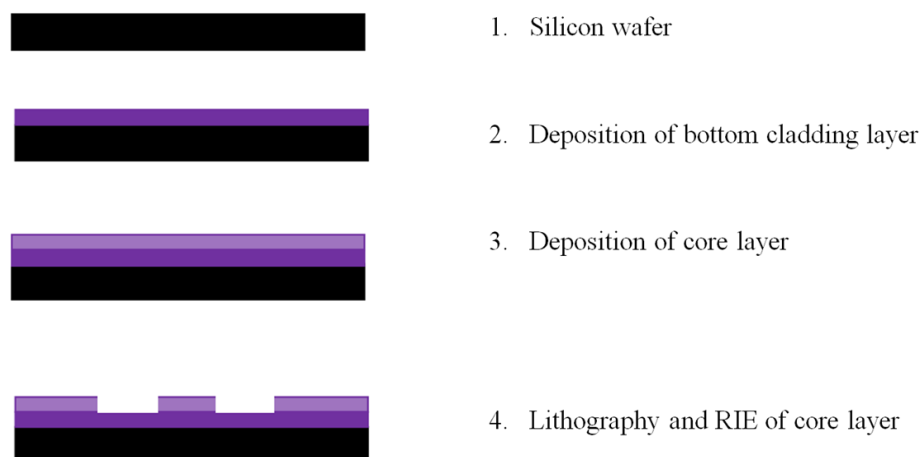


**Figure 4.6** Fabrication process steps of SOS waveguide

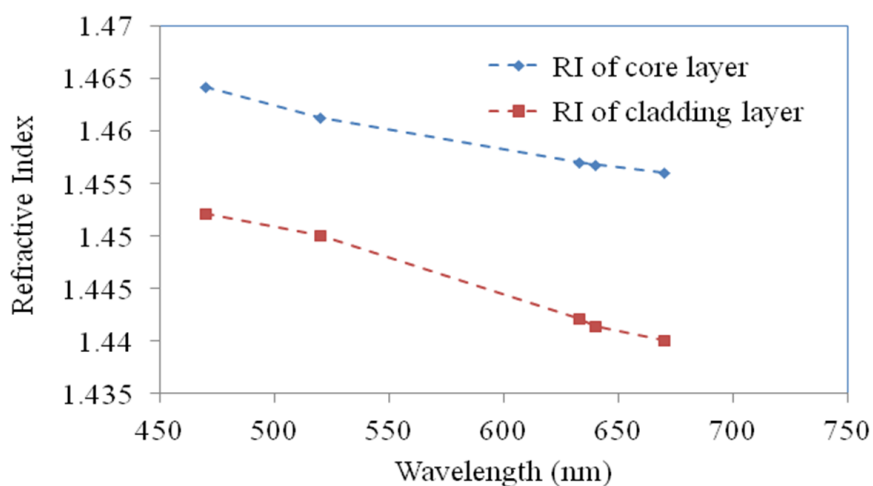


**Figure 4.7** Refractive index of the core and cladding layer against the wavelength.

In the sensing experiments, as the buffer solution containing the tagged antigen is placed on the core, the buffer solution acts as the top cladding of the waveguide. For the lateral guiding of light in the waveguide, the SOS waveguide needed to be structured to desired width. The structuring of the core was carried out by direct write

lithography (DWL-66) and reactive ion etching (RIE). The pattern of the cascaded waveguide couplers was designed in L-edit and transformed to the DWL66 laser writer and directly written on the wafer. The laser write-head of 2 mm having a resolution of 500 nm was used for writing the pattern. The photoresist AZ1518 was spun on the wafer at 3000 rpm and baked at 110<sup>0</sup>C for 2 h in an oven, which resulted in a 2 $\mu$ m thick photoresist layer. The pattern was etched using reactive ion etching (RIE) in MERIE P5000 plasma machine of Applied materials. Etching was carried out with alternating steps of 5 minutes of etch and 5 minutes of pause. The pause step will turn off the plasma and cool the wafer to room temperature. 12 etch and pause steps were carried out to etch 10 $\mu$ m of oxide without burning the photo resist mask. For the RIE, the chamber was pumped down to 50mT and the process gases, CHF<sub>3</sub>, Ar and CF<sub>4</sub> are introduced to the chamber at the flow rate of 45, 70 and 7 sccm respectively. The plasma was created by the RF power of 300W. This process gives an etch rate of 0.3 $\mu$ m/minute. The total etching time was one hour including the 30 minutes of etch pause, which resulted in the etch depth of the 10 $\mu$ m. SEM micrograph of the waveguide is shown in Figure 4.8.

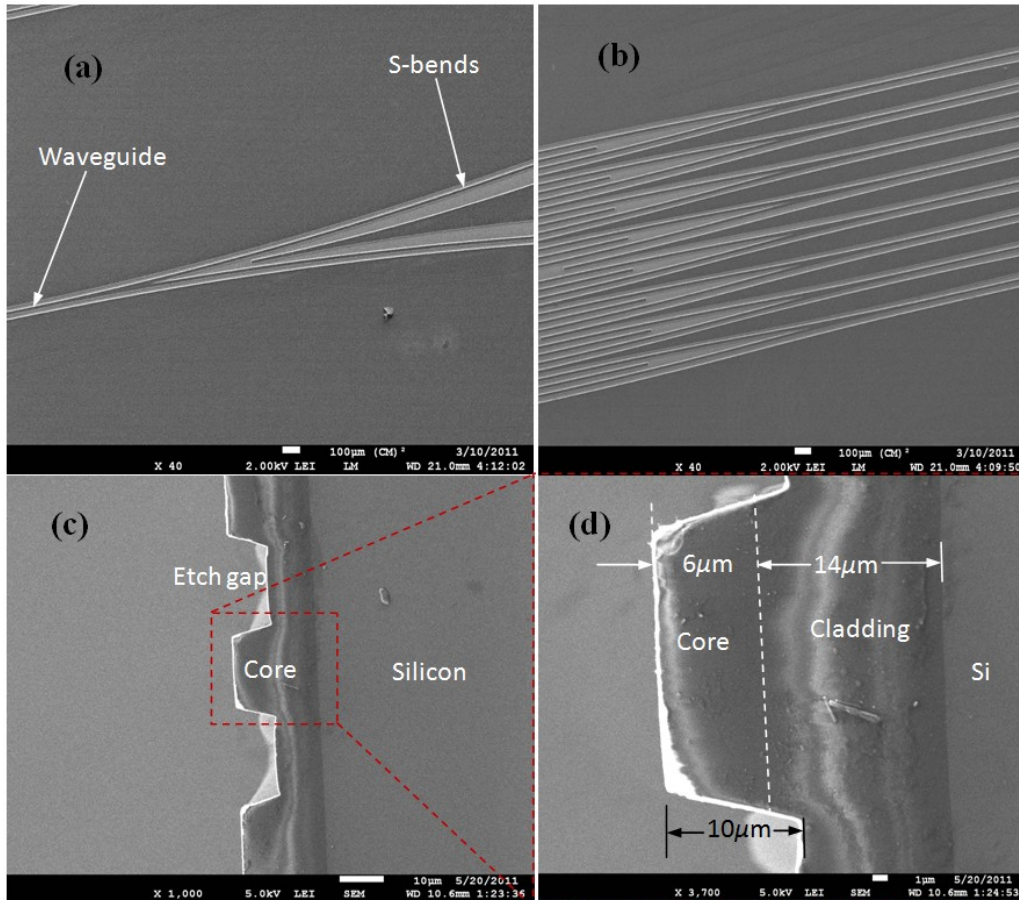
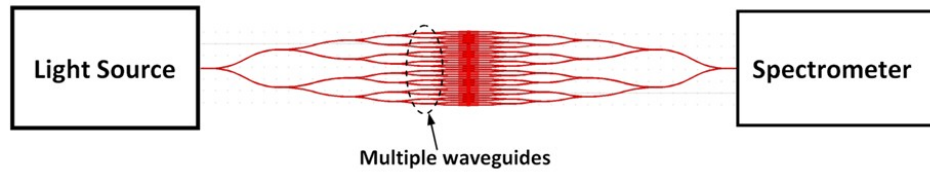
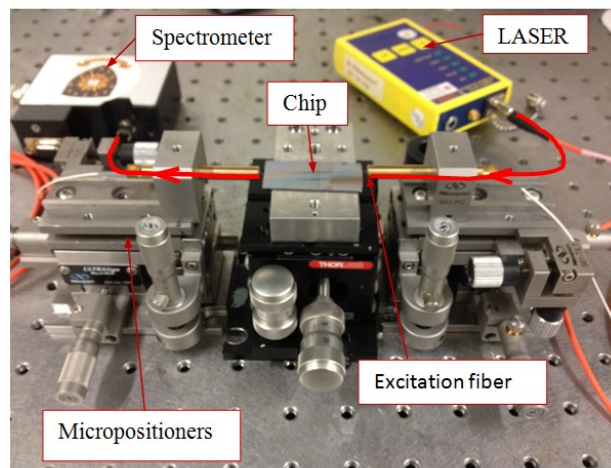


**Figure 4.8** SEM micrograph of SOS waveguide, (a) s-bend coupler of the multiple waveguide system stage S1 (b) multiple waveguides in the stage 3 (S3) of cascaded waveguide coupler (c) etch profile of the waveguide (d) dimensions of the core of the waveguide.

## 4.5 Experimental setup



(a)

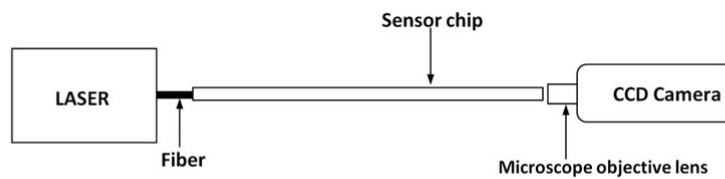


(b)

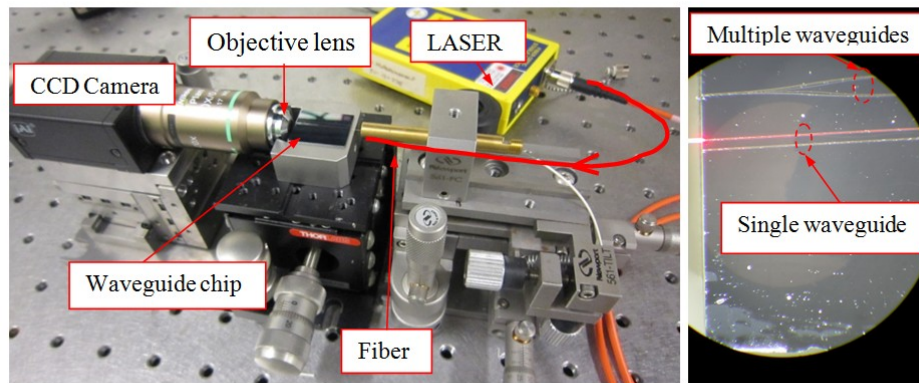
**Figure 4.9** Experimental setup for the cascaded waveguide coupler sensor, (a) schematic of the experimental setup, and (b) photograph of the experimental setup.

The experimental setup used for the SOS evanescent wave sensor is shown in Figure 4.9. Light from a laser source is coupled to the sensor chip and the other side of the waveguide is coupled to a spectrometer as shown in the schematic of the setup in Figure 4.9(a). A photograph of the experimental setup shown in Figure 4.9(b) shows different components used in the setup. This setup is built to couple effectively the light from the fiber to the SOS waveguide and to couple the fluorescence signal from

the waveguide to spectrometer. Three high precision micropositioners with actuators of  $1\mu\text{m}$  accuracy are used in the setup. Two 5-axis controllable micropositioners obtained from Newport<sup>TM</sup> are used to couple the light from the fiber to waveguide and to couple the fluorescence light from waveguide to the collection fiber. The sample was fixed to a XY-axis controllable micropositioner purchased from ThorLabs. A fiber laser (OZ Optics) of 635 nm wavelength was used as the excitation source and a commercially available spectrometer (USB 2000, Ocean Optics) is used for the fluorescence spectroscopy.



(a)

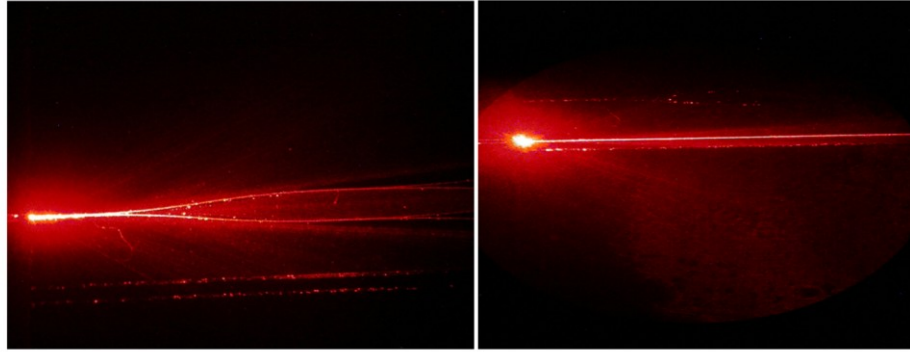


(b)

(c)

**Figure 4.10** Experimental setup for imaging the end facet of waveguide, (a) schematic diagram of the setup, (b) photograph of the experimental setup and (c) Microscope image showing the coupling of light to the waveguide taken from the top of the waveguide.

In order to confirm that the confinement of the light is taking place inside the core of the waveguide, the waveguide was cut at the middle and the facet was imaged by using the optical setup shown in Figure 4.10. A schematic diagram of the setup used for imaging the waveguide facet is shown in Figure 4.10(a). Light from the laser is coupled to the waveguide and to a CCD camera placed on in the other side of the waveguide in order to image the facet of the waveguide. A photograph of the experimental is shown in Figure 4.10(b). The Sample was fixed in a micropositioner stage as shown in Figure 4.10(b). Light from a fiber laser (OZ optics, Power-1mW) of 635 nm wavelength was directly coupled to the waveguide by a single mode fiber (9-125 $\mu\text{m}$ , core-cladding diameter) with the help of a 5 axis micropositioner stage (Newport<sup>TM</sup>). A CCD camera with a microscope objective lens (Nikon 20X) was used in the other side of the waveguide to image the confinement of light in the core. Figure 4.10(c) shows the image taken from microscope used to observe the waveguide-fiber alignment, which shows the coupling of light from fiber to the single waveguide.



(a)

(b)

**Figure 4.11** (a) Microscope image showing the waveguide with light coupled (a) multiple waveguide (b) single waveguide.

The microscope images taken from the top of the waveguide for single and multiple waveguide are shown in Figure 4.11. Since the light from the fiber is directly coupled to the waveguide and the divergence of the light beam coming out of single mode fiber is large, lot of light is scattered to the cladding. The confinement of light in both single and multiple waveguides imaged by CCD camera and processed in LabVIEW is shown in Figure 4.12.

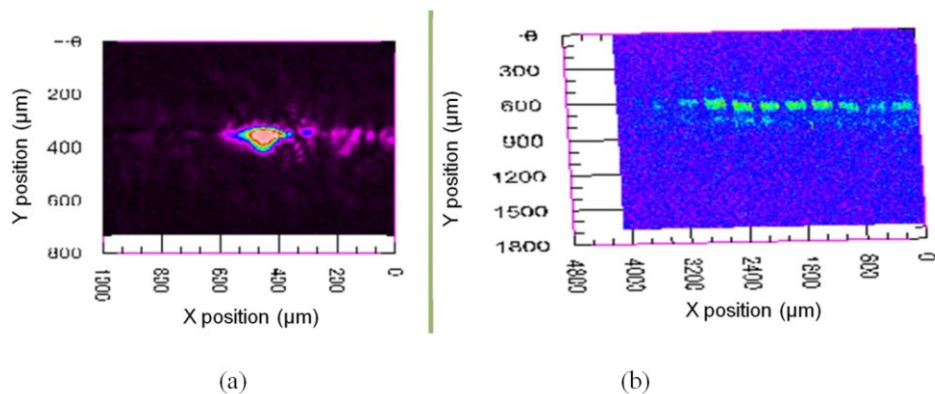


**Figure 4.12** Image of the waveguide facet (a) Single waveguide (b) Multiple waveguide

## 4.6 Biosensing experiments

### 4.6.1 *Materials*

Recombinant bovine somatotropin (rbST, Molecular Weight- 22 kDa) and the anti-rbST were purchased from Cedarlane, ON, Canada. Alexa-647, Phosphate Buffered Saline (PBS) and sodium carbonate-bicarbonate were received from Sigma-Aldrich, Canada. The PBS tablet was dissolved in deionized (DI) water at a concentration of 0.1M with a pH of 7.2. For the preparation of rbST solution, sodium carbonate bicarbonate buffer solution with a concentration of 0.1M and pH of 9.0 was used. The rbST was dissolved in sodium carbonate bicarbonate buffer at a concentration of 1 mg/ml. A gel filtration column having Sephadex G 25 beads was used to separate the unreacted FITC.

#### ***4.6.2 Tagging of rbST with Alexa-647***

The rbST solution was prepared at 1 mg/ml in 0.1M sodium carbonate bicarbonate buffer solution. Then 50 $\mu$ L of Alexa-647 solution of 5 mg/ml was added to 1 ml of rbST solution. The reaction of rbST and Alexa-647 was carried out under continuous stirring for at various times and temperatures for obtaining the best labeling ratio. After the reaction, the labeled rbST was separated from the reaction mixture by column chromatography using Sephadex G 25. Elution of column was carried out in 10 fractions of 2ml PBS. The UV-Visible absorbance spectrum of each fraction was measured by spectrophotometer (LAMBDA 650, Perkin Elmer) to assess the presence of conjugates. The degree of labeling and the concentration of rbST in the conjugates were calculated as explained in ref [94, 96]. The degree of labeling and the concentration of rbST in the conjugate were estimated at 1 and 19  $\mu$ g/ml, respectively. The conjugate was diluted to different concentration in PBS for the sensing experiments.

#### ***4.6.3 Immobilization of fluorescently tagged-rbST on the sensor chip***

A schematic representation showing various steps involved in the adsorption of fluorescently tagged-rbST onto the SOS waveguide is shown in Figure 4.13. The first step of sensing is the immobilization of anti-rbST. The anti-rbST was prepared at a concentration of 100 ng/ml in phosphate buffered saline (PBS). First, the sensor chip was cleaned in DI water with ultrasonic cleaner for 5 minutes then subsequently in acetone and ethanol. Then the samples were heated at 100<sup>0</sup>C in an oven for at least one hour. The surface of the waveguide core was modified with 3-

Aminopropyltriethoxysilane (APTES, sigma Aldrich) [114] in order to attach the anti-rbST covalently. The waveguides were immersed in ethanol containing 2% APTES for 15 minutes, rinsed in ethanol and heated at 100<sup>0</sup>C for 15 minutes. Figure 4.13 (a) shows the waveguide with the OH groups activated on the surface after cleaning and silanization. Then the waveguide was soaked in anti-rbST solution for 1 h and washed in PBS. The Figure 4.13(b) represents the sample after the anti-rbST was adsorbed. In order to block the non-specific binding site, the sample was soaked in bovine serum albumin (BSA) and the sample was washed with PBS. Figure 4.13(c) shows the samples after blocking the non-specific binding sites. Then the waveguide was fixed in the measurement setup shown in Figure 4.9 and the tagged-rbST was added on to the waveguide covering all the waveguide regions. The representation of sample with tagged-rbST is as shown in Figure 4.13(d).

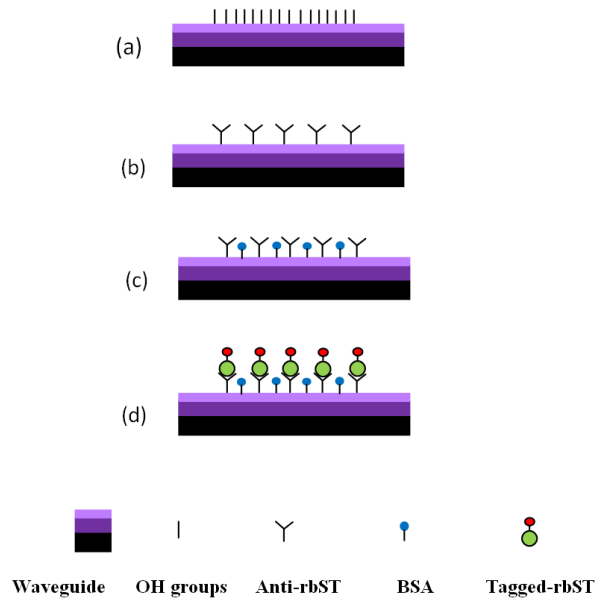


**Figure 4.13** Steps involved in the functionalization of waveguide chip, (a) modify the waveguide surface with APTES silane to absorb the anti-rbST (b) absorb anti-rbST and (c) block non-specific sites and (d) absorb the tagged rbST.

## 4.7 Results and discussion

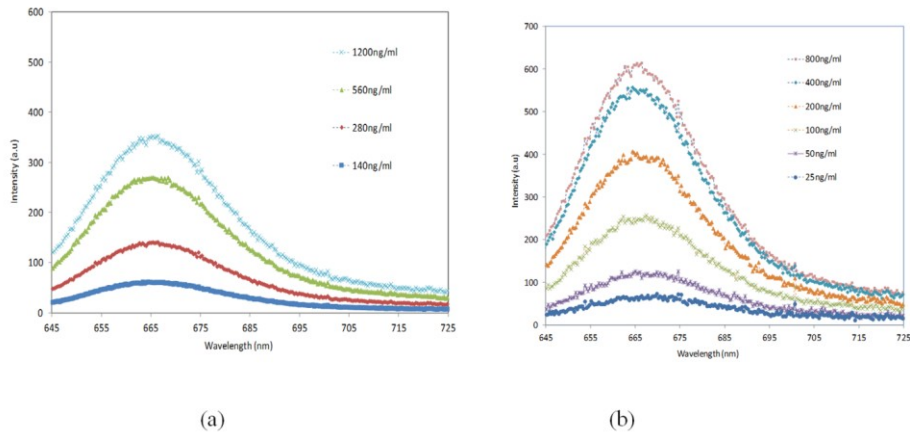


**Figure 4.14** Fluorescence signal recorded in the sensor chip after antigen-antibody binding for various concentrations of tagged-rbST, for (a) single waveguide (b) cascaded waveguide coupler.

In order to investigate the suitability of the sensor for quantitative measurements of tagged rbST, the variation of fluorescence signal against the concentration of tagged-rbST was established. Several identical SOS-waveguides chips were used for the detection experiments in order to study the variation of fluorescence signal against the concentration of tagged-rbST. The evanescent-coupled fluorescence signal is collected through the waveguides and coupled to the spectrometer. The intensity of the fluorescence spectrum was found fluctuating immediately after adding the tagged-rbST on the waveguide and fluorescence spectrum was stabilized after 10-15 minutes. The fluorescence spectrum was recorded after 15 minutes of adding the tagged-rbST. In order to assess the enhancement of the sensitivity of cascaded waveguide coupler, the detection was also carried out by using a single waveguide.

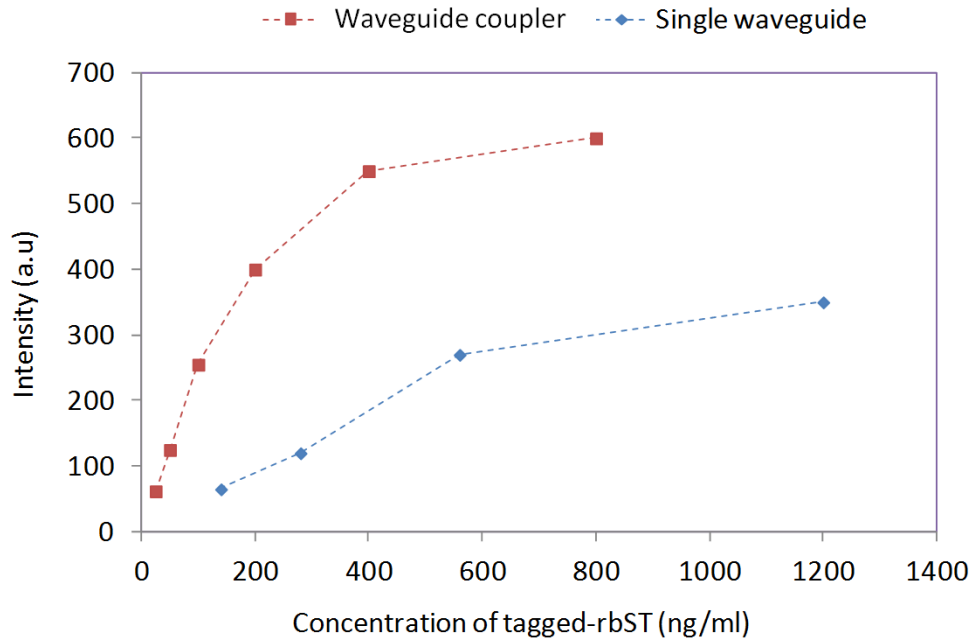


**Figure 4.15** Variation of fluorescence signal against the concentration of tagged-rbST

The fluorescence signals recorded for various concentration of tagged-rbST in single and cascaded waveguide coupler are shown in Figure 4.14 (a) and (b), respectively. For the single waveguide, limit of detection is found as low as 140 ng/ml. When the concentration of tagged-rbST was above 1200 ng/ml the sensor response was found saturating as shown in Figure 4.15. The detection limit of the cascaded waveguide coupler systems was found to be 25 ng/ml. The detection limit of the cascaded waveguide coupler was found enhanced to be more than 5 times as compared to that of the single waveguide. The sensor response was observed to be saturated when the concentration of the tagged rbST was 600 ng/ml or above for the cascaded waveguide coupler. The fluorescence signal intensity of the sensor measured for various concentration of tagged-rbST for single waveguide and cascaded waveguide coupler is presented in Figure 4.15.

When the fluorophore tagged-rbST is added to the waveguide immobilized with the anti-rbST, the tagged rbST was adsorbed onto surface of the waveguide and gets excited with the evanescent light. The fluorescence signals emitted by the tagged-rbST are collected back to waveguide. When the concentration of the tagged-rbST was increased, all the binding sites on the surfaces are eventually filled and hence the sensor output is getting saturated. Therefore, when the concentration of tagged-rbST was increased above 600ng/ml, both the single and cascaded waveguide are getting saturated as shown in Figure 4.15. Due to the higher light collection efficiency of the cascaded waveguide coupler, the output of the CWC is found to be saturating faster at low concentration of the tagged rbST (at around 600ng/ml) compared to the single waveguide (at around 1200ng/ml).

#### **4.8 Conclusions**

A novel evanescent-wave based fluorescence sensor using a cascaded waveguide coupler is designed and implemented on the silica-on-silicon platform. Advantages of SOS platform for the monolithic-integration of a cascaded waveguide coupler platform using Y splitters designed by s-bends and tapers are used for the realization of the sensor. The fluorescence collection efficiency of straight and bend waveguide was analyzed by using FDTD. The suitability of the sensor is demonstrated for the detection of Alexa-647 tagged recombinant bovine somatotropin. For the specific detection of rbST, the anti-rbST was adsorbed to the waveguide and the tagged-rbST was detected by the enhanced evanescent fluorescence coupling. The sensitivity of the proposed waveguide coupler system realized by cascading waveguides was found more than 5 times to that of the single waveguide.

## **Chapter 5: Finite-Difference Time-Domain Simulation and implementation of a morphologically-tuned gold-nano-islands integrated biosensor**

### **5.1 Introduction**

Developments of novel nano-fabrication technologies have attracted significant attention because of the plasmonic properties of nanomaterials and the feasibilities of exploiting them for the label-free detection of biological and chemical substances. Surface plasmon resonance (SPR)-based sensors have been widely reported for the label-free detection of protein-protein interaction [115, 116], DNA hybridization [88] and bacteria [117]. The SPR based sensor is based on the propagation of surface plasmon waves produced by coupling of light to a thin noble metal layer by a grating coupler or near field excitation [26]. SPR based sensors have several drawbacks including lower spectral resolution and requirements of large equipments. Noble metal nanoparticles (NPs) such as gold and silver exhibit unique optical resonance properties in the visible and near-infrared (NIR) regions of the electromagnetic spectrum, and they have been proven to be useful for the label-free detection [118-121] and feasible to integrate in a microfluidic device for the developments of lab-on-a-chip devices [57]. The optical resonance behavior of NPs is commonly referred to as localized surface plasmon resonance (LSPR), which is due to the resonance response of the free electrons of the nanoparticles to the electric field of the light. One of the main advantages of LSPR-based sensor over the SPR-based sensor is that the LSPR property of nanoparticles can be tailored to meet the requirements of different

applications and enhancing the sensitivity by changing the size and shape of nanoparticles.

LSPR based sensors are typically fabricated by metal nanoparticles immobilized on an optically transparent substrate [122, 123]. Therefore, the immobilization of nanostructures with nanoparticles of various sizes and shape is an important fabrication process for the development of nano-biosensor. Subsequently the biomolecules are adsorbed on the nanostructures and hence the biomolecular interaction can be assessed by monitoring the position and/or intensity of the LSPR band monitored by transmission or reflection spectroscopy. The essential qualities of the nanostructures for the biosensing are good adhesion to the substrate, easiness of modifying the morphology of the nanostructures to tune the optical properties to achieve higher sensitivity, etc. Some of the widely employed fabrication processes for the fabrication of nanostructures are nano-sphere lithography (NSL) [124, 125], vapor deposition [126], direct thermal deposition and electrochemical deposition [123], etc. NSL is useful for the deposition of ordered nanostructure by depositing a metallic nano-film on a self assembled polystyrene spheres. Evaporation of gold film and annealing to yield a nanostructure film is a useful method. However the expensive instrumentation and poor adhesion are the drawbacks. The convective assembly of nanoparticles using complex and expensive apparatus for the controlled deposition of nanoparticles is reported [127]. The polymer-gold (or silver) nanocomposite is also reported to be useful for the biosensing applications [90, 128, 129]. Hence the process of formation nanostructures on the substrate with suitable LSPR band is an important task in the development of nano-biosensor.

In this work, 3D Finite-Difference Time-Domain (FDTD) simulation of a gold nano-islands and nano-clusters and a comparison with the experimental results is reported. The fabrication process of the nano-islands morphology is based on an uncontrolled and simple convective assembly, which resulted in a gold aggregates with a wide absorbance spectrum spreading in the visible and near-infrared regions of light. The morphology of gold aggregates is not very useful for the biosensing [61] because of wide resonance peak. Therefore the modification of the morphology for the desired optical resonance property is achieved by a post-deposition annealing process. The tuning of morphology is analyzed by 3D FDTD simulation. In the simulation, nano-island is approximated to a hemisphere and the optical resonance of the nano-cluster is investigated with four hemispheres separated by a distance ' $d$ '. The ' $d$ ' is varied to study the effect of nano-cluster. The distance  $d$  is in fact varying during the post-deposition annealing process. The modification of LSPR of the gold-hemisphere was simulated with a protein layer of certain refractive index and thickness. In addition, effects of thickness and refractive index on the LSPR property were also investigated. The refractive index sensitivity of the gold-nano hemisphere was estimated and compared with the experimental results.

## **5.2 Localized surface plasmon resonance**

Localized surface plasmon resonance (LSPR) is due to the surface plasmon waves produced from the collective oscillations of electrons by illuminating the nanoparticles. The oscillation of electrons in metal is described by the dielectric function as by the Drude [130] model as:

$$\varepsilon = 1 - \frac{\omega_p^2}{\omega^2 + i\gamma\omega} \quad (5.1)$$

where  $\omega_p$  is the plasma frequency of the free electrons,  $\omega$  is the angular frequency of the light illuminating to the nanoparticles and  $\gamma$  is collision frequency of the electrons present in the bulk materials. In the case of nanoparticles, as the size of the nanoparticle are much smaller than ( $\sim 10$  to  $100$  nm) the wavelength of the light, the oscillation of the electrons can be approximated to a dipole oscillation, therefore, the collective oscillation of electrons due to electric field can be described by dipolar polarizability [131]  $\alpha$ :

$$\alpha = (1 + s)\varepsilon_0 V \frac{(\varepsilon - \varepsilon_m)}{(\varepsilon + s\varepsilon_m)} \quad (5.2)$$

where  $V$  is the volume of the nanoparticle,  $\varepsilon_m$  is the dielectric constant of the medium and 's' is a factor which depends on the shape of the nanoparticles. From the Equation 5.2, we can see that the polarizability  $\alpha$  is maximum when real part of the  $\varepsilon$  is equal to  $-s\varepsilon_m$ , and the  $\omega_p$  satisfying this condition is the localized surface plasmon frequency of the particle. Therefore, from the Equation 5.1 and 5.2, we can see that LSPR property depends on the bulk plasma frequency  $\omega_p$ , the geometry factor  $s$  and the medium where the nanoparticle is placed ( $\varepsilon_m$ ).

The surface plasmon results in a strong confinement of electric field in the surface of the nanoparticles, therefore, if two nanoparticles are brought together, the near-fields

of two nanoparticles will interact and the electric field experienced on each particle is a resultant field. Due to the interaction of the near-fields, the plasmon resonance of two NPs gets coupled with the influence of neighboring particles resulting in modulated LSPR band.

In this work, first, a novel method of manufacturing nano-island structure on glass is discussed. The nano-cluster morphology produced by the convective assembly was transformed to nano-islands by post-deposition annealing. The effect of annealing temperature on the morphological transformation and the optical absorbance property was characterized by SEM and UV-Visible spectroscopy, respectively. Then the nano-island morphology was simulated with a gold nano-hemisphere models and the optical property of the nano-cluster is analyzed by 4-gold hemisphere model in FDTD. The sensitivity of morphology against refractive index was simulated and compared with the experimental results.

### 5.3 Manufacturing of nano-islands on a substrate

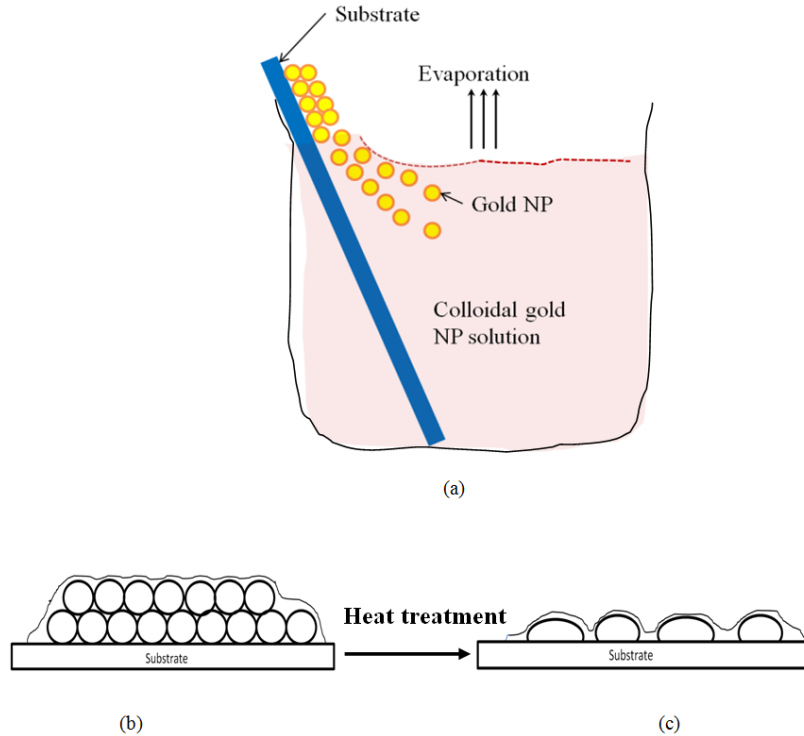


**Figure 5.1** Fabrication strategy of the gold nano-island structure on a substrate. (a) angled convective assembly (b) schematic of gold aggregates and (c) schematic of gold nano-islands structure.

The strategy designed for the formation of widely separated nano-islands is illustrated in Figure 5.1. It is relatively easy to form a multilayer of nanoparticles on the substrate in an unorganized format. For that, the particles need to be strongly adsorbed to the substrate from a colloidal suspension. Since the process of preparing the gold colloidal solution is an easy and low cost process, the gold colloidal solution

of spherical gold nanoparticles were prepared by reducing chloroauric acid by sodium citrate using Turkevich's method [132]. The nanoparticle from the colloidal suspension has been adsorbed to the substrate by using a novel angled convective assembly technique as shown in Figure 5.1(a). The nanoparticle from colloidal suspension was driven to the substrate and adsorbed upon evaporating the solvent. Even though the proposed angled convective assembly is not precise or controlled process, it is simple and useful for the formation of aggregates or multilayer of gold nanostructure as shown in Figure 5.1(b). Subsequently, by using the heat treatment, morphological transformation of the aggregates to the nano-island morphology is achieved.

The substrate was cleaned with soap solution, DI water, then rinsed with acetone, dried and rinsed with 2-propanol. Then the substrate was silanized and washed in toluene and heated in an oven at 100<sup>0</sup>C for 1 hour before the deposition process. The glass substrate was immersed in the gold colloidal solution at an angle of approximately 30<sup>0</sup> in vials and kept in the oven at temperatures between 60 and 80<sup>0</sup>C for 1-2 days, until the whole amount of gold was transferred to the substrate as shown in Figure 5.1(b).

The sample with nano-cluster had a dark blue color. The morphology of the deposition is investigated by scanning electron microscopy (SEM). Figure 5.2(a) shows the SEM micrograph of the sample after the deposition. As expected, the uncontrolled convective assembly resulted in a nano-cluster morphology. The sample was annealed at various temperatures to investigate the morphological transformations. When the sample was heat treated, the color turned to red. Figure

5.2(b) shows the morphology obtained after annealing at 400 to 450<sup>0</sup>C for 1 h. A dramatic change in morphology is observed upon annealing and the size of particle is ranging from 10 to 100 nm with an average separation distance of 10 nm. During the annealing, as the melting point of nanostructures is much lower than its bulk form, the nano-cluster is melting and due to high surface tension of the molten metal, the cluster morphology transforms to droplet-like nano-island morphology. When the annealing temperature was further increased to 550<sup>0</sup>-600<sup>0</sup>C, the separation distance between the nano-island have been found increased as shown in Figure 5.2(c). The morphology composed of nanoparticles of size ranging from 10 to 100 nm and they are widely separated each other. Around 60 to 70% of the particles in an area of 1 $\mu$ m<sup>2</sup> were found having the size between 40 to 80 nm with an average separation distance of 50 nm, when the sample was annealed at above 550<sup>0</sup>C.

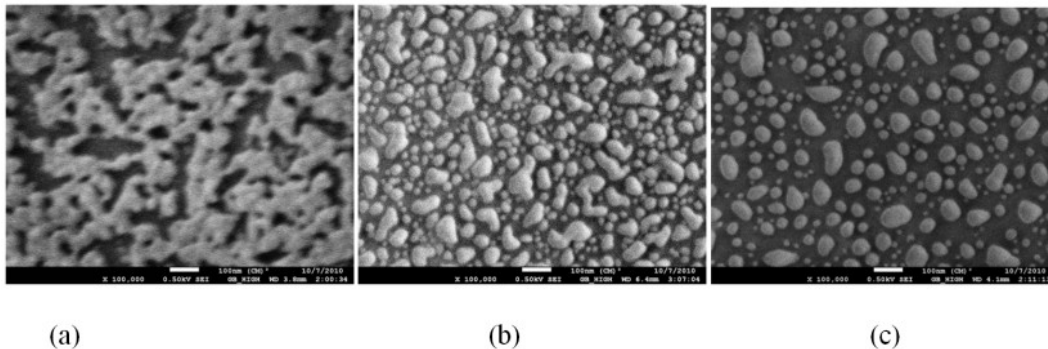


**Figure 5.2** SEM micrographs of (a) Nano-cluster obtained after deposition (b) annealed at 400-450<sup>0</sup>C (c) annealed at 550-600<sup>0</sup>C.

The LSPR property of the samples was measured by UV-Visible spectrophotometer. The UV-Visible absorbance spectrum measured for the three samples shown in

Figure 5.2, is presented in Figure 5.3. The UV-Visible spectrum of the nano-cluster morphology obtained after the convective assembly was a wide band extending from 475 nm to 675 nm as presented in Figure 5.3(a). The annealing of sample at 400-450<sup>0</sup>C resulted in an LSPR band with two peaks as shown Figure 5.3(b). When the samples were annealed at temperatures in the range of 550-600<sup>0</sup>C, a single peak was obtained as shown in Figure 5.3(c). A batch of 20 samples annealed at 550<sup>0</sup>C for 1 h had a resonance peak at 545±10 nm. The adhesion of the NPs with the substrate was found to be less good for annealing temperature at around 550<sup>0</sup>C. To increase the adhesion, the annealing temperature was further increased to 600<sup>0</sup>C and annealing was carried out for 20 h, which resulted in nano-islands morphology with good adhesion and a more stable resonance peak at 545±5 nm.

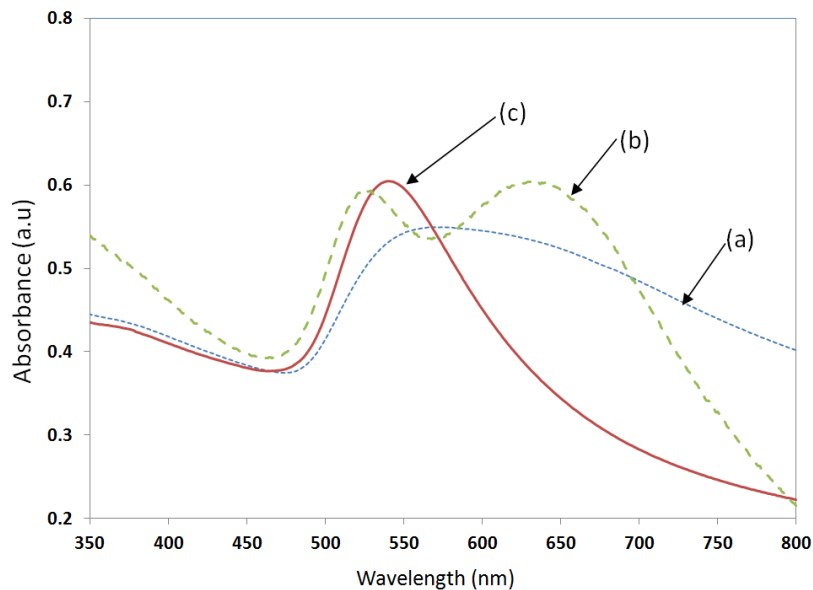


**Figure 5.3** UV-Visible absorbance spectrum of (a) non-annealed sample, (b) samples annealed at 400-450<sup>0</sup>C, and (c) samples annealed at 550-600<sup>0</sup>C.

## 5.4 FDTD modeling

The FDTD method solves the Maxwell's differential equations by discretizing using central difference in space and time and solve numerically by using computers. The four Maxwell's equations in differential form can be written as:

$$\nabla \cdot E = \frac{\rho}{\epsilon_0} \quad (5.3)$$

$$\nabla \cdot B = 0 \quad (5.4)$$

$$\nabla \times E = -\frac{\partial B}{\partial t} \quad (5.5)$$

$$\nabla \times B = \mu_0 J + \mu_0 \epsilon_0 \frac{\partial E}{\partial t} \quad (5.6)$$

The Maxwell's equations relate the temporal change of electric field  $E$  on the spatial change of magnetic field ( $H=B/\mu$ ), and vice versa. The constants  $\mu_0$  and  $\epsilon_0$  are the permeability and permittivity of the medium, respectively and  $J$  is the current density. FDTD uses a second order finite centered approximation to the space and time derivatives in Maxwell's curl equations to get a discrete electromagnetism. In FDTD method, an orthogonal cubic spatial grid called Yee unit cell is defined and hence the electric and magnetic field components are computed at each cell at time instants delayed by the half sampling time steps [133]. The material can be modeled by specifying its characteristics at every cell [134].

A commercially available software, Rsoft FullWAVE is used for the FDTD simulation of gold nano-island structure. The gold nano-island is approximated to a hemisphere and the LSPR property against the diameter of the hemisphere is

investigated. Perfectly matched layer (PML) [135] boundary condition is used on the boundaries of the simulation domain, that is the boundary walls of the simulation domain was conductive to both the magnetic and electric fields, hence the light is completely absorbing on the boundary without any reflections.

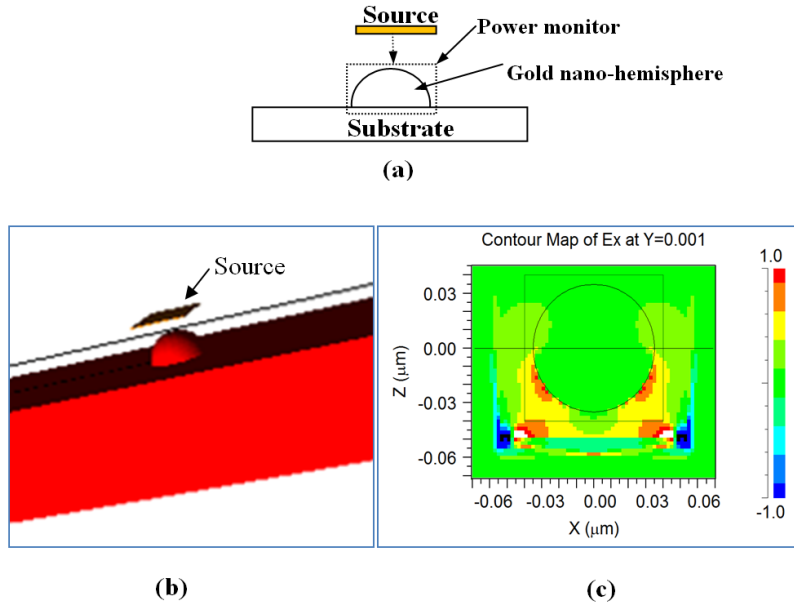


**Figure 5.4** (a) Schematic of the model (b) 3D-FDTD model of the gold hemisphere FDTD Simulation (c) Electric field distribution estimated by FDTD in the gold nano-hemisphere.

Figure 5.4 (a) shows the schematic of the model, herein a gold nano-hemisphere was excited by a source with plane waves originating from a square launch pad with transverse electric field. A pulse excitation type is used to excite the gold nano-hemisphere. The gold nano-hemisphere was kept in a power monitor to monitor the total power absorbed to the nano-hemisphere. Figure 5.4(b) shows the 3D view of the

gold nano-hemisphere modeled in the Rsoft FullWAVE. The electric field distribution on the gold nano-hemisphere simulated by FDTD is shown in Figure 5.4(C). By using the Fast Fourier Transform (FFT) algorithm, the absorbance spectrum of the gold-nano-hemisphere was computed. As the simulation domain is discretized into small elements called grids or mesh, the size of the mesh decides the accuracy of the model. Large computational resources and long time is required for the simulation with smaller mesh elements, hence a mesh convergence study is carried out to find the optimum mesh size. The optimum mesh size was found to be 1 nm.

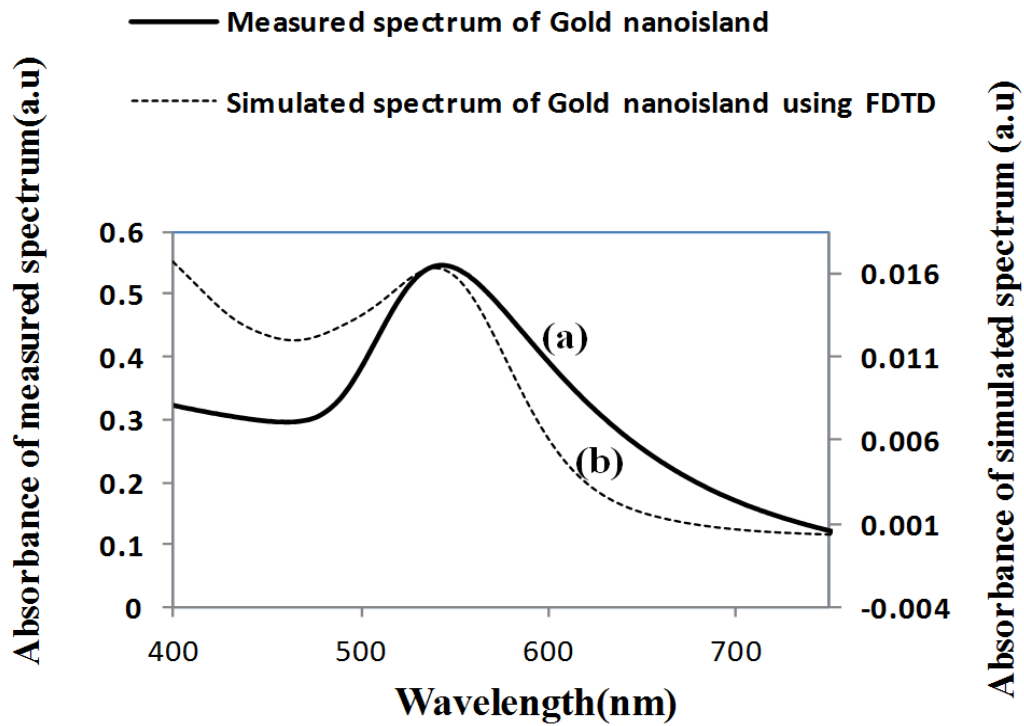


**Figure 5.5** (a) Measured LSPR spectrum (b) Simulated LSPR spectrum of the gold nano-hemisphere.

Figure 5.5(b) shows the absorbance spectrum computed by FDTD. The diameter of the gold nano-hemisphere was set at 70 nm. A comparison of the LSPR spectrum computed by the FDTD with the experimental result is shown in Figure 5.5. The measured and the simulated LSPR peaks are at 545 and 543 nm, respectively and the shape of both of the spectrum was also found similar. The size of the nano-islands on the tested structures annealed at 550<sup>0</sup>C (Figure 5.2(C)) varies from 10-100 nm while the modeling is carried out with a gold hemisphere of 70 nm. The variation in the size of the nano-islands could contribute to the difference in the shape of the spectrum in Figure 5.5. The simulation results show that the approximation of a gold nano-hemisphere by 70 nm diameter, with widely separated nano-islands morphology is closer to reality.

## **5.5 Dependence of the size of gold nano-hemisphere on the optical absorbance spectrum**

A hemisphere was simulated to establish a relation between the size and the resonance peak of the gold nano-hemisphere. The simulations carried out by increasing the diameter (D) of the gold nano-hemisphere shows that the optical absorbance peak is gradually shifting towards the higher wavelength as shown in Figure 5.6.

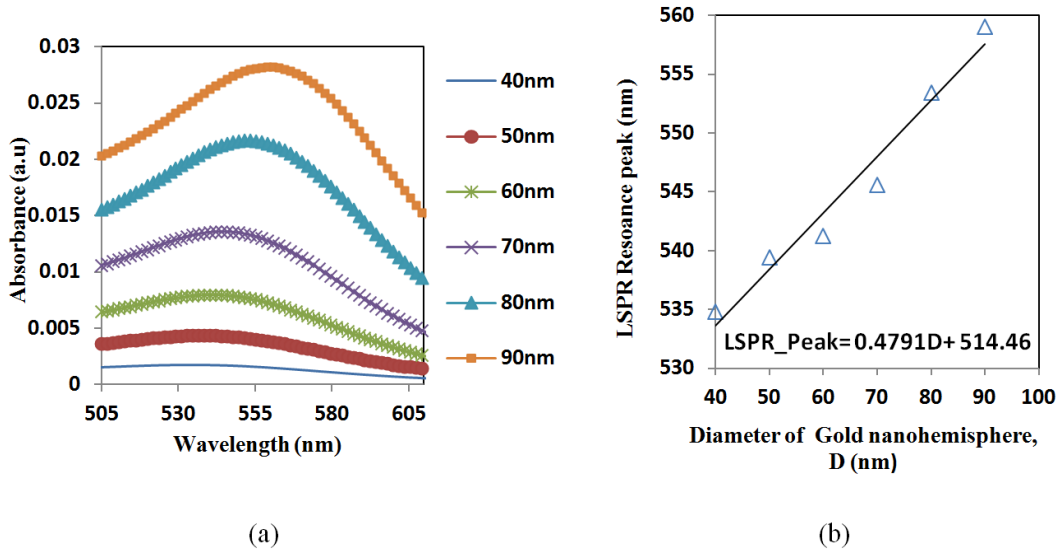


**Figure 5.6** (a) Optical absorbance spectrum of gold nano-hemisphere, (b) A red-shift of peak wavelength against the size of the gold nano-hemisphere.

The spectrum showed an increment in peak wavelength and in the intensity of LSPR spectrum against the diameter of the gold nano-hemisphere. The diameter of the gold nano-hemisphere is increased from 40 to 90 nm. A linear trend for absorbance peak wavelength is observed as shown in the Figure 5.6(b).

## 5.6 Modeling of morphology transformation

The FDTD model used for the investigation of morphological transformation is shown in Figure 5.7(a). The model consists of 4 gold nano-hemisphere separated by distance  $d$ . The diameter (D) of the hemisphere was 70 nm. The refractive index distribution of the model is shown in Figure 5.7(b). The entire four hemispheres were kept in a single power monitor to investigate resultant LSPR band. As explained

before, the structure was excited with a pulse and by using the FFT, the LSPR spectrum was obtained. The effect of the separation distance ( $d$ ) for 4 gold nano-hemispheres on the LSPR property of the morphology is also studied using this model. The spacing  $d$  was varied equally in both directions.

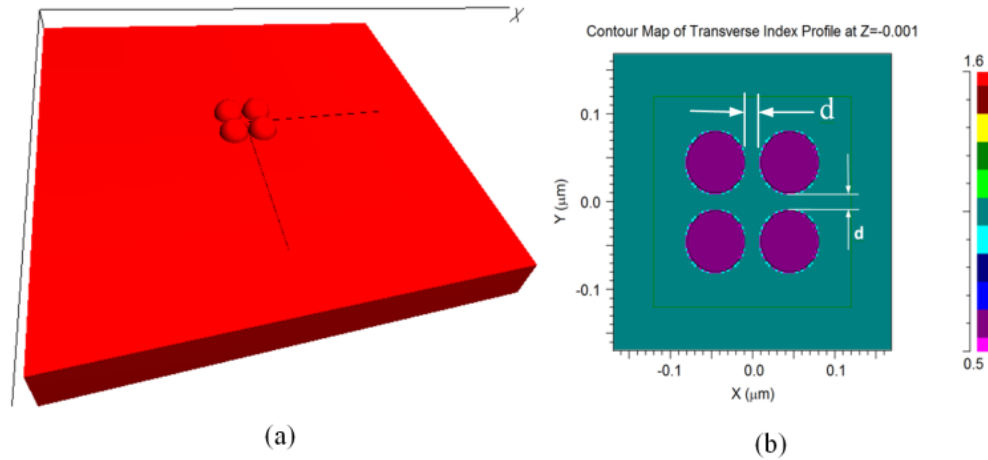


**Figure 5.7**(a) FDTD Model of 4 hemispheres morphology (b) Refractive index distribution of the FDTD Model from the top of the model.

Figure 5.8 shows the simulation results of the interparticle coupling effects on the LSPR property. The plasmon shift ( $\Delta\lambda$ ) is the shift of the peak wavelength of the LSPR spectrum of the 4 nano-hemisphere from the peak wavelength of the single hemisphere from a certain separation distance  $d$ . The separation distance  $d$  of the nanostructures is increased from 0 nm to 50 nm. The LSPR spectrum is computed. When the particles were touching each other ( $d=0$ ), the optical absorbance spectrum was a wide band as shown in Figure 5.8. When the  $d$  was increased to 1 nm, a

dramatic change in LSPR band is observed, that is, two clearly defined bands were obtained, one wide band similar to that of touching structure and a narrow peak at 725 nm. When the  $d$  was further increased, the band at higher wavelength was found to be moving towards the lower wavelength and the wide band observed in the lower wavelength was found to be slowly vanishing. When the  $d$  was increased to 25 nm or above, only a single band same as that of a single gold nano-hemisphere is observed. The LSPR spectrum of the single gold hemisphere is also presented in the Figure 5.8.

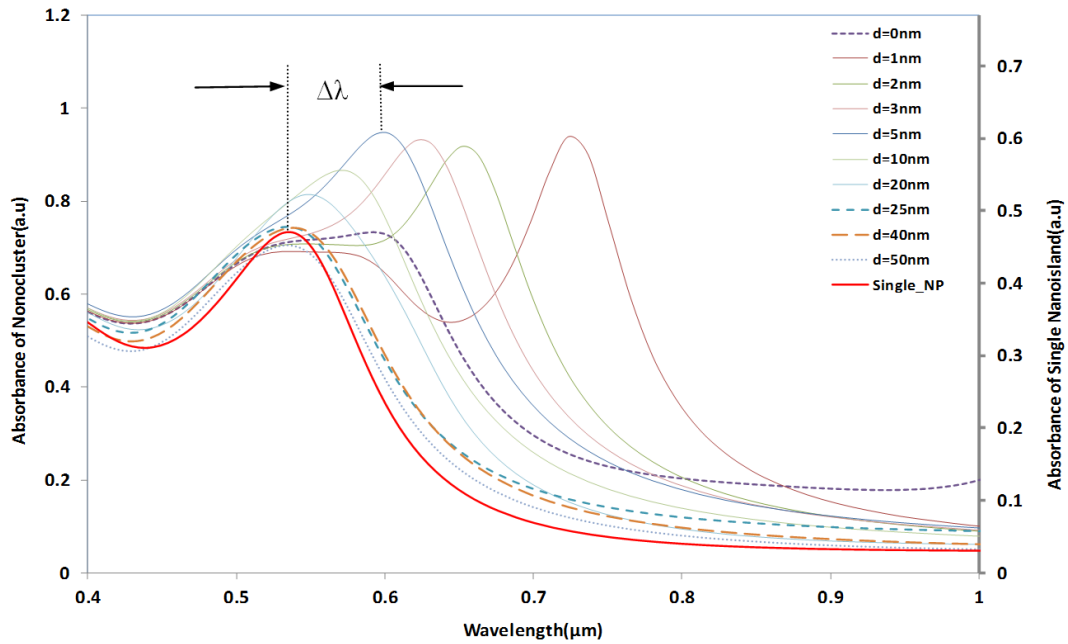


**Figure 5.8** LSPR spectrum of the gold nano-hemisphere against the particle separation distance,  $d$ .

The resultant LSPR band is arising from the near-field coupling between the particles as explained in the Section 5.2. The simulation demonstrates that the near-field coupling of the gold nano-hemisphere is negligible when the separation distance  $d$  is

25 nm or above, and the hemispheres are completely isolated from the near-field coupling.

The trend observed in Figure 5.8 was also observed in the experimental results given Figure 5.3, herein, when the samples were annealed at 400-450<sup>0</sup>C, the closely packed nano-islands morphology is obtained. Because of the strong near field coupling effects of closely packed nano-islands, the resultant LSPR band was found to have dual peaks (Figure 5.3(b)). When the annealing temperature was increased to 550-600<sup>0</sup>C, the peak in the higher wavelength is vanished and only one band is obtained due to the change in morphology and spacing ( $d$ ) similar to the results in Figure 5.8. The plasmon shift ( $\Delta\lambda$ ) normalized with the LSPR peak wavelength ( $\lambda_s$ ) of the isolated nano-island, that is  $\Delta\lambda / \lambda_s$ , is plotted against the inter-particle coupling distance ( $d$ ) normalized with respect to the diameter ( $D$ ) of the nano-island, as presented in Figure 5.9.

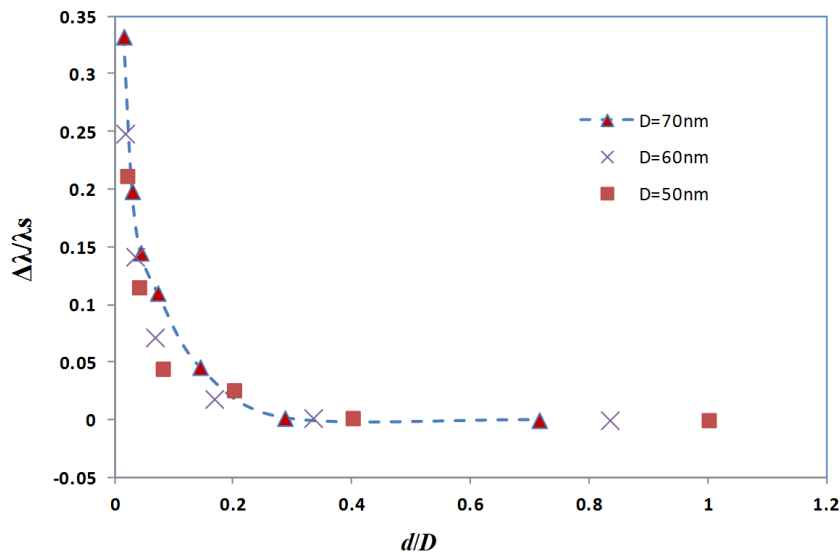


**Figure 5.9** The influence of spacing on near field coupling strength between 4 gold nano-hemispheres.

It has been already observed that the plasmon shift decays almost exponentially against the interparticle separation distance for the case of two metal nano-spheres [136, 137]. In the present study, the FDTD simulation with 4 gold-nano hemispheres also exhibited an exponential decay in the plasmon shift against the separation distance as shown in Figure 5.9. The simulations carried out for different diameters of the nano-hemispheres resulted in almost the same exponential trend. That means, the near-field coupling strength  $\Delta\lambda / \lambda_s$  falls almost exponentially over a distance of 0.3 times the diameter of the nano-islands regardless of the size of the islands. Therefore, the interparticle coupling effects of smaller islands in the annealed morphology (Figure 5.2) contributes less in the resultant LSPR band when compared to larger nano-islands.

### **5.7 Sensitivity of LSPR of the gold nano-hemisphere to adsorbing protein layer**

It is important to investigate the sensitivity of the LSPR peak to the change in refractive index for the biosensing process. In biosensing, the analytes bind to the gold nanostructure and the refractive index of the environment of the gold nanostructure changes, resulting in a shift of the LSPR band. For that, a model composed of gold nano-hemisphere with a sensing layer equivalent to protein layer having certain refractive index, covering the whole surface area of the nanostructures was used. Figure 5.10 shows the schematic representation of model having gold nano-hemisphere with a layer of protein.

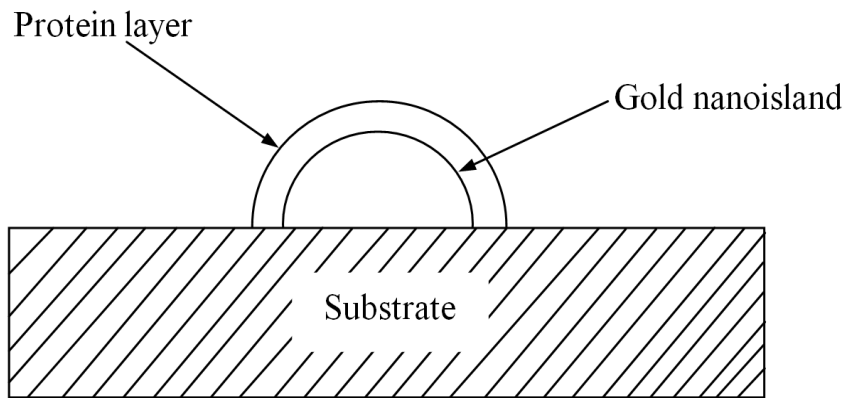


**Figure 5.10** Schematic of biosensor with gold hemispheres and a protein layer.

The thickness and the refractive index of the protein layer could affect the optical absorbance property of the nanostructure, hence the effects of both the thickness and the refractive index were investigated. First, the refractive index was kept constant and the thickness of the protein layer was varied from 0 to 140 nm, subsequently the simulation was repeated for various refractive indices. Figure 5.11 (a) and (b) show the change of LSPR spectrum of the gold-nano hemisphere against the thickness of the protein layer for the refractive index of 1.5 and 1.4 respectively.

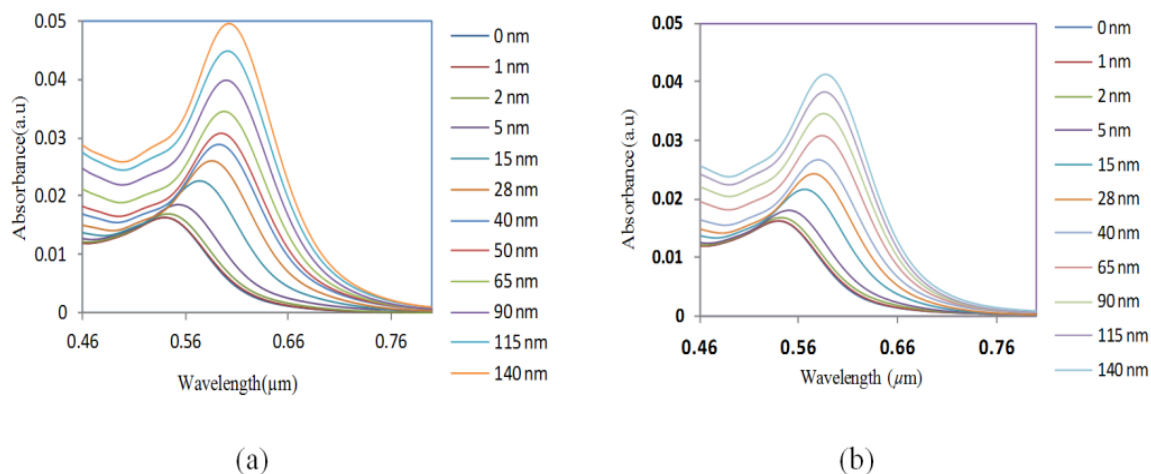


**Figure 5.11** Change of LSPR spectrum against the thickness of the protein layer with a refractive index of (a) 1.5 and (b) 1.4.

The refractive index was varied from 1.3 to 1.5 as most of the biomolecules have the refractive index in this range [138]. The results presented in the Figure 5.10 show that the shift of absorbance peak is saturating when the thickness of the protein layer is equal to or greater than 60-70 nm. Hence, the gold nano-hemisphere is suitable for the sensing of surface-assisted phenomena, which is highly desirable for the specific detection of antigen-antibody interaction occurring on a sensing substrate in a thickness layer of less than 60-70 nm.

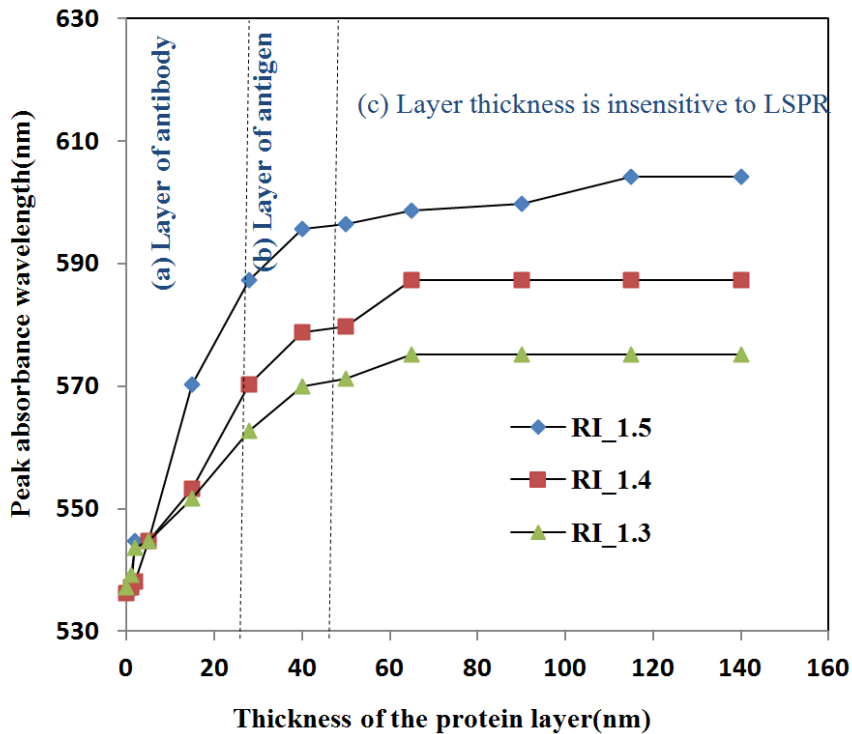


**Figure 5.12** Variation of LSPR peak against the thickness of the protein.

In Figure 5.12, three region of the thickness of the protein layer could be identified. Since the size of the large biomolecules is within 10 to 20 nm [138], the antibody of the protein layer adsorbing to the gold hemisphere for the sandwiched immunoassay comes in the region (a) of Figure 5.12. Subsequently, when the antigen is added to the antibody layer the interaction occurs in a layer of 40 to 50 nm, which happens in the region (b) of the Figure 5.12. The region above 60-70 nm is insensitive to the thickness of the bio-layer. Therefore the simulation results show that gold nano-hemisphere is highly suitable as a sensing platform for the detection of biomolecules including large biomolecules such as proteins and polypeptides.

## 5.8 Refractive index sensitivity of gold nano-hemisphere

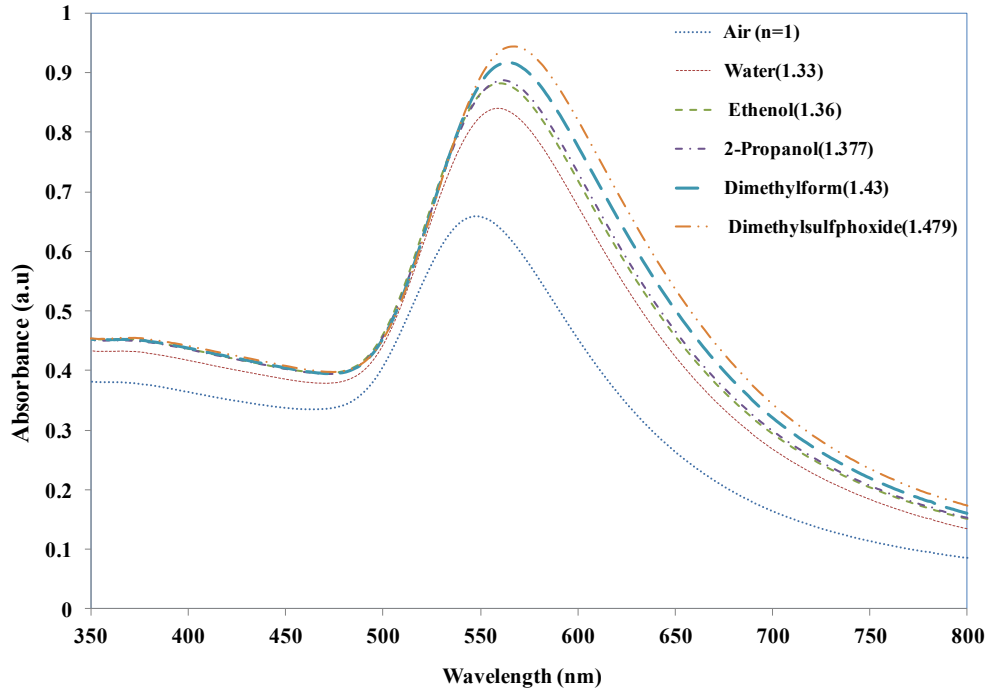


**Figure 5.13** Measured shift of LSPR band in various solvents

In order to assess the suitability of the nano-islands integrated platform for biosensing, the sensitivity of the nano-islands to the change in refractive index of the sensing layer has to be determined. Therefore the change of LSPR peak against the change of refractive is measured by using solvents having known refractive indices. Annealed samples were placed in a cuvette filled with a solvent and placed in the light path of the UV-Visible spectrophotometer. Herein, as the sample is placed in the bulk liquid the thickness of refractive index layer is insensitive to the LSPR band. The de-ionized (DI) water with a refractive index of 1.33 was used as the reference solvent. The shift of LSPR ( $\Delta\lambda$ ) for solvents was measured with reference to the

LSPR peak corresponding to DI water. The LSPR spectrum measured for various solvents are shown in Figure 5.13.

From the Section 5.7, we have seen that the LSPR peak is not sensitive to thickness of the protein layer when the thickness was greater than 60 nm, but only to the refractive index. Therefore, in order to investigate the refractive index sensitivity of gold nano-hemisphere, the hemisphere with a diameter of 70 nm was simulated with a sensing layer of 140 nm thickness and with different refractive indices. The refractive indices of the solvents used in the experiments are used in the FDTD model. Figure 5.14 shows the change of LSPR observed from the FDTD simulation for various solvents.

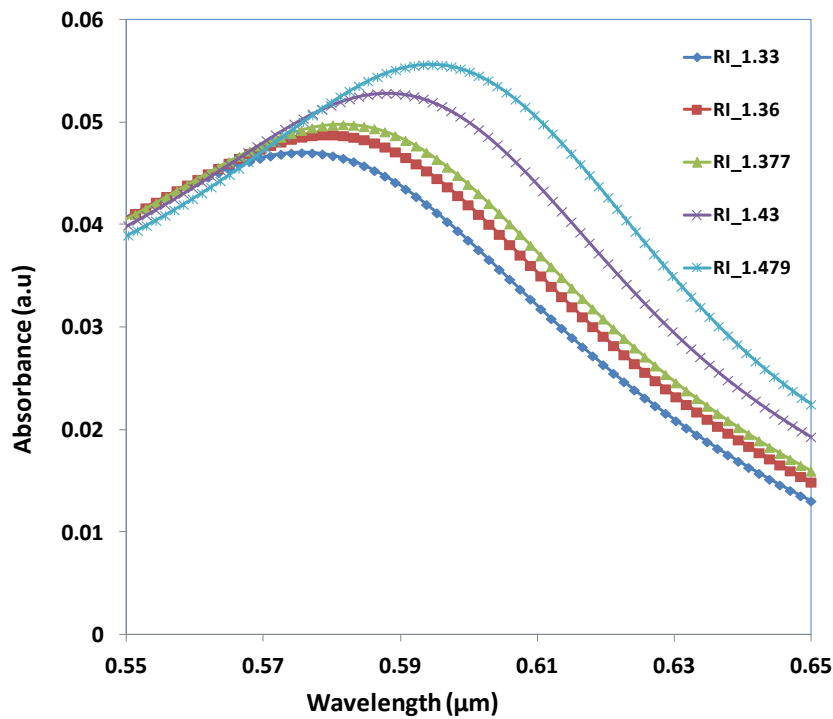


**Figure 5.14** Simulated LSPR spectrum of gold nano-hemisphere with protein layer having the refractive index of solvents.

The refractive index sensitivity can be assessed using the relation between LSPR shift ( $\Delta\lambda$ ) and the change in refractive index ( $\Delta n$ ). Where  $\Delta\lambda$  and  $\Delta n$  are defined as:

$$\Delta\lambda = \lambda_m - \lambda_w \quad (5.5)$$

$$\Delta n = n_m - n_w \quad (5.6)$$

where,  $\Delta\lambda$  is the change in the absorbance peak wavelength,  $\lambda_m$  is the absorbance peak wavelength corresponding to the medium with a known refractive index,  $\lambda_w$  is the absorbance peak wavelength corresponding to de-ionized water,  $\Delta n$  is the difference between the refractive indices of the solvent and that of water,  $n_m$  is the refractive index of the solvent and  $n_w$  is the refractive index of water.

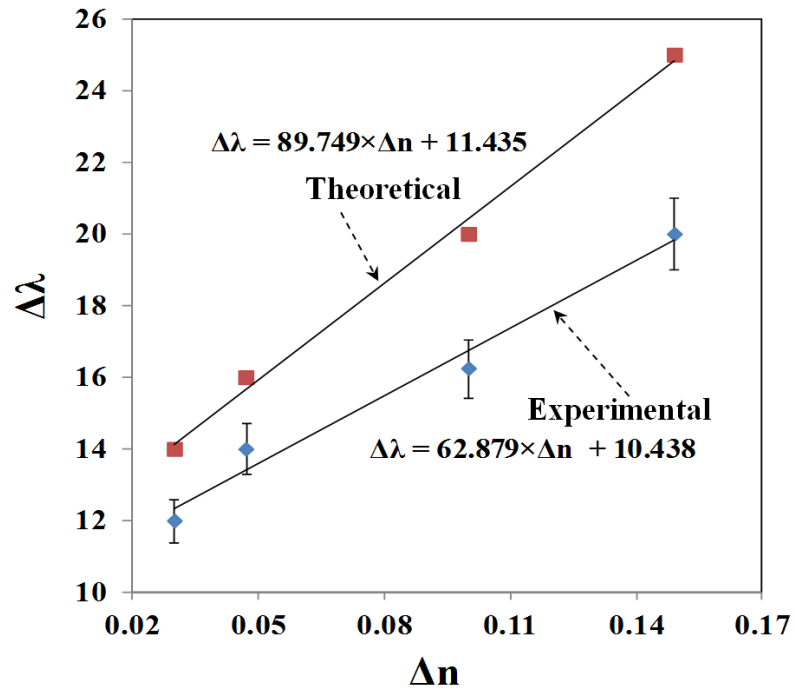


**Figure 5.15** Measured and simulated variation of LSPR shift against change in refractive index.

The variation of LSPR shift ( $\Delta\lambda$ ) against the change of refractive index ( $\Delta n$ ) is shown in Figure 5.15. The error bar given in the experimental results corresponds to the standard deviation of measurements taken from 10 samples. The LSPR sensitivity against refractive index, as measured by the slope of the graph shown in Figure 5.15 is 62.879 nm/RIU. The sensitivity predicted by FDTD simulation is 89.749 nm/RIU as shown in Figure 5.14. The slight disagreement between the simulated and the measured sensitivity is due to the approximation of the nano-islands morphology with a single gold nano-hemisphere of 70nm diameter.

## 5.9 Conclusions

FDTD modeling of a morphological transformation of nano-cluster into nano-islands and its LSPR sensitivity is presented in this paper. Formation of nano-islands morphology by a simple and low-cost convective assembly followed by a post-deposition annealing is discussed. The nano-cluster is modeled with 4 gold-nano hemisphere, and the separation distance between them is varied to study coupling effects and the resultant LSPR spectrum. The change of LSPR spectrum due to the near-field coupling and its dependence on the interparticle coupling distance between the nano-islands is also investigated. It is found that the near-field coupling strength falls exponentially for a spacing of 0.3 times the diameter of the nano-islands. Hence the field coupling effects due to smaller particles in the nano-island morphology is considered negligible. The biosensing potential of the gold-nano island is investigated with an equivalent biosensing layer having different thickness and refractive indices. The effects of thickness of the protein layer on the LSPR properties are found

negligible when the thickness was greater than 60 nm. Therefore, the nano-island morphology is highly suitable for the detection of antigen-antibody interaction even for the larger molecules such as proteins and peptides. The LSPR sensitivity against refractive index sensitivity was investigated experimentally and theoretically. The theoretical sensitivity is 89.749 nm/RIU, which is found greater than the experimentally obtained sensitivity of 62.879 nm/RIU. The simulation is carried out with a simplified model of the nano-island morphology, in which a single gold hemisphere having the diameter of 70nm is approximated with nano-island morphology obtained with the annealing temperature of 550<sup>0</sup>C. However, the sensitivity analysis shows that the simulation and experimental results have same trend.

## **Chapter 6: Gold nano-island structures integrated in a lab-on-a-chip (LOC) for plasmonic detection of bovine growth hormone**

### **6.1 Introduction**

Somatotropin (ST) is a polypeptidic growth hormone, naturally produced by the anterior pituitary gland in mammals. The polypeptide chain for bovine somatotropin consists of 191 amino acids but the composition and the biological effects depend considerably on the species. The biological effects of bovine somatotropin (bST) are associated with growth, development and reproductive functions. Its effect on milk production was discovered in 1937[2]. Since the 80s, recombinant DNA technologies allowed the production of large quantities of hormones which are used in USA and other countries to increase the milk production but the use is forbidden in Canada and in the European Union. Use of the recombinant bST (rbST) as a growth promoter is controversial [14, 16, 82] because of its potential effects on animal and human health. In order to provide meaningful information to consumers and to identify the rbST-treated animals, highly sensitive analytical methods are required.

Conventionally, the concentration of bST in various biological media was estimated by using an enzyme-linked immunosorbent assay (ELISA) [22], [23] a radioimmunoassay (RIA) [84], [24] or bioassay methods [25]. The most important limitation of ELISA assays is that the concentration of antibody can only be reported in relative terms such as “titer”, that is, a combination of affinity and concentration. More recently, a sensitive method that allows the discrimination between the recombinant and the endogenous forms of somatotropin has been developed. It is

based on liquid chromatography-mass spectrometry, combined with electrospray ionization [85] [13] [86]. The principal drawback of this approach is the complexity of the methodology involved, which, together with the very expensive instrumentation, makes this method difficult to implement for a rapid detection of bST and rbST in milk. Surface Plasmon Resonance (SPR) biosensing method has also been suggested for the detection of bST [26]. However, the measurement was carried out in an expensive plasmonic instrument (Biacore 3000). For this reason, developing a microfluidic biosensing method that allows a rapid and precise detection of growth hormones in milk becomes extremely important.

Noble metal nanostructures such as gold and silver exhibit unique optical absorbance property and hence they have been proven to be useful to a variety of fields such as photonics, SERS [139], optoelectronics, near-field microscopy, catalysis, chemical and biological sensing. The plasmonic band, also called the Localized Surface Plasmon Resonance (LSPR) band of gold and silver nanoparticles can be tuned by adjusting the size, shape and morphology or by alloying [140] [141]. The LSPR band could also be shifted to the near-infrared region, a region of particular interest for biomedical applications such as cancer hyperthermia [142]. Other biological and medical applications of gold nanoparticles and nanostructures are in the field of biological labels, biosensors, drug discovery, diagnosis and monitoring of various diseases.

The binding of analytes on immobilized gold nanoparticles, changes the local refractive index of the surrounding environment that results in a shift to longer wavelengths of the corresponding Au LSPR band. Gold and silver spherical

nanoparticles with different dimensions and configurations have been widely used to recognize and detect various bio-molecules [122, 143-151]. The growing expertise in nanofabrication methods enables the preparation of gold and silver nanostructures and patterns of various complexities. However, most research on chip-based assays has focused on two-dimensional (2D) structures, that is, a gold monolayer on glass having a low density of nanoparticles [122, 144].

In order to enhance the sensitivity of detection, multilayers of gold nanoparticles have been fabricated using layer-by-layer deposition [41, 152] or the immersion of the substrates in the colloidal gold solution for various time intervals [153]. Au multilayers, prepared by the layer-by-layer deposition method showed a higher refractive index sensitivity compared to the monolayer sensors used previously. However, the method is tedious, and involves several steps of fabrication as the nanoparticles have to be coated with polyelectrolytes [154]. Gold nanostructures for sensing purposes [155] or for SERS substrates were deposited by thermal evaporation and sputtering as well [156]. For a comprehensive review on the preparation of nanostructured film arrays see ref. [157] and references therein.

In this chapter, the fabrication and characterization of three-dimensional gold nanostructures fabricated by convective assembly is explained. The mechanism of self-assembly is based on the flow of a colloidal suspension induced by evaporation from the liquid meniscus formed at the substrate-solution interface. The technique of convective assembly relies on the interaction forces between particles and/or particles and surfaces that drive to the formation of ordered arrangements. During the deposition process, due to the strong attraction forces between the gold nanoparticles

(NP) and the gold – glass attraction, gold aggregates are formed on the substrates as shown in Figure 6.1. The rate of self-assembly is governed by the evaporation from the liquid meniscus, the particle concentration and the particle diameter. The high density of gold nanoparticles in the multilayers and the transparency of the samples allow the use of a conventional UV-Visible spectrophotometer for the measurements. The proposed method is simple and can be carried out in a general laboratory environment, without any need of special apparatus or expertise. The nanostructure deposited on glass substrates by simple angled deposition resulted in gold aggregates which were further annealed to yield an improved sensing platform. We [91] have recently shown that multilayer films, also called three-dimensionally assembled gold nanostructures can be fabricated from gold nanoparticles by convective assembly from the evaporating meniscus of aqueous suspension. Three-dimensional Au nanostructures display two plasmon bands, one around 520-530 nm that belongs to plasmon resonance of isolated gold nanoparticles and a second one, at longer wavelengths (600-700 nm) due to a collective surface plasmon oscillation [158]. The 600-700 nm Au band arises from coupling of the individual plasmon resonances when gold nanoparticles are closely spaced. The intensity of this feature is proportional to the degree of aggregation. For a comprehensive discussion on the inter-particle coupling effect, see reference [159] and references therein.

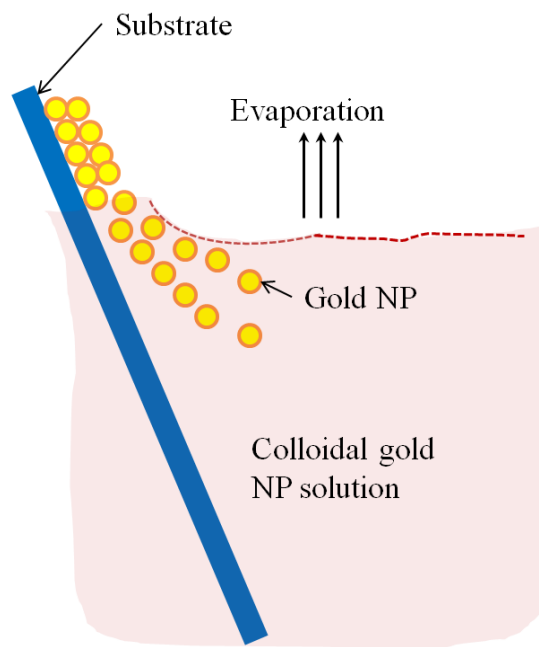


**Figure 6.1** Schematic sketch of the convective assembly process of gold nanoparticles.

In the previous work [91], gold nanoparticles and aggregates, functionalized, either with a carboxymethylated dextran hydrogel or with 11-mercaptopundecanoic acid were used for monitoring an antigen-antibody interaction. The results demonstrated that with spherical nanoparticles, a higher sensitivity of bio-sensing can be achieved by using the shift of gold LSPR band of aggregates toward longer wavelengths. However, because the collective surface plasmon oscillation results in a quite broad band, the detection of the shift upon the binding event is less precise than in the case of the sharp LSPR band corresponding to isolated particles or small aggregates. For this reason, for improving the sensitivity of the detection, a post-deposition annealing of gold multilayers was investigated in this work. The present work is focused on the bio-sensing experiments carried out by using gold nano-island structures obtained by

annealing of gold multilayers. The multilayers with different particle packing densities and degrees of aggregation are prepared by the convective self-assembly of colloidal gold using a simple oven, instead of complex and tedious processes used by other authors [160, 161]. 11-mercaptoundecanoic acid is used to form a self-assembled monolayer on the gold nanoparticles. The sensing platforms prepared by convective assembly and annealing were tested for the detection of bovine somatotropin (bST) through antigen-antibody interactions. A calibration curve that correlates the shift of Au-LSPR band with the concentration of antigen is established in the range of 5 to 1000 ng/mL and the detection limit of polypeptide is determined. The mechanism of sensing by using the annealed gold nanostructures is also discussed. Further, a microfluidic device having the gold nanoparticles integrated into a microchannel was designed, fabricated and used for the analytical process.

## **6.2 Experimental**

Hydrogen tetrachloroaurate (III) trihydrate ( $\text{HAuCl}_4 \cdot 3\text{H}_2\text{O}$ ) was purchased from Alfa Aesar. Sodium citrate, 11-mercaptoundecanoic acid in ethanol (Nano Thinks Acid 11), phosphate buffered saline (PBS),  $N,N'$ -diisopropylcarbodiimide and  $N$ -hydroxysuccinimide were obtained from Sigma-Aldrich Canada. The antigen, the natural bovine somatotropine (bST, MW 20 kDa) and its corresponding polyclonal antibody (anti-bST, raised in a guinea pig) were obtained from Dr. Parlow (National Hormone & Peptide Program, Harbor-UCLA Medical Center) and used for the immunoassay.

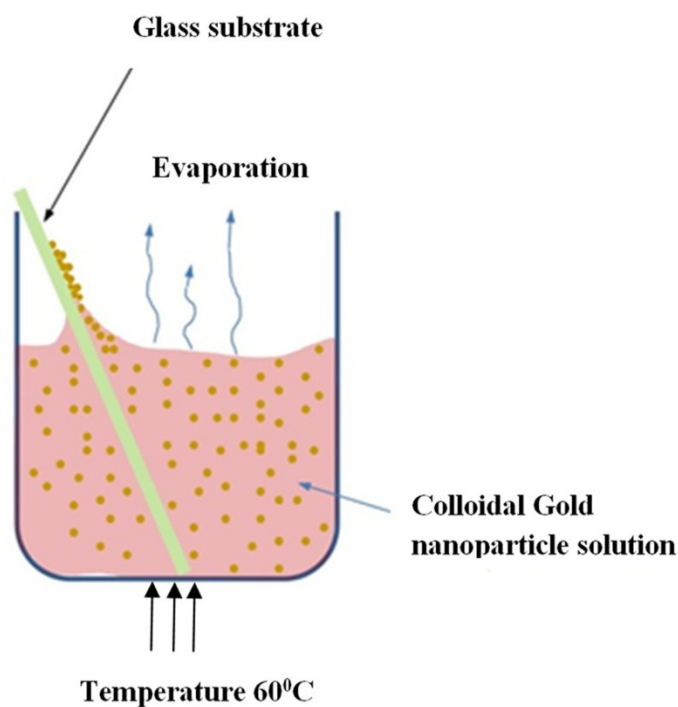


**Figure 6. 2** Schematic sketch of the deposition of gold nanostructure on glass.

Spherical gold nanoparticles were prepared by using the reduction of chloroauric acid by sodium citrate, following Turkevich's method<sup>44</sup>. Briefly, 75 mL of chloroauric acid solution containing around 45  $\mu\text{g}/\text{mL}$  gold is heated and 5 mL of 1% sodium citrate solution is added to the boiling solution. After the colour of the solution turned to purple, the solution is further boiled for 25 min and then left to cool to room temperature. Gold multilayers were deposited on freshly cleaned substrates. Glass substrates were cleaned with soap and DI water, then rinsed with acetone, dried and finally rinsed with 2-propanol. Before the deposition process, the glass substrates were kept in an oven at 100<sup>0</sup>C for 1 hour. Silanized glass substrates were immersed with an angle ( $\sim 30^0$ ) in vials containing the gold colloid solutions (3-5 mL) (Figure

6.2) and kept in the oven at temperatures between 60 and 80<sup>0</sup>C, until the whole amount of gold was transferred to the substrate (1 to 3 days).

Nanoparticle multilayer films were post-annealed in a furnace for one hour at 400<sup>0</sup>C, 500<sup>0</sup>C and 550<sup>0</sup>C, respectively. Gold nanoparticles were further functionalized with a solution of mercaptoundecanoic acid in ethanol by covering the active surface of the platform (around 150-200  $\mu$ L). For the bio-sensing experiments, the concentration of antibody on the functionalized gold structure was kept constant at 100 ng/mL and the concentration of antigen was varied between 5 and 10000 ng/mL.

The sensitivity of the sensor platform was determined by measuring the spectra of both non-annealed and annealed gold nanostructures in solvents with different refractive indices. The sensor platform was immersed in de-ionized water and, subsequently, in different solvents and kept for 2 hours before the spectral measurement. Transmission UV-Vis spectra were acquired by using a Perkin-Elmer 650 UV-Visible spectrometer. Rectangular quartz cells were used to hold the glass substrates.

### 6.3 Assembly of the microfluidic platform

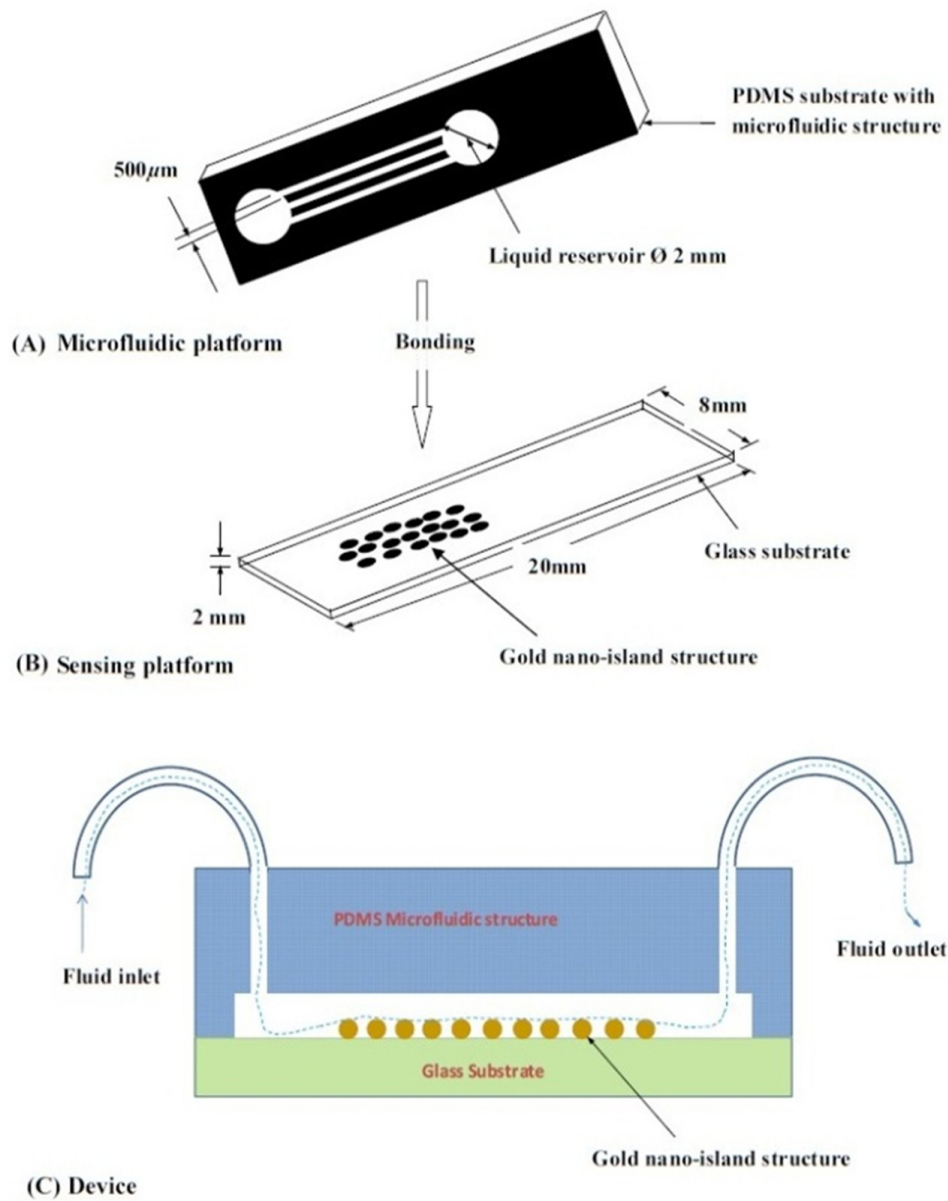


**Figure 6.3** Assembly process of the microfluidic device.

The microfluidic structure incorporates three or more parallel microfluidic channels to activate the microfluidic flow between two liquid reservoirs (Figure 6.3 (A)). The

width of the channel was chosen to be 500  $\mu\text{m}$  by considering two factors: first, the width of the light beam which was  $\sim 2$  mm and second the sealing of the channel. Due to the high flexibility of PDMS, sealing of the channel having the width of more than 500  $\mu\text{m}$  is a difficult task as the oxygen plasma treatment is used for the bonding. For this reason, the microfluidic channel was designed with three parallel microchannel of 500  $\mu\text{m}$ , separated by 200  $\mu\text{m}$ . The depth of the microchannel was 100  $\mu\text{m}$ . The microfluidic structure was fabricated on PDMS by soft lithography. The mold for casting the PDMS was fabricated on SU8 photo-resist. Patterning of SU8 is done on a silicon wafer by using UV photolithography. The SU8 mold was silanized to promote the removal of the PDMS structure from the mold. For the fabrication of the microfluidic structure, the PDMS base and curing agent (SYLGARD 184 from Dow Corning) are mixed in a 10:1 wt ratio, degassed in a vacuum desiccator to remove the gas bubbles, and casted to the mold and baked at 80<sup>0</sup>C for 5 hours.

The substrate holding the nano-island structures is shown in Figure 6.3(B). The device (Figure 6.3(C)) was fabricated by bonding the glass substrate to a PDMS substrate with the help of oxygen plasma treatment. The glass substrate containing gold nano-island structures and the PDMS slab containing the microfluidic structure were treated with oxygen plasma for 35 seconds in a plasma cleaner and bonded together immediately. The inlet and outlet tubes were fixed with the liquid reservoirs using silicone glue. Figure 6.4 shows photograph of the nanoparticle integrated microfluidic bio-sensor.

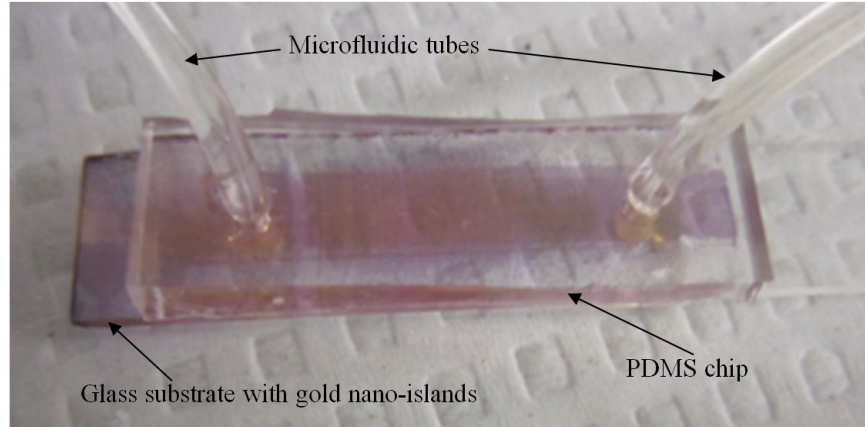


**Figure 6.4** Photograph of the nano-islands integrated microfluidic bio-sensor.

#### **6.4 The experimental procedure for the bio-sensing**

Gold nanoparticles were first functionalized with a solution of mercaptoundecanoic acid in ethanol by covering the active surface of the platform (around 150-200  $\mu\text{L}$ ). Then the cross-linker solution (N, N'-diisopropylcarbodiimide and N-hydroxysuccinimide) was dropped on the sample to covalently attach the antibody to the gold nanostructures. After 10 min, the spectrum of the functionalized gold is measured. Afterwards, an antibody solution is introduced into the sensing platform and kept in contact with the gold nanostructure for at least one hour. The change in the position of LSPR corresponding to the binding of antibody was measured. The concentration of antibody on the functionalized gold structure was kept constant and the concentration of antigen was varied between 5 and 10000 ng/mL. The excess of antibody is washed away with a PBS (Phosphate Buffered Saline) solution and a blocker (non-fat milk powder solution) is passed, then the corresponding antigen is added to the sample and the LSPR spectrum is recorded to monitor the change of

LSPR corresponding to the antigen-antibody interaction. The procedure is repeated in the microfluidic device by pumping the solution into the device.

## 6.5.1 Results and Discussion

### 6.5.1 Tuning the morphology of the 3D gold nanostructure from nanoaggregates to nano-islands

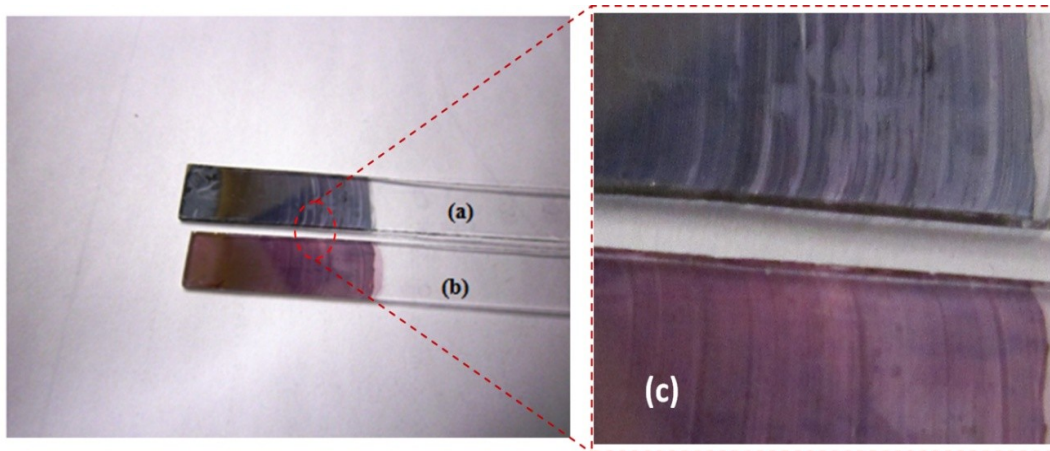


**Figure 6.5** Images of the non-annealed sample (a), sample annealed at 550<sup>0</sup>C for 1 hour (b) and enlarged images of the samples showing the stripping behavior (c).

The non-annealed samples showed a dark blue coloration (Figure 6.5 (a)) while the sample annealed at 550<sup>0</sup>C had a red tint. As it can be seen in the Figure 6.5(c), the films showed the striping behavior characteristic to samples deposited slowly by convective self-assembly [6, 38]. It is found that the stripes are uniformly distributed and the spacing between them is constant as long as the deposition temperature is the same. For samples annealed at lower temperatures, the color of the sample is not uniform. The SEM images corresponding to the two samples are shown in Figure 6.6. It can be seen that, before annealing, the nanoparticles are aggregated, forming long

chain-shaped structures with several layers of nanoparticles. Aggregation begins in the evaporating meniscus because of the strong attractive van der Waals forces between gold nanoparticles [160]. The annealed samples show nano-island morphology, with large well-separated nano-islands and smaller particles around them. The nano-island films formed by nucleation and coalescence of gold nanoparticles at 550<sup>0</sup>C are polydisperse with an average diameter of grains around 70 nm. The density of nano-islands is estimated to be around 64 islands/ $\mu\text{m}^2$  and it strongly depends on the concentration of gold in the colloidal solution.

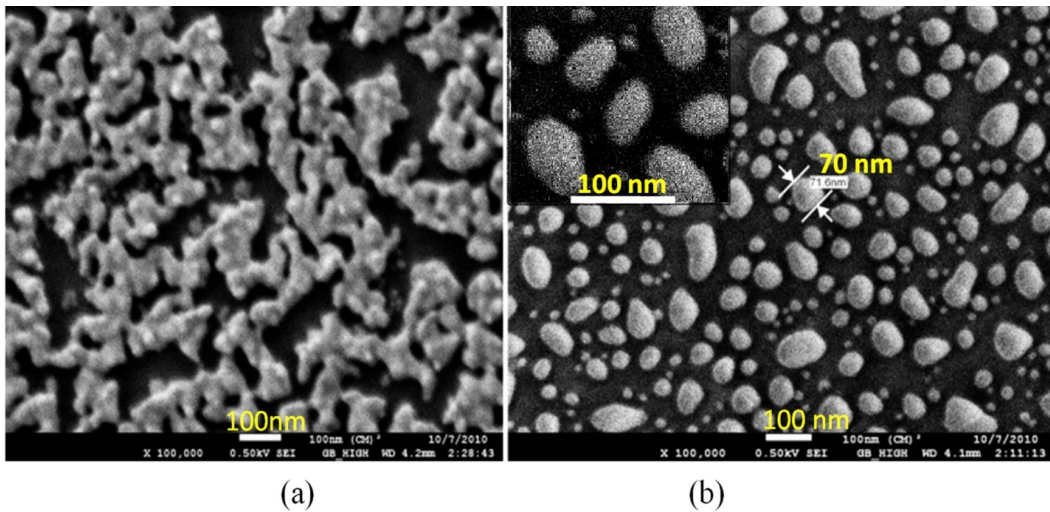


**Figure 6.6** SEM images of 3D gold nanostructures, as deposited (a) and after annealing at 550<sup>0</sup>C for 1 hour (b) (the magnification is X100000 in both images and X200000 in inset).

At temperatures higher than 350<sup>0</sup>C, for a sample with around 25 $\mu\text{g}/\text{ml}$  of Au in the colloidal solution, clearly separated nano-islands are formed. The islands look like droplets, are elongated (ellipsoid shaped) and their size varies between 10 and 100 nm. The formation of nano-islands upon annealing (at temperatures above 350<sup>0</sup>C)

was widely reported for gold nanostructures prepared by LbL (layer-by-layer) deposition [41, 152, 162] as well as by thermal [156] and electron-beam [163] evaporation. The morphology of gold nano-islands generated from LbL assembly depends on the number of layers and the nature of linkers used for building up the multilayer. It has been reported [126] that the morphology of ultrathin thermally evaporated films (less than 10 nm) can be tuned to nano-island-type structures at temperatures as low as 200<sup>0</sup>C using long annealing times (20 hours). The morphology change is thought to be induced by sintering and agglomeration of neighboring nanoparticles and diffusion coalescence that results in the formation of a single layer of laterally-spaced islands. In the case of the multilayers deposited by angled convective assembly (Figure 6.6 (a)), having the intertwined chain structure, the gold nanoparticles would melt prior mobility and coalescence. Indeed, it is known that the melting temperature of gold nanoparticles is reduced to tens to hundreds of degrees due to the particle size. Due to high surface tension of liquid gold, nano-islands with convex surfaces are formed during the annealing process and percolation occurs at a high density of nano-islands as shown in Figure 6.6(b).

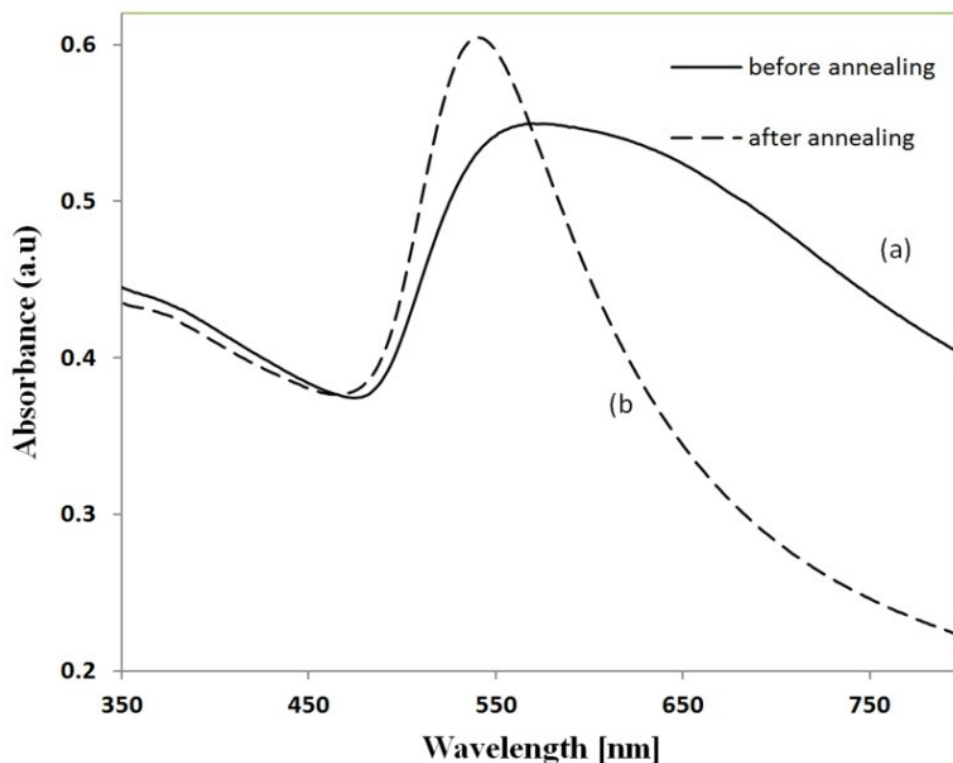


**Figure 6.7** UV-Visible spectra of gold nanostructures deposited on glass, (a) before annealing and (b) after annealing at 550<sup>0</sup>C for 1 h.

Compared to the aggregated multilayer structure, the nano-island structure is likely to provide multiple binding sites and enough room for the diffusion of bio-molecules [41]. The spectra of the non-annealed and the annealed samples were measured in the UV-Visible range (Figure 6.7). The change in morphology, induced by annealing, is accompanied by a dramatic change in the optical properties as shown in Figure 6.7(b). The gold multilayer was deposited by using a solution of 45  $\mu\text{g}/\text{mL}$  gold. Aggregated gold multilayers show a broad band in the 550-750 nm regions (Figure 6.7(a)). When heated at 550<sup>0</sup>C for an hour, the band is blue-shifted to 545 nm and becomes considerably narrower (Figure 6.7(b)). This band belongs to the nano-island structures shown in Figure 6.6 (b). The position and the shape of this band clearly

show that the island structures are particulate, not aggregated. When the concentration of the gold in solution was reduced to  $25\mu\text{g/mL}$ , the band appears to be changed as shown in Figure 6.8.

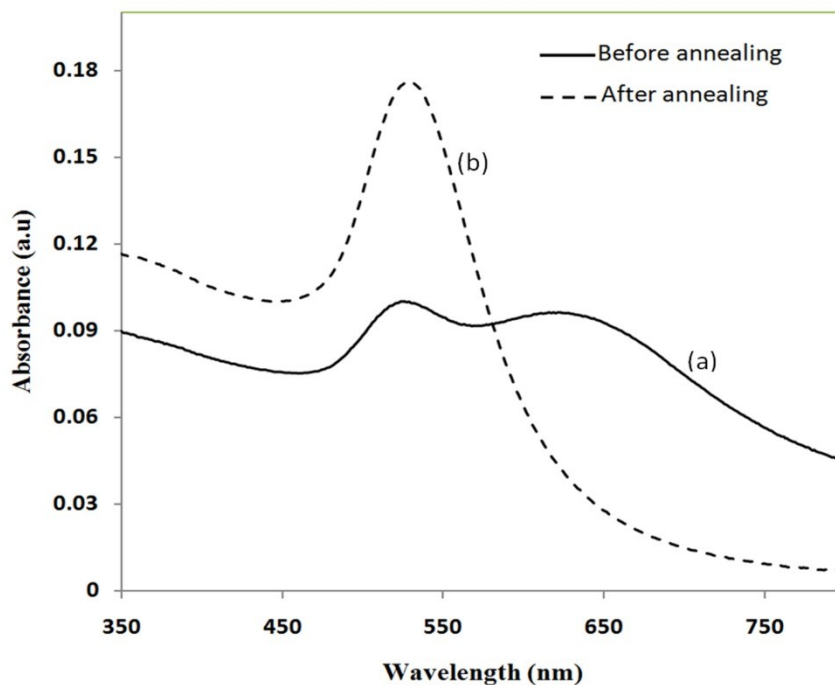


**Figure 6.8** UV-Vis spectra of gold multilayers non-annealed (a) and annealed at  $500^{\circ}\text{C}$  for 1 h (b) (multilayers deposited from a colloidal solution with a lower concentration of Au,  $25\mu\text{g/mL}$ ).

When the gold nanoparticle solution was diluted ( $25\mu\text{g/ml}$  of Au), the spectrum (Figure 6.8(a)) shows two bands. The band corresponding to aggregated gold nanostructure is situated around 620 nm showing a lower degree of aggregation and a band at 526 nm. After annealing, the spectrum shows only one narrow band at 529 nm with a noticeable higher absorbance.

## 6.6 Sensing experiments: study of the reproducibility and sensitivity of nano-island sensors

Several sensing platforms have been prepared and annealed, and both the position and the absorbance of the LSPR band were measured immediately after annealing and again, after several days. The results show a good reproducibility: for a number of 50 platforms, the position of the peaks after annealing was at 540 +/-10 nm. The position of the Au LSPR band belonging to the annealed sample may vary because of the slight differences in the preparation and annealing conditions. However, these variations would not affect the precision of the detection as the shift of the band would be the same.

The sensitivity has to be determined because it gives a preliminary assessment of the ability of the platform to be used in the actual biosensing experiment. Hence, it is important to investigate the sensitivity of the LSPR peak to the refractive index, as during the biosensing process, the analytes bind to the gold nanostructure and the refractive index of the environment of the gold nanostructure changes which results in a shift of the LSPR peak. The shift of Au-LSPR ( $\Delta\lambda$ ) upon the change of refractive index of the local environment of the nanoparticles ( $\Delta n$ ) is plotted as shown in Figure 6.9 and the slope of the curve is measured as the sensitivity of the platform. The shift of Au LSPR band in different solvents, with refractive indices in the range of 1.300-1.479 for both the non-annealed and annealed structures is shown in Figure 6.9. In order to assess the sensitivity of the sensing platform, the change of UV-Visible absorption of gold nanostructures immersed in various media was investigated before and after annealing. The sensing platforms made of non-annealed and annealed samples are introduced subsequently in the solvents given in Table 6.1.

	Solvent	Refractive index
1.	Water	1.33
2.	Ethanol	1.36
3.	2-Propanol	1.377
4.	Dimethylformamide	1.43
5.	Dimethyl sulfoxide	1.479

**Table 6.1** Solvents used for measuring the refractive index sensitivity of annealed and non-annealed sensing platforms.

The sample with gold nanostructures is immersed in a cuvette filled with the solvent with a known refractive index. In order to assess the refractive index sensitivity, the following formulas are used:

$$\Delta\lambda = \lambda_m - \lambda_w \quad (6.1)$$

$$\Delta n = n_m - n_w \quad (6.2)$$

Where,  $\Delta\lambda$  is the change in the LSPR peak wavelength,  $\Delta n$  is the difference between the refractive indices of the solvent and that of water,  $n_m$  is the refractive index of the solvent,  $\lambda_m$  is the LSPR peak wavelength corresponding to the medium with a known refractive index,  $\lambda_w$  is the absorption peak wavelength corresponding to DI water, and  $n_w$  is the refractive index of water.

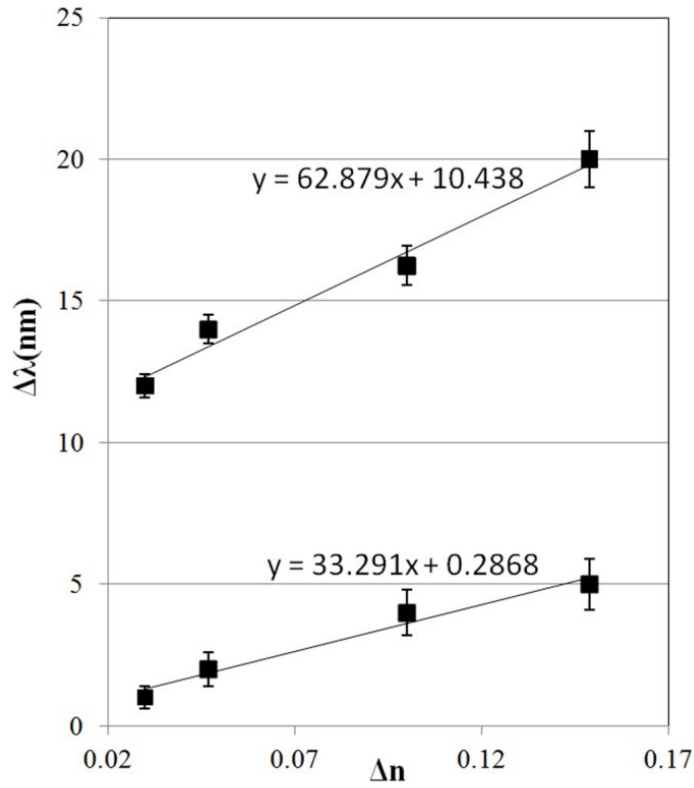


**Figure 6.9** Sensitivity of the platforms to the change in the refractive index of the environment for the annealed and for the non-annealed sample (The error bar represents the standard deviation of 10 measurements).

The sensitivity is assessed by plotting the graph of  $\Delta n$  vs.  $\Delta \lambda$  as illustrated in Figure 6.9. The sensitivity is measured as the slope of the graph shown in Figure 6.9. The sensitivity of the nano-island (annealed structure) sensor platform is much higher than that of the non-annealed one, more specifically, the sensitivity as calculated from the slope of the lines is found to be 62.879 nm/RIU, compared to 33.291 nm/RIU for the non-annealed platform. The higher sensitivity of the annealed samples, in spite of the

broad size distribution of nano-islands shown in the SEM image (Figure 6.7(b)), can be explained by their sensibly larger surface area than that of particles and aggregates. The large surface area allows the binding of a larger number of molecules (linkers and biomolecules) to gold resulting in a high sensitivity.

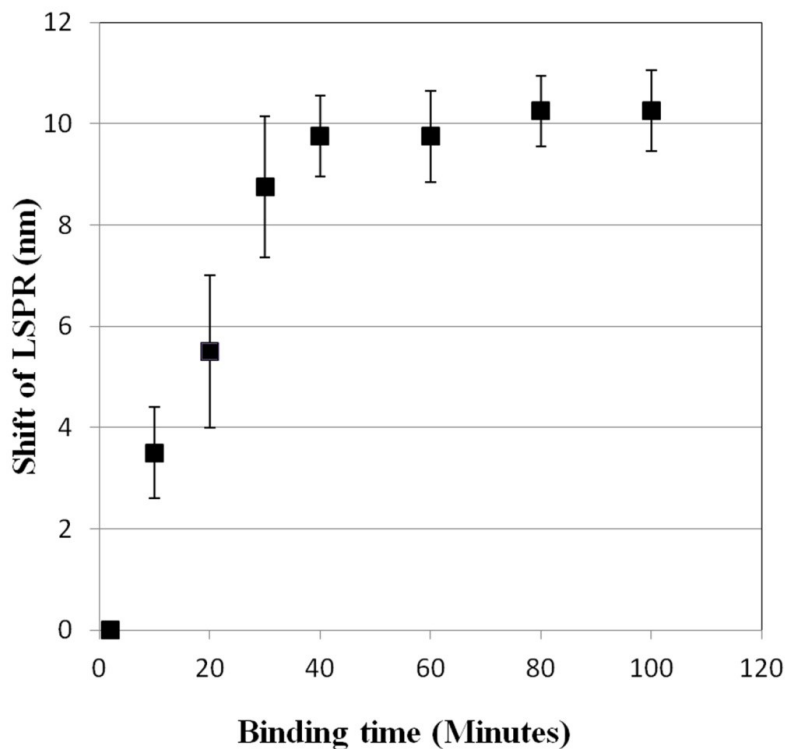


**Figure 6.10** The shift of LSPR band over the binding time of the antibody (100 ng/ml) and antigen (40 ng/ml). (Error bar represents the standard deviation of 4 measurements).

The binding kinetics of antigen-antibody interaction was investigated by using the annealed gold nanostructures. The antibody and antigen were immobilized on the sample as explained in section 6.4. The binding time as function of shift of LSPR peak is investigated in this study. Figure 6.10 shows the experimental results carried out on 4 samples for various time intervals show that around 30 to 40 minutes are

required to complete the antigen-antibody interaction. After 40 minutes, the shift of LSPR peak remained constant.

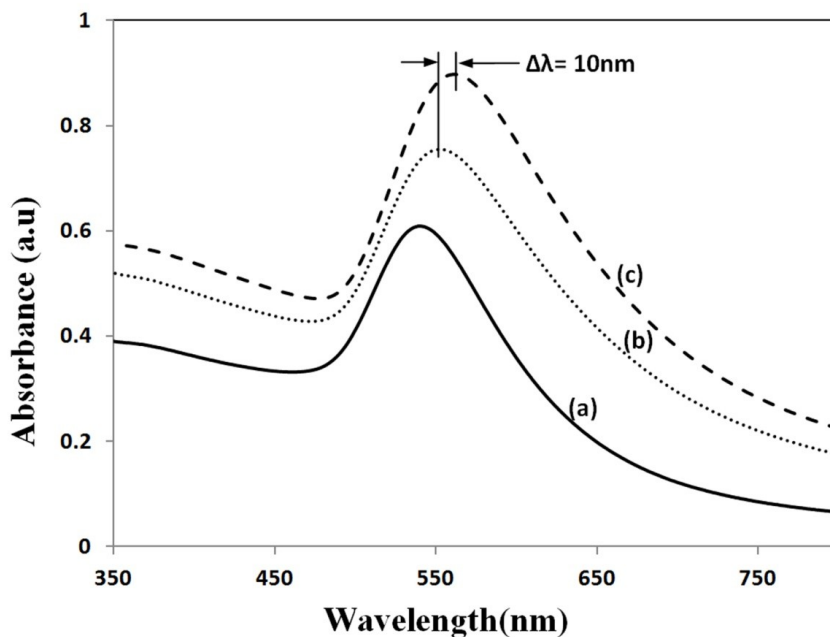


**Figure 6.11** Spectra corresponding to a concentration of 40 ng/mL bST (antigen). Annealed gold nanostructure (550<sup>0</sup>C) (a), antibody was adsorbed on the sample (b) and the antigen was adsorbed on the gold holding the antibody. The shift due to antibody-antigen interaction is 10 nm. For clarity, the spectra corresponding to different intermediate states (functionalized gold nanoparticles, activated carboxyl group, etc.) are omitted.

The change of LSPR spectra corresponding to each step in the biosensing procedure (Section 6.4) is shown in Figure 6.11. A shift of 10 nm was obtained when the concentration of antigen was 40 ng/ml. The same experiment was repeated for

various concentrations of the antigen. Figure 6.12 shows the shift in LSPR band versus the concentration of the antigen. It can be seen that there is quite a large red shift of the band due to the antibody-antigen recognition event. For the sensing experiments, only the most concentrated (45 $\mu$ g/ml) gold solution was used, which resulted in high density nano-island samples. Sensing experiments have been performed with concentrations of antigen in the range of 5 to 1000 ng/mL and a calibration curve was established. The calibration curve (Figure 6.12) shows that the shift of AuLSPR band ( $\Delta\lambda$ ) is proportional to the concentration in the range of 1-150 ng/mL (with 0.2 nm/ng/mL sensitivity). At higher concentrations, the shift is still linear but the sensitivity is considerably lower. However, for practical purposes, the low concentrations range (high sensitivity) is important. The detection limit for bST, by using a nano-island film was found to be 5 ng/mL.

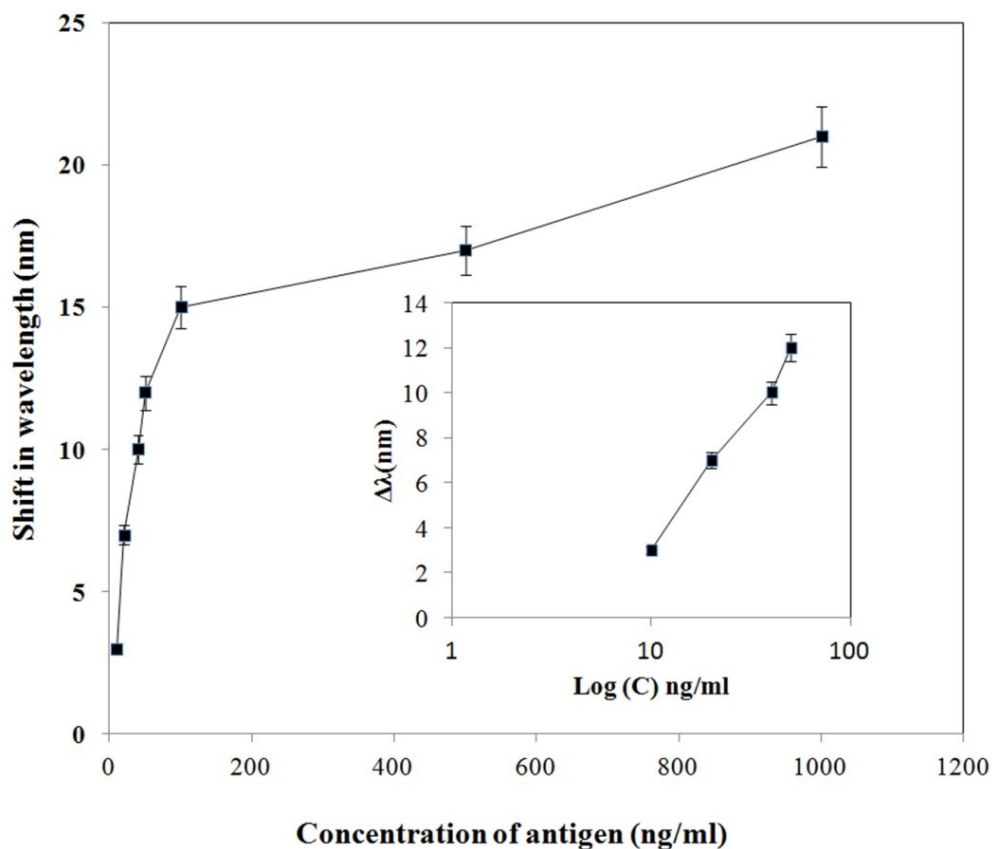


**Figure 6.12** Sensing curve: Shift in the wavelength ( $\Delta\lambda$ ) versus antigen concentration (Inset: the sensitivity for low concentration of polypeptides (between 1 and 100 ng/ml.)) (Error bars represent the standard deviation of 10 measurements).

## 6.7 Sensing experiments in a microfluidic device

The microfluidic device was used instead of the cuvette in the spectrophotometer for the sensing experiments carried out in the device. A similar device, without nanoparticles was used as reference cell for the measurement. In this setup (Figure 6.13), the light beam from a UV-Visible source is split into two parallel beams and

the sensing and the reference devices were placed vertically in the light paths. The sensing procedure as explained in section 6.4 was repeated with the device, and all the sensing steps were carried out by pumping the solutions into the microfluidic channel by using the syringe pump.

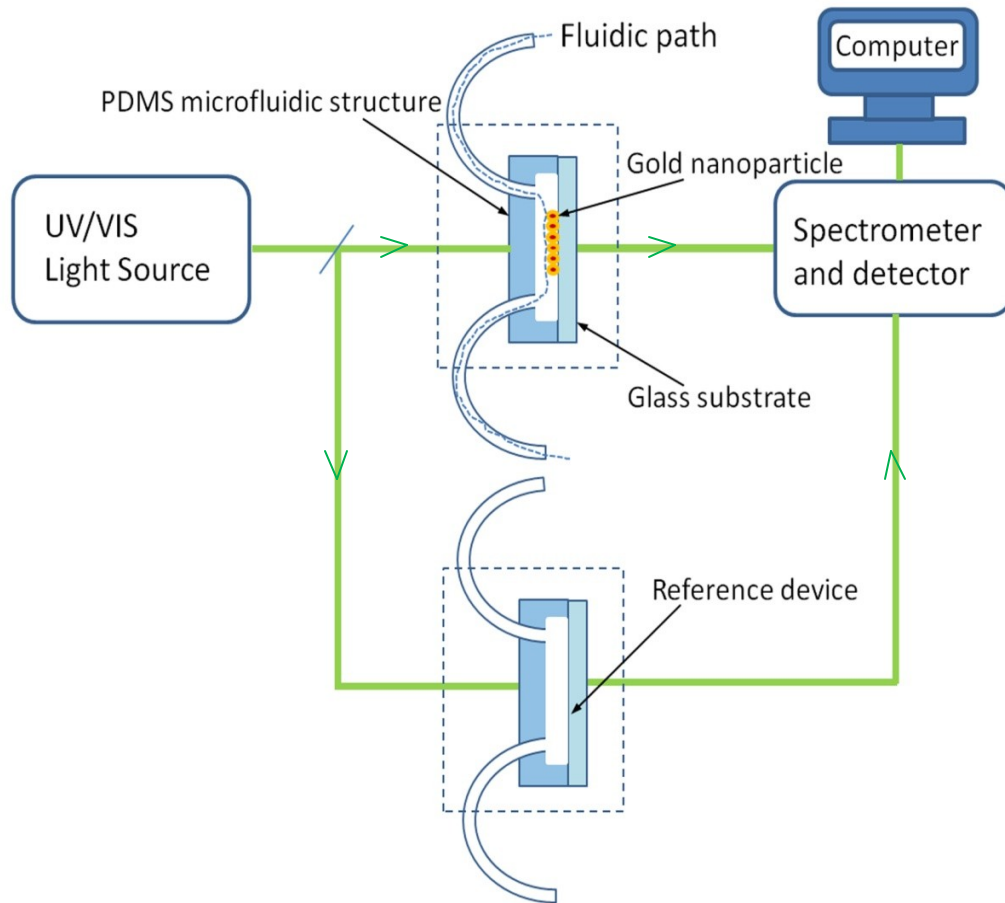


**Figure 6.13** Experimental setup of PDMS/ glass nano- integrated micro bio-sensor.

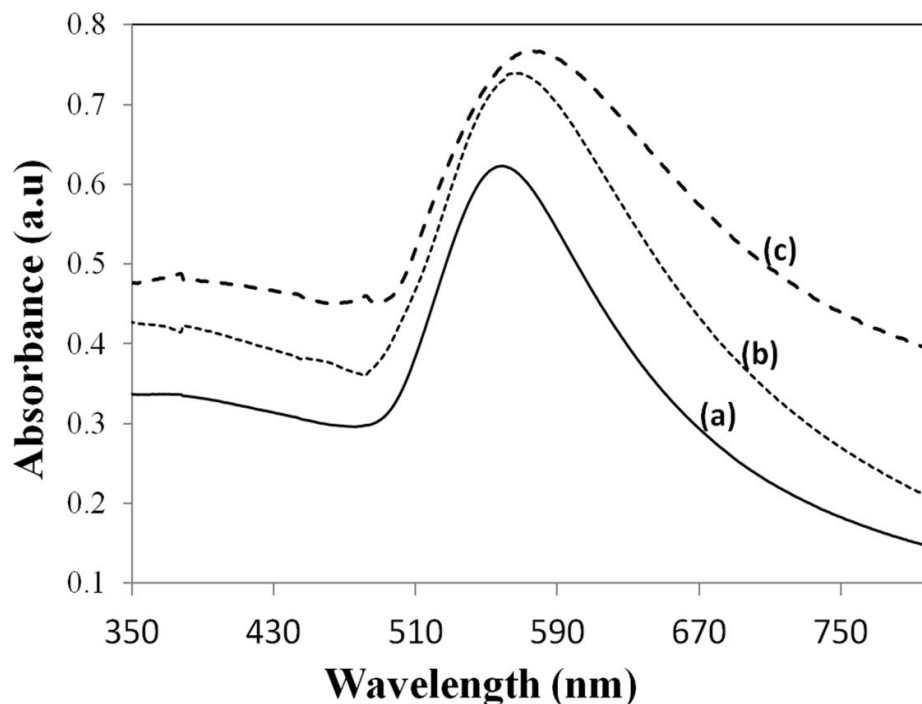


**Figure 6.14** Sensing results in the device.

The absorbance spectra were recorded with the microfluidic device (Figure 6.14). The curve (a) in Figure 6.14 shows the Au LSPR band before starting the sensing experiment. The Au-LSPR band was recorded (Figure 6.14(b)) after absorbing the antibody of bST on the functionalized nanoparticles through pumping the solution in the microfluidic channel. The curve (c) in the Figure 6.12 shows the LSPR band upon introducing the corresponding antigen. A shift of LSPR band of around 10 nm is recorded upon the interaction of the antigen (40 ng/ml) and antibody (100 ng/ml). The shift of LSPR band is the same as the sensing results obtained on the glass sample (Figure 6.11). Several experiments (3-4 measurements) were carried out in the device and they confirmed the reproducibility of the method (Figure 6.15). The sensing

curve of gold nano-island structure on glass samples (Figure 6.12) is also included in the Figure 6.15 for comparison.

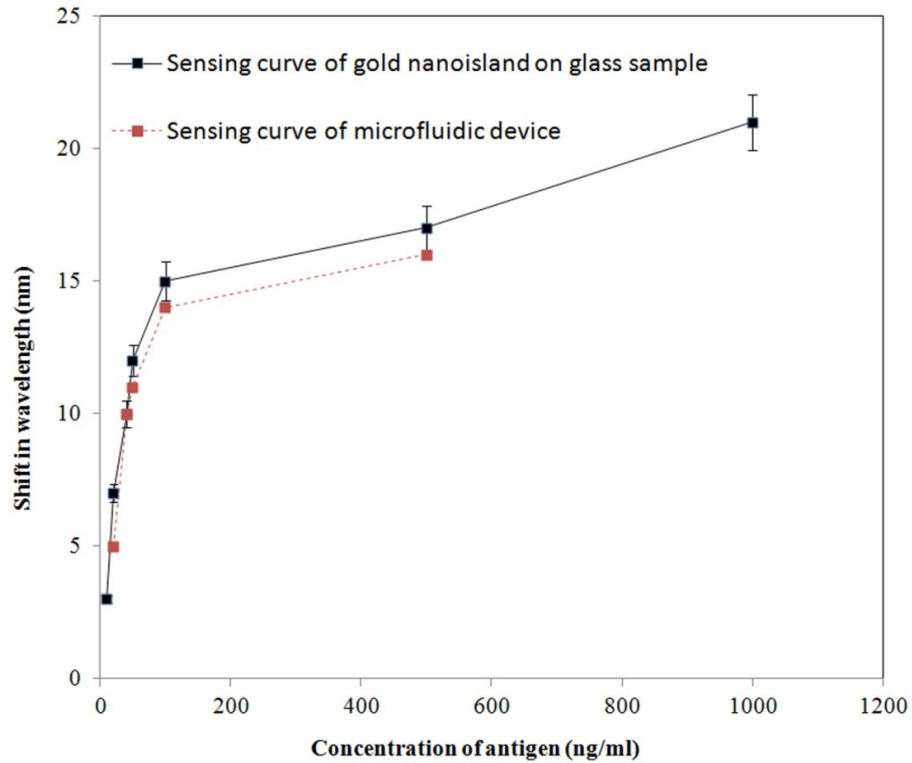


**Figure 6.15** Sensing result in the microfluidic device.

## 6.8 Conclusions

A novel and simple method of preparation of multilayers of gold nanoparticles on glass substrates is reported. The nanostructure obtained from the angled deposition method shows chain-shaped structures with a broad UV-visible absorption spectrum. The morphology of the non-annealed structures was modified to an island-like structure by annealing at various temperatures. The sensitivity of both, non-annealed and annealed platforms was investigated by using solvents with known refractive

indices. The sensing results showed a higher sensitivity for the annealed samples. The annealed platform was used for the sensing of bovine somatotropin (bST) by using an immunoassay format. The proposed sensing platform showed a detection limit as low as 5 ng/ml of bST. Further, the sensing platform was integrated into a microfluidic device and sensing experiments were carried out. The results demonstrated the suitability of nano-island structures, integrated into a lab-on-a-chip device to detect bovine somatotropin with a good sensitivity.

## **Chapter 7: Silver-polydimethylsiloxane nanocomposite integrated lab-on-a-chip for plasmonic detection of bovine growth hormone**

### **7.1 Introduction**

The localized surface plasmon resonance (LSPR) property of metallic nanoparticles has been widely used as a label-free technique for the detection of binding events in real time [122, 144]. The sensing mechanism of LSPR-based methods is the change in the position and/or the intensity of the LSPR band, upon the change of the refractive index of the surrounding medium. Silver and gold nanoparticles exhibit strong absorption bands in the visible and near infrared regions and show a strong dependence on the refractive index of the surrounding medium, thereby they are highly useful for the plasmonic detection of biomolecules.

One of the main fabrication process steps of LSPR-based sensing is the immobilization of nanoparticles on a substrate [164]. Subsequently the biomolecules are attached to the nanoparticles through various linkers and detected by monitoring the changes in the LSPR band by using an optical setup consisting of UV-Visible source and spectrometer. Several techniques such as nanosphere lithography (NSL) [124, 125], vapor deposition [165], thermal evaporation [123] and electrochemical deposition [166] are reported for the immobilization of nanoparticles on various substrates. Using NSL, ordered nanostructures can be deposited with the help of self assembled polystyrene spheres and vacuum deposition. A widely reported method of fabrication of nano-island structure is the deposition of thin film of gold on the substrate by vacuum deposition and annealing to yield nano-island morphology. In

this case, the melting temperature of the thin gold film is highly reduced from that of bulk and hence the gold layer melts even at very lower temperatures, typically around 500<sup>0</sup>C, thereby forming nano-island structures [167]. Fabrication of gold aggregates or three dimensionally assembled gold nanostructures was reported by convective self assembly by evaporating meniscus of aqueous suspension [91]. In the convective assembly, colloidal suspensions are driven and deposited to the substrate which is immersed in the solution when the aqueous solution is evaporated.

In order to adopt the fabrication methods discussed above for the biosensing applications in a lab-on-a-chip, they must possess qualities such as good adhesion to the substrates, good optical properties such as narrow absorption peak, feasibility of modifying the structural and optical properties for different applications and feasibilities of integrating them in a microfluidic environment. The direct thermal evaporation and convective assembly are the two commonly used techniques for the fabrication of LSPR based assays. However, the adhesion of the deposited layer is poor [168]. Since the bioassays involve several surface functionalization steps, the nanoparticles must be strongly adsorbed onto the substrates, otherwise, the subsequent measurements would result in errors. In this context, it is highly desirable to develop alternatives for the LSPR based sensing. The polymer-NP nanocomposites [90, 128] offers good solution to adhesion issues, in which, nanoparticles are embedded in the surface of the polymer through the reduction [128] reaction induced at the interface of the aqueous solution of corresponding metal salts and the polymer. Since the nanoparticles are embedded to the surface layer through the electrochemical

reaction, the adhesion of the particle with the substrate is much stronger than other deposition processes.

Recently, the integration of nanoparticles in microfluidic devices [169] has attracted significant attentions because it facilitates the fabrication of highly sensitive sensing platforms in a compact form. Microfluidic chip based bioassays has many benefits including consumption of low sample volumes, fast response and the feasibilities of developing high throughput detection systems in portable formats. Silicon, glass and polymeric material such as PDMS are the commonly used structural material for microfluidic chips. The PDMS is an excellent material used for the fabrication of microfluidics and optical devices. The PDMS has several advantages, such as, it is easy to prepare for the fabrication of high-aspect ratio 3D microfluidic structures by using soft lithography, it is easy to bond with glass or PDMS itself to provide a hermetic sealing of the microfluidic channels, PDMS is biocompatible and highly transparent in UV and visible lights and most importantly, the material and fabrication cost are very low compared to conventional microfabrication processes. In addition, because of low glass transition temperature, excellent flexibility, high thermal and oxidative stability, the PDMS has been a very attractive polymer for the fabrication of nanocomposites. Gold (or silver)-PDMS nanocomposites are important functional materials with interesting potential applications such as sensors. Previously the composite materials are produced by immersing the PDMS substrate having rich curing agent contents, in the aqueous solution of corresponding metal salts. However, the absorbance spectrum of nanocomposite [128] showed a wide resonance band.

The application of silver-PDMS for the detection of antigen-antibody interaction of bovine growth hormone called bovine somatotropin (bST) is reported in this work. The silver-PDMS nanocomposite, produced by immersing the PDMS substrate in the silver nitrate aqueous solution followed by annealing to tune the morphology and optical properties, are used for the detection of bovine somatotropin (bST) through the antigen-antibody interaction.

Bovine somatotropin is a polypeptide growth hormone naturally produced by the anterior pituitary gland in mammals. The effect of bST in the production of milk was reported in 1937[2]. Later by 80's, with the emergence of the recombinant DNA technologies, the large quantities of artificial hormones are produced and used for increasing the milk productions in USA and some Asian countries [93]. Application of bST is for food production in dairy industry may potentially harm the health of animal and humankind [14]. Hence, efficient analytical methods are required to develop. Traditionally, the concentration of bST was estimated by using ELISA (enzyme-linked immunosorbent assay) [22, 25] or radioimmunoassay (RIA) [84]. ELISA provides the information of antibody in a relative form that is based on a combination of affinity and concentration. The Liquid chromatography-mass spectrometry (LC-MS) combined with electrospray ionization is a recently developed method [13, 85] which can distinguish the natural and recombinant forms of somatotropin. However, it is a complex method requiring expensive instruments. In this context, developing a low cost microfluidic biosensing platform with the capabilities of detecting growth hormones rapidly and precisely is very important.

In this work, label free sensing of bST by using the localized surface plasmon resonance (LSPR) property of silver-PDMS nanocomposite is presented. The silver-PDMS nanocomposite is synthesized by a simple and low cost process. The LSPR spectrum of the silver-PDMS nanocomposite produced by immersing the PDMS substrates in silver nitrate solution is found to have a broad spectrum [129], which is not ideal for the biosensing with high sensitivity. Hence, the morphology and the optical property of the silver-PDMS composite are tuned by annealing at various temperatures and times. The annealed silver-PDMS nanocomposite is demonstrated for the detection of antigen-antibody interaction of bST. Further, the synthesis of Ag-PDMS sensing element is carried out in microfluidic device for the realization of a lab-on-a-chip. A micro sensing wall is fabricated across an optical path realized by integrating optical fibers directly into a microfluidic device. Subsequently the micro sensing wall was integrated with silver-PDMS nanocomposite through reaction with the silver nitrate aqueous solution in the device. This sensor chip was demonstrated for the detection of antigen-antibody interaction of bovine somatotropin (bST).

## **7.2 Method**

Conventionally, plasmonic biosensing experiment is conducted with help of a spectrophotometer, in which, the samples having the nanoparticles are placed directly in the cuvette of spectrophotometer and measurements were taken. The drawbacks of this approach are that they need large amount of reagents and expensive instruments. Hence the integration of nanosensing platforms into microfluidic environment is a useful approach for developing a Lab-on-a-chip based on plasmonic technique.

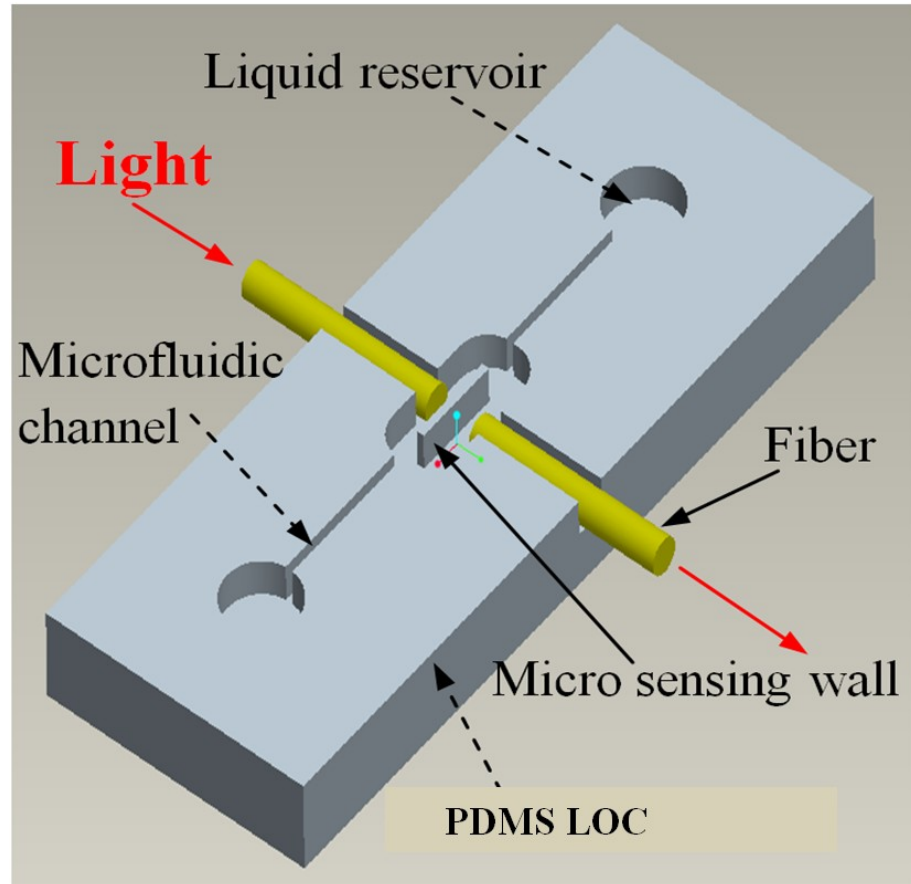


**Figure 7.1** Schematic of the proposed Lab-on-a-chip

In this work, a sensing element is integrated in a microfluidic environment across an optical path. The sensing element of Silver-PDMS nanocomposite is synthesized in a microfluidic sensing cell. A schematic illustration of the proposed Lab-on-a-chip is shown in the Figure 7.1. The device is designed to be fabricated in PDMS. The PDMS chip formed by soft lithography consists of a sensing cell, a micro wall as sensing element and two optical fibers. The optical fibers are inserted to the sensing cell and aligned with the sensing wall as shown in Figure 1. The PDMS micro sensing wall is integrated with silver-PDMS nanocomposite by in-situ synthesis with silver

nitrate aqueous solution inside the sensing cell. Light from a white light source (UV-Visible) is coupled to the sensing element through an optical fiber integrated to the PDMS structure. A fiber integrated on the other side of the sensing element collects and couples the light to a spectrometer. This optical setup is used to measure the LSPR spectrum of Ag-PDMS nanocomposite formed on the sensing element. Subsequently, all the microfluidic parts were sealed with a PDMS layer and fluidic ports were attached for pumping the bio-liquids and reagents.

### **7.3 Experimental method and results**

#### **7.3.1 Materials**

The Sylgard® 184 elastomer kit and curing agent for the PDMS fabrication were purchased from Dow Corning. The silver nitrate was purchased from Sigma Aldrich. Deionized (DI) water obtained from NANO pure ultrapure water system (Barnstead) with 18M $\Omega$  resistivity was used in all the experiments. Natural bovine somatotropine (bST, MW 20 kDa) and its corresponding antibody (Anti-bST raised in a guinea pig) were obtained from Harbor-UCLA Medical Center (National Hormone & Peptide Program). 11-mercaptoundecanoic acid in ethanol (Nano Thinks Acid 11), N,N'-diisopropylcarbodiimide and N-hydroxysuccinimide phosphate buffered saline (PBS) were obtained from Sigma Aldrich, Canada. PBS was dissolved in DI water at 0.1M concentration and 7.2 pH. The bST diluted in PBS at a concentration of 5000 ng/ml was used as stock solution and stored at 3-5<sup>0</sup>C. The anti-bST obtained in powder form was dissolved in PBS at 5000ng/ml and stored in refrigerator at 3-5<sup>0</sup>C.

### ***7.3.2 Preparation of silver-PDMS nanocomposite substrate***

The PDMS base and curing agent are mixed in 4:1 (wt) ratio. The mixture was placed in vacuum desiccators and degassed to remove the gas bubbles. The PDMS was casted onto a flat polished silicon wafer surface to prepare the PDMS substrates. Prior to the casting of PDMS, the silicon wafer was silanized by 0.1 ml of the trichlorosilane in a covered Petri dish on a hot plate at 55<sup>0</sup>C for 5 hours. The silicon wafer was placed in a petridish and the PDMS was poured on the wafer to a thickness of ~2 mm and baked at 80<sup>0</sup>C for 5 hours. Then the PDMS layer was cut into samples of 0.5×4 cm size. The silver nitrate solution of 22 mM concentration was used for the preparation of samples. The PDMS samples were incubated in the silver nitrate solution for 20 hours. The dependence of the immersion time of PDMS sample in silver nitrate solution on the optical properties of the silver-PDMS was reported in ref [129]. The optical and structural properties of the samples under different annealing conditions were investigated by using UV-visible spectrophotometer, scanning electron microscopy (SEM) and Atomic Force Microscopy (AFM).

### 7.3.3 *Tuning of morphology and optical property of the silver-PDMS nanocomposite*

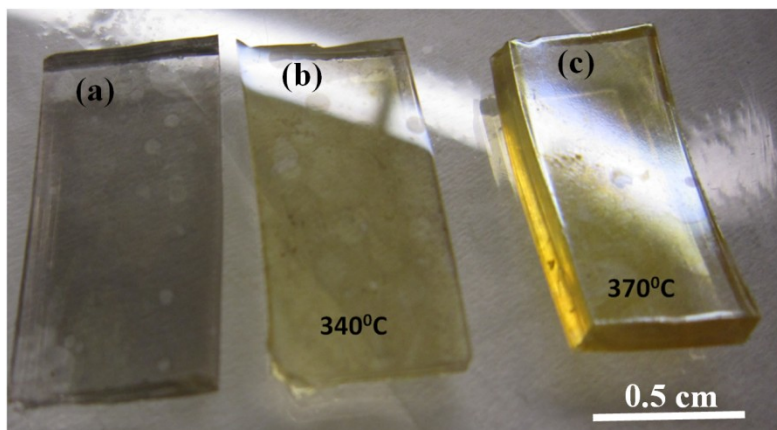


**Figure 7. 2** Images of the Ag-PDMS samples (a) non-annealed (b) annealed at 340<sup>0</sup>C (c) annealed at 370<sup>0</sup>C

Figure 7.2 (a) shows the PDMS samples after incubating in the silver nitrate solution for 20 hours. The presence of the curing agent together with the oligomers in the PDMS permits the formation of silver nanoparticle on the surface layer of the PDMS by the reduction reaction of AgNO<sub>3</sub>. The silver PDMS nanocompoiste produced in this way was found to have a dark gray color as shown in Figure 7.2(a). The sample was annealed at various temperatures to tune the morphology and optical properties. The color of the sample was turned to yellow as shown in Figure 7.2 (b) and (c) when the sample was annealed. The samples annealed above 350<sup>0</sup>C was found slightly deformed and also the color turned to a dark yellow as shown in Figure 7.2(c). The structural change of nanocomposite upon annealing was investigated using SEM.

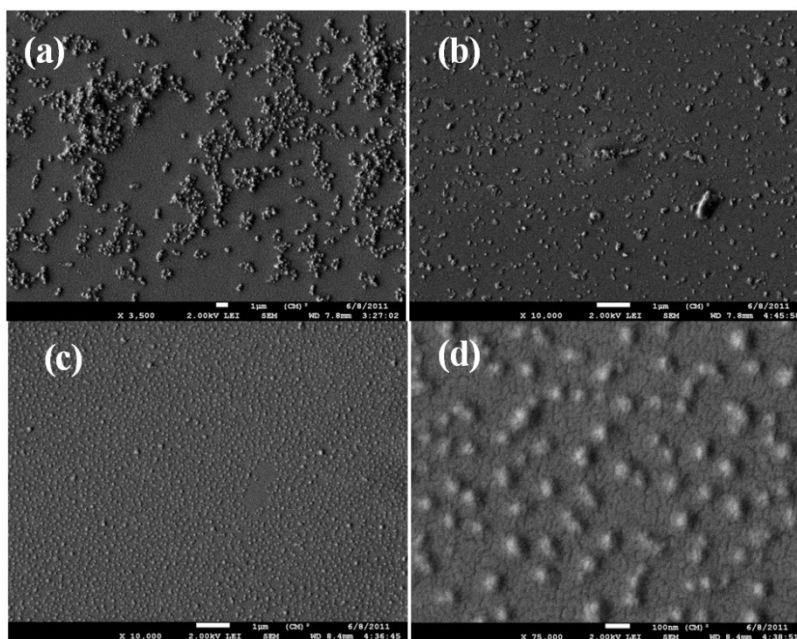


**Figure 7.3** SEM image of (a) non-annealed sample, (b) annealed at 340<sup>0</sup>C, (c) annealed at 370<sup>0</sup>C and (d) enlarged image (X75000) of sample annealed at 370<sup>0</sup>C.

The morphology of the silver-PDMS nanocomposite after incubation in silver nitrate solution for 20 hours is shown in Figure 7.3(a). A thin layer of gold of thickness ~5 nm was sputtered on the PDMS to clearly image the morphology. The surface of the composite is found to have silver NP aggregates. The morphology of the composite includes silver aggregates of size ranging from 100 nm to 1  $\mu$ m. When the substrate was annealed at temperatures in the range of 340<sup>0</sup>C to 370<sup>0</sup>C for 20 minutes, the morphology change as shown in Figure 7.3 is thought to be induced by melting of the silver aggregates and detaching from the PDMS surface. Indeed, it is known that the melting temperature of metallic nanoparticles is strongly reduced by hundreds of

degrees due to the smaller particle size. The smaller particles diffused into the surface layer and remained on the surface. When the annealing temperature was 340<sup>0</sup>C, the silver aggregates were found not completely removed as shown in Figure 7.3(b). For the complete removal of the silver aggregates, the annealing temperature was further increased to 370<sup>0</sup>C, which resulted in a surface embedded with well-ordered nanospheres having the diameter of around 30 nm as shown in Figure 7.3(c) and (d).

The preliminary sensing experiments carried out on the sample annealed at various temperatures indicated that that the samples annealed at higher temperature has less sensitivity. The sample annealed at 340<sup>0</sup>C is found to have better sensitivity. In order to investigate the dependence of temperature on the distribution of the nanoparticles on the composite and the sensitivity, the AFM characterization was also carried out.

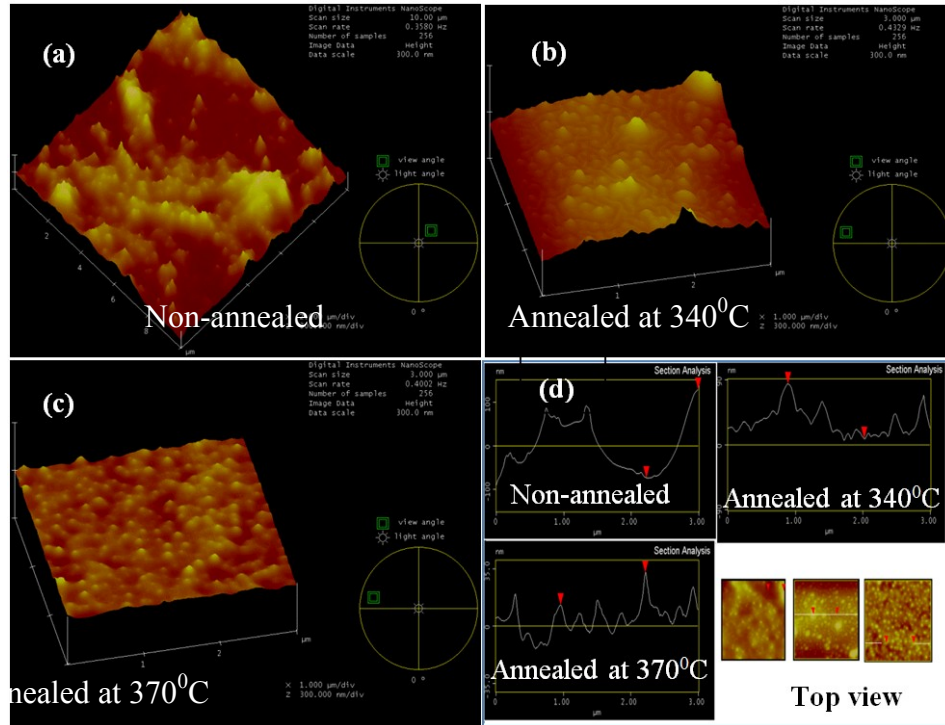


**Figure 7.4** AFM characterization of silver-PDMS nanocomposite (a) non-annealed (b) annealed at 340<sup>0</sup>C, (c) annealed at 370<sup>0</sup>C and (d) line profile showing the height of the nanoparticle in composite.

The AFM characterizations of the silver-PDMS nanocomposite shown in Figure 7.4 shows that morphological change due to annealing is similar to the one observed in the SEM micrographs (Figure 7.3). The line profile of the composite for the samples annealed at various temperatures shown in Figure 7.4(d) indicates that annealing at higher temperature results in the migration of nanoparticle deeper into the composite. The average height of the nanoparticle in the non-annealed composite was ~120 nm, and the height reduced to ~70 nm for samples annealed at 340<sup>0</sup>C. The height of NP was further reduced to ~ 20 nm for the sample annealed at 370<sup>0</sup>C. The top view of the morphology of the sample is shown in Figure 7.4(d).

The absorbance property of the nanocomposite in the UV-visible range was investigated by using the UV-Visible spectrophotometer. The spectrum of the non-annealed sample shown in Figure 5(a) has an absorbance maximum at 440 nm with a wide band. This wide band extending in the region between 370 to 650 nm, belongs to the silver aggregates. When the sample was annealed at 340<sup>0</sup>C, the band is blue shifted to 410 nm and became narrower as shown in Figure 7.5(b).

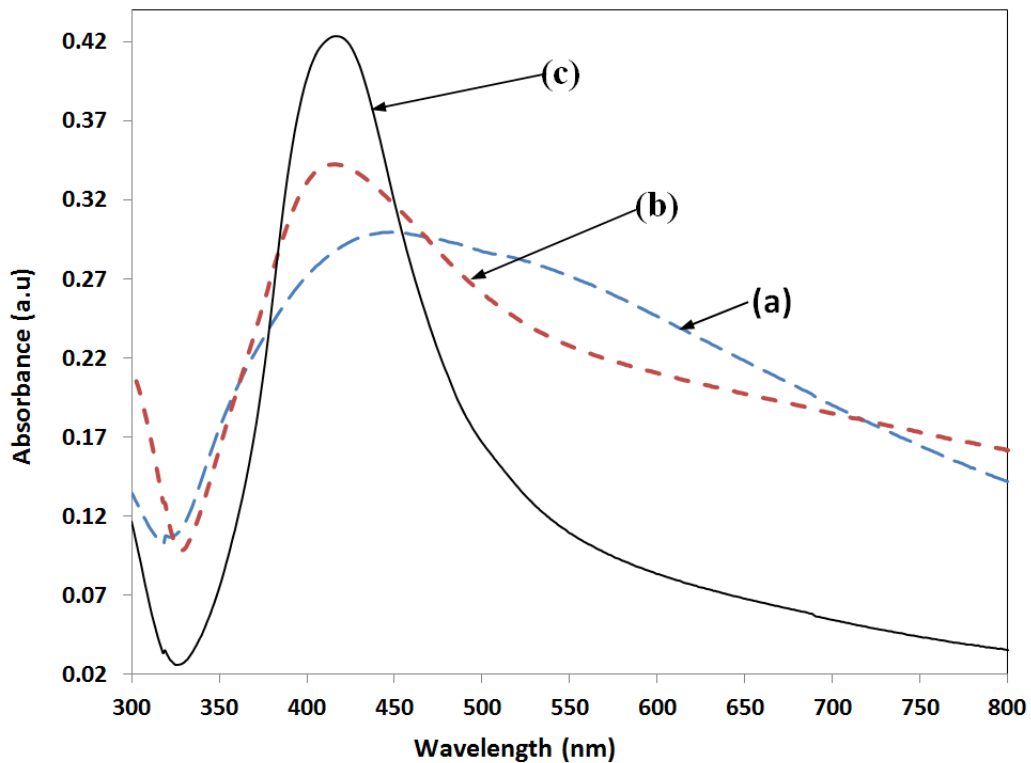


**Figure 7.5** Absorbance spectrum of the silver-PDMS nanocomposite of (a) non-annealed, (b) annealed at 340<sup>0</sup>C (c) annealed at 370<sup>0</sup>C.

The wide band of the silver aggregates is resulting from the near field coupling effects of neighboring particles in the aggregates, that is, when the distance between the particle is considerably shorter, an electrodynamic interaction mechanism is expected [170]. Upon annealing, aggregates are melting and breaking into smaller particles and also the interparticle distance is increased. As a result, the near field coupling between the particles is decreased, resulting in a blue shift of band to 412 nm. When the annealing temperature was further increased to 370<sup>0</sup>C, the band becomes considerably narrower and the absorbance intensity was considerably increased as shown in Figure 7.5 (c). For the biosensing experiments the sample having sharp resonance peak is useful, however, the annealing at higher temperatures resulted in the migration of particle to composite as revealed in the AFM characterization. Since the particle is inside the PDMS, less surface area of the particle is accessible to bind the biomolecules, which could result in less sensitivity for the sample annealed at higher temperatures.

## 7.4 Procedure for the biosensing on silver-PDMS substrate

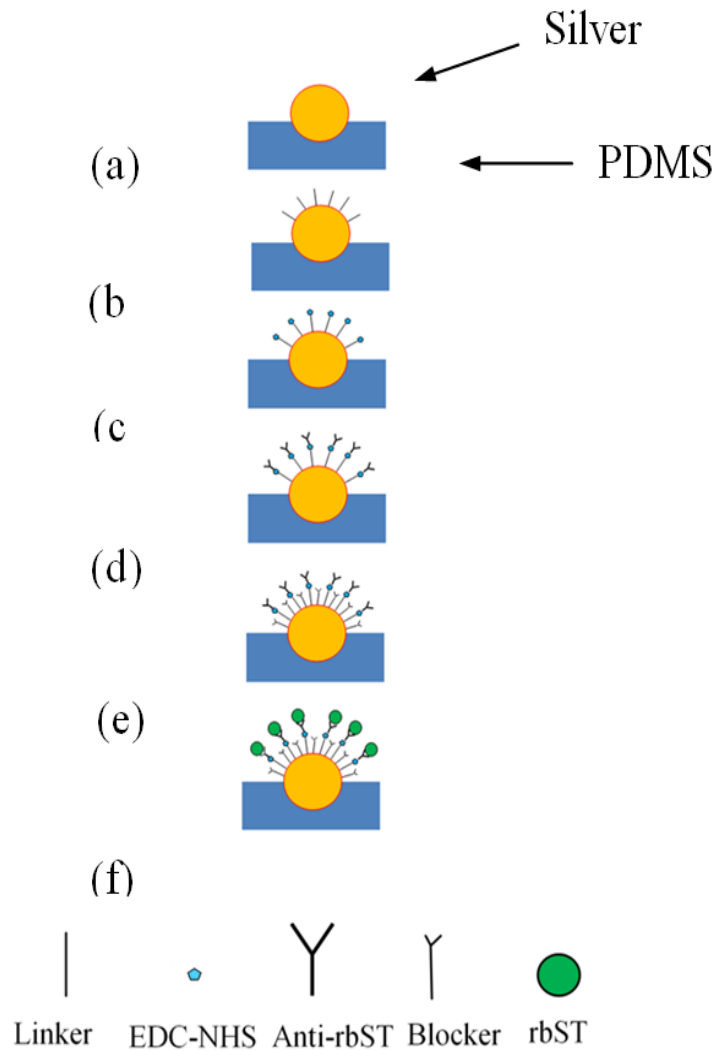


**Figure 7.6** Various steps in the biosensing.

The silver-PDMS substrate was treated with oxygen plasma for 35 seconds to transform the surface of the sample to hydrophilic. Figure 7.6 shows various steps in the biosensing by using silver-PDMS nanocomposite. The silver-PDMS substrate shown in Figure 7.6 (a) was functionalized with around 150-200  $\mu\text{L}$  of

mercaptoundecanoic acid (in ethanol) and the cross-linker (N, N'-diisopropylcarbodiimide and N-hydroxysuccinimide) for one hour in order to attach the peptides covalently to the silver nanoparticles. Figure 7.6(C) shows the Ag-PDMD sample after introducing the linker and cross-linker. The sample was washed in PBS. The linker and cross linker attach the antibody of the bST covalently with the silver NP. Then, the antibody corresponding to the bST was introduced onto the sensing platform and kept in contact with silver NP for at least one hour. The change of LSPR corresponding to the binding of antibody was measure by UV-Visible spectrophotometer (LAMBDA 650, Perkin Elmer). The concentration of antibody on the functionalized silver-PDMS was kept constant and the concentration of antigen was varied between 5 and 10000 ng/mL. The excess antibody is washed away with PBS (Phosphate Buffered Saline) solution. Figure 7.6(d) shows the sample after antibody is absorbed. Blocker (1% non-fat milk powder in PBS solution) is passed and washed with PBS. Figure 7.6(e) represents the sample after the blocker is introduced. The proteins in the milk powder solution bind to areas not covered by antibody and hence act as a blocker. Then bST solution is introduced to the sample and kept for one hour. The sample after absorbing the bST on the sample is as shown in Figure 7.6(f). The LSPR spectra were recorded to monitor the change in LSPR corresponding to the antigen-antibody interaction.

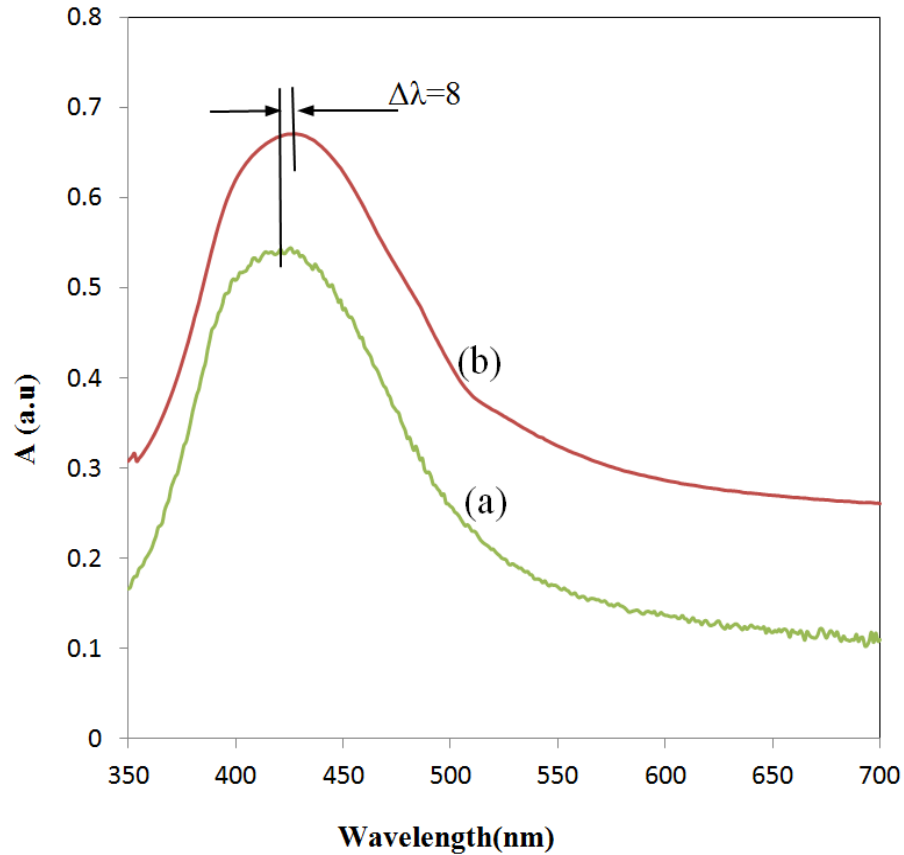


**Figure 7.7** Shift of LSPR spectra of silver-PDMS upon antigen-antibody interaction, (a) LSPR spectrum of the silver-PDMS nanocomposite functionalized with antibody (100 ng/ml) and (b) LSPR spectrum of the composite after adding antigen (150 ng/ml).

The samples annealed at 340<sup>0</sup>C and 370<sup>0</sup>C were tested for the biosensing experiments. During the sensing process, the LSPR spectrum of the silver-PDMS nanocomposite was recorded during each step of biosensing. The anti-bST (100 ng/ml concentration) was added to the surface functionalized silver-PDMS nanocomposite. Figure 7.7(a) shows the absorbance spectrum of the Ag-PDMS sample after adding the anti-bST. The antigen (bST, 100 ng/ml) was added to the sample and kept for one

hour, which resulted in a red shift of 8 nm as shown in Figure 7(b). In addition, the band width is found to become wider. The experiments were repeated with various concentration of antigen in order to assess the sensitivity of the platform as shown in Figure 7.8.

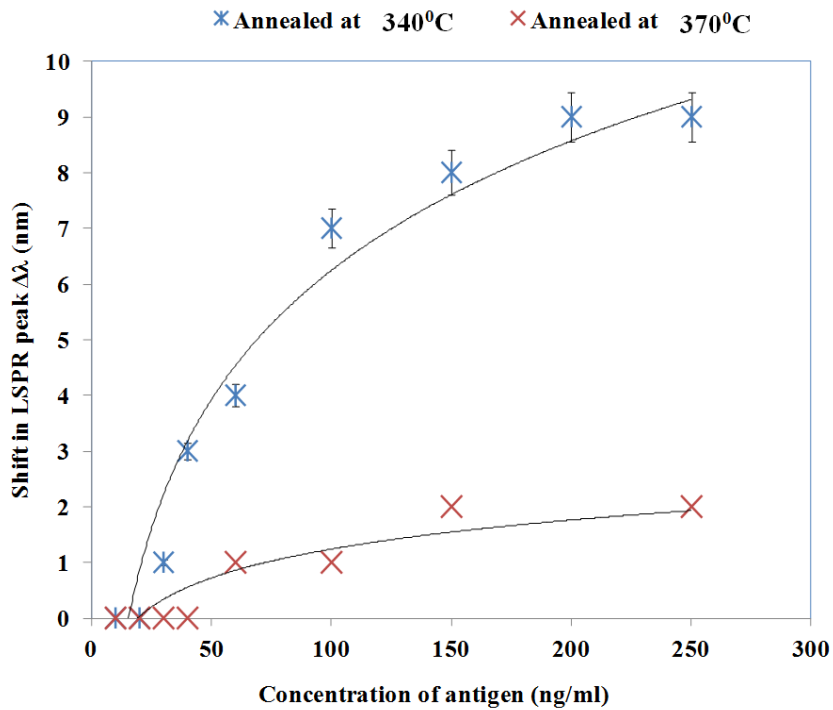


**Figure 7.8** Effect of annealing temperature and concentration of bST on biosensing with Ag-PDMS substrate.

The tested variation of the shift in LSPR band against the concentrations of antigen shown in Figure 7.8 shows almost a linear shift in the range of 50 to 100 ng/ml concentration for the samples annealed at 340°C. In order to investigate the reproducibility of the results, the sensing experiments were conducted on 5 samples

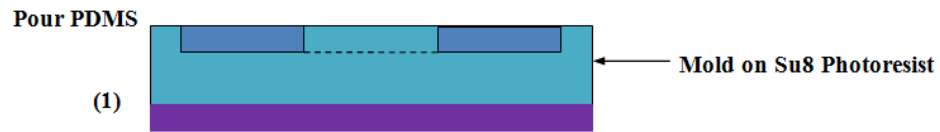
for each concentration. An error bar representing a standard deviation is included in Figure 7.8. The detection limit of the silver-PDMS nanocomposites annealed at 340<sup>0</sup>C was found to be as low as 20 ng/ml.

The sensing experiments conducted on the sample annealed at 370<sup>0</sup>C or above showed less sensitivity as shown in Figure 7.8. Only one or two nanometer of shift is observed for the concentration of 200 to 500 ng/ml of antigen. The reason for the reduction in sensitivity for the samples annealed at higher temperature is due to migration of particles into the substrate. The AFM characterization presented in Figure 4 revealed that the annealing of sample at higher temperature causes the migration of particle deeper into the PDMS, which essentially make the particles less accessible for the binding of bio-molecules resulting in reduced sensitivity.

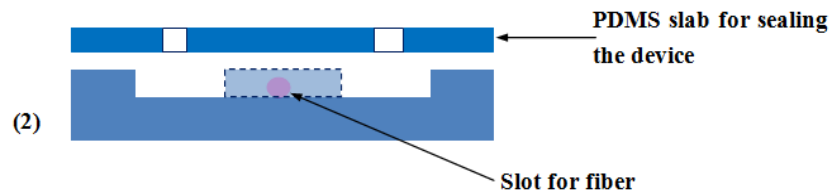
## **7.5 Fabrication of Lab-on-a-chip**

The lab-on-a-chip is realized by in-situ synthesis of silver-PDMS nanocomposite in a microfluidic channel. Different process steps involved in the fabrication of the lab-on-a-chip are shown in Figure 7.9.

1. Fabrication microfluidic device on PDMS by soft lithography



2. Bonding of the PDMS device and integration of fibers



3. In situ synthesis of silver-PDMS nanocomposite in the microfluidic device by injecting silver nitrate into the device.

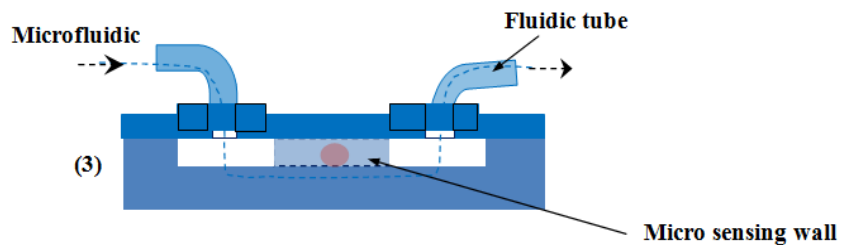
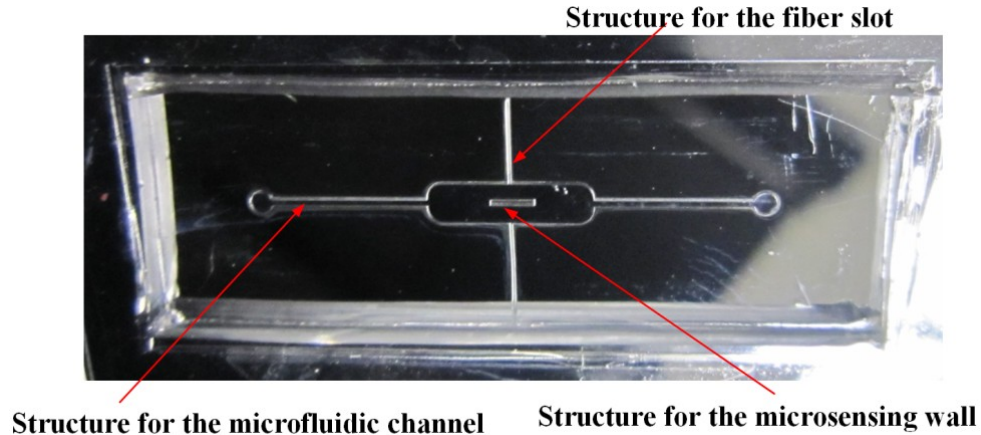


Figure 7.9 Fabrication process steps of the lab-on-a-chip.

The first step in the fabrication of lab-on-a-chip is the making of mold for casting the PDMS chip. The soft lithography is used for fabricating the PDMS chip. The mold fabricated in SU-8 photoresist on a silicon substrate shown in Figure 7.10 was used for casting the PDMS chips. The mold was fabricated by UV-photolithography. The SU8 negative photoresist (SU8 2035 Microchem) was spun on the silicon wafer at

2000 rpm for 30 seconds, which resulted in an SU8 layer with thickness of 60-70  $\mu\text{m}$ . Then the photoresist was baked at 80<sup>0</sup>C for 10 minutes. Since the diameter of the fiber used to couple the light to the microfluidic channel is 125 $\mu\text{m}$  (core diameter 9 $\mu\text{m}$ ), the depth of the slot for inserting the fiber must be  $\sim$ 125  $\mu\text{m}$ . As the thickness of the photoresist layer decides the depth of the channel, the photoresist was spun again at 2000 rpm for 30 seconds to yield a thickness of  $\sim$ 125  $\mu\text{m}$ . The resist was baked again at 80<sup>0</sup>C for 10 minutes. The photo resist was exposed by UV light for 30 seconds through a mask. The UV-exposed photoresist layer was baked at 80<sup>0</sup>C for 10 minutes and developed in SU8 developer for about 15 minutes. The fabricated mold shown in Figure 10 was silanised for 8 hours before casting the PDMS on it.



**Figure 7.10** Mold for the microfluidic device

The PDMS microfluidic chip shown in Figure 7.1 was fabricated by soft lithography. The PDMS base and curing agents are mixed as explained in Section 3.2 and casted to the mold as shown in the step 1 of Figure 7.9.

A thin PDMS slab of 2 mm thickness was bonded with the chip as shown in Figure 7.9 (step-2). Two holes of diameter of 1 mm were punched on the PDMS layer corresponding to the place of liquid reservoirs in the microfluidic chip to insert the inlet and outlet tubes of the lab-on-a-chip. The thin PDMS slab and the PDMS microfluidic chip were exposed to the oxygen plasma for 35 seconds to seal the device. The plasma exposure is carried out in the instrument obtained from Harrick plasma. Then the samples were immediately kept in contact in order to yield a strong leak proof bond. The fluidic tubes were inserted to the holes of the sealing layer of the device as shown in Figure 7.9 (step-3). Two single mode pigtailed fibers with SMA connectors were inserted to the slots of the fibers with the help of micropositioners. The fabricated lab-on-a-chip is shown in Figure 7.11.

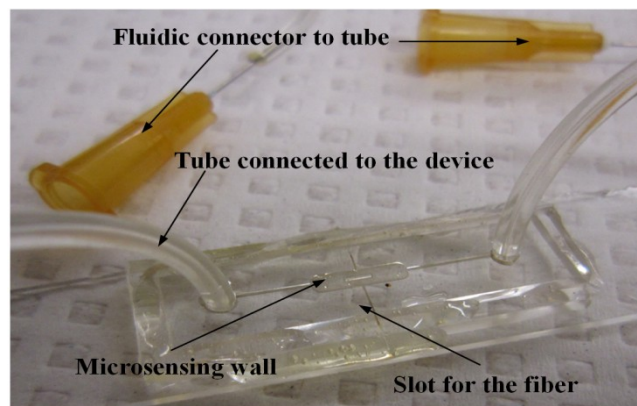


**Figure 7.11** Silver-PDMS nanocomposite integrated lab-on-a-chip

## **7.6 Integration of silver-PDMS nanocomposite into a LOC environment**

A schematic sketch of the experimental setup for the silver-PDMS nanocomposite integrated LOC is shown in Figure 7.12. Light from a UV-visible source is coupled to the device through the fiber integrated with the device. Another fiber integrated on the other side of the micro sensing wall couples the light to a spectrometer as shown in Figure 7.12. A closer view of the lab-on-a-chip fabricated on PDMS is shown in Figure 7.13(a). The experimental setup used for the lab-on-a-chip shown in Figure 7.13(c) includes a UV-visible source and a spectrometer (USB 2000 Ocean Optics). Two single mode pigtailed fibers are integrated to the device and each is connected to the light source and the spectrometer as shown in Figure 7.13(c). For integrating the fiber to the device, two high precision micropositioners were used. The spectrometer was connected to a computer in order to record the spectra. The UV-visible spectrum of the device is recorded by the spectrometer as a reference signal for the subsequent measurement. Then, the silver nitrate solution was pumped to the device and kept for 20 hours. Subsequently, the device was cleaned by pumping DI water through the LOC for 2 minutes. The UV-visible spectrum recorded from the device is similar to the one of the Ag-PDMS substrate (Figure 7.5). The fiber and fluidic tubes were removed and the device was kept in an oven and annealed at 340<sup>0</sup>C for 30 minutes. The bonding of the device was found unaffected by the annealing. Then the fibers were inserted to the slot and fluidic tubes were connected and sealed. The absorbance spectrum was recorded again as shown in Figure 14. The spectrum 7.14 (a) and (b) show the UV-visible absorbance spectrum for the silver-PDMS nanocomposite integrated in the LOC before and after annealing, respectively. The spectra recorded

before and after annealing are similar to that of spectra obtained for Ag-PDMS substrate presented in Figure 7.5. After annealing, the spectrum was blue shifted to around 410 nm and also became narrower as shown in Figure 7.14.

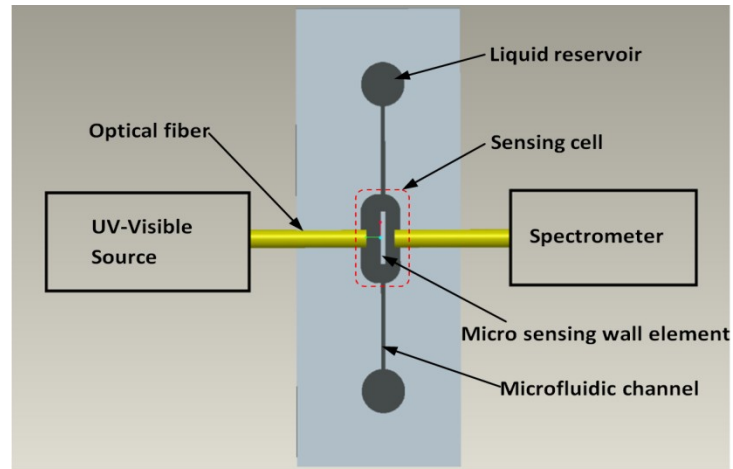


**Figure 7.12** schematic top view of the test arrangement with UV-visible source and spectrometer.

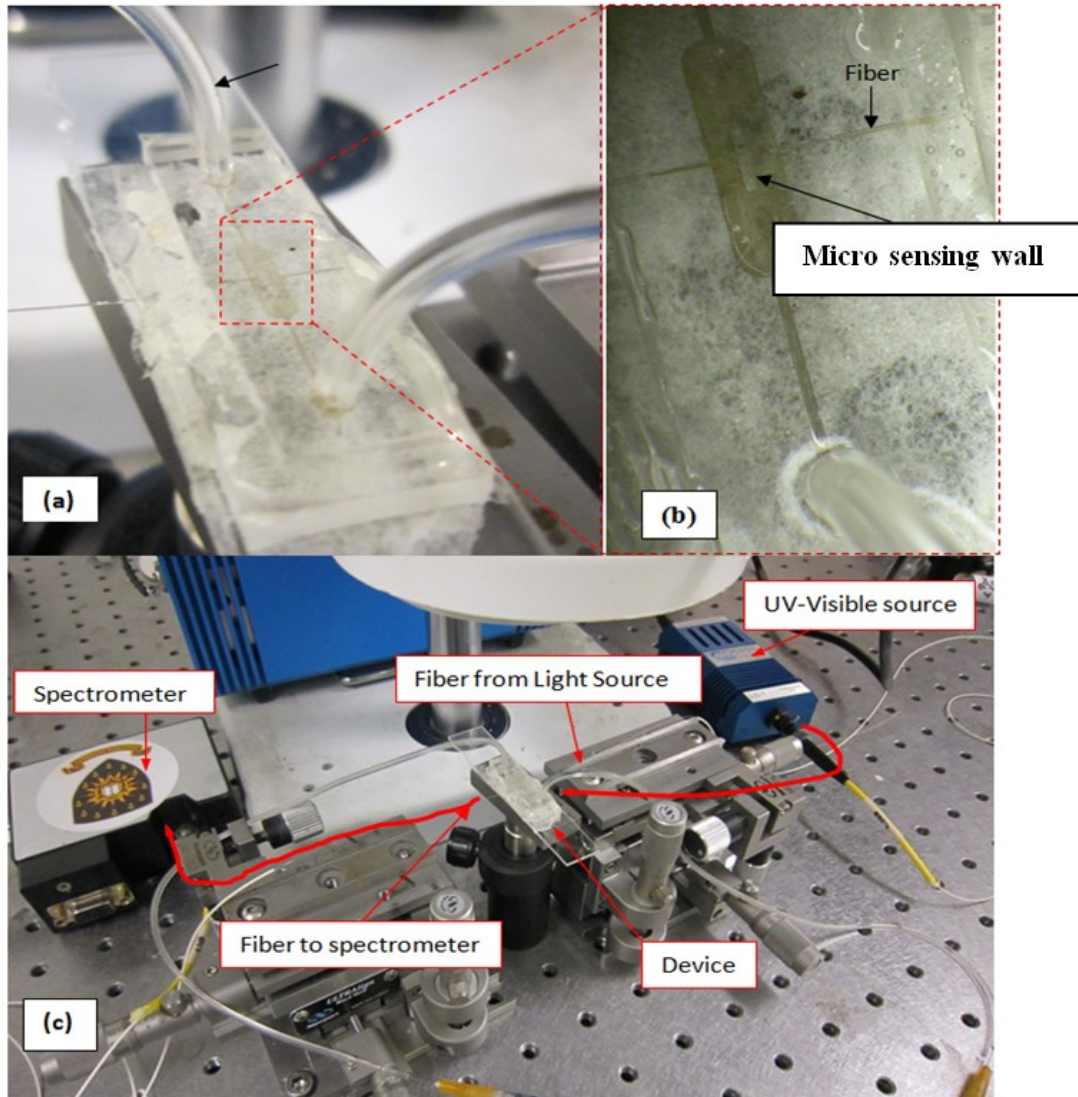


**Figure 7.13** (a) Device under test (b) closer view of the test section of the device through microscope (c) Experimental setup for the Lab-on-a-chip.

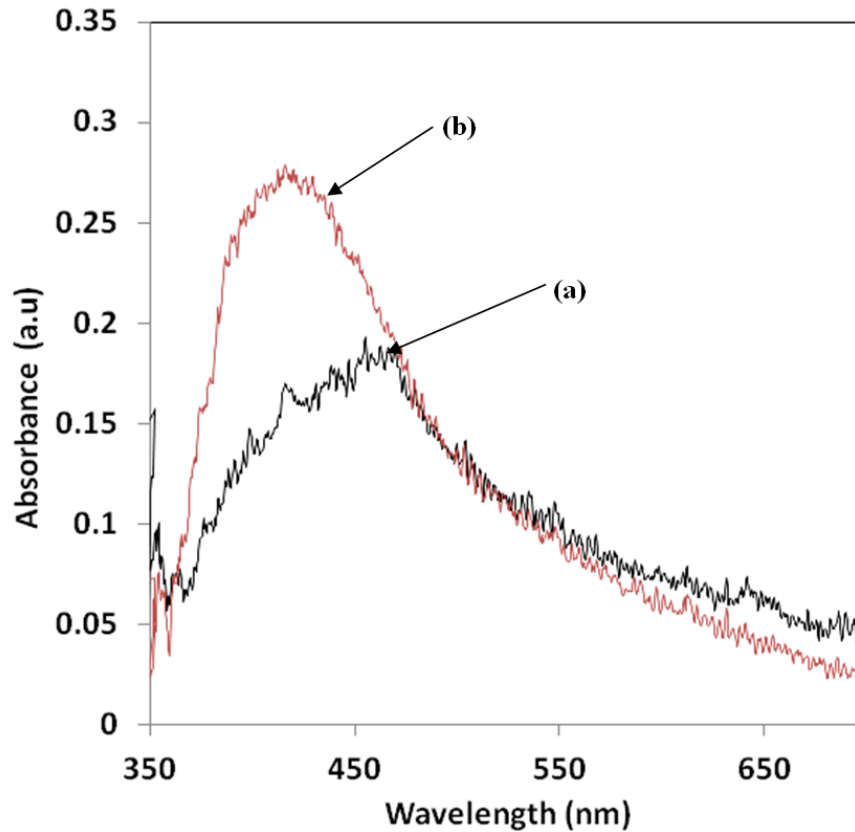


**Figure 7.14** UV-Visible spectra recorded using the lab-on-a-chip, (a) Spectrum recorded before annealing the device and (b) Spectrum recorded after annealing the device.

## 7.7 Biosensing in the Lab-on-a-chip

The sensing procedure explained in the Section 7.4 was repeated in the device by pumping all the reagents. The absorbance spectrum was recorded after pumping the antigen and keeping antibody for one hour as shown in Figure 7.15(a). The spectrum recorded after adding the antigen shows a shift in wavelength of around 12 nm in the LSPR spectrum as shown in Figure 7.15(b). The shift of LSPR peak obtained for the

experiments on the substrate is closely matching with the shift obtained on the LOC device. Few experiments repeated on the LOC platform confirm that an LOC can be realized with the silver-PDMS nanocomposite by preserving the sensitivity obtained on the Ag-PDMD substrate. Shift obtained using the LOC device is 12 nm for the concentration of 100 ng/ml as compared to the shift of 8 nm obtained using the Ag-PDMS substrate for the same concentration of 100 ng/ml of antigen. This proves that LOC is having higher sensitivity in addition to high throughput.

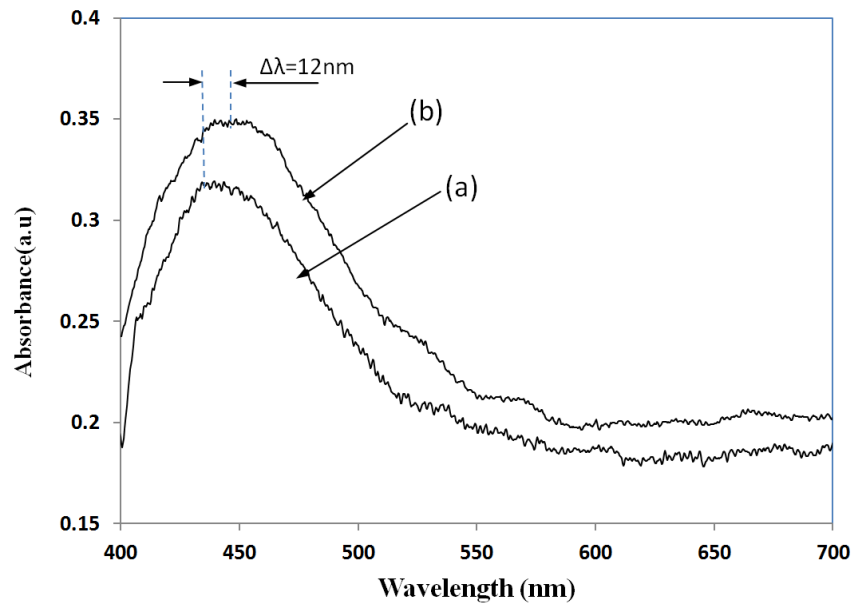


**Figure 7.15** The sensing results conducted in the lab-on-a-chip, (a) spectrum recorded after adding the antibody (100ng/ml) and (b) spectrum after adding the antigen (100ng/ml).

For the sensing experiments in the LOC, very small amounts of reagents and biomaterial are used. For each steps in the biosensing, less than 0.1 ml of solution was

sufficient to carry out the sensing experiments in the LOC, however, for the experiments in the substrate requires around one ml of reagents for each steps of the biosensing.

## **7.8 Conclusions**

The feasibility of integration of silver-PDMS nanocomposite into a microfluidic device for the detection of antigen-antibody interaction of bovine growth hormone is demonstrated. The silver-PDMS nanocomposite produced by immersing the PDMS slabs containing rich curing agent in silver nitrate aqueous solution exhibits aggregation of silver particle on the surface with a wide UV-visible absorbance band. The morphology of Ag-PDMS nanocomposite was tuned to achieve the desired narrow absorbance band by annealing at various temperatures. The annealing resulted in a uniformly embedded silver particle on the surface of the PDMS substrate. The samples annealed at temperatures higher than 350<sup>0</sup>C was found to be less sensitive for the biosensing experiments. Annealing at higher temperatures forces the migration of particle deeper into the substrate, which could be the reason for the reduction in sensitivity. Subsequently, a silver-PDMS nanocomposite integrated lab-on-a-chip is fabricated and the performance is tested as well. Ag-PDMS nanocomposite integrated LOC resulted in a higher sensitivity compared to the measurements obtained on Ag-PDMS nanocomposite substrate. LOC showed a LSPR shift of 12 nm compared to 8 nm for substrate. The consumption of bio-liquids and reagents for the LOC is 10 times lesser than that of the Ag-PDMS substrate, is also a benefit of carrying out the detection in the lab-on-a-chip.

## **Chapter 8: Nano-islands integrated evanescence-based lab-on-a-chip on silica-on-silicon and PDMS hybrid platform for the detection of recombinant growth hormone**

### **8.1 Introduction**

Bovine growth hormone, also known as bovine somatotropin (bST) is a growth promoter widely used in some countries in dairy farming for increasing the production of milk and meat. With the injection of hormone to animals, the milk production has been reported to be increased more than 5% to 40% [171-173]. The commercial use of growth hormone was made possible with the discovery of recombinant DNA technology which could produce large amounts of artificial growth hormone called recombinant bovine somatotropin (rbST) using hybridization technique. The use of rbST in dairy farming is still controversial due to its potential effects on the health of cattle and consumers [14, 16, 82]. Therefore, a rapid and precise method of detection of rbST has a lot of demand for regulation.

The enzyme-linked immunosorbent assay (ELISA) [22, 23], radioimmunoassay (RIA) [24] or bioassay method [25] or SPR [26] and LSPR-based sensor [61] are reported for the detection of growth hormone. The fluorescent tagging and detection using a lab-on-a-chip platform [60] and the use of a novel cascaded waveguides coupler (CWC) on silica-on-silicon platform are also attempted. ELISA can predict the concentration of rbST in a relative form that is based on the concentration and affinity. The liquid chromatography-mass spectrometry (LC-MS) [13, 85], combined with electrospray ionization is a very powerful technique which can discriminate the

natural and artificial form of the growth hormone, however, the method is complex and expensive. In this work, a miniaturized sensor platform is developed for the detection of recombinant growth hormone. The sensor uses a label-free detection method by using the LSPR property of nano-island on silica-silicon waveguide integrated in a microfluidic device.

The optical detection is one of the most widely used methods of bio-detection [42]. Labeled [96] and label free [88, 144] detection are the two major approaches of the optical detection method. In the labeled detection, fluorescence dye molecules are tagged with biomolecules and detected in an optical microfluidics platform. Labeled detection is an expensive and time consuming process as it needs the optimization of the fluorophore-biomolecule labeling conditions, also the accuracy depends on the labeling process. As a result, label-free detection has gained increased attention in the biomedical field. The label-free detection methods reported in literatures are autofluorescence [174], confocal Raman spectroscopy [175], surface plasmon resonance [140], localized surface plasmon resonance [88, 149] and evanescent [103, 107, 109].

The surface plasmon resonance (SPR) is a widely reported label-free detection of biological and chemical species. The SPR sensor works based on the plasmon waves produced by coupling the light to a thin layer of metal by using grating coupler or field excitation. The basic mechanism of SPR sensor is the modulation of plasmon resonance band with the adsorption of bio-species to the metal layer. Metallic nanoparticles such as gold and silver exhibit strong plasmonic property called localized surface plasmon resonance (LSPR) in the ultraviolet and visible region of

electromagnetic spectrum. The plasmonic property of the gold nanoparticle is widely reported [124, 151] for the detection of biological species as the plasmonic properties of gold NPs are sensitive to the change in the refractive index of the surrounding medium. Conventionally, the biosensors reported by using metallic nanoparticles (NP) are substrate-based [176]. In this method, the NPs are immobilized on a transparent substrate and the biomolecules are adsorbed and detected by monitoring the changes of plasmon band by using the transmission or reflection spectroscopy. The advantages of LSPR based detection over the SPR detection are that no need of any complex light coupling optics and the feasibility modifying the plasmonic property by tuning the shape and size of the nanoparticles.

Evanescent-wave is the exponentially decaying tail of the propagating wave in a waveguide, which can interact with bio-species immobilized on the waveguide. Evanescent wave sensors by using optical fibers [106] or planar waveguides [177] are reported for the labeled and label-free detection of the bio-species. For the label-free evanescent sensor, the interaction of evanescent wave with the biomolecules immobilized on the core of the waveguide results in the loss of the propagating waves due to the absorption of evanescent wave. Since the depth of penetration of evanescent wave sensor implemented by a straight waveguide having uniform diameter is less, the sensitivity is less. However, the sensitivity can be increased by increasing the species evanescent-wave interaction length. Alternatively, the sensitivity of the evanescent wave sensors were reported to be increased by techniques such as selective ray launching [108], tapering of fiber probes [109] and use of bends [110] in waveguides. In this work, a novel method of integration gold

nano-islands on silica-on-silicon waveguide is used for the development of an evanescent wave sensor integrated in a PDMS microfluidic chip.

Recently, the integration of nano-materials in the microfluidics environments has gained a lot of attentions due to the feasibilities of developing micro total analysis systems ( $\mu$ TAS) or lab-on-a-chips (LOCs) devices with higher sensitivity [57]. Lab-on-a-chips are gaining increased interest because of their capability to perform biological and chemical detections with reduced consumption of reagents and materials [44, 63]. Since the LOCs are miniaturized devices, they are portable and capable of performing the detection and analysis faster than the macroscopic instruments. By miniaturizing and integrating various process modules such as fluidics and optical detections components in a single chip, the LOCs have been able to perform different bio-analytical processes. Integration of microfluidics with optical components is one of the challenging tasks in the fabrication of optical LOCs. Also, the fabrication techniques of integration of nano-features in the microfluidic environments are gaining more attentions [57], because of the unique optical properties of nano-structure that are useful for the biosensing.

Miniaturizations of conventional SPR systems are reported for biosensing purpose [178, 179]. Some of the commercial devices such as Biacore systems are already available with the integration of SPR sensors in microfluidics, wherein a flat layer of gold is used in a Kretschmann configuration with a prism coupling of light to excite plasmon waves. However, the microfluidics based SPR system is complex and it needs complicated optics and expensive instruments. Integration of nanoparticle in the microfluidic device is a useful approach as the optical setup required for such a

sensor is simple, as compared to SPR or confocal Raman spectroscopy based sensors. However, the integration of nanoparticles in microfluidics requires novel nanofabrication techniques compatible with the microfluidic fabrication process and materials.

In this work, a miniaturized analytical device is developed by integrating gold nano-islands on a silica-on-silicon (SOS) waveguide. The SOS waveguide is further hybrid integrated in a microfluidic device fabricated on polydimethylsiloxane (PDMS). As the nano-islands are on the core of the waveguide, the evanescent tail of the propagating waves interacts with the gold and changes the transmittance spectrum. The bio-species adsorbed on the gold nano features change the local refractive index of the gold, which essentially modifies the transmittance spectrum of the light propagating through the SOS waveguide, hence a nano-enhanced evanescent mechanism is achieved. The integration process of gold nano-islands on the SOS chip is compatible for the fabrication of a lab-on-a-chip. In this design, the sensor chip is integrated into a microfluidic environment by using soft lithography on PDMS for the realization of a low cost LOC. The proposed nano-integrated LOC is demonstrated for the detection of recombinant growth hormone.

In order to understand the enhancement of evanescent sensing, a simplified model of the proposed device is simulated by 3D Finite-difference time-domain (FDTD) method by using the Rsoft, FullWAVE.

## **8.2 Materials and method**

### **8.2.1 Materials**

Recombinant bovine somatotropin (rbST, MW 22 kDa) and its antibody (Anti-bST) were received from Cedarlane, ON, Canada. The rbST diluted in PBS at a concentration of 5000 ng/ml was used as stock solution and stored at 3-5<sup>0</sup>C. The anti-bST obtained in powder form was dissolved in PBS at a concentration of 5000 ng/ml and stored in refrigerator at 3-5<sup>0</sup>C. Hydrogen tetrachloroaurate (III) trihydrate (HAuCl<sub>4</sub>.3H<sub>2</sub>O) was received from Alfa Aesar. Sodium citrate, 11-mercaptoundecanoic acid in ethanol (Nano Thinks Acid 11), N,N'-diisopropylcarbodiimide and N-hydroxysuccinimide phosphate buffered saline (PBS) were obtained from Sigma Aldrich, Canada. PBS dissolved in DI water at a concentration of 0.1M and pH of 7.2. The SYLGARD184 elastomer kit and curing agent for the PDMS fabrication were obtained from Dow Corning.

### **8.2.2 Gold nano-islands integrated LOC**

The integration process of the proposed device is illustrated in Figure 8.1. The device has two main parts, one is the silica-on-silicon (SOS) waveguide with gold nano-islands integrated on it and the other part is a PDMS microfluidic chips. The SOS waveguide has two layers of silicon dioxide deposited on silicon substrate. The first silicon dioxide layer acts as the bottom cladding layer for the waveguide, while the second layer with higher refractive index than the cladding acts the core of the waveguide. The core layer is micromachined to certain width for the lateral confinement of light. The gold nano-islands are integrated on the core to modify the evanescent field of the waveguide due to the localized surface plasmon property of

the gold nano-islands. The schematic of the SOS waveguide integrated with gold nano-islands is shown in Figure 8.1(b).

The PDMS chip has a microfluidic channel and two liquid reservoirs as shown in Figure 8.1(a). The chip is bonded with the SOS waveguide so that the bio-species can be pumped through the gold nano-islands integrated on the SOS waveguide. The fluidic tubes are fixed with the liquid reservoir to facilitate the microfluidic flow through the device. When the bio-species are adsorbed to the gold nano-islands, their bio-interaction influences the evanescent field as measured through the waveguide.

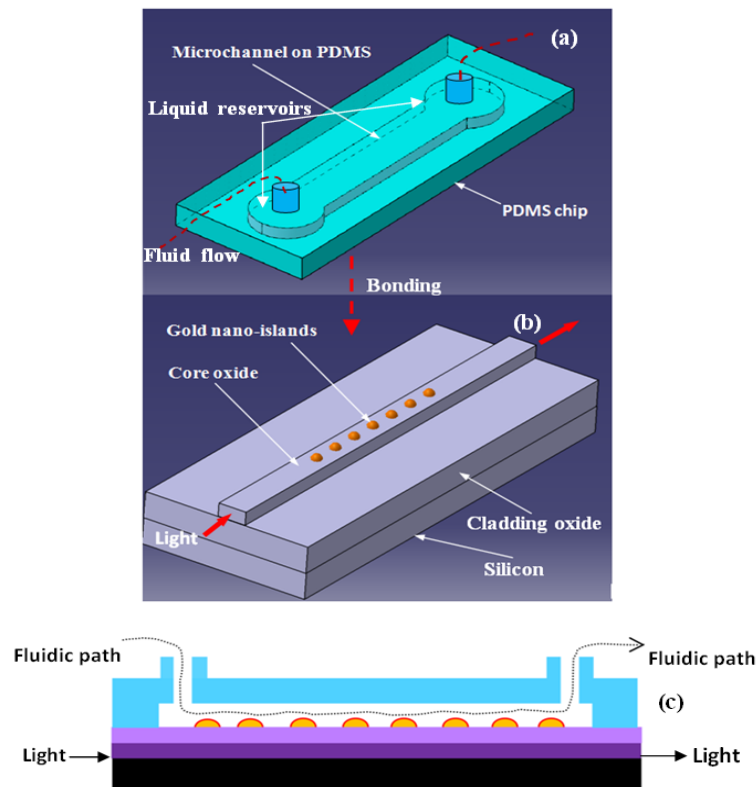


**Figure 8.1** Schematic diagram of integration process of the LOC, (a) PDMS microfluidic chip (a) SOS optical chip integrated with gold nano-islands and (c) sectional view of the LOC.

The fabrication process flow of the nano-islands integrated LOC is shown in Figure 8.2. The device is fabricated on silica-on-silicon (SOS) waveguide. Figure 8.2(b) shows the SOS waveguide with two layer of silicon dioxide. The first layer with lower refractive index and the second layer with higher refractive index act as the bottom cladding and core of the waveguide, respectively.

Then the nano-islands are integrated on the core of the SOS waveguide by convective assembly (Figure 8. 2(c)). Subsequently, the microfluidic chip fabricated on PDMS by soft-lithography is bonded with the SOS waveguide and the LOC is realized as shown in Figure 8.2(d). The fabrication details of all the steps given in Figure 8.2 are explained in Sections 3 to 5.

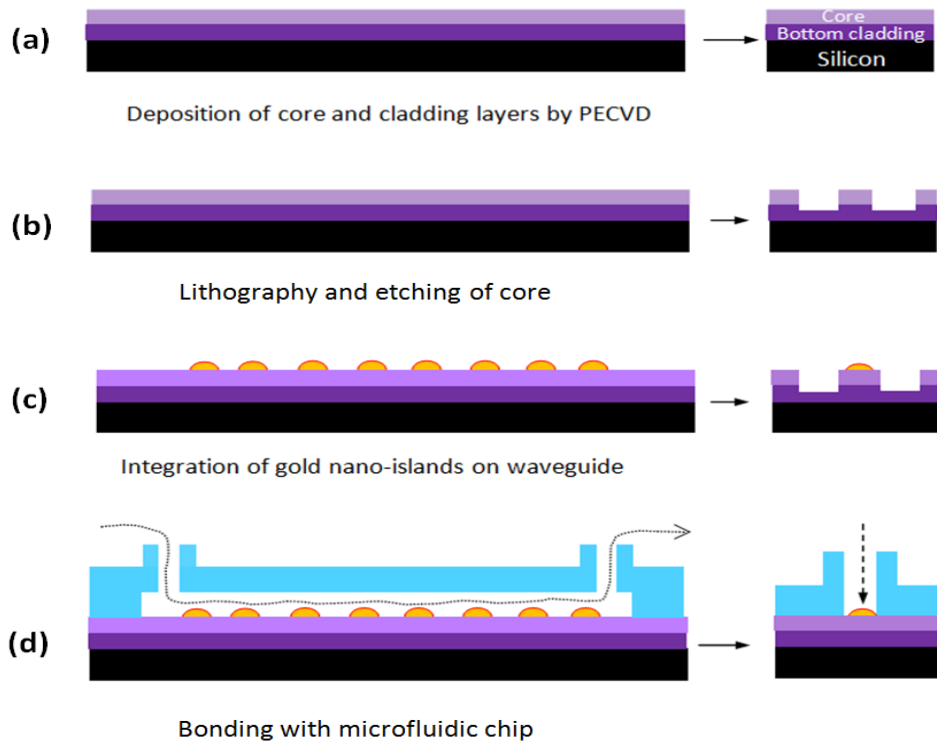


**Figure 8.2** Fabrication process steps of gold nano-islands integrated LOC

### 8.3 Fabrication of silica-on-silicon optical chip

The fabrication of silica-on-silicon waveguide involves the deposition and micromachining of silicon dioxide layers. The plasma enhanced chemical vapor deposition (PECVD) was used for the deposition of silicon dioxide layers. For the PECVD deposition, PlasmaLab 80 Plus instrument of Oxford instruments is used. Different deposition process parameters are optimized to achieve necessary refractive indices for the cladding and core. For depositing the cladding oxide, the chamber pressure and substrate temperature was set 1000mT and 300<sup>0</sup>C, respectively. The gas mixture of silane and nitrogen (5 percent SiH<sub>4</sub>, 95 percent N<sub>2</sub>) was introduced to the chamber at the flow rate of 170 sccm. The nitrous oxide (N<sub>2</sub>O) was introduced to the PECVD chamber at the flow rate of 710 sccm. Then the plasma was created by RF power of 20W at 13.56 MHz. The deposition rate was 50 nm/minute. The deposition was carried out for 4 hours and 30 minutes. The thickness of oxide layer was approximately 14 $\mu$ m for the bottom cladding of the waveguide. To obtain higher refractive index for the core layer, the flow rate of the silane and nitrogen mixture and N<sub>2</sub>O was increased to 500 sccm, and the RF power was increased 200W. The refractive indices of the silicon dioxide layers were measured by ellipsometry (Spectroscopic ellipsometer, Model: VASE, Sopra). The refractive indices for the core and cladding were 1.445 and 1.457, respectively at a wavelength of 635 nm.

The micromachining of the core was carried out by using direct write lithography (DWL) and reactive ion etching (RIE). The mask pattern was designed in L-edit software and used in the DWL-66 laser writer and the patterns were written directly on the wafer. The DWL write head of 2 mm having a resolution of 500 nm was used.

The AZ1518 photoresist was used for the lithography. The resist layer of thickness of  $2\ \mu\text{m}$  was by spun at 3000 rpm for 30s and baked at  $110^{\circ}\text{C}$  for 2 h in an oven. The pattern was etched in MERIE P5000 plasma machine of Applied materials. For the RIE, the chamber pressure was set to 50 mT and the process gases,  $\text{CHF}_3$ , Ar and  $\text{CF}_4$  were introduced at the flow rate of 45, 70 and 7 sccm, respectively. The plasma was created by the RF power of 300W. This process gives the etch rate of  $0.3\ \mu\text{m}/\text{minutes}$ . RIE was carried out for one hour including the 30 minutes of etch pause steps to prevent the burring of photoresist, which resulted in the etch depth of the  $10\ \mu\text{m}$ . The SEM micrograph of the waveguide is shown in Figure 8.3.

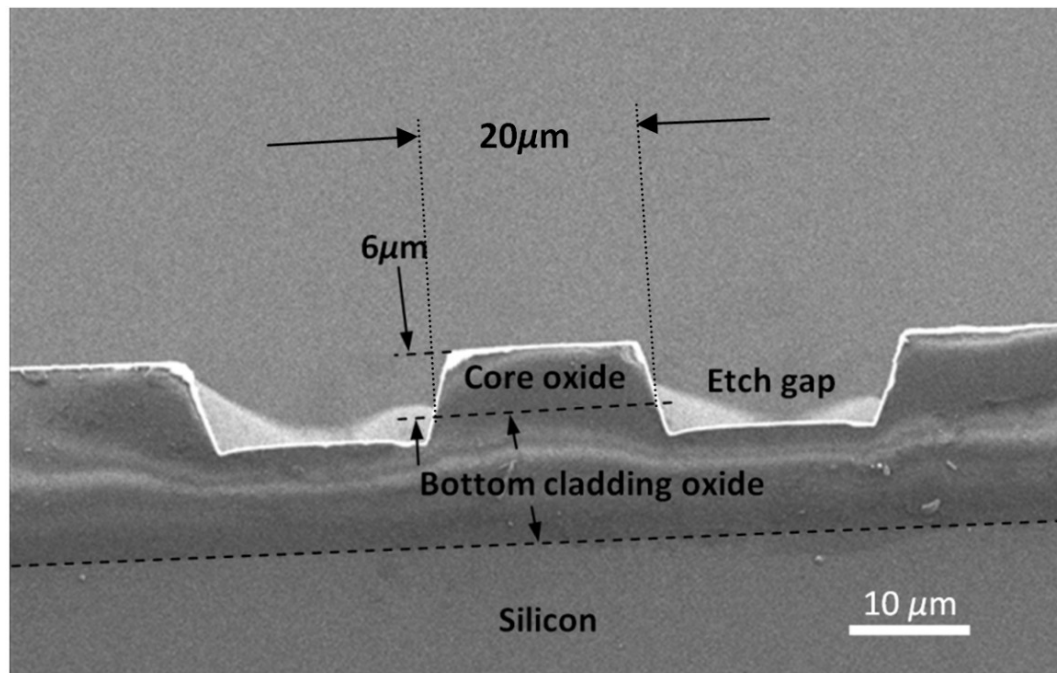


**Figure 8.3** SEM image of the SOS waveguide showing the sectional view of waveguide with the core and cladding dimensions.

## 8.4 Integration of nano-islands on the silica-on-silicon waveguide

The nano-islands are integrated on the SOS waveguide using angled convective assembly [61] in colloidal gold solution that was prepared by Turkevich's method [132]. The spherical gold nanoparticles were absorbed to the SOS waveguide by evaporating the aqueous solution containing the gold nanoparticles as shown in Figure 8.4(a).

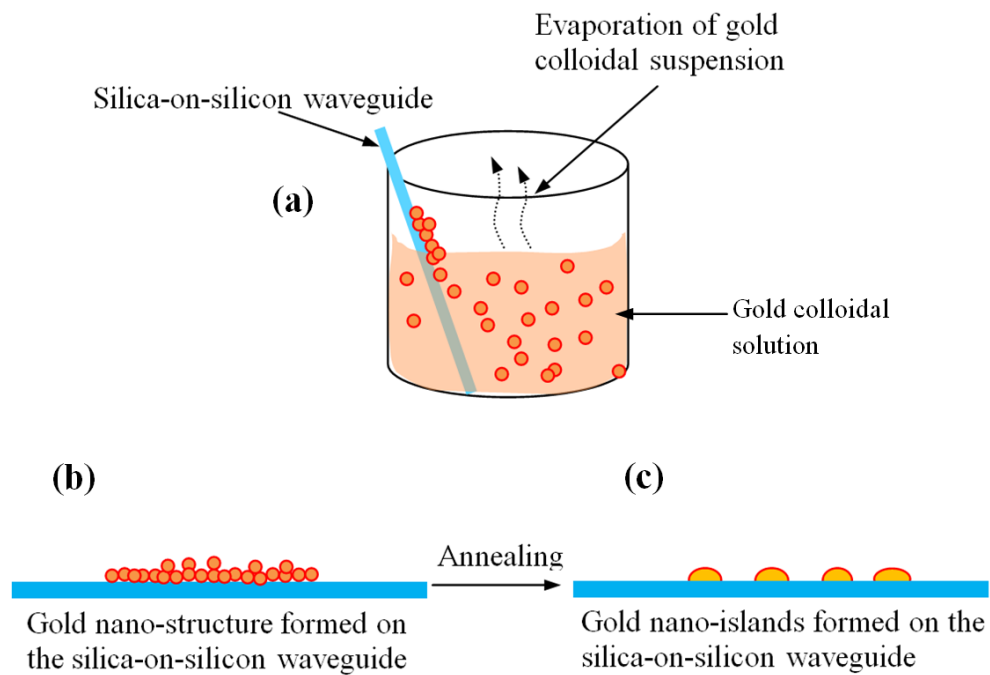


**Figure 8.4** Illustration of the method of integration of gold nano-islands on the silica-on-silicon optical chip. (a) SOS waveguide in gold colloidal solution, (b) gold nano-structure on the waveguide and (c) Gold nano-islands on silica-on-silicon optical chip.

The process of integration of gold nano-islands on the silica-on-silicon waveguide is illustrated in Figure 8.4. Before the deposition, the SOS waveguides were cleaned with soap solution and DI water, then rinsed with acetone, dried and finally rinsed with 2-propanol. The waveguides were silanized and heated at 100<sup>0</sup>C for 1 h and immersed in the gold colloid solution and kept in an oven at temperatures between 60 and 80<sup>0</sup>C as shown in Figure 8.4 (a). The solution was evaporated entirely in 2 days. During the evaporation of the aqueous solution, the gold nanoparticles from the solution drive to the surface and a nano-cluster was deposited on the waveguide (Figure 8. 4(b)). The nano-cluster morphology was transformed to nano-islands by a post deposition annealing as shown in Figure 8.4(c). In order to investigate the morphology of the deposited gold nanoparticle, SEM characterization was carried out. As the proposed convective assembly is not a controlled process, the morphology of the deposited layer of gold is found to be of nano-clusters as shown in Figure 8.5(a). A closer view of the nano-cluster formed on the waveguide is shown in Figure 8.5(b).

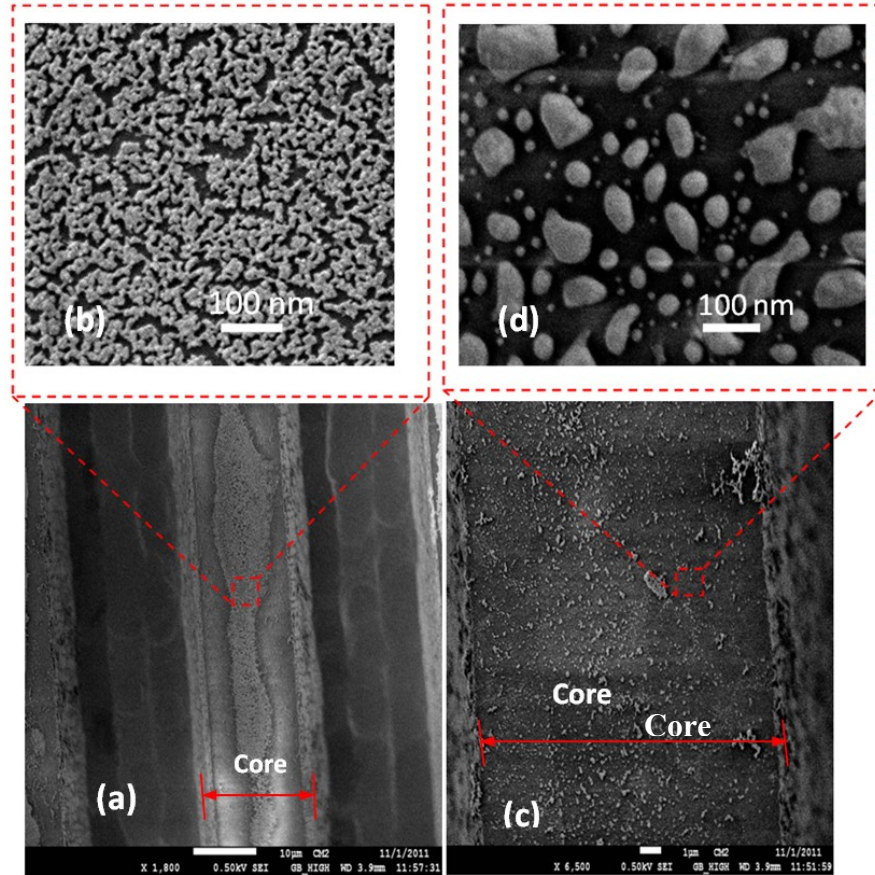


**Figure 8.5** SEM micrograph of gold nano-islands integrated silica-on-silicon waveguide (a) waveguide with gold nano-cluster (b) closer view of the nano clusters, (c) the waveguide after annealing and (d) closer view of waveguide after annealing.

The plasmonic property of the nano-cluster formed on the glass substrate was already measured [61, 91], which showed that the nano-cluster morphology has a wide LSPR band and it was found not good for the biosensing. By using a post deposition annealing process the morphology of the deposition was transformed to nano-islands. During the annealing, the nano-cluster melts and due to high surface tension of the molten metal, a nano-island morphology is formed as shown in Figure 8.5(d).

## 8.5 Fabrication of the gold nano-island integrated LOC

In order to fabricate the proposed device, the SOS optical chip with nano-islands was bonded with microfluidic chip. The microfluidic chip was fabricated on the PDMS using soft lithography technique. The microfluidic chips consist of a microchannel of width  $200\ \mu\text{m}$  and length  $1\ \text{cm}$  with two liquid reservoirs at the ends of the microchannel as shown in Figure 8.6. The schematic of the microfluidic chip is shown in Figure 8.6.

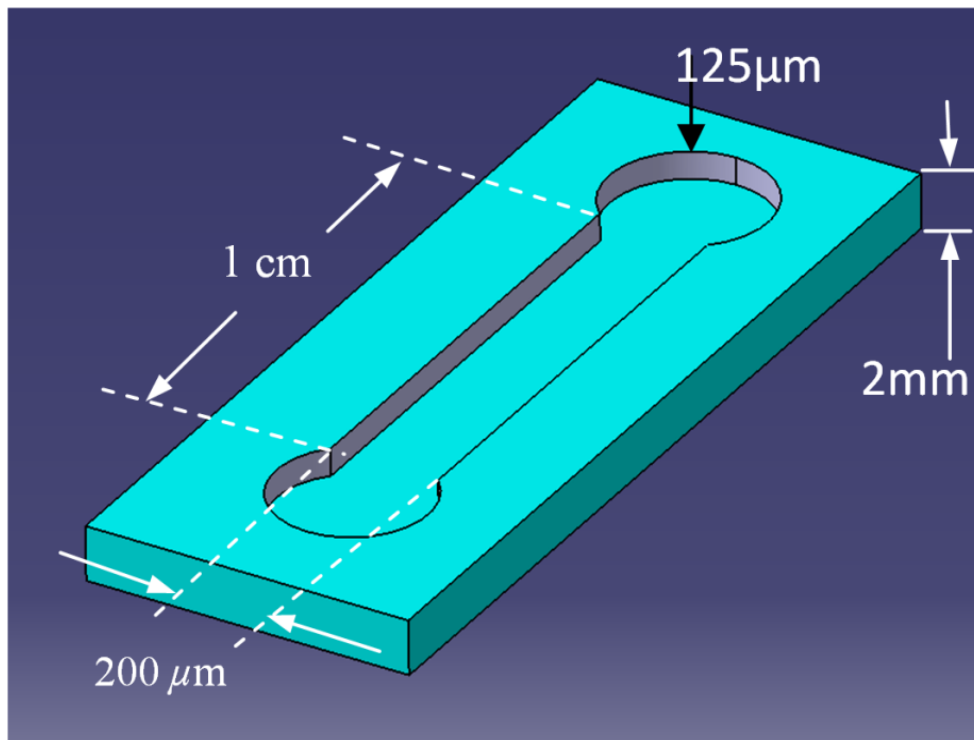


**Figure 8.6** Schematic of the microfluidic chip.

The PDMS chip was fabricated by soft lithography. A mold for casting the PDMS was fabricated by using SU8 photoresist. The mold is the negative pattern of the chip shown in Figure 8. 6. During the bonding of the SOS chip with PDMS chip, the core

of the waveguide must be inside the microchannel, hence the width of the channel was chosen to  $200\mu\text{m}$  to simplify the aligning task during the bonding. The depth of the channel was chosen to  $125\mu\text{m}$  to avoid the possible collapsing of the channel to the core during the bonding. The mold for the microfluidic chip was fabricated by UV- photolithography on SU8 photoresist. A negative photoresist (SU8-2035 Microchem) was spun twice on a silicon substrate for 30 seconds at 2000 rpm to form the resist layer with thickness of  $125\mu\text{m}$ . The resist was beaked at  $80^{\circ}\text{C}$  for 10 minutes after each spinning. Then the resist was exposed by UV light for 30 seconds through a mask. After the UV exposure, the resist was baked again and the pattern was developed in 15 minutes. The mold was silanized before casting the PDMS. The base and curing agent of the PDMS was mixed and degassed in a vacuum desiccator to remove the gas bubble and casted in the mold. The PDMS was cured at  $80^{\circ}\text{C}$  for 5 hours and the microfluidic chip was removed from the mold.

The chips were bonded by oxygen plasma techniques. The PDMS chip and the waveguide were cleaned by DI water and dried and loaded to oxygen plasma instrument. The samples were exposed to the oxygen plasma for 35 seconds. The bonding was carried out under a microscope to align the microfluidic channel with the waveguide. The fluidic tubes are inserted to the reservoirs and fixed to pump the bio-liquids to the device. PDMS was put on the SOS-PDMS interface to prevent the leakage through the etch gap of SOS waveguide, and immediately baked in an oven to prevent the flow of PDMS into the microchannel. Figure 8.7 shows the gold nano-island integrated LOC.

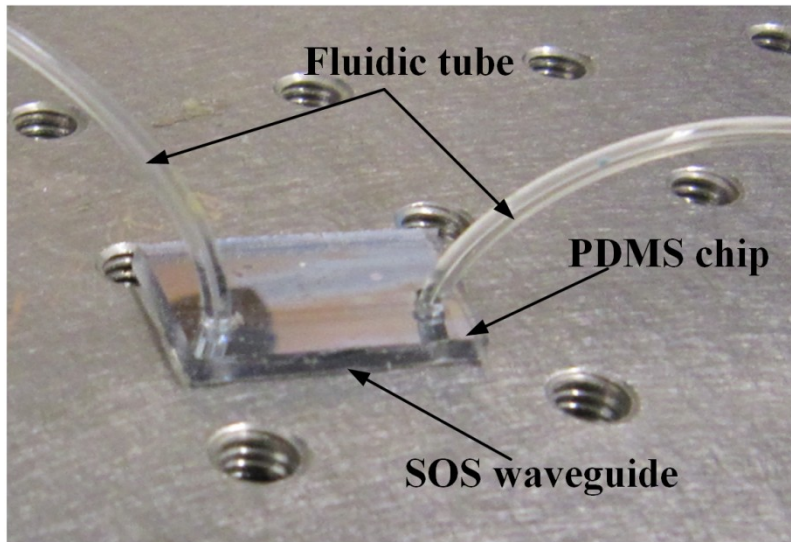


**Figure 8.7** Gold nano-islands integrated LOC

## **8.6 FDTD simulation of the device**

In order to investigate the effects of nano-islands on the propagation of light through the SOS optical chip, a simplified model of device is simulated by using FDTD technique. The FDTD method solves the Maxwell's differential equations by discretizing using central difference in space and time followed by solving them numerically by computers. The simulation domain is discretized into small elements called grid, and the accuracy of the FDTD computation depends on the size of the grid elements. As the simulation of real device require large computational resources, a simplified model of the device with a waveguide having the square cross section of  $1 \times 1 \mu\text{m}$  and a gold nano-hemisphere on the core of the waveguide is used for the FDTD simulation. The FDTD model used for the simulation is shown in Figure 8.8.

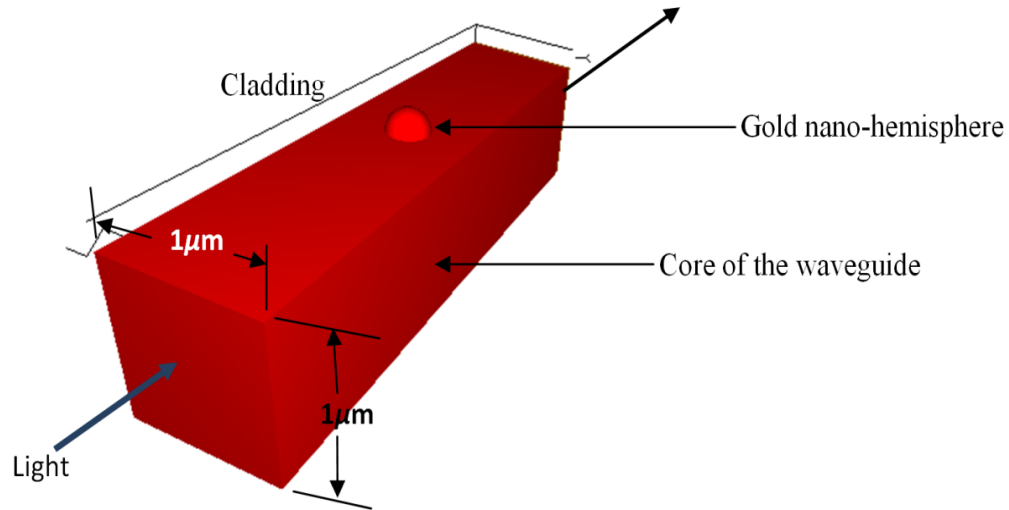


**Figure 8.8** FDTD model of the device.

The refractive index of the core was set to 1.46. A gold nano-hemisphere having the diameter of 70 nm is placed on the surface of the core. In order to assess the biosensing performance of the device, the refractive index of the cladding, that is, the region around the core is varied between 1 to 1.4 in the simulation. In order to compute the absorbance of the light due to the gold nano-sphere a power monitor is placed around the nano-hemisphere. An optical pulse with wavelength of 500 nm is used as the excitation source in the simulation. The power monitor placed with the nano-island can calculate the absorbance spectrum by using Fast Fourier Transform (FFT) algorithm.

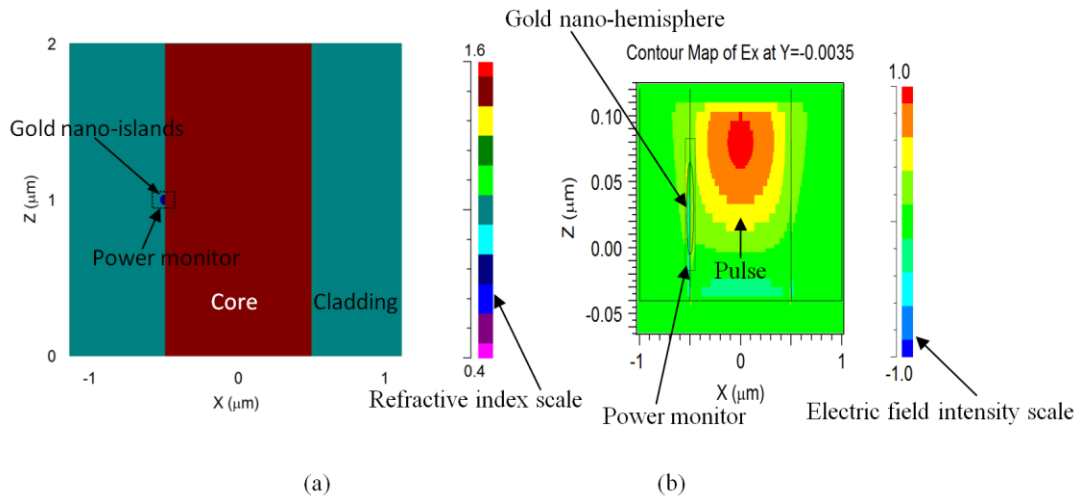


**Figure 8. 9** (a) Refractive index of the model (b) Electric field distribution in the model

Figure 8.9(a) and (b) shows the refractive index distribution of the model and the FDTD simulation showing the propagation of pulse through the waveguide. Figure 8.9(b) shows the electric field distribution in the model computed by FullWAVE during propagation of light pulse.

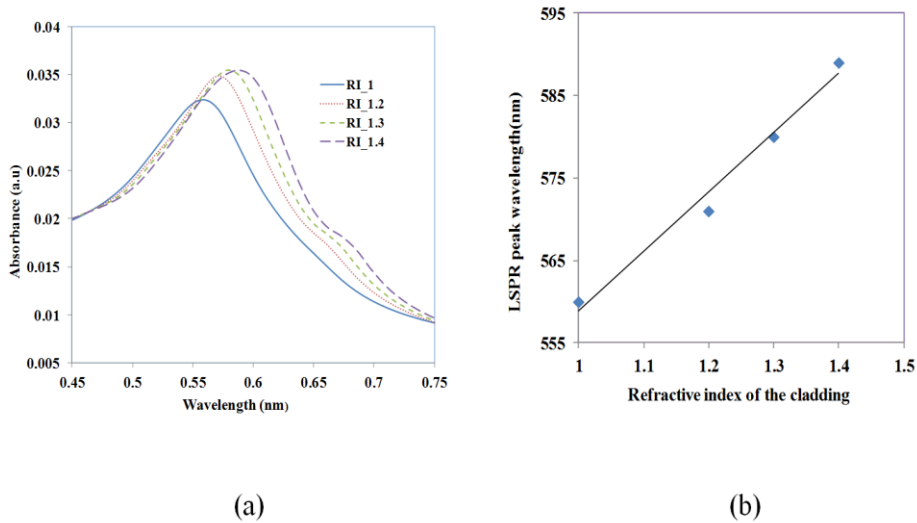


**Figure 8.10** (a) LSPR spectrum of the gold nano-island integrated on the core of the SOS waveguide and (b) LSPR peak wavelength against the refractive index of the cladding of the SOS waveguide.

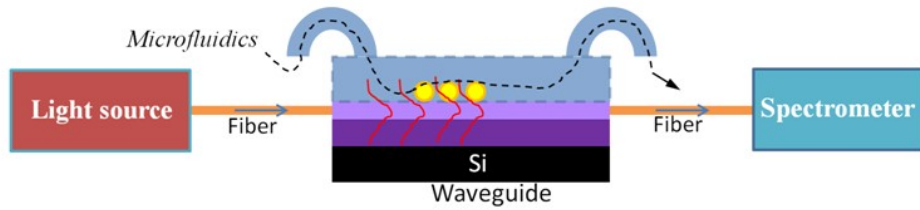
Figure 8.10 shows the FDTD simulation results of the gold nano-islands integrated device. Figure 8.10 (a) shows the absorbance spectra of the gold nano-island with diameter of 70 nm located on the surface of the core of the waveguide. As the evanescent field of the light propagating through the waveguide is extending to the cladding, the gold nano-island located at the core-cladding interface are excited by the evanescent field, which results in a collective oscillation of electrons of the gold nano-island at certain wavelengths and the absorption of light. This phenomenon is referred to as localized surface plasmon resonance (LSPR). The Figure 8.10 (a) shows the LSPR spectrum of the gold nano-islands by the excitation of evanescent field. The LSPR peak was measured at 560 nm when the cladding index was 1. The LSPR is sensitive to the local refractive index of the gold nano-island. The simulations

carried out by changing the cladding index to 1.2, 1.3 and 1.4 showed that LSPR peak is shifting to higher wavelength and also the band is becoming wider as shown in Figure 8.10(a). The intensity of the LSPR band is also found increasing with the refractive index. A linear trend in the shift of LSPR peak against the refractive index is observed as presented in Figure 8.10(b).

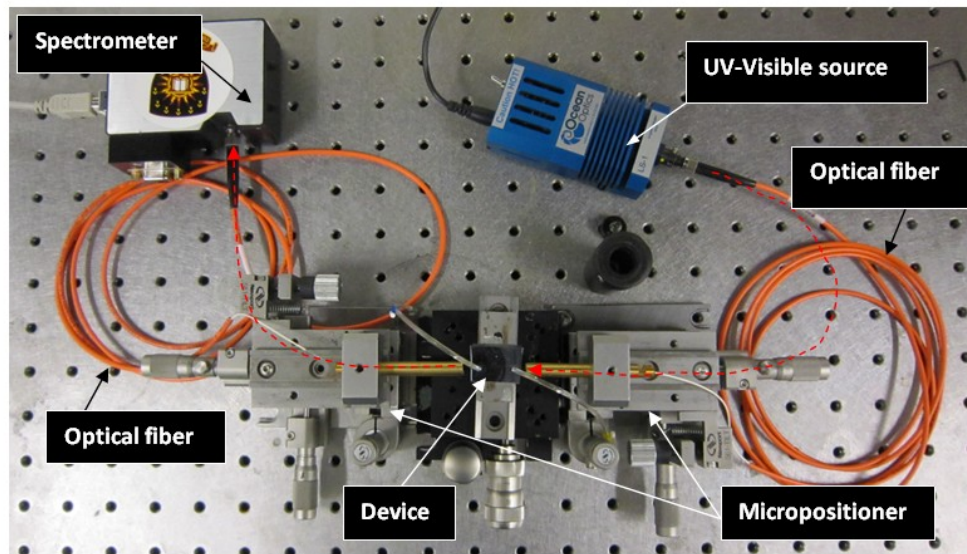
The FDTD simulation demonstrates that the nano-island integrated waveguide is useful for the biosensing applications. During the biosensing, the bio-species are adsorbed to the gold nano-islands and the local refractive index changes, hence the spectrum of the propagating light modifies, is the basic mechanism of the proposed device.

## **8.7 Experimental setup for nano-islands integrated LOC**

The schematic and photograph of the experimental setup of the device is shown in Figure 8. 11. The setup includes an UV-visible source, device under test (DUT) and spectrometer as shown in Figure 8.11(a). Light from the UV-visible source (Ocean optics LS-1) is coupled to the SOS waveguide through a fiber using a high precision micropositioners. The device is fixed in single axis controllable stage between the two 5 axis controllable micropositioner stages. Similarly, spectrometer (Ocean Optics USB 2000) is coupled to the output side of the waveguide using a multimode fiber as shown in Figure 8.11(b).



(a)



(b)

**Figure 8.11** Testing setup for nano-enhanced evanescence measurement (a) Schematic of the experimental setup (b) Photograph of the experimental setup.

Before starting the bio-sensing experiments in the device, a device without nano-islands was fixed in the setup and a reference spectrum corresponds to the source signal was recorded by the spectrometer. This reference spectrum was used for measuring the transmittance spectrum of the nano-islands integrated LOC. PBS solution was pumped to the device during all the measurements. After taking the reference spectrum, the nano-island integrated LOC was fixed to the measurement

setup. The transmittance spectrum recorded from nano-island integrated LOC is shown in Figure 8.12.

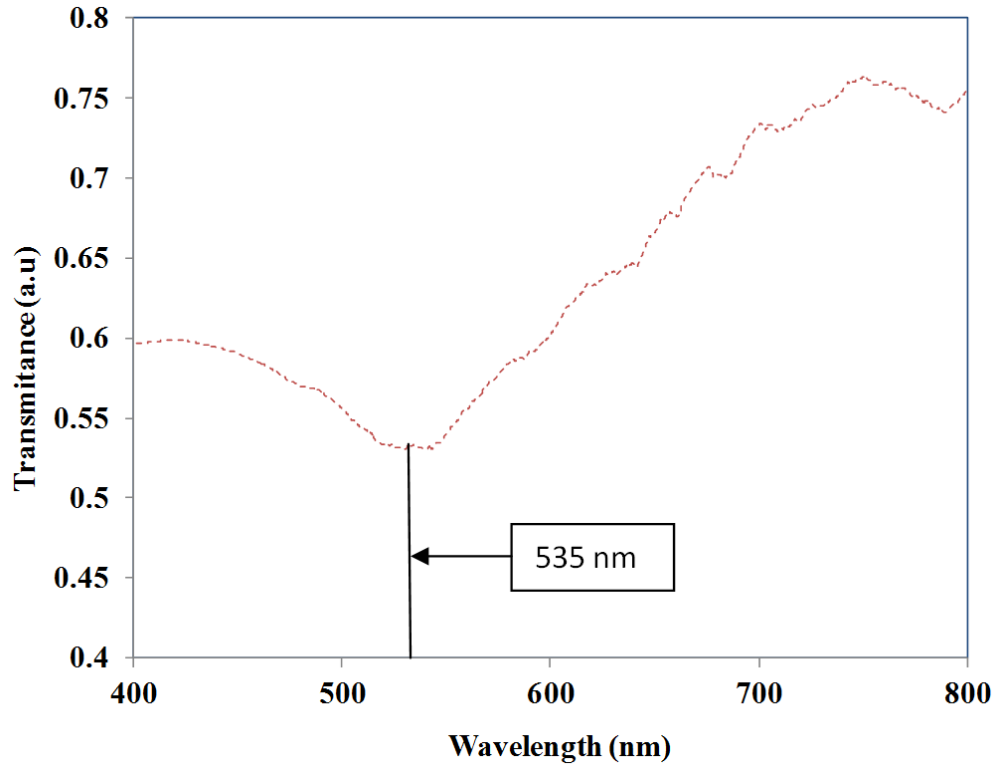


**Figure 8.12** Transmittance spectrum recorded in the nano-island integrated LOC.

Figure 8.12 shows the transmittance spectrum of the light propagating through the device. When the UV-visible light was coupled to the device, due to interaction of evanescent waves with gold nano-island, certain wavelengths are absorbed by the localized surface plasmon resonance of the gold nano-island. Minimum transmittance was observed in the transmittance spectrum at  $535 \pm 10$  nm for the measurements taken in 10 devices. The transmission minimum corresponds to the absorbance peak due to the LSPR of the gold nano-islands.

## 8.8 Biosensing

Biosensing experiments are carried out by pumping the reagents and rbST solutions to the device. Figure 8.13 illustrates various steps in the detection of recombinant growth hormone. Before starting the experiments de-ionized water was pumped to the device for 1 minute to clean the device.

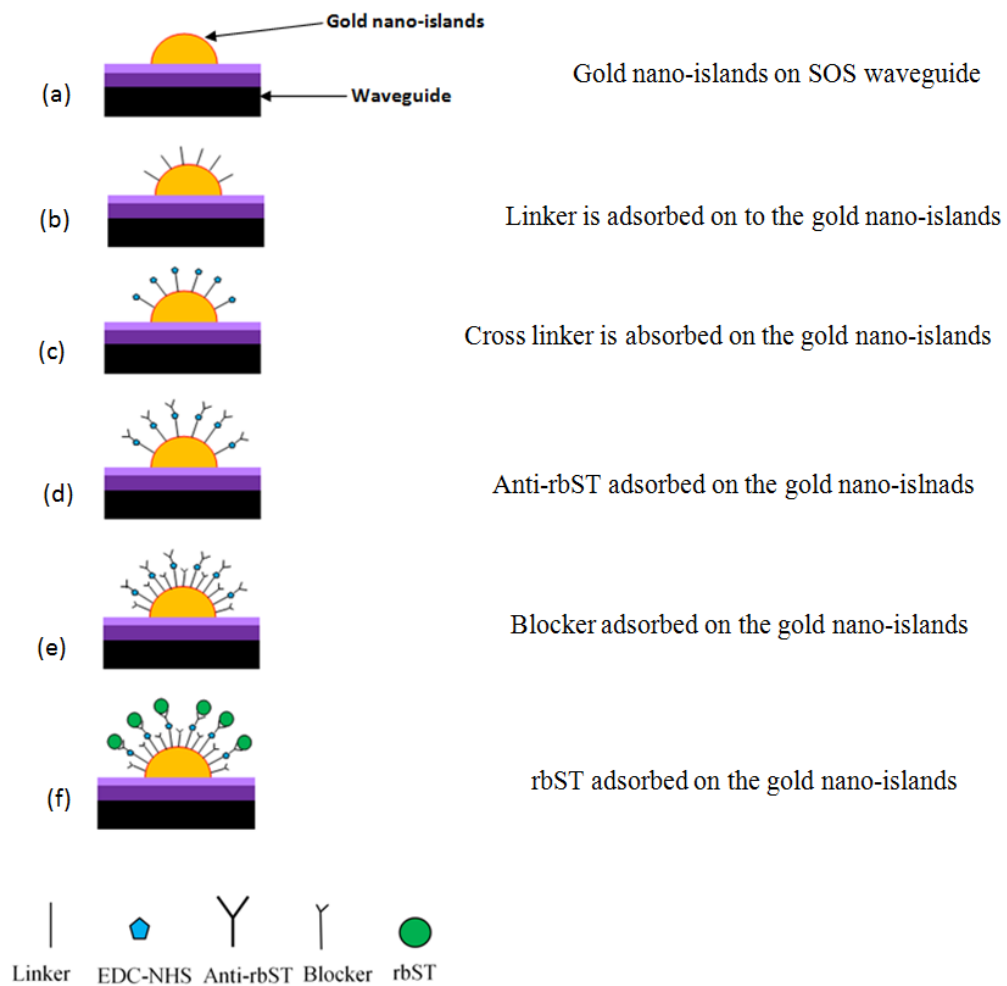


**Figure 8.13** Steps used in the detection of rbST in the nano-islands integrated LOC.

Figure 8.13(a) represents gold nano-islands on the silica-on-silicon waveguide in the microfluidic device. Then the linker solution, mercaptoundecanoic acid in ethanol was pumped to the device and kept for 1 hour and washed by passing PBS for 10 seconds. Figure 8.13(b) shows sample after passing the linker solution. Then the cross-linker solution (N, N'-diisopropylcarbodiimide and N-hydroxysuccinimide (EDC-NHS)) was pumped and kept for one hour and washed by pumping PBS solution for 10 seconds. The linker and cross-linker modify the surface of the gold so that the biomolecules can be attached to the gold. Figure 8.13(c) shows the gold nano-island after pumping the cross-linker. Then the antibody (ant-rbST) was pumped to the device and kept for 1 hour followed by washing in PBS. Figure 8.13(d) represent the sample after anti-rbST was adsorbed to the gold nano-hemisphere. Then the transmittance spectrum was measured after anti-rbST was adsorbed to the gold nano-island. During the measurement of transmittance spectrum, PBS solution was filled in the microchannel. In order to prevent the non-specific binding of rbST to the gold nano-islands, a blocker solution prepared from the non fat milk powder was used. The milk solution (1%) was pumped to the device and kept for 1 hour and washed with PBS. Figure 8.13(e) represents the sample after the blocker solution was adsorbed to the sample. Finally the rbST was pumped to the device and kept for 1 hour and washed with PBS (Figure 8.13(d)). Then the transmittance spectrum was recorded with PBS filled in the microchannel. The red shift of the transmittance minimum from the step (d) to (f) is estimated as a measure of the antigen-antibody interaction of the rbST. The sensitivity of the device was investigated for various concentration of rbST.

## 8.8 Results and discussion

The antibody-antigen interaction of rbST that occurs on the gold nano-islands and waveguide change the refractive index and/or the thickness of the biolayer absorbed on the gold nano-island. The change of local refractive index modifies the plasmonic band of the gold nano-islands. The shift of the plasmonic band is used as a measure of the antibody-antigen interaction of rbST. In the present work, the transmittance spectrum of the light propagating through the device is analyzed to detect rbST. Figure 8.14 shows the transmittance spectrum recorded at various steps of the biosensing process.

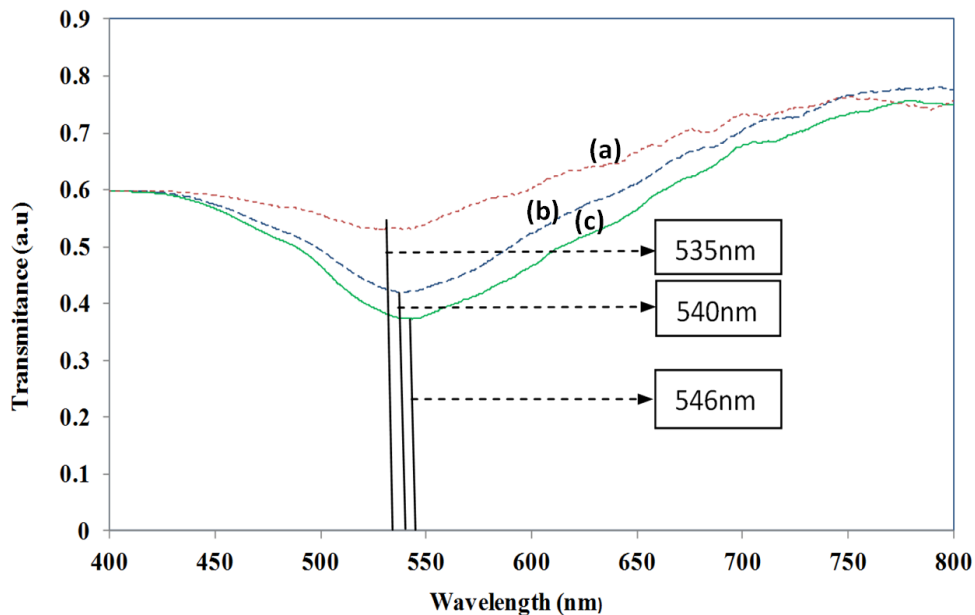


**Figure 8.14** Change of transmittance spectrum against the antibody-antigen interaction of rbST (a) Spectrum with gold nano-islands on the waveguide (b) spectrum after antibody (anti-rbST: 100 ng/ml) is adsorbed to the gold nano-islands and (c) spectrum after antigen (rbST: 800 ng/ml) is adsorbed to gold nano-islands.

Figure 8.14 (a) shows the transmittance spectrum recorded before starting the biosensing process. The spectrum with minimum transmittance recorded at 535 nm corresponds to the absorbance peak of the gold nano-islands integrated on the waveguide. The spectrum was shifted to 540 nm after the antibody of a concentration of 100 ng/ml was immobilized to the gold nano-islands. The band is found to become wider as shown in Figure 8.14 (b). Figure 8.14 (c) shows the spectrum recorded after rbST at a concentration of 800 ng/ml interacted with antibody immobilized on the gold nano-islands. The band became wider and also the transmittance minimum was further red shifted to 546 nm. A red shift of 6 nm in the transmittance spectrum is due to the modification of LSPR property of the gold nano-islands due to the interaction of the anti-rbST and rbST.

The suitability of the sensor for the quantitative measurements of rbST is investigated with various concentration of rbST. The concentration of the anti-rbST was kept at 100 ng/ml and concentration of rbST is varied between 10 to 800 ng/ml.

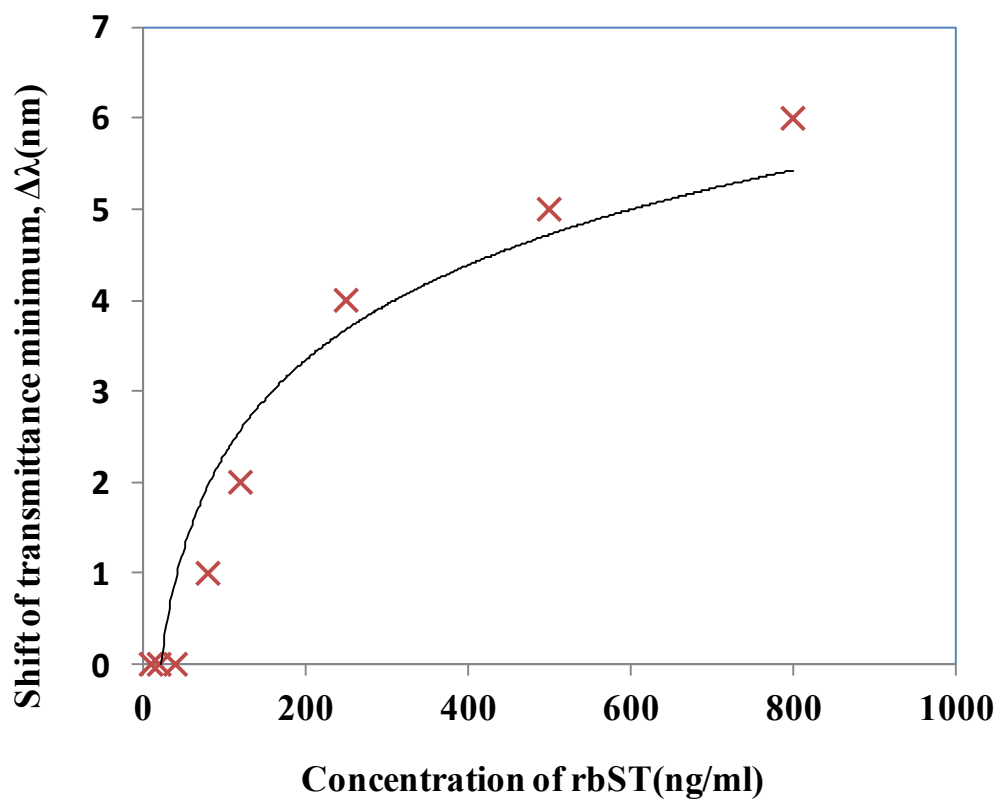


**Figure 8.15** Effect of concentration of rbST on the shift of minimum transmittance due to antibody-antigen interaction of rbST.

Figure 8.15 shows the tested variation of the shift of minimum transmittance against the concentration of the rbST. Variation of shift in the transmittance spectrum can be observed as shown in Figure 8.15. The sensor response is found slightly saturating after 500 ng/ml. A shift of 1 nm is observed when the concentration of rbST was reduced to 80 ng/ml. A trend line is fitted to the data in Figure 8.15 and the limit of detection of the device is found to be as low as 20 ng/ml.

The concentration of bST in milk is reported to be of the order of 1-10 ng/ml [100]. The rbST may be found in the milk of the cattle treated with [61][59][58][58] rbST, and concentration of rbST present in the milk may be of the order of hundreds of ng/ml [101], depending on the quantity of the rbST used for the production of milk. Hence the proposed device is suitable for the detection of rbST in milk.

## **8.9 Conclusions**

A lab-on-a-chip is developed by integrating gold nano-islands on the silica-on-silicon waveguide and PDMS microfluidic chips. The device works based on the modification of transmittance spectrum due to the absorption of light by the enhanced evanescence due to the gold nano-islands. The transmittance spectrum is modified due to the interaction of evanescent field of the propagating light with the gold nano-island. The device is demonstrated for the detection of recombinant growth hormone. The effect of concentration of rbST on the shift of transmittance spectrum is investigated and the detection limit of the device is estimated. The detection limit of the device is found to be 20 ng/ml.

## **Chapter 9: Detection of recombinant bovine growth hormone (rbST) in milk using gold nano-islands biosensor**

### **9.1 Introduction**

The bovine growth hormone (BGH), also known as somatotropin (bST) is a polypeptide chain of 191 amino acids naturally produced in mammals, which influences the growth and the reproductive systems[13]. The bST has been frequently used as a growth promoter in dairy farming to increase the production of milk [180]. The bST increases the milk production by partitioning the nutrients absorbed to the cows. The increase of production of milk has been widely reported in literature by the bST treated animal animals. The commercialization of the use of bST became possible with the discovery of recombinant DNA technology which could produce artificial hormone in a large amount [181]. The use of rbST for the milk production is allowed in some countries including Unities states, however many countries including Canada and European Union banned rbST. The use of rbST is controversial mainly due to its potential effects on the health of animal and consumers [14].

Typically, a 100g of cow milk contains water (88.9g), proteins (3.1g) fat (3.5g) sugar (4.4g), cholesterol (10mg) calcium (100mg) saturated fatty acids (2.3g), monounsaturated fatty acids(0.8g) and Polyunsaturated fatty acids (0.1g). The milk contains a large variety of proteins and majority of the proteins in milk is Caseins and the remaining types of proteins in milk includes array of enzymes, proteins required for transporting nutrients, proteins required for resisting the diseases that is antibody and protein which controls the growth. It is reported that the concentration of natural

growth hormone in milk is 1-10ng/ml [100] however the milk of the animal treated with rbST may contains rbST traces and the amount of rbST in the milk may be in the range of 100ng/ml depending upon the usage of rbST in animal [101]. Therefore, separation of proteins from the milk is a common sample pre-treatment in the detection of growth hormone in milk.

A large variety of separation process are used in analytical chemistry, however, solid phase extraction (SPE) is the most powerful method as it is faster and accurate. Traditionally, SPE systems were used with chromatographic system for the quantitative and qualitative analysis of bio-molecules. Recently M.H Le Barton et al[101] proposed a detection method of rbST in milk using Liquid chromatography combined with mass spectroscopy (LC-MS)[13], in which a solid phase extraction (SPE) method is used to separate rbST from the rbST spiked milk. Various other methods of detection of proteins have already been demonstrated for the detection of growth hormone. The traditional approaches of detection of growth hormone are ELISA (enzyme-linked immunosorbent assay)[22], radio immunoassays (RIA)[84], bio-assay methods and surface plasmon resonance (SPR) based immunoassays[26].

In this chapter, the detection of rbST separated from the milk by SPE is carried out by the plasmonic property of the gold nano-islands. The gold nanoparticles are extensively used for the label-free detection of the proteins due to its strong optical absorbance properties in the ultra-violet and visible regions of the electromagnetic spectrum. The plasmon band, also called localized surface plasmon resonance (LSPR) is due to the collective oscillation of electrons at certain frequencies. LSPR is sensitive to change of refractive index of the surrounding environments hence they

have been useful for immunoassays. The gold nano-islands are formed on the glass substrates by convective assembly as explained in ref [61] and used for the detection of rbST separated from the milk.

The SPE process essentially removes the proteins like casein from milk and gives the solution of mixture of other proteins and the rbST. A known amount of rbST was added to the skimmed milk and the protein mixture was separated. The SPE experiments were repeated for milk with various amounts of rbST. Then the concentration of rbST in the milk and the shift of LSPR property of the gold nano-islands were investigated. In order to make sure that the other proteins in separation mixture are not adsorbed to the gold nano-islands, the gold nano-islands were functionalized with the anti-rbST prior to the detection process.

### **9.3 Materials**

Acetonitrile, Trifluoroacetic acid (TFA), phosphate buffered saline (PBS), N,N'-diisopropylcarbodiimide N-hydroxysuccinimide and SPE C4 cartridge (500mg/6ml) were purchased from Sigma-Aldrich Canada. Hydrogen tetrachloroaurate (III) trihydrate ( $\text{HAuCl}_4 \cdot 3\text{H}_2\text{O}$ ) was purchased from Alfa Aesar. Recombinant bovine somatotropine and corresponding anti-rbST was received from Cedarlane, ON, Canada.

### 9.3 Solid phase extraction (SPE)

Known amount of rbST was added to the milk and separated by solid phase extraction (SPE) technique. Figure 9.1 shows the SPE column technique for the separation of rbST from milk. SPE C4 column was used.

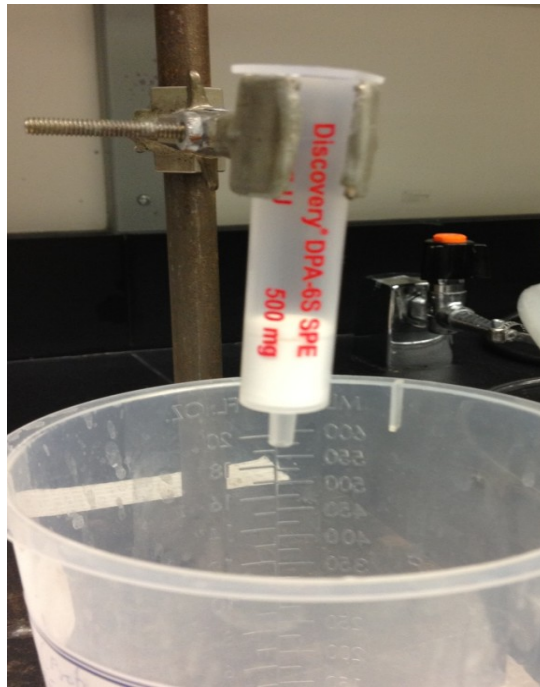


**Figure 9.1** SPE C4 column setup

The SPE C4 column was conditioned with 10ml of methanol and 10 ml of water. Then the mixture of rbST and milk was added to the column. The washing of the column is a step by step process, first with 5ml of water with 0.1% of trifluoroacetic acid and followed by the mixture of 5ml of water and acetomitrile in 70:30(v/v) with 0.1% TFA. During this process casein is washed away from the column. The next step in the SPE is the collection of sample containing mixture of protein in the milk.

The column was eluted with 7 ml water/acetonitrile mixture 20:80 (v/v containing 0.1% TFA). The absorbance spectrum of the sample containing various amounts of rbST was measured by using UV-visible spectrometer.

#### 9.4 Results and discussion

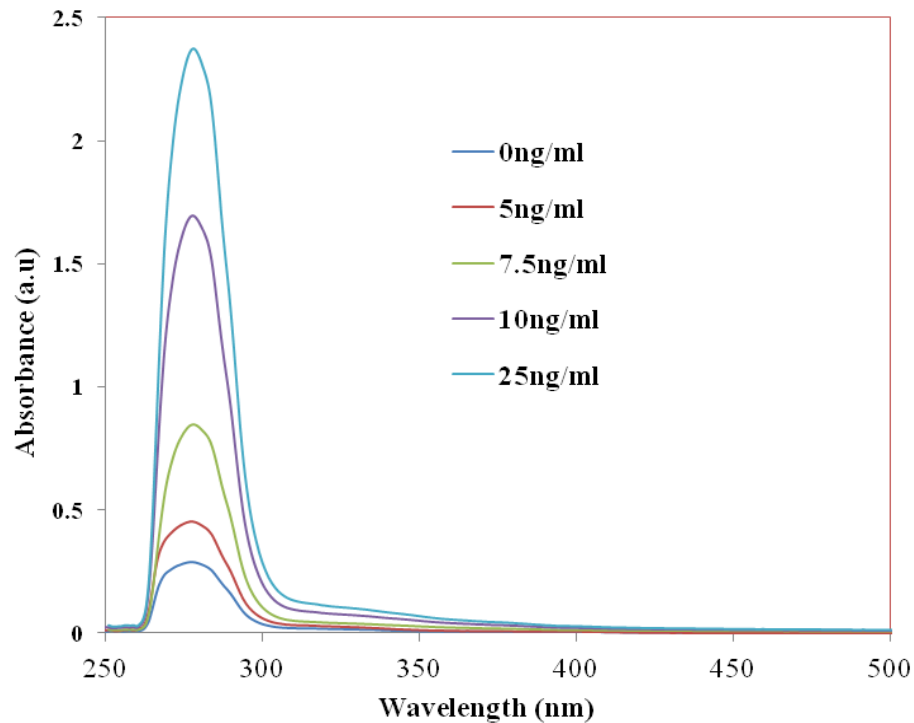


**Figure 9.2** Absorbance spectrum of the protein mixture separated from milk.

Figure 9.2 shows the UV-visible absorbance spectrum recorded for the SPE samples. As most the protein has an absorbance peak at 280nm, it is impossible detect a specific protein from a complex mixture by measuring absorbance spectrum. However, it can be seen from Figure 9.2 that the absorbance peak is increasing with the concentration of rbST spiked in milk.

For the specific detection of rbST in the SPE samples, a glass substrate with gold nano-islands was used. The manufacturing process of the gold nano-islands and the biosensing process are explained Chapter 5 and Chapter 6, respectively. For the biosensing, the anti-rbST was functionalized initially with the gold nano-islands. In order to attach anti-rbST, mercaptoundecanoic acid (in ethanol) is used as a linker molecule. The mercaptoundecanoic acid was placed on the gold and kept for an hour and the samples were washed in ethanol. Then cross linkers are added to the samples (N'-diisopropylcarbodiimide N-hydroxysuccinimide) and washed in phosphate buffered saline. The antibody was absorbed and washed in PBS. The change of LSPR spectrum of gold nano-islands was measured after absorbing the anti-rbST. Then a blocker solution, nonfat milk powder solution was added to the sample and blocked the non-specific sites of gold nano-islands as explained in Section 7.4. Finally the SPE samples were adsorbed to the gold and kept for one hour. The LSPR spectrum recorded at various steps of biosensing is shown in Figure 9.3(a).

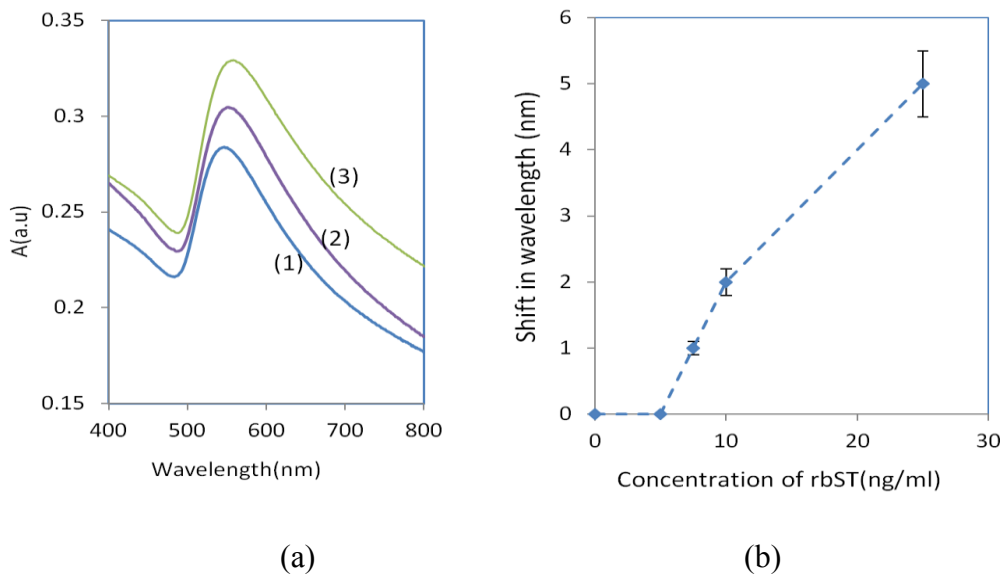


**Figure 9.3** (a) Change of LSPR property of the gold nano-island structure in the various stages of the immunoassay ((1) before the starting the immunoassay, (2) after anti-rbST was adsorbed to the gold and (3) after rbST was adsorbed to the gold). (b) The sensing experiments carried out for various concentration of the rbST; shift of LSPR as a function of concentration of rbST (ng/ml).

Figure 9.3(a) shows the shift of LSPR spectrum of the gold nano-islands due to the adsorption of antibody and antigen. A shift of 5nm was obtained with the SPE sample containing 25ng/ml of rbST. The concentration of the antibody was 100 ng/ml. The sensing was repeated with the SPE samples having various concentration of rbST as shown in Figure 9.3(b).

## **9.5 Conclusions**

Separation of rbST from milk is carried out by solid phase extraction for the detection. The skimmed milk samples spiked with rbST of various concentrations were found to have an absorbance peak in the UV-visible absorbance spectrum, and intensity of the absorbance peak was found increasing with the concentration. Since most of the protein molecules have absorption at 280nm wavelength, the detection of rbST by measuring the absorption spectrum of the SPE sample is not possible, hence the specific detection of rbST in the SPE samples was demonstrated with the plasmonic property of the gold nano-island formed on the glass substrate.

## **Chapter 10: Monolithically integrated lab-on-a-chip on silica-on-silicon platform**

### **10.1 Introduction**

Spectroscopy is a commonly used technique in analytical chemistry to detect a substance through the electromagnetic waves emitted or absorbed by them. Hence, the spectrometer is a major component that needs to be miniaturized and integrated with the lab-on-a-chip. In literature, there are few attempts reported for the fabrication of micro-spectrometers. Arrayed waveguide gratings (AWG) [182, 183], grating spectrometers [184], super prism based spectrometers [185] are some of the micro-spectrometer configurations reported in literature. A diffraction grating spectrometer with a thermally tunable micro-ring resonator is also developed recently [186]. Planar waveguide Echelle grating micro-spectrometers have been implemented for optical communication applications [187].

Dispersive elements are generally used in the micro-spectrometer because they are easy to miniaturize. A major drawback of the miniaturization of a dispersive element is that the spectral resolution will be decreasing with the size. Hence a trade-off between the size and the spectral resolution must be established in design.

The advantages of the integrated photonics platform for the miniaturization of lab-on-a-chips were discussed in previous chapters. Optical and microfluidic components required for the bio-detection can be monolithically integrated on the silica-on-silicon platform. In this chapter, monolithic integration of optical waveguides, microfluidics

and a micro-spectrometer is discussed for the fabrication of a monolithically integrated lab-on-a-chip.

## 10.2 Monolithically integrated lab-on-a-chip

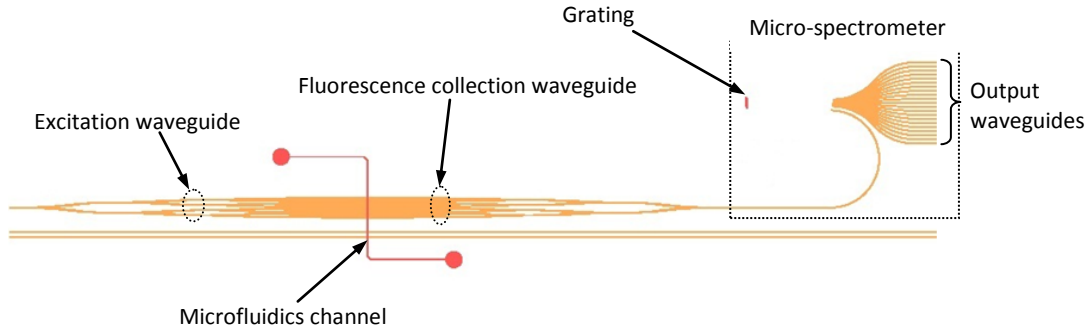


**Figure 10.1** Schematic of monolithically integrated lab-on-a-chip

Figure 10.1 shows the schematic diagram of the monolithically integrated lab-on-a-chip, in which a microfluidic channel, waveguides and a spectrometer are monolithically integrated on silica-on-silicon platform. This chip is designed for the detection of tagged rbST. The tagged rbST can be pumped to the micro channel and the light can be coupled to the micro channel through excitation waveguide. The fluorescence signal from the tagged rbST can be collected through the collection waveguides and guided to the micro-spectrometer. The concave grating in the micro-spectrometer separates the emission and excitation wavelengths and couples to the output waveguides.

### 10.3 Basics of diffraction grating

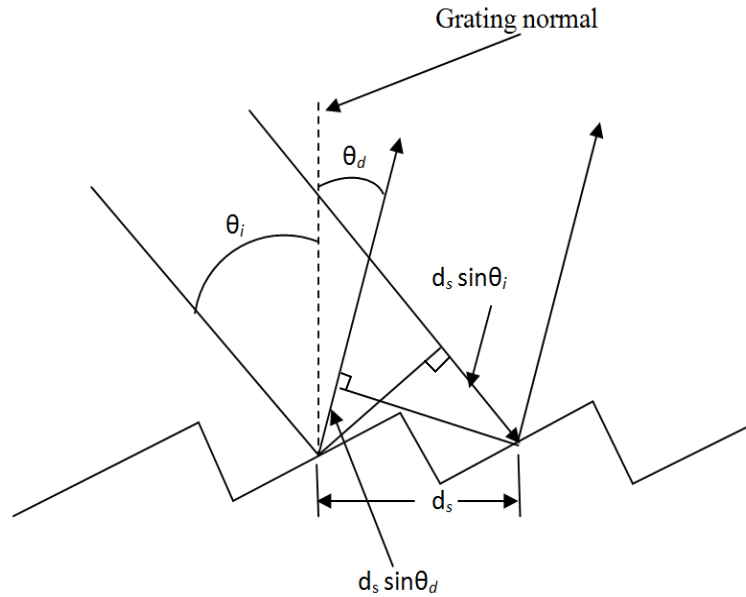


**Figure 10.2** Diffraction on grating surface, showing the relation between the rays diffracted from the adjacent grooves.

Figure 10.2 shows the illumination of a diffraction grating surface and the diffraction of light from the grating surface. Each groove in the grating acts as a tiny source of reflected light. The grating can diffract the incident light into clearly distinguished directions and a unique set of angles exists at which the light diffracted from all facets is in phase. The relation between the incident and diffracted angle can be estimated by the grating equation that can be derived by tracing the rays on a grating surface. In Figure 10.2, let  $\theta_i$  and  $\theta_d$  be the incident and diffracted angle of the rays measured from the normal to the grating, respectively. Then, it can be seen that the geometrical

path difference ( $\Delta l$ ) between the light diffracted from successive grooves in the direction  $\theta_d$  is:

$$\Delta l = d_s \sin(\theta_i) - d_s \sin(\theta_d) \quad (10.1)$$

where  $d_s$  is the groove spacing. As per the principle of diffraction, the diffracted rays will be in phase only when the path difference is equal to or integral multiple of wavelengths. The rays diffracting in phase will be constructively interfered. This wavelength dependent constructive and destructive interference leads to separation of wavelength is space angularly.

Therefore the Equation 10.1 can be written as:

$$\sin(\theta_m) = \sin(\theta_i) + m \frac{\lambda}{d_s} \quad (10.2)$$

where order of diffraction,  $m = 1, 2, 3, \dots$  and  $\lambda$  is the wavelength of light.

For  $m=0$ , all wavelengths will be superimposed and hence the grating acts as a reflecting surface. For  $m \neq 0$ , diffraction is wavelength depended so that the wavelengths of incoming light are specially separated.

In 1883, Rowland demonstrated the advantages of concave diffraction gratings. Concave grating has the self focusing ability. Typical configuration of Rowland circle spectrograph is shown in Figure 10.3. Herein, the source and detectors (D1, D2, and D3) are arranged in an imaginary circle called Rowland circle. Radius of curvature of the diffraction grating is double of the Rowland circle. Depending upon the order of diffraction used in the spectrograph, and using the grating equation, the position and spacing between the detectors can be calculated.

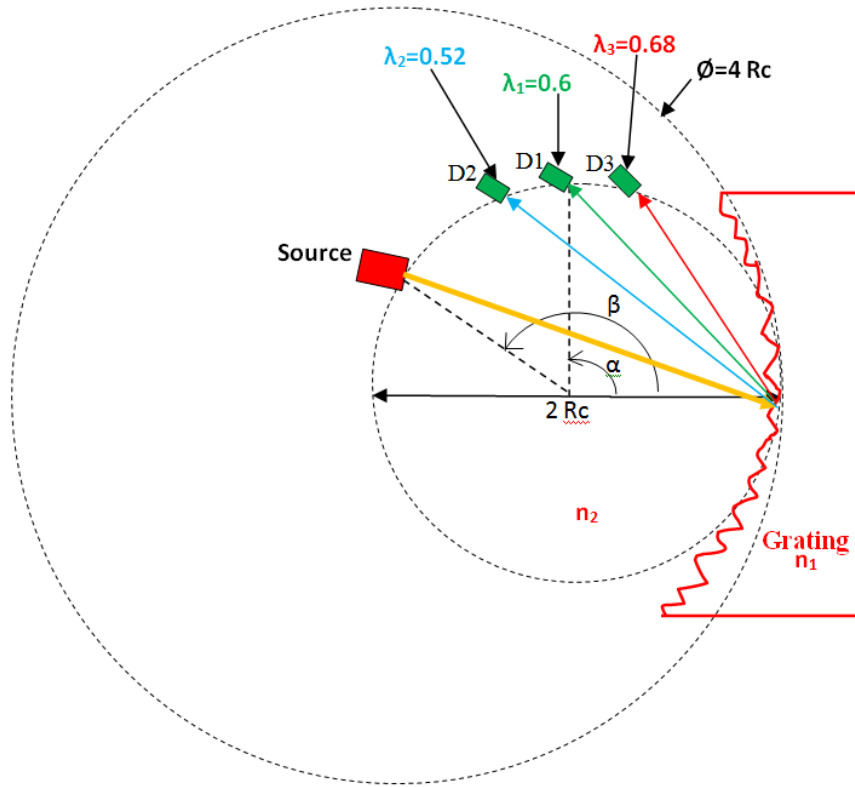


**Figure 10.3** Rowland spectrograph configuration.

#### **10.4 Modeling of concave grating based micro-spectrometer by FDTD**

Modeling of concave spectrometer is carried out by using Frequency Difference Time Domain Method (FDTD) using a commercial tool called Rsoft FullWAVE. The parameters used for the simulation are given in Table 10.1. Configuration of the grating spectrometer modeled in Rsoft FullWAVE is shown in Figure 10.3 (a) and the efficiency of light received in each detector is shown in Figure 10.5

Sl no	Parameter	Value
1	Rc	25 $\mu\text{m}$
2	n <sub>2</sub>	1.45
3	n <sub>1</sub>	1
4	$\beta$	150 <sup>0</sup>
5	$\alpha$	90 <sup>0</sup>
6	Diffraction order (m)	2 <sup>nd</sup>
7	Grating period (d <sub>s</sub> )	0.5 $\mu\text{m}$
8	Number of facets	26

**Table 10.1.** Parameters used for the simulations.

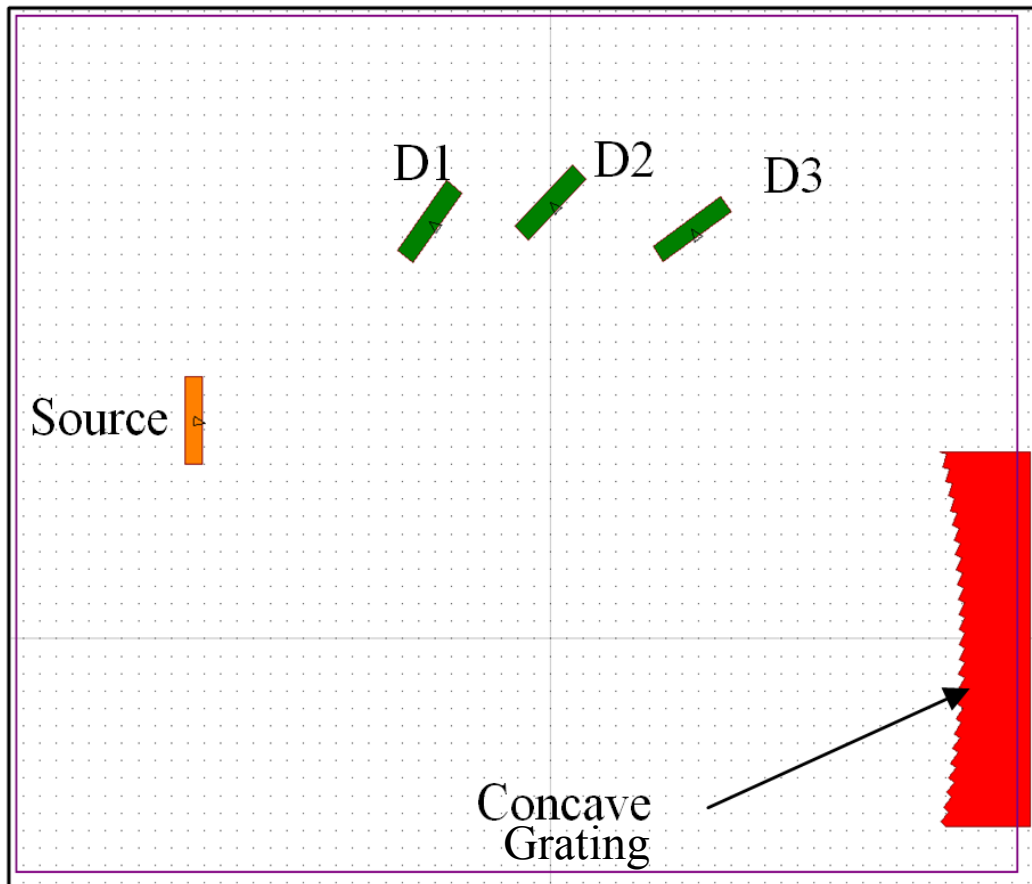


**Figure 10.4** FDTD model of the concave spectrometer

Figure 10.4 shows the configuration of the FDTD model simulated by Rsoft FullWAVE. In simulation, the concave grating was illuminated with an optical pulse with center wavelength of 600nm. Three power monitors (D1, D2, and D3) are placed on the Rowland configuration as shown in Figure 10.4. The spectrum of the light received on each power monitor is computed by Fast Fourier Transform (FFT) algorithm of the Rsoft FullWAVE. Perfectly matched layer (PML) boundary conditions are used on the walls of simulation domain for the FDTD simulation [135]. The efficiency the concave grating calculated is presented in Figure 10.5. The efficiency of the concave grating was in the range of 1 to 5% as shown in Figure 10.5. In order to increase the efficiency of the spectrometer, aluminum coating on the grating surface was reported in ref. [187]. The FDTD simulation carried out with aluminum coating on the present spectrometer configuration shows that the efficiency of the spectrometer has been increased 35 to 40% as shown in Figure 10.5.

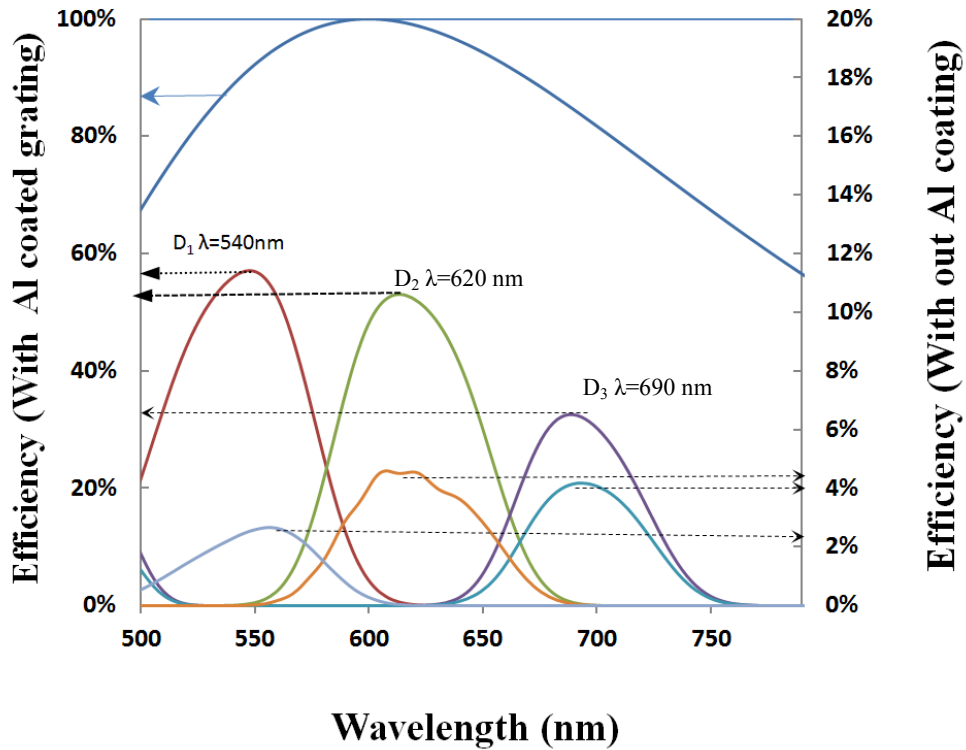


**Figure 10.5** Efficiency calculated for the configuration shown in Figure 10.4, Aluminum coated grating facet is shown to be enhancing the efficiency.

## 10.5 Fabrication of monolithically integrated lab-on-a-chip

The monolithically integrated LOC was fabricated on silica-on-a-silicon platform by single step lithography and etching. A single mask including the patterns of the microfluidic channel, waveguide and micro-spectrometer was designed in L-edit as shown in Figure 10.1.

The first step in the fabrication of device is deposition of silicon dioxide layers. Two layers namely bottom cladding and core of the waveguide was deposited by plasma enhanced chemical vapor deposition. The pattern designed in L-edit was directly

written on wafer by direct write lithography (DWL). The detailed fabrication and characterization of the device are given in Chapter 4.

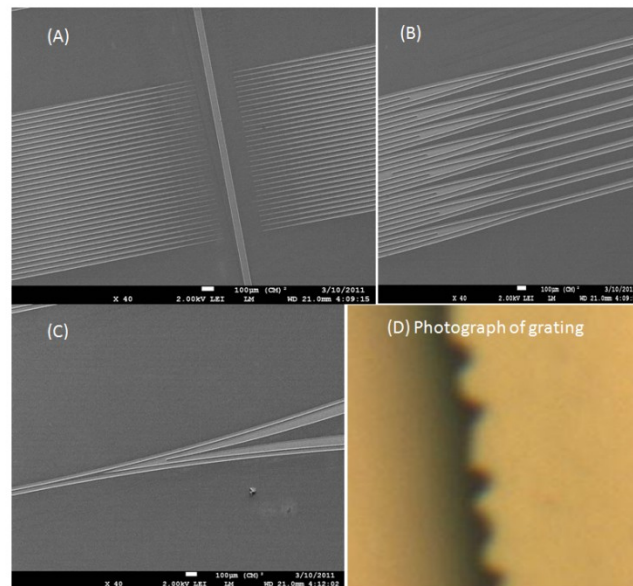
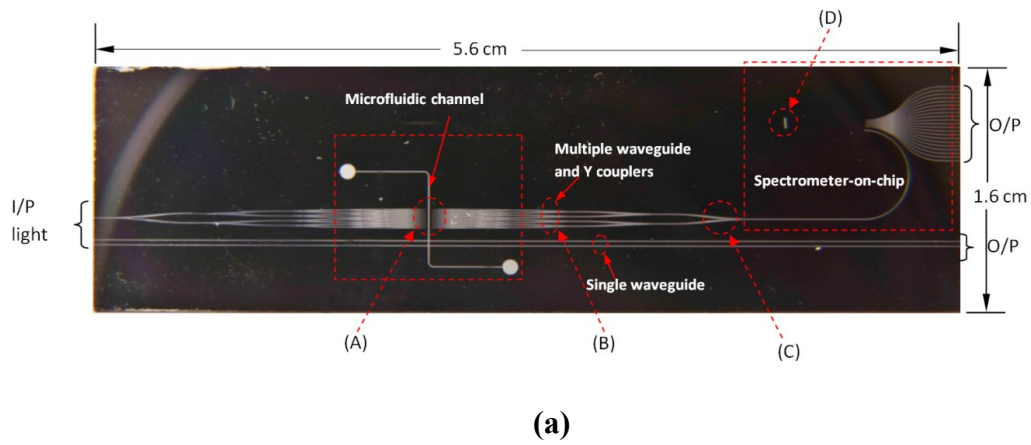


**Figure10.6** (a) Photograph of the lab-on-a-chip (b) SEM image taken at different regions of Lab-on-a-chip: (A) At waveguide microfluidic intersection, (B) 8 Y Couplers (C) final Y coupler (D) Photograph of the grating.

Figure 10.6 (a) shows the photograph of the optical Lab-on-a-chip (LOC) etched on the silica-on-silicon platform. Figure 10.6 (b) shows the SEM image taken on the device. In the Figure 10.6 (a), Close up (A) shows the multiple waveguide-microfluidic intersection region, herein, 32 tapered waveguide are placed across the microfluidic channel. Close up (B) shows eight Y couplers which combines the light collected through the multiple waveguide. Close up (C) shows the final Y coupler and (D) shows the the grating imaged through a microscope. As the resolution of the DWL laser writer with the write head of 2mm is 500nm and the minimum feature size of the grating of the spectrometer is 500nm, the grating structure could not be written on and etched. The irregular shape of the grating after reactive ion etching is shown Figure 10.6(b) (D).

## 10.6 Conclusions

A monolithically integrated lab-on-a-chip is fabricated on silicon-on-silicon platform. A micro-spectrometer is designed by FDTD simulation and the efficiency of the spectrometer with and without and aluminum coating on the grating facet illustrated that the aluminum coating enhanced the efficiency by 10 to 15 times. Using a novel single step lithography and reactive ion etching, micro fluidic channel, waveguides and micro-spectrometers are monolithically integrated. However, the grating features could not be fabricated precisely due to its small size. By using the electron beam lithography, grating patterns can be transferred to the wafer precisely in future.

## **Chapter 11: Conclusions and future scope of the works**

### **11.1 Conclusions**

The objective of this thesis is to develop lab-on-a-chip devices for the detection of growth hormone in milk. Two types of detection methods such as labeled and label-free detection methods are investigated for the detection of the growth hormone. For the labeled detection of the recombinant somatotropin (rbST), the rbST was tagged with two types of fluorophores such as Alexa Fluor-647 and FITC. Both of the detection methods are implemented in lab-on-a-chip platforms.

A low cost lab-on-a-chip was fabricated by integrating silica-on-silicon waveguide with a PDMS microfluidic chip for fluorescence detection experiments. This lab-on-a-chip was a hybrid integrated optical microfluidic system, which utilizes the advantages of PDMS for the microfluidic circuits and the silica-on-silicon waveguide for the optical detection. A novel microfluidic assisted chemical polishing ( $\mu$ CP) of microchannel wall is proposed in this work. The main advantage of proposed hybrid integration approach is that any complex microfluidics circuits required for the micro total analysis system ( $\mu$ TAS) can be fabricated on PDMS and a low cost  $\mu$ TAS can be realized by integrating the SOS waveguide. Fluorescence detection ability of the lab-on-a-chip was initially investigated with quantum dots.

The detection of fluorophore-tagged rbST was carried out in the SOS-PDMS lab-on-a-chip. The detection limit of the device was found to be 240ng/ml and 312ng/ml for the Alexa-647 and FITC tagged rbST, respectively. The degrees of labeling were 10 and 1 for the FITC and Alexa-647, respectively and found that sensitivity of the

tagged FITC is lower than the unbound FITC due to higher degree of labeling and the associated decays in the quantum yield of FITC.

In order to have lower detection limit and the specificity to the detection, a novel evanescent wave sensor using a cascaded waveguide coupler (CWC) is modeled and implemented. The CWC was designed with optical power splitters and combiners made up of s-bends couplers and tapered waveguide. In CWC configuration, a large surface area to bind the tagged rbST is achieved and hence the sensitivity is greatly enhanced by splitting a single waveguide into multiple paths by s-bend splitters and subsequently combining them back to a single waveguide by s-bends combiners. Anti-rbST was functionalized on the waveguide to achieve the specificity to the detection. The detection limit of the CWC system is as low as 25ng/ml.

A novel process of manufacturing gold nano-island morphology is developed for the label-free detection of growth hormone. 3D FDTD simulation of gold nano-islands and its bio-sensing potential was carried out. A simple and low cost deposition method by using an angled convective assembly resulted in nano-cluster morphology. Due to the interparticle coupling effects, the nano-cluster morphology had a wide absorbance spectrum. By using a simple post deposition annealing, the nano-cluster morphology was transformed to nano-island morphology due to the lower melting point of nano-structure. The nano-island morphology has a wide distribution of nano-islands with size ranging from 10-100nm. The effect of near field coupling and its effect on the absorbance spectrum were observed in both the simulation and experiments. It is observed in the simulation that the smaller particle has less influence on the LSPR spectrum due to its weaker near field coupling. Gold nano-

islands were approximated with a gold hemisphere and simulated by using FDTD, which gives the results comparable with experiments when the diameter of the hemisphere was at 70nm. A dielectric layer equivalent to the bio-layer was placed covering the whole surface of the hemisphere and simulation results shows that the LSPR spectrum is strongly influenced by the thickness and refractive index of the dielectric layer. The LSPR spectrum is found to be insensitive to the thickness when the thickness of the dielectric layer was above 60nm, which shows that nano-island was highly suitable for the detection of events taking place very close to the surface of the nano-islands.

Refractive index sensitivity of the annealed and non-annealed platform investigated with known refractive index solution shows that the annealed platform has a refractive index sensitivity of 62.879nm/RIU compared to the lower sensitivity of 33.291 nm/RIU for the non-annealed platform. The nano-island deposited on the glass substrate was investigated for the label free detection of growth hormone (bST) and detection limit of the nano-islands was as low as 5ng/ml. As the manufacturing process of gold nano-islands was compatible with the microfabrication process, a nano-islands integrated lab-on-a-chip is developed with PDMS microfluidic chip.

The feasibility of using silver-PDMS nanocomposite for the detection growth hormone is investigated. The morphology and optical absorbance property of the silver-PDMS was tuned by heat treatment. It is observed the increase of the annealing temperature resulting in a narrow absorbance peak. The bio-sensitivity of sample annealed at higher temperature is less, as the higher annealing temperature lead to the migration of silver nanoparticles into the PDMS and hence it is less accessible for the

adsorption of biospecies. Subsequently a novel method of integration of silver-PDMS nano-composite in a PDMS microfluidic device is carried by in situ synthesis of silver-PDMS nanocomposite in a PDMS microfluidic chip and a lab-on-a-chip device is fabricated. Label free detection of growth hormone is demonstrated with the silver-PDMS nanocomposite integrated lab-on-a-chip. The sensitivity of the detection process was carried out by silver-PDMS substrate and the silver-PDMS integrated lab-on-a-chip. The sensitivity of the lab-on-a-chip was much higher.

A novel nano-island integrated evanescent wave based lab-on-a-chip was developed by adopting the manufacturing process of nano-islands on the glass explained in Chapter 5. Gold nano-islands were integrated on silica-on-silicon waveguide for a nano-enhanced evanescence sensor. The SOS chip with nano-islands was integrated into a PDMS microfluidics chip and a lab-on-a-chip was developed. The lab-on-a-chip was demonstrated for the label-free detection of rbST.

The separation of rbST from the milk is carried out by using the solid phase extraction (SPE) and detected by using the gold nano-islands.

Finally a monolithically integrated lab-on-a-chip was fabricated by integrating a micro-spectrometer, microfluidic channel and optical waveguide for the simultaneous detection of multiple analytes by tagging with different fluorphores having various optical properties.

The micro-spectrometer was modeled for operating in the range of 500-700nm by using FDTD techniques. Use of an aluminum coating on the grating facet is found to have enhanced the efficiency of the spectrometer. A novel method of monolithic integration of micro-spectrometer, microfluidic channel and waveguides was

proposed and implemented with single step lithography and etching. This process was carried out by a single mask composed of the features of the micro-spectrometer, microfluidic channel and optical waveguide. The patterns were etched in a single step micromachining. As the size of the grating was 500nm, a precise fabrication of the spectrometer was not successful. It is possible to fabricate the micro-spectrometer by using high resolution lithography such as e-beam lithography.

Table 11.1 illustrates comparison of various lab-on-a-chip platforms developed in this thesis

	<b>Device</b>	<b>Method of integration</b>	<b>Advantages</b>	<b>Limit of detection(LOD)</b>
1	SOS-PDMS Lab-on-a-chip (Chapter 2 and 3)	Hybrid	Simple fabrication method, Labeled detection	240ng/ml
2	Cascaded coupler waveguide (CWC) (Chapter 4)	Monolithic	Higher sensitivity and specificity, labeled detection	25ng/ml
3	Nano-islands integrated LOC (Chapter 5 and 6)	Hybrid	Higher sensitivity, specificity and label free detection	5ng/ml
4	Silver-PDMS Lab-on-a-chip (Chapter 7)	Monolithic	Good adhesion of nanoparticles with the PDMS, easy fabrication	20ng/ml
5	Nano-island integrated SOS-PDMS lab-on-a-chip (Chapter 8)	Hybrid	Label free detection of silica-on-silicon platform	20ng/ml

**Table 11.1** Comparison of Lab-on-a-chips developed in this thesis.

Following are the major contributions of this thesis:

1. A low cost lab-on-a-chip is developed on silica-on-silicon and PDMS hybrid platform and the coupling of light from the microchannel to the waveguide is enhanced by a novel microfluidic assisted chemical polishing of microchannel wall.
2. Fluorescence tagging and detection of growth hormone in SOS-PDMS lab-on-a-chip.
3. Novel method of enhancing the detection sensitivity by a cascaded waveguide coupler.
4. A novel method of deposition of gold nano-islands on glass and a glass-PDMS lab-on-a-chip for label free detection of growth hormone.
5. Integration of silver-PDMS nano-composite in a PDMS lab-on-a-chip for the label free detection of growth hormone.
6. Integration of gold nano-islands on silica-on-silicon waveguide and in a PDMS microfluidics channel for the development of a novel nano-enhanced evanescence based lab-on-a-chip.
7. Separation of growth hormone from milk by solid phase extraction and detection by gold nano-islands.
8. Fabrication of a monolithically integrated lab-on-a-chip on silica-on-silicon platform by the integration multiple waveguides, microfluidics channel and micro-spectrometer.

## 11.2 Future works

Various methods of fabrication of lab-on-a-chip for the detection of rbST are carried out in this thesis. In present work, a commercial spectrometer is used for the spectroscopy tasks. To miniaturize the spectrometer and to develop a standalone device, a monolithically integrated sensor platform having micro-spectrometer, microfluidic channel and optical waveguide is attempted, however, it was not successful mainly because it needs high resolution lithography to fabricate the gratings. With the developments of processes to fabricate the grating, a multi analytes detection platform in a compact form could be possible.

The separation of rbST from milk was carried out by solid phase extraction. It would be good to miniaturize this module and integrated with lab-on-a-chip platform for the rapid detection of growth hormone in milk for the point of need (PON) applications. Different separation process needs to investigate to test the performances and feasibility of integration with the lab-on-a-chip.

## References

- [1] B. A. Cooke, R. J. B. King and H. Van Der Molen, *Hormones and their Actions*. Elsevier Publishing Company, 1988.
- [2] G. S. Asimov and N. K. Krouze, "The lactogenic preparations from the anterior pituitary and the increase in milk yield from cows." *J. Dairy Sci.*, vol. 20, pp. 289-306, 1937.
- [3] M. H. Le Breton, S. Rochereau-Roulet, G. Pinel, L. Bailly-Chouriberry, G. Rychen, S. Jurjanz, T. Goldmann and B. Le Bizec, "Direct determination of recombinant bovine somatotropin in plasma from a treated goat by liquid chromatography/high-resolution mass spectrometry," *Rapid Communications in Mass Spectrometry*, vol. 22, pp. 3130-3136, 2008.
- [4] R. Bryan, "Biochemistry. by D. Voet and JG Voet," *Acta Crystallographica Section D: Biological Crystallography*, vol. 52, pp. 610-610, 1996.
- [5] X. Zhang, K. Nieforth, J. M. Lang, R. Rouzier-Panis, J. Reynes, A. Dorr, S. Kolis, M. R. Stiles, T. Kinchelov and I. H. Patel, "Pharmacokinetics of plasma enfuvirtide after subcutaneous administration to patients with human immunodeficiency virus: Inverse Gaussian density absorption and 2-compartment disposition." *Clin. Pharmacol. Ther.*, vol. 72, pp. 10, 2002.
- [6] H. John, M. Walden, S. Schäfer, S. Genz and W. G. Forssmann, "Analytical procedures for quantification of peptides in pharmaceutical research by liquid chromatography–mass spectrometry," *Analytical and Bioanalytical Chemistry*, vol. 378, pp. 883-897, 2004.
- [7] K. Prokai-Tatrai and L. Prokai, "Prodrug design for brain delivery of small-and medium-sized neuropeptides." *Methods in Molecular Biology (Clifton, NJ)*, vol. 789, pp. 313, 2011.
- [8] A. Oosterkamp, E. Gelpi and J. Abian, "Quantitative peptide bioanalysis using column-switching nano liquid chromatography/mass spectrometry," *Journal of Mass Spectrometry*, vol. 33, pp. 976-983, 1998.
- [9] S. S. de Kock, J. P. Rodgers and B. C. Swanepoel, "Growth hormone abuse in the horse: preliminary assessment of a mass spectrometric procedure for IGF-1 identification and quantitation," *Rapid Communications in Mass Spectrometry*, vol. 15, pp. 1191-1197, 2001.
- [10] W. Weckwerth, L. Willmitzer and O. Fiehn, "Comparative quantification and identification of phosphoproteins using stable isotope labeling and liquid chromatography/mass spectrometry," *Rapid Communications in Mass Spectrometry*, vol. 14, pp. 1677-1681, 2000.

- [11] L. M. Souza, T. C. Boone, D. Murdock, K. Langley, J. Wypych, D. Fenton, S. Johnson, P. H. Lai, R. Everett and R. Y. Hsu, "Application of recombinant DNA technologies to studies on chicken growth hormone," *J. Exp. Zool.*, vol. 232, pp. 465-473, 1984.
- [12] K. Stelwagen, A. M. Verrinder Gibbins and B. W. McBride, "Applications of recombinant DNA technology to improve milk production: a review," *Livest. Prod. Sci.*, vol. 31, pp. 153-178, 1992.
- [13] N. Rochut, B. Le Bizec, F. Monteau and F. André, "ESI-MS for the measurement of bovine and porcine somatotropins: Mass spectrometry for the study of natural mechanisms," *Analisis*, vol. 28, pp. 280-284, 2000.
- [14] F. H. Buttel, "The recombinant BGH controversy in the United States: toward a new consumption politics of food?" *Agriculture and Human Values*, vol. 17, pp. 5-20, 2000.
- [15] P. P. Groenewegen, B. W. McBride, J. H. Burton and T. H. Elsasser, "Bioactivity of milk from bST-treated cows," *J. Nutr.*, vol. 120, pp. 514-520, May, 1990.
- [16] J. Burkhardt, "On the ethics of technical change: The case of bST1," *Technology in Society*, vol. 14, pp. 221-243, 1992.
- [17] G. Rouser, A. Siakotos and S. Fleischer, "Quantitative analysis of phospholipids by thin-layer chromatography and phosphorus analysis of spots," *Lipids*, vol. 1, pp. 85-86, 1966.
- [18] R. Gohlke, "Time-of-flight mass spectrometry and gas-liquid partition chromatography," *Anal. Chem.*, vol. 31, pp. 535-541, 1959.
- [19] R. S. Gohlke and F. W. McLafferty, "Early gas chromatography/mass spectrometry," *J. Am. Soc. Mass Spectrom.*, vol. 4, pp. 367-371, 1993.
- [20] P. Přikryl, L. Havlíčková, V. Pacáková, J. Hradilová, K. Štulík and P. Hofta, "An evaluation of GC-MS and HPLC-FD methods for analysis of protein binders in paintings," *Journal of Separation Science*, vol. 29, pp. 2653-2663, 2006.
- [21] M. I. Churchwell, N. C. Twaddle, L. R. Meeker and D. R. Doerge, "Improving LC-MS sensitivity through increases in chromatographic performance: Comparisons of UPLC-ES/MS/MS to HPLC-ES/MS/MS," *Journal of Chromatography B*, vol. 825, pp. 134-143, 2005.
- [22] L. Castiglieo, G. Iannone, G. Grifoni, R. Rosati, D. Gianfaldoni and A. Guidi, "Natural and recombinant bovine somatotropin: immunodetection with a sandwich ELISA," *J. Dairy Res.*, vol. 74, pp. 79-85, 2007.

- [23] X. Zhao, B. McBride, L. Trouten-Radford, L. Golfman and J. Burton, "Somatotropin and insulin-like growth factor-I concentrations in plasma and milk after daily or sustained-release exogenous somatotropin administrations," *Domest. Anim. Endocrinol.*, vol. 11, pp. 209-216, 1994.
- [24] P. Groenewegen, B. McBride, J. Burton and T. Elsasser, "Bioactivity of milk from rbST treated cows," *J. Nutr.*, vol. 120, pp. 514-520, 1990.
- [25] C. M. Zwickl, H. W. Smith and P. H. Bick, "Rapid and sensitive ELISA method for the determination of bovine somatotropin in blood and milk," *J. Agric. Food Chem.*, vol. 38, pp. 1358-1362, 1990.
- [26] T. H. J. Heutmekers, M. G. E. G. Bremer, W. Haasnoot and M. W. F. Nielen, "A rapid surface plasmon resonance (SPR) biosensor immunoassay for screening of somatotropins in injection preparations," *Anal. Chim. Acta*, vol. 586, pp. 239-245, 2007.
- [27] J. N. Liang and B. Chakrabarti, "Spectroscopic investigations of bovine lens crystallins. 1. Circular dichroism and intrinsic fluorescence," *Biochemistry (N. Y.)*, vol. 21, pp. 1847-1852, 1982.
- [28] M. K. Lawless, S. Hopkins and M. K. Anwer, "Quantitation of a 36-amino-acid peptide inhibitor of HIV-1 membrane fusion in animal and human plasma using high-performance liquid chromatography and fluorescence detection," *Journal of Chromatography B: Biomedical Sciences and Applications*, vol. 707, pp. 213-217, 1998.
- [29] T. Feltkamp, "Conjugation of fluorescein isothiocyanate to antibodies: I. Experiments on the conditions of conjugation," *Immunology*, vol. 18, pp. 865, 1970.
- [30] Sigma Aldrich, "Technical bulletin FluoroTag FITC conjugation kit," .
- [31] P. Abgrall and A. Gue, "Lab-on-chip technologies: making a microfluidic network and coupling it into a complete microsystem—a review," *J Micromech Microengineering*, vol. 17, pp. R15, 2007.
- [32] M. Packirisamy and S. Badilescu, *BioMEMS: Science and Engineering Perspectives*. CRC Press, 2011.
- [33] E. Wachter and T. Thundat, "Micromechanical sensors for chemical and physical measurements," *Rev. Sci. Instrum.*, vol. 66, pp. 3662-3667, 1995.
- [34] R. Bashir, "BioMEMS: state-of-the-art in detection, opportunities and prospects," *Adv. Drug Deliv. Rev.*, vol. 56, pp. 1565-1586, 2004.

- [35] J. Yakovleva, R. Davidsson, M. Bengtsson, T. Laurell and J. Emnéus, "Microfluidic enzyme immunosensors with immobilised protein A and G using chemiluminescence detection," *Biosensors and Bioelectronics*, vol. 19, pp. 21-34, 2003.
- [36] J. Homola, S. S. Yee and G. Gauglitz, "Surface plasmon resonance sensors: review," *Sensors Actuators B: Chem.*, vol. 54, pp. 3-15, 1999.
- [37] K. A. Willets and R. P. Van Duyne, "Localized surface plasmon resonance spectroscopy and sensing," *Annu. Rev. Phys. Chem.*, vol. 58, pp. 267-297, 2007.
- [38] A. Messica, A. Greenstein and A. Katzir, "Theory of fiber-optic, evanescent-wave spectroscopy and sensors," *Appl. Opt.*, vol. 35, pp. 2274-2284, 1996.
- [39] A. Manz, N. Graber and H. Widmer, "Miniaturized total chemical analysis systems: a novel concept for chemical sensing," *Sensors Actuators B: Chem.*, vol. 1, pp. 244-248, 1990.
- [40] A. Manz, J. C. Fettinger, E. Verpoorte, H. Lüdi, H. Widmer and D. Harrison, "Micromachining of monocrystalline silicon and glass for chemical analysis systems A look into next century's technology or just a fashionable craze?" *TrAC Trends in Analytical Chemistry*, vol. 10, pp. 144-149, 1991.
- [41] L. Guo, G. Chen and D. H. Kim, "Three-dimensionally assembled gold nanostructures for plasmonic biosensors," *Anal. Chem.*, vol. 82, pp. 5147-5153, 2010.
- [42] S. Götz and U. Karst, "Recent developments in optical detection methods for microchip separations," *Analytical and Bioanalytical Chemistry*, vol. 387, pp. 183-192, 2007.
- [43] P. A. Auroux, D. Iossifidis, D. R. Reyes and A. Manz, "Micro total analysis systems. 2. Analytical standard operations and applications," *Anal. Chem.*, vol. 74, pp. 2637-2652, 2002.
- [44] T. Vilknér, D. Janásek and A. Manz, "Micro total analysis systems. Recent developments," *Anal. Chem.*, vol. 76, pp. 3373-3386, 2004.
- [45] J. Hu, V. Tarasov, A. Agarwal, L. Kimerling, N. Carlie, L. Petit and K. Richardson, "Fabrication and testing of planar chalcogenide waveguide integrated microfluidic sensor," *Optics Express*, vol. 15, pp. 2307-2314, 2007.
- [46] S. C. Jacobson and J. M. Ramsey, "Integrated microdevice for DNA restriction fragment analysis," *Anal. Chem.*, vol. 68, pp. 720-723, 1996.

- [47] M. A. Burns, B. N. Johnson, S. N. Brahmasandra, K. Handique, J. R. Webster, M. Krishnan, T. S. Sammarco, P. M. Man, D. Jones and D. Heldsinger, "An integrated nanoliter DNA analysis device," *Science*, vol. 282, pp. 484-487, 1998.
- [48] P. Friis, K. Hoppe, O. Leistiko, K. B. Mogensen, J. Hübner and J. P. Kutter, "Monolithic integration of microfluidic channels and optical waveguides in silica on silicon," *Appl. Opt.*, vol. 40, pp. 6246-6251, 2001.
- [49] H. Ou, "Different index contrast silica-on-silicon waveguides by PECVD," *Electron. Lett.*, vol. 39, pp. 212-213, 2003.
- [50] J. M. Ruano, A. Glidle, A. Cleary, A. Walmsley, J. S. Aitchison and J. M. Cooper, "Design and fabrication of a silica on silicon integrated optical biochip as a fluorescence microarray platform," *Biosensors and Bioelectronics*, vol. 18, pp. 175-184, 2003.
- [51] K. B. Mogensen, J. El-Ali, A. Wolff and J. P. Kutter, "Integration of polymer waveguides for optical detection in microfabricated chemical analysis systems," *Appl. Opt.*, vol. 42, pp. 4072-4079, 2003.
- [52] A. Leeds, E. Van Keuren, M. Durst, T. Schneider, J. Currie and M. Paranjape, "Integration of microfluidic and microoptical elements using a single-mask photolithographic step," *Sensors and Actuators A: Physical*, vol. 115, pp. 571-580, 2004.
- [53] S. Balslev, A. Jorgensen, B. Bilenberg, K. B. Mogensen, D. Snakenborg, O. Geschke, J. Kutter and A. Kristensen, "Lab-on-a-chip with integrated optical transducers," *Lab Chip*, vol. 6, pp. 213-217, 2006.
- [54] D. A. Chang-Yen, R. K. Eich and B. K. Gale, "A monolithic PDMS waveguide system fabricated using soft-lithography techniques," *J. Lightwave Technol.*, vol. 23, pp. 2088, 2005.
- [55] A. Chandrasekaran and M. Packirisamy, "Enhanced fluorescence-based bio-detection through selective integration of reflectors in microfluidic lab-on-a-chip," *Sens Rev*, vol. 28, pp. 33-38, 2008.
- [56] M. Packirisamy and A. Balakrishnan, *Planar Waveguide Based Grating Device and Spectrometer for Species-Specific Wavelength Detection*, 2008.
- [57] M. Medina-Sánchez, S. Miserere and A. Merkoçi, "Nanomaterials and lab-on-a-chip technologies," *Lab on a Chip*, 2012.
- [58] Y. Zhang, Y. Tang, Y. H. Hsieh, C. Y. Hsu, J. Xi, K. J. Lin and X. Jiang, "Towards a high-throughput label-free detection system combining localized-surface plasmon resonance and microfluidics," *Lab on a Chip*, 2012.

- [59] J. Ozhikandathil and M. Packirisamy, "Silica-on-silicon waveguide integrated polydimethylsiloxane lab-on-a-chip for quantum dot fluorescence bio-detection," *J. Biomed. Opt.*, vol. 17, pp. 017006, 2012.
- [60] J. Ozhikandathil, S. Badilescu and M. Packirisamy, "Detection of Fluorophore-Tagged Recombinant Bovine Somatotropin (rbST) by using a Silica-on-silicon (SOS)-PDMS Lab-on-a-chip," *IEEE Sensor Journal*, Accepted for publication, 2012.
- [61] J. Ozhikandathil, S. Badilescu and M. Packirisamy, "Gold nanoisland structures integrated in a lab-on-a-chip for plasmonic detection of bovine growth hormone," *J. Biomed. Opt.*, vol. 17, July, 2012.
- [62] D. Boturyn, J. L. Coll, E. Garanger, M. C. Favrot and P. Dumy, "Template assembled cyclopeptides as multimeric system for integrin targeting and endocytosis," *J. Am. Chem. Soc.*, vol. 126, pp. 5730-5739, 2004.
- [63] D. R. Reyes, D. Iossifidis, P. A. Auroux and A. Manz, "Micro total analysis systems. 1. Introduction, theory, and technology," *Anal. Chem.*, vol. 74, pp. 2623-2636, 2002.
- [64] H. Sato, H. Matsumura, S. Keino and S. Shoji, "An all SU-8 microfluidic chip with built-in 3D fine microstructures," *J Micromech Microengineering*, vol. 16, pp. 2318, 2006.
- [65] G. S. Fiorini and D. T. Chiu, "Disposable microfluidic devices: fabrication, function, and application," *BioTechniques*, vol. 38, pp. 429, 2005.
- [66] R. Pal, M. Yang, R. Lin, B. Johnson, N. Srivastava, S. Razzacki, K. Chomistek, D. Heldsinger, R. Haque and V. Ugaz, "An integrated microfluidic device for influenza and other genetic analyses," *Lab Chip*, vol. 5, pp. 1024-1032, 2005.
- [67] N. Panchuk-Voloshina, R. P. Haugland, J. Bishop-Stewart, M. K. Bhalgat, P. J. Millard, F. Mao, W. Y. Leung and R. P. Haugland, "Alexa dyes, a series of new fluorescent dyes that yield exceptionally bright, photostable conjugates," *Journal of Histochemistry & Cytochemistry*, vol. 47, pp. 1179, 1999.
- [68] K. E. Sapsford, T. Pons, I. L. Medintz and H. Mattoussi, "Biosensing with luminescent semiconductor quantum dots," *Sensors*, vol. 6, pp. 925-953, 2006.
- [69] A. Chandrasekaran and M. Packirisamy, "Integrated microfluidic biophotonic chip for laser induced fluorescence detection," *Biomed. Microdevices*, vol. 12, pp. 923-933, 2010.
- [70] J. Ozhikandathil and M. Packirisamy, "Silica-on-silicon (SOS)-PDMS platform integrated lab-on-a-chip (LOC) for quantum dot applications," in *Proceedings of SPIE*, 2010, pp. 775004.

- [71] T. Akimoto, H. Nanbu and E. Ikawa, "Reactive ion etching lag on high rate oxide etching using high density plasma," *Journal of Vacuum Science & Technology B: Microelectronics and Nanometer Structures*, vol. 13, pp. 2390-2393, 1995.
- [72] L. A. Donohue, J. Hopkins, R. Barnett, A. Newton and A. Barker, "Developments in si and SiO<sub>2</sub> etching for MEMS based optical applications," in *Proc. of SPIE Vol*, 2003, pp. 45.
- [73] C. Hnatovsky, R. Taylor, E. Simova, P. Rajeev, D. Rayner, V. Bhardwaj and P. Corkum, "Fabrication of microchannels in glass using focused femtosecond laser radiation and selective chemical etching," *Appl. Phys. A*, vol. 84, pp. 47-61, 2006.
- [74] J. Ozhikandathil, A. Morrison, M. Packirisamy and R. Wüthrich, "Low resistive silicon substrate as an etch-stop layer for drilling thick SiO<sub>2</sub> by spark assisted chemical engraving (SACE)," *Microsystem Technologies*, pp. 1-8, 2011.
- [75] L. Szekely and R. Freitag, "Fabrication of a versatile microanalytical system without need for clean room conditions," *Anal. Chim. Acta*, vol. 512, pp. 39-47, 2004.
- [76] K. Achuthan, J. Curry, M. Lacy, D. Campbell and S. Babu, "Investigation of pad deformation and conditioning during the CMP of silicon dioxide films," *J Electron Mater*, vol. 25, pp. 1628-1632, 1996.
- [77] Y. X. Li, P. French and R. Wolffenbuttel, "Plasma planarization for sensor applications," *Microelectromechanical Systems, Journal of*, vol. 4, pp. 132-138, 1995.
- [78] E. R. Goldman, E. D. Balighian, H. Mattoussi, M. K. Kuno, J. M. Mauro, P. T. Tran and G. P. Anderson, "Avidin: a natural bridge for quantum dot-antibody conjugates," *J. Am. Chem. Soc.*, vol. 124, pp. 6378-6382, 2002.
- [79] E. R. Goldman, A. R. Clapp, G. P. Anderson, H. T. Uyeda, J. M. Mauro, I. L. Medintz and H. Mattoussi, "Multiplexed toxin analysis using four colors of quantum dot fluororeagents," *Anal. Chem.*, vol. 76, pp. 684-688, 2004.
- [80] L. Yang and Y. Li, "Simultaneous detection of Escherichia coli O157: H7 and Salmonella Typhimurium using quantum dots as fluorescence labels," *Analyst*, vol. 131, pp. 394-401, 2005.
- [81] D. Gerion, F. Chen, B. Kannan, A. Fu, W. J. Parak, D. J. Chen, A. Majumdar and A. P. Alivisatos, "Room-temperature single-nucleotide polymorphism and multiallele DNA detection using fluorescent nanocrystals and microarrays," *Anal. Chem.*, vol. 75, pp. 4766-4772, 2003.
- [82] J. J. Molnar, K. A. Cummins and P. F. Nowak, "Bovine Somatotropin: Biotechnology Product and Social Issue in the United States Dairy Industry1," *J. Dairy Sci.*, vol. 73, pp. 3084-3093, 1990.

- [83] C. Soderholm, D. Otterby, J. Linn, F. Ehle, J. Wheaton, W. Hansen and R. Annexstad, "Effects of recombinant bovine somatotropin on milk production, body composition, and physiological parameters," *J. Dairy Sci.*, vol. 71, pp. 355-365, 1988.
- [84] A. Torkelson, K. Dwyer, G. Rogan and R. Ryan, "Radioimmunoassay of somatotropin in milk from cows administered recombinant bovine somatotropin," *J. Dairy Sci.*, vol. 70, pp. 146, 1987.
- [85] M. L. Scippo, G. Degand, A. Duyckaerts and G. Maghuin-Rogister, "Identification of bovine somatotropine-treated cows; Identification des vaches laitieres traitees a la somatotropine bovine," *Annales De Medecine Veterinaire (Belgium)*, 1997.
- [86] M. H. Le Breton , S. Rochereau-Roulet, G. Pinel, F. Monteau and B. Le Bizec, "Agilent technologies application note," 2008.
- [87] B. Bilenberg, T. Nielsen, B. Clausen and A. Kristensen, "PMMA to SU-8 bonding for polymer based lab-on-a-chip systems with integrated optics," *J Micromech Microengineering*, vol. 14, pp. 814, 2004.
- [88] T. Endo, K. Kerman, N. Nagatani, Y. Takamura and E. Tamiya, "Label-free detection of peptide nucleic acid-DNA hybridization using localized surface plasmon resonance based optical biosensor," *Anal. Chem.*, vol. 77, pp. 6976-6984, 2005.
- [89] E. M. Phizicky and S. Fields, "Protein-protein interactions: methods for detection and analysis." *Microbiol. Rev.*, vol. 59, pp. 94-123, 1995.
- [90] J. Ozhikandathil, S. Badilescu and M. Packirisamy, "Synthesis and characterization of silver-PDMS nanocomposite for the biosensing applications," in *Proceedings of SPIE*, 2011, pp. 800707.
- [91] J. Ozhikandathil, S. Badilescu and M. Packirisamy, "Synthesis and optical properties of immobilized spherical and non-spherical gold nanoparticles for detection of polypeptides and microfluidics applications," in *International Conference on Nanotechnology, Fundamentals and Applications*, Ottawa, Canada, 2010, .
- [92] H. Giloh and J. W. Sedat, "Fluorescence microscopy: reduced photobleaching of rhodamine and fluorescein protein conjugates by n-propyl gallate," *Science*, vol. 217, pp. 1252, 1982.
- [93] W. A. Staines, B. Meister, T. Melander, J. I. Nagy and T. Hökfelt, "Three-color immunofluorescence histochemistry allowing triple labeling within a single section." *Journal of Histochemistry & Cytochemistry*, vol. 36, pp. 145, 1988.

- [94] R. M. Mckinney, J. T. Spillane and G. W. Pearce, "Factors affecting the rate of reaction of fluorescein isothiocyanate with serum proteins," *The Journal of Immunology*, vol. 93, pp. 232, 1964.
- [95] J. Ozhikandathil and M. Packirisamy. Silica-on-silicon waveguide integrated polydimethylsiloxane lab-on-a-chip for quantum dot fluorescence bio-detection. *J. Biomed. Opt.* 17, 017006, 2012 .
- [96] B. Wood, S. Thompson and G. Goldstein, "Fluorescent antibody staining. 3. Preparation of fluorescein-isothiocyanate-labeled antibodies." *Journal of Immunology (Baltimore, Md.: 1950)*, vol. 95, pp. 225, 1965.
- [97] E. Jablonski, L. Brand and S. Roseman, "Sugar transport by the bacterial phosphotransferase system. Preparation of a fluorescein derivative of the glucose-specific phosphocarrier protein IIIGlc and its binding to the phosphocarrier protein HPr." *J. Biol. Chem.*, vol. 258, pp. 9690, 1983.
- [98] G. Horváth, M. Petrás, G. Szentesi, Á. Fábíán, J. W. Park, G. Vereb and J. Szöllösi, "Selecting the right fluorophores and flow cytometer for fluorescence resonance energy transfer measurements," *Cytometry Part A*, vol. 65, pp. 148-157, 2005.
- [99] G. Hungerford, J. Benesch, J. F. Mano and R. L. Reis, "Effect of the labelling ratio on the photophysics of fluorescein isothiocyanate (FITC) conjugated to bovine serum albumin," *Photochem.Photobiol.Sci.*, vol. 6, pp. 152-158, 2006.
- [100] M. F. McGrath, G. Bogosian, A. C. Fabellar, R. L. Staub, J. L. Vicini and L. A. Widger, "Measurement of bovine somatotropin (bST) and insulin-like growth factor-1 (IGF-1) in bovine milk using an electrochemiluminescent assay," *J. Agric. Food Chem.*, vol. 56, pp. 7044-7048, 2008.
- [101] M. H. Le Breton, A. Beck-Henzelin, J. Richoz-Payot, S. Rochereau-Roulet, G. Pinel, T. Delatour and B. Le Bizec, "Detection of recombinant bovine somatotropin in milk and effect of industrial processes on its stability," *Anal. Chim. Acta*, vol. 672, pp. 45-49, 2010.
- [102] D. A. Stuart, A. J. Haes, C. R. Yonzon, E. M. Hicks and R. P. Van Duyne, "Biological applications of localised surface plasmonic phenomena," *Nanobiotechnology, IEE Proceedings -*, vol. 152, pp. 13-32, 2005.
- [103] A. Chandrasekaran and M. Packirisamy, "Experimental investigation of evanescence-based infrared biodetection technique for micro-total-analysis systems," *J. Biomed. Opt.*, vol. 14, pp. 054050, 2009.

- [104] H. Helmers, P. Greco, R. Rustad, R. Kherrat, G. Bouvier and P. Benech, "Performance of a compact, hybrid optical evanescent-wave sensor for chemical and biological applications," *Appl. Opt.*, vol. 35, pp. 676-680, 1996.
- [105] A. P. Abel, M. G. Weller, G. L. Duveneck, M. Ehrat and H. M. Widmer, "Fiber-optic evanescent wave biosensor for the detection of oligonucleotides," *Anal. Chem.*, vol. 68, pp. 2905-2912, 1996.
- [106] P. Radhakrishnan, V. Nampoore and C. Vallabhan, "Fiber optic sensor based on evanescent wave absorption," *Optical Engineering*, vol. 32, pp. 692-694, 1993.
- [107] R. Srivastava, C. Bao and C. Gomez-Reino, "Planar-surface-waveguide evanescent-wave chemical sensors," *Sensors and Actuators A: Physical*, vol. 51, pp. 165-171, 1996.
- [108] C. Singh, H. Isobe, T. Fujinami and M. Ogita, "Effect of launching angle of light on critical micelle concentration determination using an optical fiber sensor based on adsorption effect," *Japanese Journal of Applied Physics*, vol. 43, pp. 3429, 2004.
- [109] J. P. Golden, G. P. Anderson, S. Rabbany and F. Ligler, "An evanescent wave biosensor. II. Fluorescent signal acquisition from tapered fiber optic probes," *Biomedical Engineering, IEEE Transactions on*, vol. 41, pp. 585-591, 1994.
- [110] B. Gupta, H. Dodeja and A. Tomar, "Fibre-optic evanescent field absorption sensor based on a U-shaped probe," *Opt. Quant. Electron.*, vol. 28, pp. 1629-1639, 1996.
- [111] A. Prabhakar and S. Mukherji, "Microfabricated polymer chip with integrated U-bend waveguides for evanescent field absorption based detection," *Lab Chip*, vol. 10, pp. 748-754, 2010.
- [112] C. Carniglia, L. Mandel and K. Drexhage, "Absorption and emission of evanescent photons," *JOSA*, vol. 62, pp. 479-486, 1972.
- [113] D. Marcuse, "Launching light into fiber cores from sources located in the cladding," *Lightwave Technology, Journal of*, vol. 6, pp. 1273-1279, 1988.
- [114] K. E. Sapsford and F. S. Ligler, "Real-time analysis of protein adsorption to a variety of thin films," *Biosensors and Bioelectronics*, vol. 19, pp. 1045-1055, 2004.
- [115] E. M. Larsson, J. Alegret, M. Käll and D. S. Sutherland, "Sensing characteristics of NIR localized surface plasmon resonances in gold nanorings for application as ultrasensitive biosensors," *Nano Letters*, vol. 7, pp. 1256-1263, 2007.

- [116] T. Chung, S. Y. Lee, E. Y. Song, H. Chun and B. Lee, "Plasmonic Nanostructures for Nano-Scale Bio-Sensing," *Sensors*, vol. 11, pp. 10907-10929, 2011.
- [117] N. Sanvicens, C. Pastells, N. Pascual and M. Marco, "Nanoparticle-based biosensors for detection of pathogenic bacteria," *TrAC Trends in Analytical Chemistry*, vol. 28, pp. 1243-1252, 2009.
- [118] S. S. R. Dasary, A. K. Singh, D. Senapati, H. Yu and P. C. Ray, "Gold nanoparticle based label-free SERS probe for ultrasensitive and selective detection of trinitrotoluene," *J. Am. Chem. Soc.*, vol. 131, pp. 13806-13812, 2009.
- [119] G. J. Nusz, S. M. Marinakos, A. C. Curry, A. Dahlin, F. Höök, A. Wax and A. Chilkoti, "Label-free plasmonic detection of biomolecular binding by a single gold nanorod," *Anal. Chem.*, vol. 80, pp. 984-989, 2008.
- [120] Y. Yuan, J. Zhang, H. Zhang and X. Yang, "Silver nanoparticle based label-free colorimetric immunosensor for rapid detection of neurogenin 1," *Analyst*, vol. 137, pp. 496-501, 2011.
- [121] S. Roy, C. K. Dixit, R. Woolley, R. O'Kennedy and C. McDonagh, "Label-free Optical Characterization Methods for Detecting Amine Silanization Driven Gold Nanoparticle Self-assembly," *Langmuir*, 2011.
- [122] N. Nath and A. Chilkoti, "Label-free biosensing by surface plasmon resonance of nanoparticles on glass: optimization of nanoparticle size," *Anal. Chem.*, vol. 76, pp. 5370-5378, 2004.
- [123] S. Szunerits, V. G. Praig, M. Manesse and R. Boukherroub, "Gold island films on indium tin oxide for localized surface plasmon sensing," *Nanotechnology*, vol. 19, pp. 195712, 2008.
- [124] A. J. Haes, S. Zou, G. C. Schatz and R. P. Van Duyne, "Nanoscale optical biosensor: short range distance dependence of the localized surface plasmon resonance of noble metal nanoparticles," *The Journal of Physical Chemistry B*, vol. 108, pp. 6961-6968, 2004.
- [125] C. R. Yonzon, D. A. Stuart, X. Zhang, A. D. McFarland, C. L. Haynes and R. P. Van Duyne, "Towards advanced chemical and biological nanosensors--An overview," *Talanta*, vol. 67, pp. 438-448, 2005.
- [126] I. Doron-Mor, H. Cohen, Z. Barkay, A. Shanzer, A. Vaskevich and I. Rubinstein, "Sensitivity of Transmission Surface Plasmon Resonance (T-SPR) Spectroscopy: Self-Assembled Multilayers on Evaporated Gold Island Films," *Chemistry--A European Journal*, vol. 11, pp. 5555-5562, 2005.

- [127] B. G. Prevo, J. C. Fuller III and O. D. Velev, "Rapid deposition of gold nanoparticle films with controlled thickness and structure by convective assembly," *Chemistry of Materials*, vol. 17, pp. 28-35, 2005.
- [128] Q. Zhang, J. J. Xu, Y. Liu and H. Y. Chen, "In-situ synthesis of poly (dimethylsiloxane)–gold nanoparticles composite films and its application in microfluidic systems," *Lab Chip*, vol. 8, pp. 352-357, 2007.
- [129] P. Devi, S. Badilescu, M. Packirisamy and P. Jeevanandam, "Synthesis of gold-poly (dimethylsiloxane) nanocomposite through a polymer-mediated silver/gold galvanic replacement reaction," *Gold Bulletin*, vol. 43, pp. 307, 2010.
- [130] U. Kreibig and M. Vollmer, "Optical properties of metal clusters," 1995.
- [131] P. K. Jain, S. Eustis and M. A. El-Sayed, "Plasmon coupling in nanorod assemblies: optical absorption, discrete dipole approximation simulation, and exciton-coupling model," *The Journal of Physical Chemistry B*, vol. 110, pp. 18243-18253, 2006.
- [132] J. Turkevich, P. C. Stevenson and J. Hillier, "A study of the nucleation and growth processes in the synthesis of colloidal gold," *Discuss. Faraday Soc.*, vol. 11, pp. 55-75, 1951.
- [133] K. Yee, "Numerical solution of initial boundary value problems involving Maxwell's equations in isotropic media," *Antennas and Propagation, IEEE Transactions on*, vol. 14, pp. 302-307, 1966.
- [134] W. Chew, "Electromagnetic theory on a lattice," *J. Appl. Phys.*, vol. 75, pp. 4843-4850, 1994.
- [135] J. P. Berenger, "A perfectly matched layer for the absorption of electromagnetic waves," *Journal of Computational Physics*, vol. 114, pp. 185-200, 1994.
- [136] P. K. Jain and M. A. El-Sayed, "Plasmonic coupling in noble metal nanostructures," *Chemical Physics Letters*, vol. 487, pp. 153-164, 2010.
- [137] P. K. Jain and M. A. El-Sayed, "Surface plasmon coupling and its universal size scaling in metal nanostructures of complex geometry: elongated particle pairs and nanosphere trimers," *The Journal of Physical Chemistry C*, vol. 112, pp. 4954-4960, 2008.
- [138] J. Vörös, "The density and refractive index of adsorbing protein layers," *Biophys. J.*, vol. 87, pp. 553-561, 2004.
- [139] V. Canpean and S. Astilean, "Multifunctional plasmonic sensors on low-cost subwavelength metallic nanoholes arrays," *Lab Chip*, vol. 9, pp. 3574-3579, 2009.

- [140] D. Stuart, A. Haes, C. Yonzon, E. Hicks and R. Van Duyne, "Biological applications of localised surface plasmonic phenomena," in *Nanobiotechnology, IEE Proceedings-*, 2005, pp. 13-32.
- [141] A. J. Haes, L. Chang, W. L. Klein and R. P. Van Duyne, "Detection of a biomarker for Alzheimer's disease from synthetic and clinical samples using a nanoscale optical biosensor," *J. Am. Chem. Soc.*, vol. 127, pp. 2264-2271, 2005.
- [142] B. G. Prevo, S. A. Esakoff, A. Mikhailovsky and J. A. Zasadzinski, "Scalable Routes to Gold Nanoshells with Tunable Sizes and Response to Near-Infrared Pulsed-Laser Irradiation," *Small*, vol. 4, pp. 1183-1195, 2008.
- [143] N. Nath and A. Chilkoti, "A colorimetric gold nanoparticle sensor to interrogate biomolecular interactions in real time on a surface," *Anal. Chem.*, vol. 74, pp. 504-509, 2002.
- [144] N. Nath and A. Chilkoti, "Label free colorimetric biosensing using nanoparticles," *J. Fluoresc.*, vol. 14, pp. 377-389, 2004.
- [145] A. L. Weikel, S. D. Conklin and J. N. Richardson, "A multiple reflection attenuated total reflectance sensor incorporating a glass-indium tin oxide surface modified via direct attachment or film encapsulation of colloidal gold nanoparticles," *Sensors Actuators B: Chem.*, vol. 110, pp. 112-119, 2005.
- [146] F. Frederix, J. M. Friedt, K. H. Choi, W. Laureyn, A. Campitelli, D. Mondelaers, G. Maes and G. Borghs, "Biosensing based on light absorption of nanoscaled gold and silver particles," *Anal. Chem.*, vol. 75, pp. 6894-6900, 2003.
- [147] J. C. Hulteen, D. A. Treichel, M. T. Smith, M. L. Duval, T. R. Jensen and R. P. Van Duyne, "Nanosphere lithography: size-tunable silver nanoparticle and surface cluster arrays," *The Journal of Physical Chemistry B*, vol. 103, pp. 3854-3863, 1999.
- [148] F. Fida, L. Varin, S. Badilescu, M. Kahrizi and V. V. Truong, "Gold Nanoparticle Ring and Hole Structures for Sensing Proteins and Antigen–Antibody Interactions," *Plasmonics*, vol. 4, pp. 201-207, 2009.
- [149] K. Fujiwara, H. Watarai, H. Itoh, E. Nakahama and N. Ogawa, "Measurement of antibody binding to protein immobilized on gold nanoparticles by localized surface plasmon spectroscopy," *Analytical and Bioanalytical Chemistry*, vol. 386, pp. 639-644, 2006.
- [150] M. D. Malinsky, K. L. Kelly, G. C. Schatz and R. P. Van Duyne, "Chain length dependence and sensing capabilities of the localized surface plasmon resonance of silver nanoparticles chemically modified with alkanethiol self-assembled monolayers," *J. Am. Chem. Soc.*, vol. 123, pp. 1471-1482, 2001.

- [151] J. Ye, K. Bonroy, D. Nelis, F. Frederix, J. D'Haen, G. Maes and G. Borghs, "Enhanced localized surface plasmon resonance sensing on three-dimensional gold nanoparticles assemblies," *Colloids Surf. Physicochem. Eng. Aspects*, vol. 321, pp. 313-317, 2008.
- [152] F. Toderas, M. Baia, L. Baia and S. Astilean, "Controlling gold nanoparticle assemblies for efficient surface-enhanced Raman scattering and localized surface plasmon resonance sensors," *Nanotechnology*, vol. 18, pp. 255702, 2007.
- [153] W. Xiaqin, N. Kensuke, Z. Meifang, K. Hidekatsu, I. Hideaki and C. Yoshiki, "Self-organized Multilayer Films and Porous Nanocomposites of Gold Nanoparticles with Octa(3-aminopropyl)octasilsesquioxane," *J. Inorg. Organometallic Mater.*, vol. 17, pp. 447-457, 2007.
- [154] S. Szunerits, M. R. Das and R. Boukherroub, "Short-and long-range sensing on gold nanostructures, deposited on glass, coated with silicon oxide films of different thicknesses," *The Journal of Physical Chemistry C*, vol. 112, pp. 8239-8243, 2008.
- [155] S. Szunerits, V. G. Praig, M. Manesse and R. Boukherroub, "Gold island films on indium tin oxide for localized surface plasmon sensing," *Nanotechnology*, vol. 19, pp. 195712, 2008.
- [156] Y. Flegler and M. Rosenbluh, "Surface Plasmons and Surface Enhanced Raman Spectra of Aggregated and Alloyed Gold-Silver Nanoparticles," *Research Letters in Optics*, vol. 2009, pp. 1-6, 2009.
- [157] Y. S. Shon, H. Y. Choi, M. S. Guerrero and C. Kwon, "Preparation of nanostructured film arrays for transmission localized surface plasmon sensing," *Plasmonics*, vol. 4, pp. 95-105, 2009.
- [158] K. C. Grabar, R. G. Freeman, M. B. Hommer and M. J. Natan, "Preparation and characterization of Au colloid monolayers," *Anal. Chem.*, vol. 67, pp. 735-743, 1995.
- [159] S. K. Ghosh and T. Pal, "Interparticle coupling effect on the surface plasmon resonance of gold nanoparticles: from theory to applications," *Chem. Rev.*, vol. 107, pp. 4797-4862, 2007.
- [160] J. J. Diao, F. S. Qiu, G. D. Chen and M. E. Reeves, "Surface vertical deposition for gold nanoparticle film," *J. Phys. D*, vol. 36, pp. L25, 2003.
- [161] B. G. Prevo and O. D. Velev, "Controlled, rapid deposition of structured coatings from micro-and nanoparticle suspensions," *Langmuir*, vol. 20, pp. 2099-2107, 2004.

- [162] H. Y. Choi, M. S. Guerrero, M. Aquino, C. Kwon and Y. S. Shon, "Preparation of Gold Nanoisland Arrays from Layer-by-Layer Assembled Nanoparticle Multilayer Films," *Bull.Korean Chem.Soc.*, vol. 31, pp. 291, 2010.
- [163] P. J. Alet, L. Eude and S. Palacin, "Transition from thin gold layers to nano-islands on TCO for catalyzing the growth of one-dimensional nanostructures," *Physica Status Solidi (a)*, vol. 205, pp. 1429-1434, 2008.
- [164] M. H. Park, X. Duan, Y. Ofir, B. Czeran, D. Patra, X. Y. Ling, J. Huskens and V. M. Rotello, "Chemically Directed Immobilization of Nanoparticles onto Gold Substrates for Orthogonal Assembly Using Dithiocarbamate Bond Formation," *ACS Applied Materials & Interfaces*, vol. 2, pp. 795-799, 2010.
- [165] I. Doron-Mor, H. Cohen, Z. Barkay, A. Shanzer, A. Vaskevich and I. Rubinstein, "Sensitivity of Transmission Surface Plasmon Resonance (T-SPR) Spectroscopy: Self-Assembled Multilayers on Evaporated Gold Island Films," *Chemistry—A European Journal*, vol. 11, pp. 5555-5562, 2005.
- [166] J. Zhang, M. Kambayashi and M. Oyama, "A novel electrode surface fabricated by directly attaching gold nanospheres and nanorods onto indium tin oxide substrate with a seed mediated growth process," *Electrochemistry Communications*, vol. 6, pp. 683-688, 2004.
- [167] G. Gupta, D. Tanaka, Y. Ito, D. Shibata, M. Shimojo, K. Furuya, K. Mitsui and K. Kajikawa, "Absorption spectroscopy of gold nanoisland films: optical and structural characterization," *Nanotechnology*, vol. 20, pp. 025703, 2009.
- [168] S. R. Wasserman, H. Biebuyck and G. M. Whitesides, "Monolayers of 11-trichlorosilylundecyl thioacetate: A system that promotes adhesion between silicon dioxide and evaporated gold," *J. Mater. Res.*, vol. 4, pp. 886-892, 1989.
- [169] C. Huang, K. Bonroy, G. Reekmans, W. Laureyn, K. Verhaegen, I. De Vlaminck, L. Lagae and G. Borghs, "Localized surface plasmon resonance biosensor integrated with microfluidic chip," *Biomed. Microdevices*, vol. 11, pp. 893-901, 2009.
- [170] W. Rechberger, A. Hohenau, A. Leitner, J. Krenn, B. Lamprecht and F. Aussenegg, "Optical properties of two interacting gold nanoparticles," *Opt. Commun.*, vol. 220, pp. 137-141, 2003.
- [171] J. Burton, G. MacLeod, B. McBride, J. Burton, K. Bateman, I. McMillan and R. Eggert, "Overall efficacy of chronically administered recombinant bovine somatotropin to lactating dairy cows," *J. Dairy Sci.*, vol. 73, pp. 2157-2167, 1990.
- [172] B. McBride, J. Burton, J. Gibson, J. Burton and R. Eggert, "Use of recombinant bovine somatotropin for up to two consecutive lactations on dairy production traits," *J. Dairy Sci.*, vol. 73, pp. 3248-3257, 1990.

- [173] T. D. Etherton and D. E. Bauman, "Biology of somatotropin in growth and lactation of domestic animals," *Physiol. Rev.*, vol. 78, pp. 745-761, 1998.
- [174] J. Emmelkamp, F. Wolbers, H. Andersson, R. S. DaCosta, B. C. Wilson, I. Vermes and A. van den Berg, "The potential of autofluorescence for the detection of single living cells for label-free cell sorting in microfluidic systems," *Electrophoresis*, vol. 25, pp. 3740-3745, 2004.
- [175] A. C. Romano, E. M. Espana, S. H. Yoo, M. T. Budak, J. M. Wolosin and S. C. G. Tseng, "Different cell sizes in human limbal and central corneal basal epithelia measured by confocal microscopy and flow cytometry," *Invest. Ophthalmol. Vis. Sci.*, vol. 44, pp. 5125-5129, 2003.
- [176] N. Nath and A. Chilkoti, "Label-free biosensing by surface plasmon resonance of nanoparticles on glass: optimization of nanoparticle size," *Anal. Chem.*, vol. 76, pp. 5370-5378, 2004.
- [177] J. Bürck, B. Zimmermann, J. Mayer and H. J. Ache, "Integrated optical NIR-evanescent wave absorbance sensor for chemical analysis," *Fresenius J. Anal. Chem.*, vol. 354, pp. 284-290, 1996.
- [178] A. De Leebeeck, L. K. S. Kumar, V. de Lange, D. Sinton, R. Gordon and A. G. Brolo, "On-chip surface-based detection with nanohole arrays," *Anal. Chem.*, vol. 79, pp. 4094-4100, 2007.
- [179] X. Hoa, A. Kirk and M. Tabrizian, "Towards integrated and sensitive surface plasmon resonance biosensors: a review of recent progress," *Biosensors and Bioelectronics*, vol. 23, pp. 151-160, 2007.
- [180] A. Saha, H. A. Love and R. Schwart, "Adoption of emerging technologies under output uncertainty," *Am. J. Agric. Econ.*, pp. 836-846, 1994.
- [181] S. Ahmed and A. Khosa, "An introduction to DNA technologies and their role in livestock production: A review," *JAPS, Journal of Animal and Plant Sciences*, vol. 20, pp. 305-314, 2010.
- [182] T. Fukazawa, F. Ohno and T. Baba, "Very compact arrayed-waveguide-grating demultiplexer using Si photonic wire waveguides," *Jpn.J.Appl.Phys*, vol. 43, pp. L673-L675, 2004.
- [183] K. Kodate and Y. Komai, "Compact spectroscopic sensor using an arrayed waveguide grating," *Journal of Optics A: Pure and Applied Optics*, vol. 10, pp. 044011, 2008.

- [184] F. Horst, W. M. J. Green, B. Offrein and Y. Vlasov, "Echelle grating WDM (de-) multiplexers in SOI technology based on a design with two stigmatic points," in *Proc. SPIE*, 2008, pp. 69960R.
- [185] B. Momeni, M. Chamanzar, E. Shah Hosseini, M. Askari, M. Soltani and A. Adibi, "Strong angular dispersion using higher bands of planar silicon photonic crystals," *Optics Express*, vol. 16, pp. 14213-14220, 2008.
- [186] R. F. Wolffenbuttel, "State-of-the-art in integrated optical microspectrometers," *Instrumentation and Measurement, IEEE Transactions on*, vol. 53, pp. 197-202, 2004.
- [187] S. Janz, A. Balakrishnan, S. Charbonneau, P. Cheben, M. Cloutier, A. Delâge, K. Dossou, L. Erickson, M. Gao and P. Krug, "Planar waveguide echelle gratings in silica-on-silicon," *Photonics Technology Letters, IEEE*, vol. 16, pp. 503-505, 2004.
- [188] R. Wüthrich and V. Fascio, "Machining of non-conducting materials using electrochemical discharge phenomenon--an overview," *Int. J. Mach. Tools Manuf.*, vol. 45, pp. 1095-1108, 2005.
- [189] R. Wüthrich, C. Comninellis and H. Bleuler, "Bubble evolution on vertical electrodes under extreme current densities," *Electrochim. Acta*, vol. 50, pp. 5242-5246, 2005.
- [190] R. Wüthrich and L. Hof, "The gas film in spark assisted chemical engraving (SACE)—a key element for micro-machining applications," *Int. J. Mach. Tools Manuf.*, vol. 46, pp. 828-835, 2006.
- [191] V. Fascio, H. Langen, H. Bleuler and C. Comninellis, "Investigations of the spark assisted chemical engraving," *Electrochemistry Communications*, vol. 5, pp. 203-207, 2003.
- [192] A. Daridon, V. Fascio, J. Lichtenberg, R. Wütrich, H. Langen, E. Verpoorte and N. F. de Rooij, "Multi-layer microfluidic glass chips for microanalytical applications," *Fresenius J. Anal. Chem.*, vol. 371, pp. 261-269, 2001.
- [193] V. Jain and S. Chak, "Electrochemical spark trepanning of alumina and quartz," *Mach. Sci. Technol.*, vol. 4, pp. 277-290, 2000.
- [194] N. Gautam and V. K. Jain, "Experimental investigations into ECSD process using various tool kinematics," *Int. J. Mach. Tools Manuf.*, vol. 38, pp. 15-27, 1998.
- [195] R. Wüthrich, U. Spaelter, Y. Wu and H. Bleuler, "A systematic characterization method for gravity-feed micro-hole drilling in glass with spark assisted chemical engraving (SACE)," *J Micromech Microengineering*, vol. 16, pp. 1891, 2006.

- [196] M. Jalali, P. Maillard and R. Wüthrich, "Toward a better understanding of glass gravity-feed micro-hole drilling with electrochemical discharges," *J Micromech Microengineering*, vol. 19, pp. 045001, 2009.
- [197] D. J. Kim, Y. Ahn, S. H. Lee and Y. K. Kim, "Voltage pulse frequency and duty ratio effects in an electrochemical discharge microdrilling process of Pyrex glass," *Int. J. Mach. Tools Manuf.*, vol. 46, pp. 1064-1067, 2006.
- [198] A. Allagui and R. Wüthrich, "Gas film formation time and gas film life time during electrochemical discharge phenomenon," *Electrochim. Acta*, vol. 54, pp. 5336-5343, 2009.
- [199] Z. P. Zheng, J. K. Lin, F. Y. Huang and B. H. Yan, "Improving the machining efficiency in electrochemical discharge machining (ECDM) microhole drilling by offset pulse voltage," *J Micromech Microengineering*, vol. 18, pp. 025014, 2008.

## **Appendix A: Low resistive silicon substrate as an etch-stop layer for drilling thick SiO<sub>2</sub> by Spark Assisted Chemical Engraving**

Appendix A is reproduced from the paper published in Journal of Microsystems technologies [ref 66]: *Jayan Ozhikandathil, Andrew Morrison, Muthukumaran Packirisamy, Rolf Wuthrich, "Low resistive silicon substrate as an etch-stop layer for drilling thick SiO<sub>2</sub> by spark assisted chemical engraving (SACE)," Journal of Microsystem Technologies, pp. 1-8, 2011.*

Spark Assisted Chemical Engraving (SACE) is used for the micromachining of silica layer deposited on silicon substrate for the fabrication of lab-on-a-chip in the beginning of the project. LOC could not be realized by SACE due to the high roughness of the micromachining process. However, in this work, it is demonstrated that the low resistive silicon can be used as good etch stop layer for the micromachining of silica layer by using SACE.

### **Abstract**

Controlling precisely the drilling depth in Spark assisted chemical engraving (SACE) remains challenging, particularly for low depths. The possibility of using an electrically conductive material as an etch-stop layer for SACE gravity-feed drilling is investigated in this paper. Micromachining of 30-35 $\mu$ m thick SiO<sub>2</sub> layers made on low resistive silicon substrate using constant DC and pulsed DC voltage demonstrated the etch-stop function of the conductive silicon layer. Measurements of etch rates and hole profiles along with scanning electron microscope (SEM) imaging reveal the

mechanism underlying the etch-stop mechanism. Low resistive silicon is demonstrated to be a good etch-stop layer for SACE gravity-feed drilling. Demonstration of machining of SiO<sub>2</sub> layer on silicon as a substrate and an etch-stop layer opens up new possibilities to adapt SACE for developing devices on silicon platform.

## **A1. Introduction**

Micromachining of thick silicon dioxide layer is an important requirement for fabrication of optical BioMEMS. Typically, Lab-On-a-Chip (LOC) devices based on optical detection techniques require the integration of microfluidic channels, micromixers, microreactors, and microphotonic elements together on silicon dioxide [71]. Presently, this requirement can be met by Deep Reactive Ion Etching (DRIE). DRIE requires complicated thin film deposition and photolithography techniques which make the process long and expensive. Also, mask/SiO<sub>2</sub> selectivity is an inherent issue which limits the machining of high aspect ratio structures. Though wet chemical based SiO<sub>2</sub> etchants (e.g. Buffered Hydrofluoric Acid) are well established for the machining of thin oxide films, they cannot be used for machining thick oxide because of the selectivity issues and the formation of curved sidewalls due to isotropic etching behaviour. Other possible technologies are laser machining and mechanical (ultra-sonic machining and power blasting) machining which are expensive and can seriously damage the material with micro cracks. In this work, we report the micromachining of thick SiO<sub>2</sub> using Spark Assisted Chemical Engraving (SACE) with low resistivity silicon substrate as etch-stop layer.

SACE is a non-conventional low cost micromachining technique based on electrochemical discharge phenomena [188, 189] which is well known in the literature as electrochemical discharge machining (ECDM) and electrochemical spark machining (ECSM), . The basic setup for SACE includes an electrochemical cell in which, in general, the cathode acts as a tool-electrode and the anode as counter-electrode. When the voltage applied across the electrodes is higher than a critical value, so that the current density on the tool-electrode is typically above  $1\text{A}/\text{mm}^2$  (for 30wt% NaOH electrolyte), bubbles forms vigorously on the tool-electrode and coalesce into a continuous gas film across which electrical discharges take place[190]. Bringing the tool-electrode close enough to the work-piece allows machining. This technology has been successfully employed for micromachining of non-conducting materials[188] such as glass[191, 192], quartz [193, 194] , and ceramics. Even though SACE is a low cost process and suitable for high aspect ratio machining, a serious issue which prevents its industrial adaptation is the non-repeatability of machining rate. As machining rate of glass is very fast, typically about  $100\mu\text{m}/\text{s}$  down to an etch depth of around  $50\mu\text{m}$ [195], precise machining of structures with less than  $50\mu\text{m}$  thickness is a challenging issue requiring precise online measurement of machining depth and fast shutdown of the process. A rapid shutdown of the process is difficult because the machining does not stop quickly as soon as machining voltage is switched off due to ongoing chemical etching. This demands an alternative etch-stop mechanism for SACE micromachining. A mechanism proposed here uses an electrically conductive layer as an etch-stop layer. This is based on the idea that once the tool electrode contacts with the conductive

etch-stop layer, the current density is reduced well below the critical value of  $1\text{A}/\text{mm}^2$  required to form a gas film around it, due to the increase in surface area. Inhibiting the formation of the gas film at the current density below the critical value stops the electrical discharge activity around the tool-electrode leading to the stopping of machining.

This etch-stop mechanism is investigated by drilling microholes in a silicon dioxide layer of  $30\text{-}35\mu\text{m}$  on a silicon substrate using constant DC and pulsed DC voltages. SACE micromachining of such a thin material layer on silicon was never reported before and it is not obvious that it will withstand SACE machining. A low resistivity silicon (100) substrate was used to investigate the possibility to employ it as an etch-stop layer for the SACE micromachining. This is the first report of employing SACE for micromachining of silicon dioxide deposited as a layer on silicon and the demonstration of using low resistivity silicon substrate as an etch-stop layer. This opens up new possibilities to adapt SACE for developing opto-microfluidics devices compatible for silicon platform.

## **A2. Experimental details**

A layer of  $30$  to  $35\mu\text{m}$  thick silicon dioxide on silicon substrate was used as a sample which is shown in Figure 1(a). Schematic of the sample with micro holes drilled at different places is shown in Figure 1(b). A variation of  $5\mu\text{m}$  in the thickness of oxide layer is observed. This sample was fabricated by CVD (Chemical Vapour Deposition) deposition of  $\text{SiO}_2$  on a (100) silicon wafer. The resistivity of the silicon wafer was found to be varying between  $2\text{-}4\Omega\text{-cm}$ . The sample was attached to a standard microscope glass slide and fixed in the processing cell filled with a  $30\text{wt}\%$  NaOH

solution prepared from deionised water. The processing cell was mounted on a XY micro-positioning stage which is arranged underneath the tool electrode. The SACE machining was carried out using a setup similar to the one explained in the reference [195].

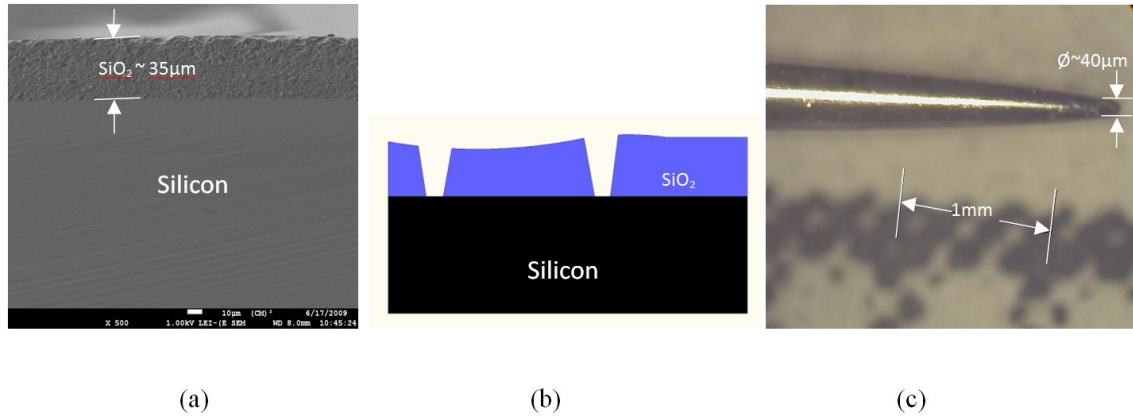


**Figure A1** (a) SEM micrograph illustrating the SiO<sub>2</sub> layer on Silicon substrate (b) An illustration of the microholes on different places of SiO<sub>2</sub> Layer, (c) Tool electrode used for the SACE micromachining.

The tool-electrode, a cylindrical needle of stainless steel having a tip diameter of  $\sim 40\mu\text{m}$  (Figure 1c), was mounted on a machining head designed for gravity feed drilling and monitoring the progress of machining. A voice coil actuator embedded in the machining head ensures the necessary force for the gravity feed drilling (0.8N in the present work). A commercially available optical sensor (SFH 9201 reflective optics) incorporated in the machining head monitors the progress of drilling with an error of less than  $\pm 1\mu\text{m}$ . Sensor data was acquired with a commercial DSP system using an AD interface at 1 kHz sampling rate. The machining head was attached to a

micro-stage which helps to position precisely the tool electrode in the XY-plane.

A 40V/4A power supply, based on a PA92 MOSFET amplifier which is capable of stabilizing the output voltage from the possible fluctuations due to the discharge activity, was used. Current during machining operations was measured with a current probe (Hall sensor) and recorded simultaneously to the drilling evolution at 1kHz acquisition rate.

In the experiments for each set of parameters seven holes were made. Drilling was done for 7 seconds in all the experiments. SEM pictures were taken to evaluate the geometrical profile of the holes. A Mitutoyo SJ-400 surface roughness tester (0.00025 $\mu$ m resolution on 8 $\mu$ m range) was used to investigate etch profile of holes.

### **A3. Results and discussion**

#### ***A3.1 Machining on (100) Silicon substrate***

In the first series of experiments the possibility of using a conductive substrate as an etch-stop layer for SACE gravity-feed drilling is investigated. Drilling on a (100) silicon wafer of 2-4 $\Omega$ -cm resistivity was carried out.

Figure 2 shows the variation of the relative movement  $z(t)$  of the tool and the corresponding electrode current as function of time during the drilling of silicon using SACE at 30V supply. From the current signal, one can see that the power source is attempting to supply a high current (7A spike) before limiting itself to 3.5A (internal limitation of the device). As expected, due to the high electrode surface, no gas film can be formed and no discharge activity is observed in the current signal. In this interval, tool will be slightly pushed upward due to the bubbles formation and the

thermal expansion of the tool. After about 2 seconds, the power supply shuts down automatically by switching to its overload mode. The process restarts periodically as the power supply leaves the overload mode.

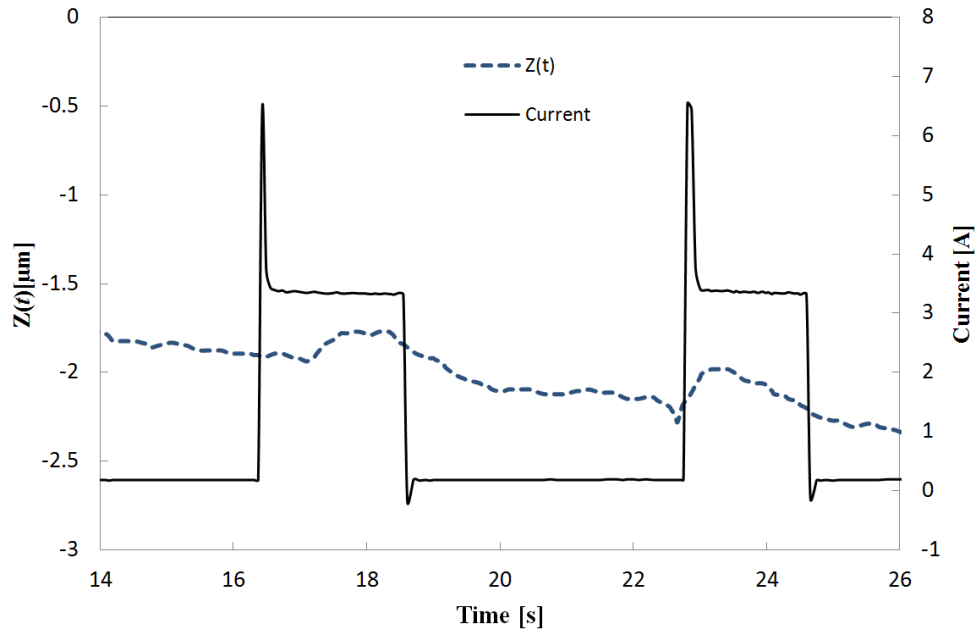


**Figure A2.** Relative movement of tool  $Z(t)$  and current signal in SACE machining of Silicon

Silicon is found to be slightly etched due to thermal induced chemical phenomenon during the time of high current (3.5A). An effective gas film formation required for the SACE machining is not observed in this experiment. This concludes that the low resistivity silicon act as a good etch-stop layer for SACE gravity-feed drilling.

### ***A3.2 DC micromachining of thick $\text{SiO}_2$ layer on low resistivity silicon***

Micro-holes were drilled with DC voltage of 27, 28, 29 and 30V. Machining was carried out for the duration of 7 seconds. For each voltage, 7 holes were drilled to check the repeatability of machining characteristics. Figure 3(a) shows the material

removal rate of SACE with voltage from 27 to 30V. Only the first 1.7 seconds are shown as no further increase in the drilling depth was observed from 1.7 to 7 seconds. Etching begins about 100ms after the machining voltage is switched on as seen in Figure 3(a). During this interval, gas bubbles are vigorously formed around the electrode and they slightly push the electrode upward. After this interval, one can identify two different regions in the evolution depending up on the martial removal rate. In the first region, from 150 to 250ms, machining is fast and almost independent of voltage until the etch depth of about 20 $\mu$ m. In the second region, i.e. after 250ms of machining, the machining was found to be slowly progressing at different etch rates and eventually stops at different etch depths for different voltages. The drilling evolution in the first region is similar to the previously reported glass machining [195].

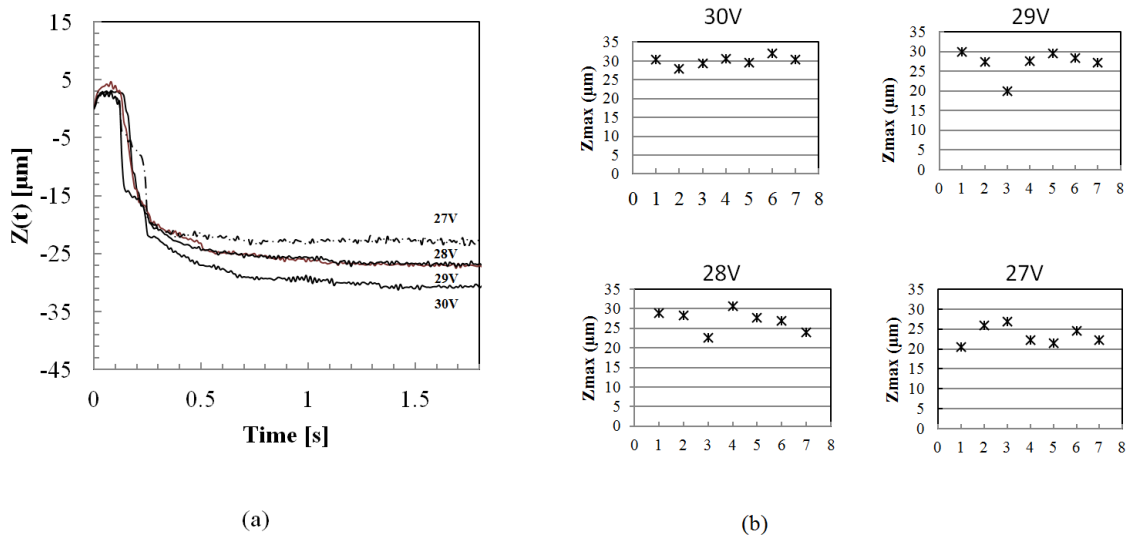


**Figure A3** (a) Progress of drilling depth  $Z(t)$  (Mean over 7 drillings) for different voltages (b) Maximum drilling depth  $Z_{max}$  after 7 seconds for various voltages.

Maximum etch depth reached of all the seven holes for different voltages is illustrated in Figure 3(b). The variation of the maximum reached depths for a given voltage is within the variation of the thickness of the deposited SiO<sub>2</sub> layer. However, there is a clear dependence of the maximum depth with machining voltage. Further, contrary as in the case of the experiments reported in section 3.1, no inhibition of the formation of the gas film is observed in the current signal. To investigate the mechanism responsible of the etch-stop, micro-hole profiles were also studied.

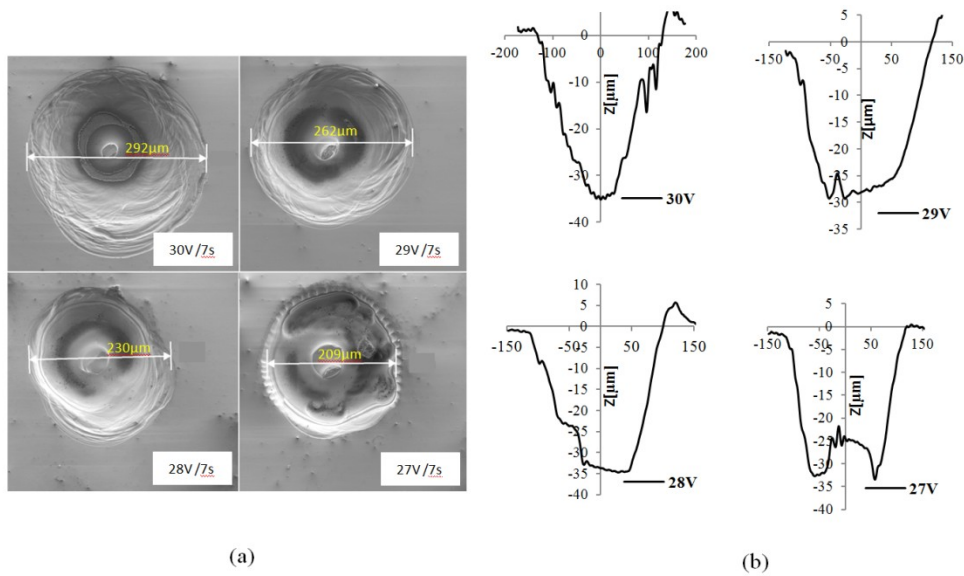


**Figure A4** (a) SEM micrograph of drilled holes under different DC voltage, (b) Profile of etched holes under different DC voltages.

Figure 4 shows representative sample of micro-hole entrance (SEM micro-graphs) and profiles obtained after drilling for 7s. Even the SiO<sub>2</sub> is quite thin, it remained bonded to the silicon substrate. Machining voltage has a significant influence on the entrance diameter and the etch profile. For 27V, the entrance diameter is measured at 209 µm and increases by 30 µm when voltage is increased for one volt increase as

shown in Figure 5. It can be seen further from Figure 5 that the difference between entrance and bottom diameter (measured at 30 $\mu$ m depth) is also increasing when the voltage increases from 27 to 30V.

In summary, etch profiles of higher machining voltage (30V) are more V shaped whereas for lower machining voltages, they are more U shaped as seen from Figure 4(b). Also an irregular micro-bump in the bottom parts of the hole is observed. The bump is larger for lower voltages than for high machining voltages. Hole entrance is also more irregular (Figure 4a) for low voltages. From these etch profiles, it is apparent that the difference in the etch-stop at different voltages is due to the micro-bumps formation. The profiles also provide an indication about the mechanism of the etch-stop.

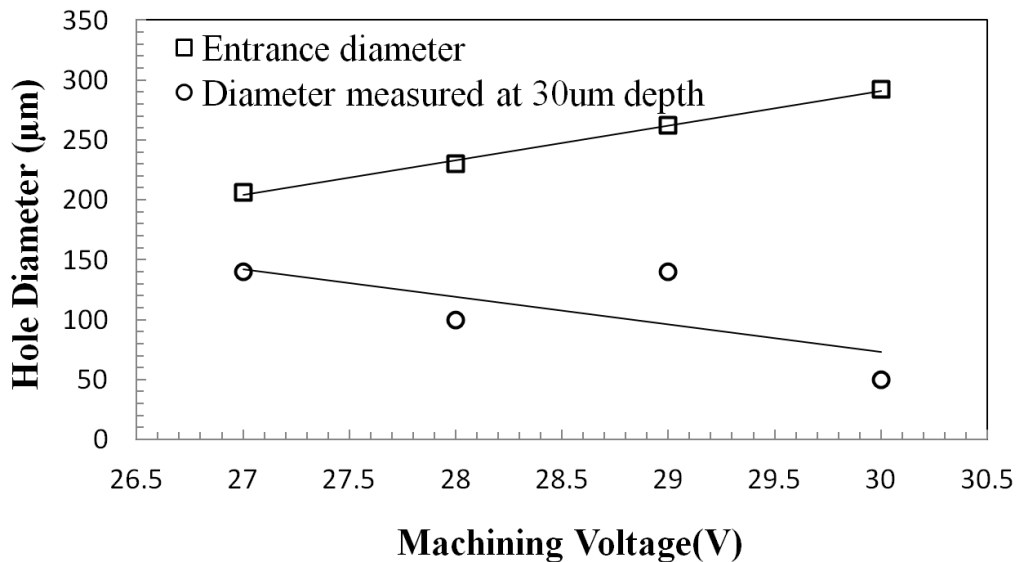


**Figure A5** Illustration of verticality of the hole as a function of voltage

Figure 6 shows a schematic of the micro-hole together with the tool-electrode based on the latest model for gravity-feed SACE drilling[196]. Most likely the tool-electrode is touching on the bump formed at the bottom part of the hole or maybe in direct contact with the silicon. The bottom surface of the micro-hole, of surface area of about  $0.002 \text{ mm}^2$ , is electrically conductive and is in contact with the tool-electrode. This surface becomes an extension of the tool-electrode electrically resulting in the formation of gas film on the surface that prevents further machining. Besides the etch-stop mechanism, the profiles of the drilled structures show the formation of V or U shaped holes. This aspect was already observed by Kim *et al.*[197] in the context of pulsed voltage drilling of glass. We propose here the following mechanism to be responsible of this effect. Recently the mean life-time of the gas film formed around the tool-electrode was investigated as a function of voltage [198]. It was found that gas film life-time increases with the voltage. Therefore, when low machining voltage is used, the short life-time of gas film allows frequent and smooth flow of electrolyte into the hole leading to more vertical or U shaped hole. To further verify this mechanism, experiments using pulsed voltage allowing controlled formation and detachment of the gas film on the tool-electrode are conducted.

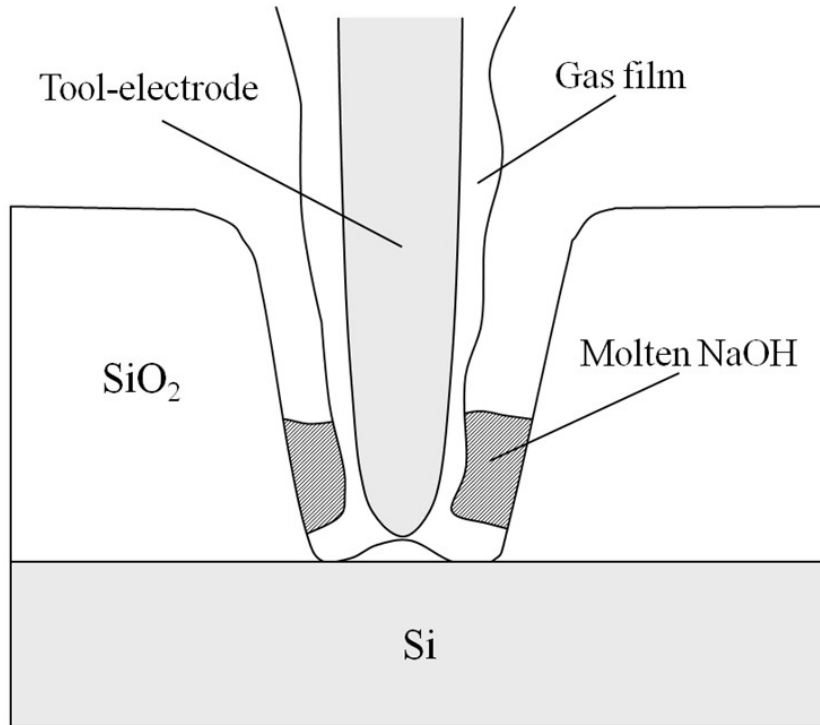
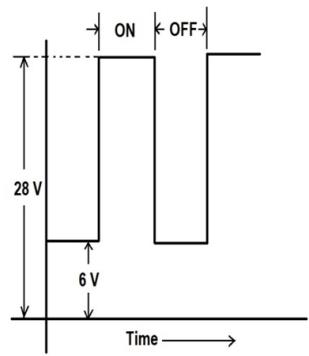


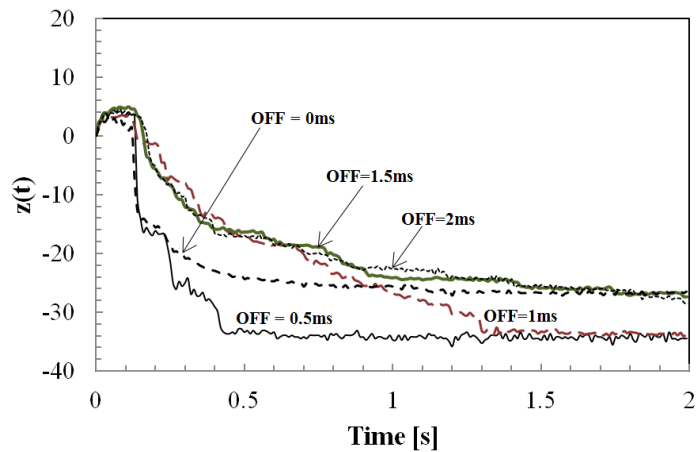
**Figure A6** Schematic of SACE drilling of SiO<sub>2</sub> deposited on Si by gravity-feed.

### ***A3.3 Drilling using pulsed DC voltage***

The gas film forming around the tool electrode can be controlled by the ON and OFF duration of pulsed voltage. The pulse signal used is shown in Figure 7(a). Pulse ON time voltage was kept at 28V and OFF time voltage was kept at 6V[199]. ON time of the pulse was kept at 2ms while OFF time was varied as 0.5ms, 1ms, 1.5ms and 2ms. According to [Error! Reference source not found.], the gas film formation time and mean life time of the gas film is 2.4ms and 1.6ms respectively for the machining voltage of 28V. With the selected parameters, the presence of the gas film was controlled by the pulse OFF time.



(a)



(b)

**Figure A7** (a) Pulse voltage used for SACE machining, (b) Progress of etching for pulses with various OFF time and constant ON time of 2 ms at 28V.

Figure 7(b) shows the variation of material removal rate for different OFF times (for the constant DC (with 28V) is also included for comparison). Material removal rate increases when the pulse OFF time reduces. Further, the maximal reached depth decreases with increasing pulse OFF time reaching the same maximal depth as in the case of DC drilling at 28V. Analysis of the etch profiles (Figure 8 and Figure 9) shows how the profile progressively changes from a V to a U shaped profile as pulse OFF time increases. This result demonstrates clearly that the shape of the drilled hole is not a function of the machining voltage but of the mean gas film life time. The absence of the gas film promotes flow of electrolyte into the hole, making the sharp side walls.

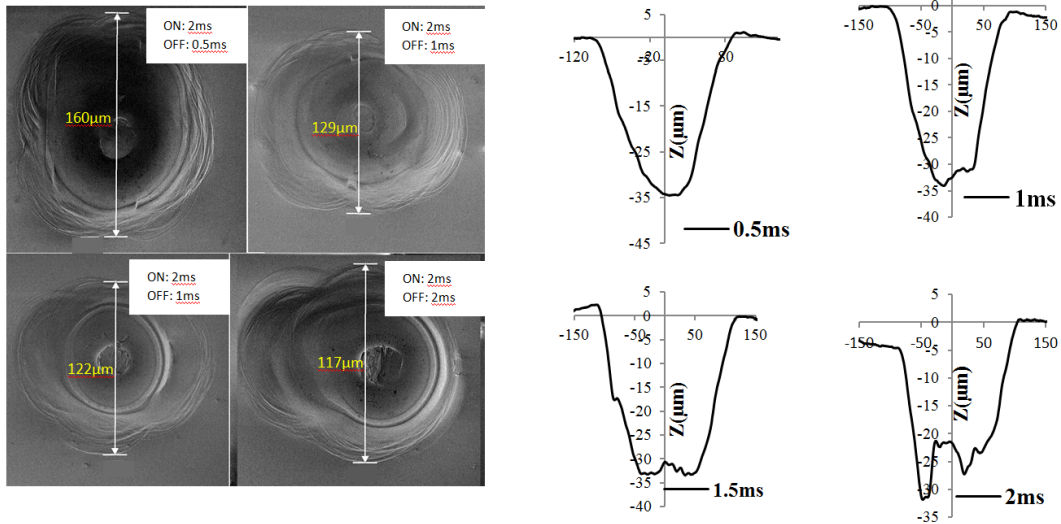


**Figure A8** (a) SEM micrographs of drilled hole with different pulse OFF time, and constant ON time. (b) Etch profile of hole with different pulse OFF time and constant ON time.

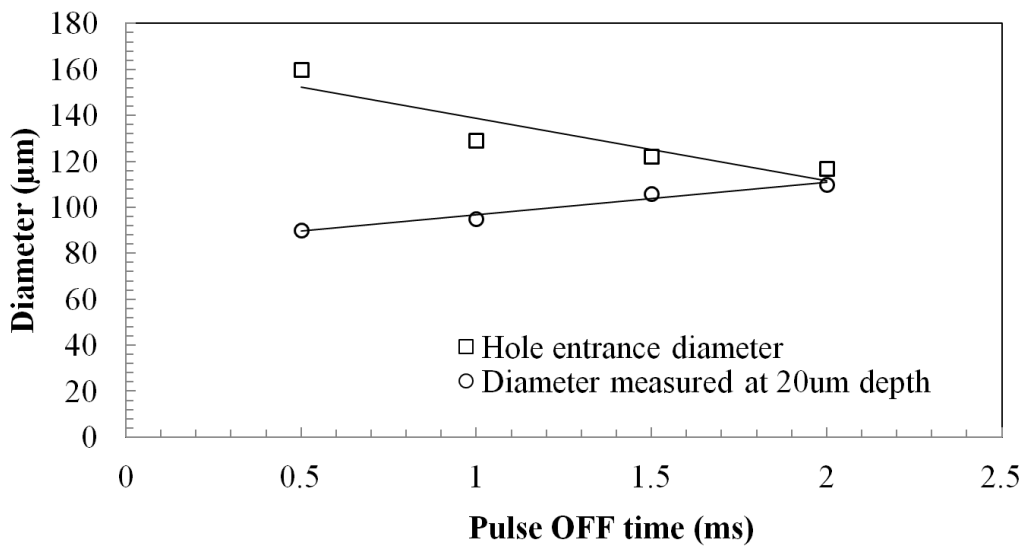


**Figure A9** Variation of verticality of the hole against of pulse OFF time.

#### A4. Conclusions

SACE micromachining of amorphous silica layer is presented. Microholes on 35 μm

thick silica layer on a silicon substrate were made using constant DC and pulsed DC machining voltages. The utilisation of silicon as an etch-stop layer for SACE gravity-feed drilling was demonstrated. Two mechanisms leading to this result could be identified as:

- For bulk silicon, machining stops due to inhibition of electrical discharge activity around the tool-electrode due to its contact with the conducting substrate;
- For buried silicon, machining stops because the silicon acts as a prolongation of the tool-electrode on which a gas film is formed protecting it from further etching.

Further a mechanism, based on the gas film life-time, responsible for the formation of V- or U-shaped micro-holes was proposed.

Demonstration of machining a SiO<sub>2</sub> layer on silicon substrate and utilisation of the silicon substrate as an etch-stop layer would open up new possibilities to adapt SACE for developing devices compatible with the silicon platform.